EXPERIMENTAL STUDIES ON FRICTION COEFFICIENT OF AL 6061-T6 ALLOY CONTACTS UNDER FULL SLIDING

Thesis
submitted in partial fulfillment of the requirements for the degree of

DOCTOR OF PHILOSOPHY

by

SRINIVASULA REDDY I.
(155072 AM15F04)

DEPARTMENT OF WATER RESOURCES AND OCEAN ENGINEERING
NATIONAL INSTITUTE OF TECHNOLOGY KARNATAKA
SURATHKAL, MANGALORE - 575 025, INDIA

JULY, 2021

EXPERIMENTAL STUDIES ON FRICTION COEFFICIENT OF AL 6061-T6 ALLOY CONTACTS UNDER FULL SLIDING

Thesis
submitted in partial fulfillment of the requirements for the degree of

DOCTOR OF PHILOSOPHY

by

SRINIVASULA REDDY I.
(155072 AM15F04)

Under the guidance of

Dr. VADIVUCHEZHIAN KALIVEERAN
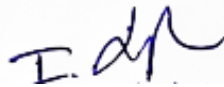Assistant Professor

DEPARTMENT OF WATER RESOURCES AND OCEAN ENGINEERING
NATIONAL INSTITUTE OF TECHNOLOGY KARNATAKA
SURATHKAL, MANGALORE - 575 025, INDIA

JULY, 2021

DECLARATION

I hereby declare that the Ph.D. Thesis entitled **"EXPERIMENTAL STUDIES ON FRICTION COEFFICIENT OF AL 6061-T6 ALLOY CONTACTS UNDER FULL SLIDING"** which is being submitted to **National Institute of Technology Karnataka, Surathkal,** for the partial fulfillment of the requirement for the award of degree of **Doctor of Philosophy** in the **Department of Water Resources and Ocean Engineering** is a bonafide report of the work carried out by me. The material contained in this Ph.D. Thesis has not been submitted to any university or Institution for the award of any degree.

…………………………………………………..

SRINIVASULA REDDY I. (155072 AM15F04)

Department of Water Resources and Ocean Engineering

National Institute of Technology Karnataka, Surathkal

Place: NITK, SURATHKAL.

Date: 16th JULY 2021

CERTIFICATE

This is to certify that the Ph.D. Thesis entitled **"EXPERIMENTAL STUDIES ON FRICTION COEFFICIENT OF AL 6061-T6 ALLOY CONTACTS UNDER FULL SLIDING"** submitted by **SRINIVASULA REDDY I. (155072 AM15F04),** as the record of the work carried out by him, is accepted as the Ph.D. Thesis submission in partial fulfillment of the requirements for the award of the degree of **Doctor of Philosophy** in the **Department of Water Resources and Ocean Engineering, National Institute of Technology Karnataka, Surathkal**, is a bonafide work carried out by him under my supervision and guidance**.**

02/08/2021

....

Dr. VADIVUCHEZHIAN KALIVEERAN

Assistant Professor

Department of Water Resources and Ocean Engineering

National Institute of Technology Karnataka, Surathkal

....

Chairman - DRPC

Department of Water Resources and Ocean Engineering

National Institute of Technology Karnataka, Surathkal

ACKNOWLEDGEMENT

ABSTRACT

Aim of the present research work is to study dry sliding coefficient of friction of aluminium to aluminium contacts in detail and to study evolution of coefficient of friction with change in normal load, sliding speed and temperature. Dry sliding experiments were conducted using pin on disk type tribometer. Specimens (both pin and disk) were fabricated using Al 6061-T6 alloy. The disk specimen has dimensions of 165 mm diameter and 8 mm thickness; the pin specimen dimensions are 30 mm length, 6 mm x 6 mm cross-section and 3 mm radius of curvature at cylindrical contact. Experiments were conducted with cylinder on flat contact configuration. Dry sliding experiments were conducted by applying normal loads of 1 kg, 1.5 kg and 2 kg; at different sliding speeds of 1.25 m/s, 2 m/s and 3 m/s; at different temperatures room temperature (31 ± 1 °C), 60 °C, 100 °C and 150 °C. The coefficient of friction at contact interface is influenced by both frictional heat generated and external temperature. The frictional heat at contact interface was estimated by measuring temperatures at 3 mm and 7 mm from contact interface of pin specimen during dry sliding experiments. One-dimensional inverse heat transfer model was developed using Finite Element Method and Beck's algorithm to estimate the contact interface temperature. The inverse heat transfer model was validated by using *ANSYS* transient thermal analysis. Maximum bulk temperature at contact interface was observed for all the experimental conditions at room temperature. Temperature due to frictional heat at contact interface increased with increase in normal load and sliding speed. The maximum frictional heat of 100 °C was observed at 2 kg normal load and 3 m/s sliding speed condition. The frictional heat and external heat source temperatures are the reasons for formation of oxide layer at contact interface during sliding which ultimately changes the coefficient of friction of contact pair. Coefficient of fiction, after the first cycle of sliding, stabilized stage, unsteady state and steady state are reported elaborately in this study. The coefficient of friction and wear rate were more influenced by increase in normal load than by increase in sliding speed and temperature. Adhesive and abrasive wear mechanisms were observed in dry sliding of Al 6061-T6 alloy contacts from the microscopic analysis of worn contact surfaces. Under normal loads of 1 kg and 1.5 kg, Al 6061-T6 alloy showed better wear

resistance at higher temperatures when compared to that at room temperature.

TABLE OF CONTENTS

CHAPTER 4

CHAPTER 5

CHAPTER 6

CONCLUSIONS   **133**

LIST OF FIGURES

LIST OF TABLES

NOMENCLATURE

c specific heat, J/(kg °C)

dq change in heat flux, W/m^2

E(x) residual

k thermal conductivity, W/ (m °C)

L length of pin considered for analysis, 7 mm

N$_i$ interpolation function

n$_{max}$ end time step number

t time, s

T temperature, °C

T$_{est}$ estimated temperature, °C

T$_{mea}$ measured temperature, °C

T_i^n temperature at node i and time step n, °C

$\dot{T}$ differential of temperature with time

q heat flux, W/m^2

q$_{cor}$ corrected heat flux, W/m^2

u constant, 4

W$_i$ weight function

x distance from the contact interface, m

Greek symbols

ρ density of material, kg/m^3

Δt time step size, s

ε small fraction, 0.0001

ϕ sensitivity coefficient

Superscripts

j real number, 1, 2, …. u.

n time step number

Subscript

i node number

CHAPTER 1

INTRODUCTION AND LITERATURE SURVEY

1.1 GENERAL

Aluminium alloys are used in marine, automobile, aerospace and civil construction industries due to their high strength to weight ratio, good corrosion resistance, ease of weldability, low electrical resistance and good machinability properties (Sharma, 2001). Applications of these alloys play vital role in naval structures such as deckhouses, hulls, hatch covers of commercial ships, ladders, railings, windows and doors. In marine engineering, the load capacity of ships is increased by replacing the steel components with aluminum alloy components to reduce the dead weight of components by 50 - 60 %. The properties of pure aluminium can be enhanced by adding different elements to the aluminium which are known as aluminum alloys. Aluminum is having 1xxx series, 2xxx series, 3xxx series, 5xxx series, 6xxx series, 7xxx series and 8xxx series alloys. Al 6061-T6 is the most commonly used structural alloy having silicon and magnesium as major alloying elements.

Coefficient of friction is defined as the ratio of forces acting parallel and perpendicular to the interacting surfaces when the surfaces are in relative motion (Peter J. Blau, 2008). Coefficient of fiction is, a dimension less quantity, intrinsic property of two contacting surfaces, which depends on number of parameters and the measurement of coefficient of friction is quite difficult in laboratory. The coefficient of friction is dependent on space and time, which requires a careful, extensive and thorough study before designing the engineering components. Coefficient of friction of contacting materials is dependent on parameters such as normal pressure at contact surface, frequency of loading, duration of loading, mode of sliding, environment at contact interface etc.

1.2 MOTIVATION

Most of the structural components in offshore structures experience dynamic loads due to wave forces, ocean currents, wind forces and earthquake-induced loads. Onshore structures experience dynamic loads due to wind forces and earthquake-induced loads. Jacket platforms are the conventional structures used for oil production and drilling platforms in water depths up to 300 m. Factor of safety in design of these structures can be improved by reducing the effect of dynamic loads acting on these structures. Energy dissipation methods are the emerging methods in effective design of structures subjected to dynamic loads. Researchers (Imad and Borislav, 2002; Komachi et al., 2011; Habib Saeed Monir and Keyvan Zeynali, 2013) had concentrated on development of friction dampers. The friction damper used by Imad and Borislav (2002) is given in Figure 1.1. Imad and Borislav (2002) studied the performance of steel frames with friction dampers using numerical and experimental methods. Friction damper dissipates the dynamic loads acting on the structures due to effect of friction between friction pads. The efficiency of friction damper depends on material of pad, bolt pressure, amplitude of relative displacement between the friction pads and frequency of dynamic loads. Komachi et al. (2011) worked on retrofitting of jacket platforms using friction dampers. Friction dampers consisting of steel friction pads can reduce transverse displacement of offshore platforms up to 65%. Habib Saeed Monir and Keyvan Zeynali (2013) used friction dampers to improve the structural stiffness and as energy dissipaters in framed structures.
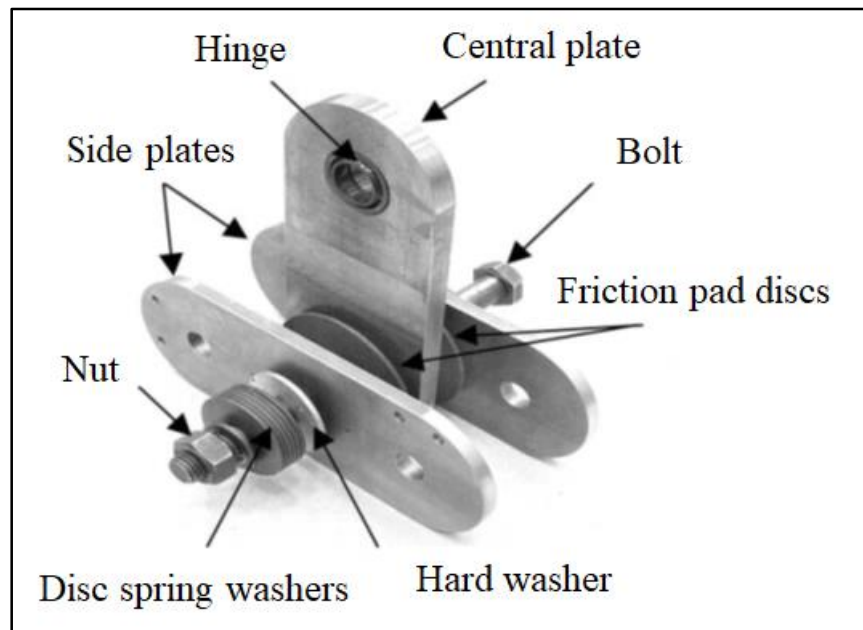
Figure 1.1: Component of friction damper device (Imad and Borislav, 2002).

Efficiency of automobiles can be improved by reducing the weight of automobile components. Researchers (Howell and Ball, 1995; Mikael Eriksson and Staffan Jacobson, 2000; Hiroaki Nakanishi et al., 2002; Shorowordi et al., 2004; Jiang Lan et al., 2012; Agbeleye et al., 2017) had focussed on replacement of conventional cast-iron materials with aluminium alloys in brake pad and brake rotor. The schematic of brake disk with pad arrangement is given in Figure 1.2. Howell and Ball (1995) investigated friction and wear characteristics of magnesium/silicon aluminium metal matrix composites (MMC). Wear resistance of these alloys were improved by using solid graphite lubricant at the material contact interface. Aluminium metal matrix composite brake rotors showed better friction performance and wear resistance than conventional brake pad material. Mikael Eriksson and Staffan Jacobson (2000) investigated friction characteristics of organic brake pads against cast iron disk. Hiroaki Nakanishi et al., (2002) investigated suitability of aluminium metal matrix composites for manufacturing of brake rotor and brake pad. Heat resistance of aluminium brake pads was improved by introducing hard particles on surface of brake pad material. Shorowordi et al., (2004) studied the effect of sliding velocity on tribological parameters of aluminium MMC sliding against phenolic brake pads. Applications of Al 6061 alloy in brake disks for high-speed trains were investigated by Jiang Lan et al. (2012). Heat dissipation during emergency braking of high-speed

3

trains was studied both experimentally and numerically. The coefficient of friction of 0.32 was considered for numerical analysis of disk-pad contact. Tribological characteristics of aluminium-clay composites used for brake disk were studied by Agbeleye et al. (2017). Aluminium alloy Al 6063 and aluminium-clay composite were used for the study. Composites made with 15 wt% of clay exhibited better tribological properties.
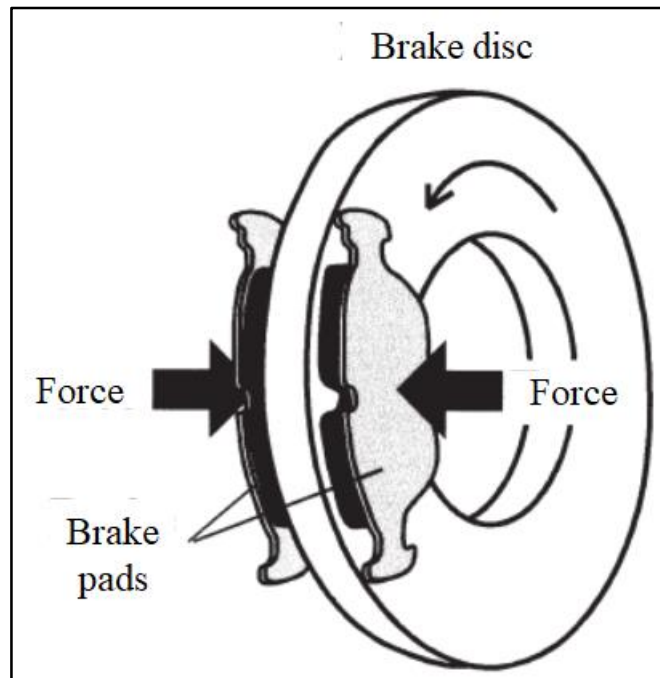
Figure 1.2: Schematic of disk brake and forces from brake pads (Mikael Eriksson and Staffan Jacobson, 2000).

Researchers (Pathak and Mohan, 2005; Sarmistha Das et al., 2007; Joy Mathavan and Amar Patnaik, 2016; Maciej Dyzia, 2017) also concentrated on applications of aluminium alloys in automobile bearing, engine piston, cam follower and crank follower. Pathak and Mohan, (2005) studied wear of different aluminium alloy bearings under lubricated sliding condition. Aluminium-lead alloy showed better wear resistance than aluminium-tin alloy even contithough strength of aluminium-lead alloy was lower when compared to that of aluminium-tin alloy. Erol Feyzullahoglu and Nehir Sakiroglu (2010) worked on aluminium-based journal bearing materials under lubricated sliding condition. Joy Mathavan and Amar Patnaik (2016) observed lower coefficient of friction in aluminium-silicon alloy and aluminium-chromium alloy; higher coefficient of friction was observed in aluminium-nickel alloy. Frictional

heat was more for aluminium-silicon alloys when compared to that in other alloys under study. Sarmistha Das et al., (2007) worked on wear characteristics of aluminium-silicon alloy and steel contacts to study the wear mechanisms of cylinder and piston surfaces in automobile engine. Maciej Dyzia (2017) manufactured cylinder pistons (Figure 3.3) with aluminium metal matrix composites (AlSi7Mg2Sr0.03 / SiCp) to study friction characteristics of cylinder pistons.
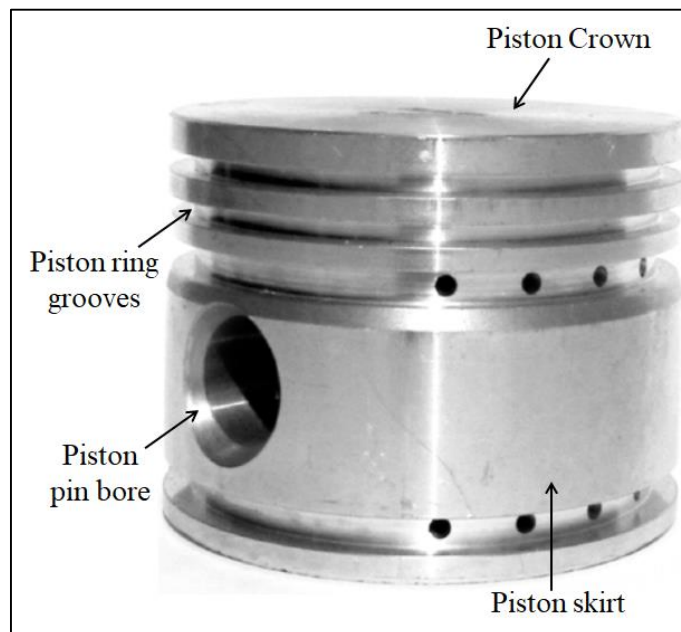
Figure 1.3: AlSi7Mg2Sr0.03/SiCp composite Piston specimen used by Maciej Dyzia (2017).

The efficiency of the friction dampers can be improved by conducting extensive studies on frictional properties of different materials. There is scope for research in metallurgical and mechanical characterization of materials to improve efficiency of friction dampers. The friction characteristics of brake disk and engine cylinder components depend on temperature and loading parameters. So, it is important to study the effect of temperature, normal load and sliding speed on coefficient of friction and wear characteristics of a material. The present study concentrates on frictional properties of aluminium to aluminium contacts under different loading conditions.

1.3 LITERATURE REVIEW

A survey of existing literature on full sliding experimental setups, effect of normal load, sliding speed and temperature on coefficient of friction and wear of metals; frictional heat measurement and frictional heat estimation techniques are discussed in this section.

1.3.1 Types of friction and their measuring techniques

Friction is defined as the resistance to the free motion of two bodies when they are rolling or sliding one over another. The schematic picture of rolling and sliding motion of bodies is given in Figure 1.4. The ratio of frictional force (F) and normal load (W) on the friction surface is called coefficient of friction (μ).
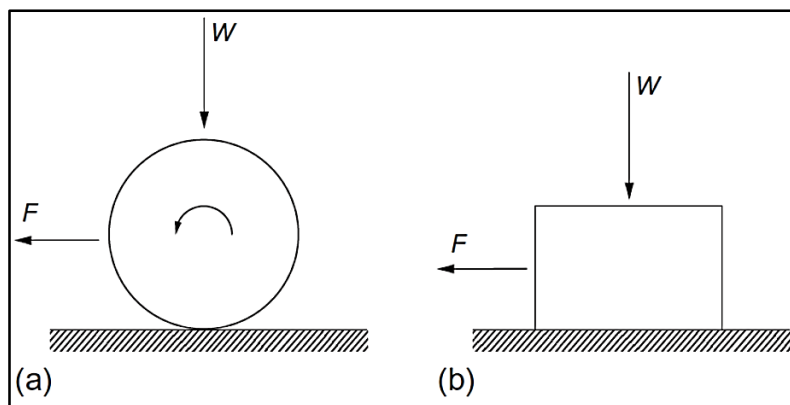
Figure 1.4: Force (F) required to move a body of weight (W) during (a) rolling and (b) sliding (Ian Hutchings and Philip Shipway, 2017).

Measuring coefficient of friction in laboratory requires experimental facility to simulate the real frictional phenomenon (rolling or sliding). Researchers used different experimental setups to measure coefficient of friction. The conventional experimental setups used to study the tribological performance of materials are given in Figure 1.5. Four ball friction setup was used by Muhammad Ilman Hakimi Chua Abdullah et al., (2014) to study the performance of engine oil on rolling friction coefficient of automobile engine components. Anyszka et al., (2015) used block on ring type friction tester to study the tribological performance of silicon rubber matrix used for wire covers. The friction and wear behaviour of lubricated artificial cartilage was studied using reciprocating sliding type experimental setup (Yarimitsu et al.,

2016). Standard pin on disk type experimental setup was used by Kouami Auxence Melardot Aboua et al. (2019) to study the effect of carbon diffusion on friction and wear behaviour of diamond-like carbon coating. In the present study pin on disk type experimental setup was used to study the friction characteristics of Al6061-T6 alloy.
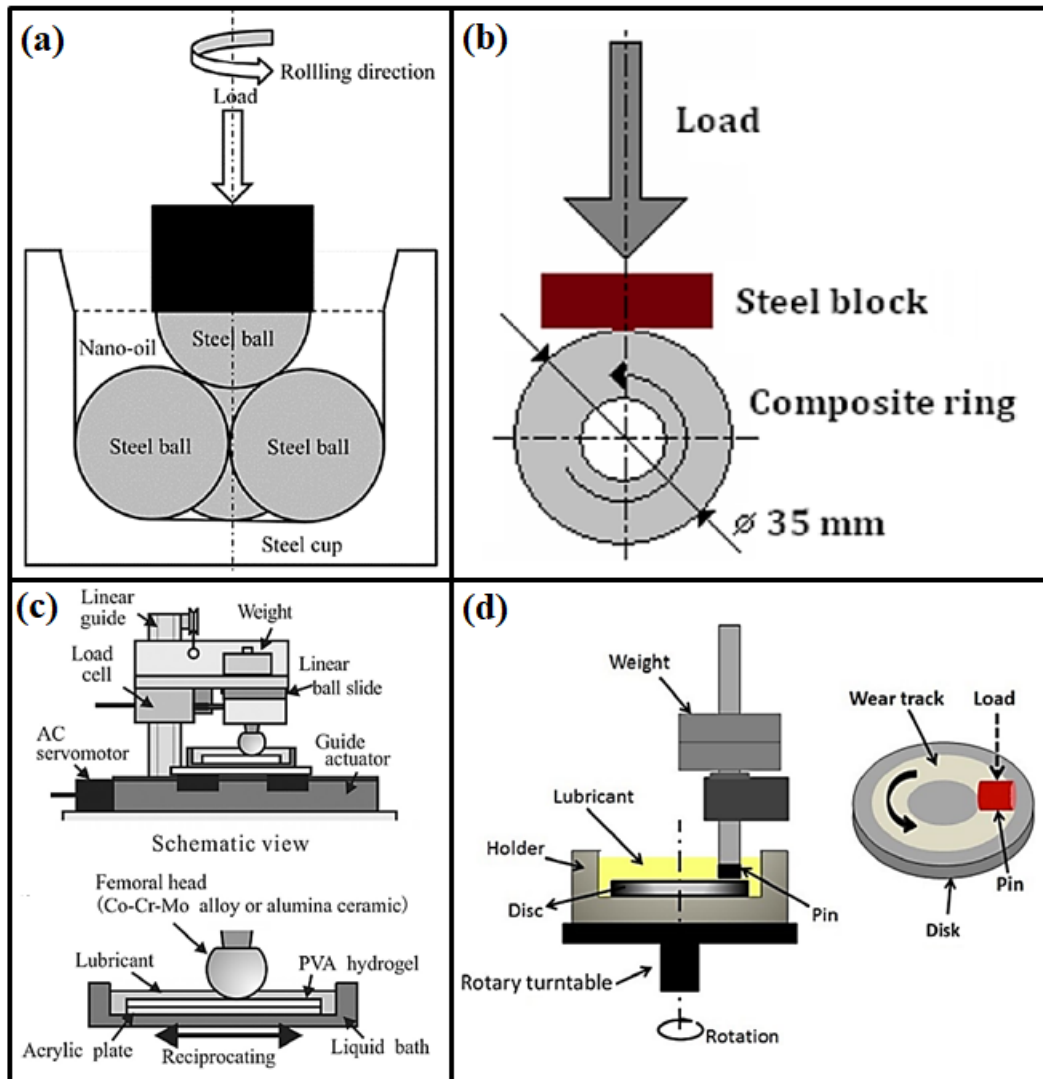
Figure 1.5: (a) Rolling friction tester (Muhammad Ilman Hakimi Chua Abdullah et al., 2014), (b) Block on ring type friction tester (Anyszka er al., 2015), (c) reciprocating sliding friction tester (Yarimitsu et al., 2016) and (d) Pin on disk sliding friction tester (Kouami Auxence Melardot Aboua et al., 2019).

1.3.2 Effect of normal load and sliding speed on coefficient of friction

Kayaba (1961) investigated usage of aluminium materials for bearing applications. Dry sliding tests were conducted using aluminium as pin specimens and mild steel as disk specimens. Decrease in coefficient of friction was observed with increase in normal load and increase in sliding speed under lower normal loading conditions. But coefficient of friction results were contradictory at higher normal loading conditions. The authors stated that friction force at aluminium alloy contacts increases rapidly due to adhesion. Even the friction forces reach stabilized value, the friction force may vary suddenly due to adhesion in aluminium alloys.

Sharma (2001) investigated the sliding wear behaviour of Al6061 reinforced with garnet particulates. He had conducted experiments at normal load of 10 N - 50 N and sliding velocity of 1.25 m/s – 3.05 m/s. The author concluded that the addition of garnet particulates to Al6061 alloy improves wear resistance and reduces the coefficient of friction. Experiments were conducted using specimens of surface roughness (R_a) 2 µm against steel disc. Both Al6061 alloy and garnet particulate Al6061 alloys showed increase in coefficient of friction and wear rate with increase in normal load. Al6061 reinforced with garnet particulates showed decrease in coefficient of friction with increase in sliding speed whereas the pure Al6061 alloy had resulted increase in coefficient of friction with increase in sliding speed at sliding speeds above 1.85 m/s. A similar trend was observed by Wang and Rack (1991) in Al 7091 alloy and SiC reinforced Al7091 alloys. The increase in coefficient of friction of Al6061 alloy with increase in sliding speed was due to formation of Al_2O_3 and increase in Al_2O_3 layer thickness at higher sliding speeds whereas in reinforced Al6061 garnet particulates act as solid lubricant which leads to decrease in coefficient of friction.

Shorowordi et al., (2004) studied the effect of sliding velocity on wear and friction characteristics of aluminium Metal Matrix Composite (MMC) sliding against phenolic brake pads. Experiments were conducted at two sliding speeds of 1.62 m/s and 4.17 m/s. Coefficient of friction was obtained from the data recorded and wear was calculated from mass loss measurement data. The coefficient of friction and wear

loss decreased with increase in sliding velocity. The reduction of both friction coefficient and wear with increase in sliding speed resulted due to formation of compact transfer layer (which contains phenolic material) on MMC at higher sliding speeds.

Uyyuru et al., (2007) worked on suitability of Al-Si/SiC$_p$ composites as automobile brake disk material. Full sliding experiments were conducted using pin on disk tribo-tester with Al-MMC as disk specimen and brake pad material (polymer matrix composite) as pin specimen. They observed increase in wear rate of Al-Si/SiC$_p$ composites with increase in normal load. Coefficient of friction of Al-Si/SiC$_p$ composites decreased with increase in normal load. Coefficient of friction was around 0.3 at different normal load conditions and the effect of normal load on coefficient of friction was insignificant when compared to that of wear rate. Both coefficient of friction and wear rate were inversely proportional with sliding speed. The increase in wear rate with increase in normal load was due to formation of tribo-layer and failure of tribo-layer which also resulted in decrease in coefficient of friction. During higher sliding speeds, tribo-layer persists for long time which leads to decrease in wear rate and coefficient of friction.

Ramesh et al., (2010) investigated the effect of silicon nitride particles on friction and wear characteristics of Al6061 metal matrix composites. Addition of silicon nitride particles helped in decreasing coefficient of friction and wear rate. The coefficient of friction and wear rate showed directly proportional relationship with sliding velocity in metal matrix alloy. The coefficient of friction and wear rate showed inversely proportional relationship with sliding velocity in metal matrix composite alloy. The reduction in coefficient of friction with increase in reinforcement was due to formation of oxide layer, which acts as solid lubricant. These oxide layers were also called as tribo-chemical layer or mechanically mixed layer (Venkataraman and Sundararajan, 2000; Riahi and Alpas, 2001). This phenomenon was also mentioned by several researchers (Ramesh and Sheshadri, 2003; Mondal et al., 2007).

Al-Qutub et al., (2013) observed friction and wear behaviour of Al6061 monolithic alloy and Al6061 alloy reinforced with 1 wt% carbon nanotube. Experiments were

conducted using 6 mm cylindrical pin having flat contact and steel disk as counterface. Carbon nanotube reinforced composites showed, lower coefficient of friction and wear rate when compared to monolithic Al6061 alloy up to 15 N normal load, higher coefficient of friction and wear rate when compared to monolithic Al6061 alloy at normal load above 15 N. Abrasive wear mechanism was observed at lower normal loads. At higher normal loads, adhesive wear mechanism was observed in monolithic Al6061 alloy, delamination and sub-surface fracturing were dominant in carbon tube reinforced Al6061 alloys. The fluctuation in coefficient of friction at high normal load represents excessive sub-surface fracturing and delamination of material surface. The authors observed delamination wear mechanism in monolithic Al 6061 alloy which was recognized by minor scratches on surface of wear track.

Radhika et al., (2014) studied the influence of load, sliding speed and surrounding temperature on the AlSi10Mg alloy reinforced with 3 wt% graphite and 9 wt% alumina. The authors considered sphere on flat contact configuration to conduct dry sliding experiments. From their study, authors concluded that the load had highest influence on wear followed by temperature and sliding speed. From the SEM analysis, at lower normal load, sliding speed and temperature, shallow grooves were observed on worn surface which represents mild wear. Severe wear at higher temperature was due to material softening and delamination wear mechanism.

Mark A. Sidebottom and Brandon A. Krick (2015) concluded that errors in measuring frictional force were minimal in spherical contact (Hertzian contact) than errors in flat on flat contact. The error calculations were done by comparing the integral solution of measured coefficient of friction with actual coefficient of friction.

Rajesh et al., (2016) reported about friction and wear rate of different stainless steel (SS 304, SS 316 and SS 202) and mild steel materials. EN-31 disk specimens were used to conduct experiments. They observed increase in coefficient of friction and wear rate with increase in normal load for all the tested materials. The wear resistance of steel had improved significantly by adding more carbon to the steel.

Rusin (2016) investigated on tribological characteristics of pure aluminium-steel contacts during full sliding. Results showed increase in coefficient of friction with

increase in contact pressure up to 1 MPa; decrease in coefficient of friction with increase in contact pressure above 1 MPa. At lower contact pressure the coefficient of friction reached to 0.74. The authors observed thicker oxide layers at lower contact pressure when compared to oxide layers formed at higher contact pressure. The increase in coefficient of friction was due to increase in bulges on surface of wear track during sliding. Hardness of oxide layers was more, when compared to hardness of steel. Wear of steel disk was observed due to scratching of harder aluminium oxide particles on steel disk.

Yuchun Huang et al., (2017) studied the effect of friction layer thickness on tribological performance of Ni_3Al-Ag-MoO_3 alloy. Full sliding experiments were conducted using sphere on flat contact configuration. They observed formation of friction layer at contact interface during sliding and thickness of friction layer depends on loading parameters and contact temperature. Friction layer improves wear resistance and antifriction characteristics of the contacting materials by avoiding crack formation and spalling of material during sliding. The decrease in coefficient of friction with increase in normal load and contact temperature was due to increase in friction layer thickness. At 12 N normal load and 400 °C contact temperature, further increase in normal load or contact temperature leads to softening of material and decrease in shear strength between friction layer and base material. This leads to increase in wear rate by failure of entire friction layer. Wang et al., (2010) also observed a similar phenomenon during their study on effect of temperature on micro friction.

Shuaihang Pan et al., (2018) were among the few researchers who had studied the tribo-electric characteristics of aluminium to aluminium contacts. Experiments were conducted using flat on flat contact reciprocating motion type tribometer. Increase in coefficient of friction was observed with increase in normal load up to 30 N and coefficient of friction decreased with further increase in normal load (Figure 1.6). Along with the tribological parameters the authors also observed electrical conductivity between the contact pairs. Increase in electrical conductivity with increase in normal load was observed up to 30 N normal load and above 30 N normal load electrical conductivity was observed as zero. Initially, increase in electrical

conductivity was due to increase in contact area with increase in normal load. Later, the zero electrical conductivity was due to formation of oxide layer at contact interface at higher normal load. Ultimately, the oxide layer formation decreased the coefficient of friction.
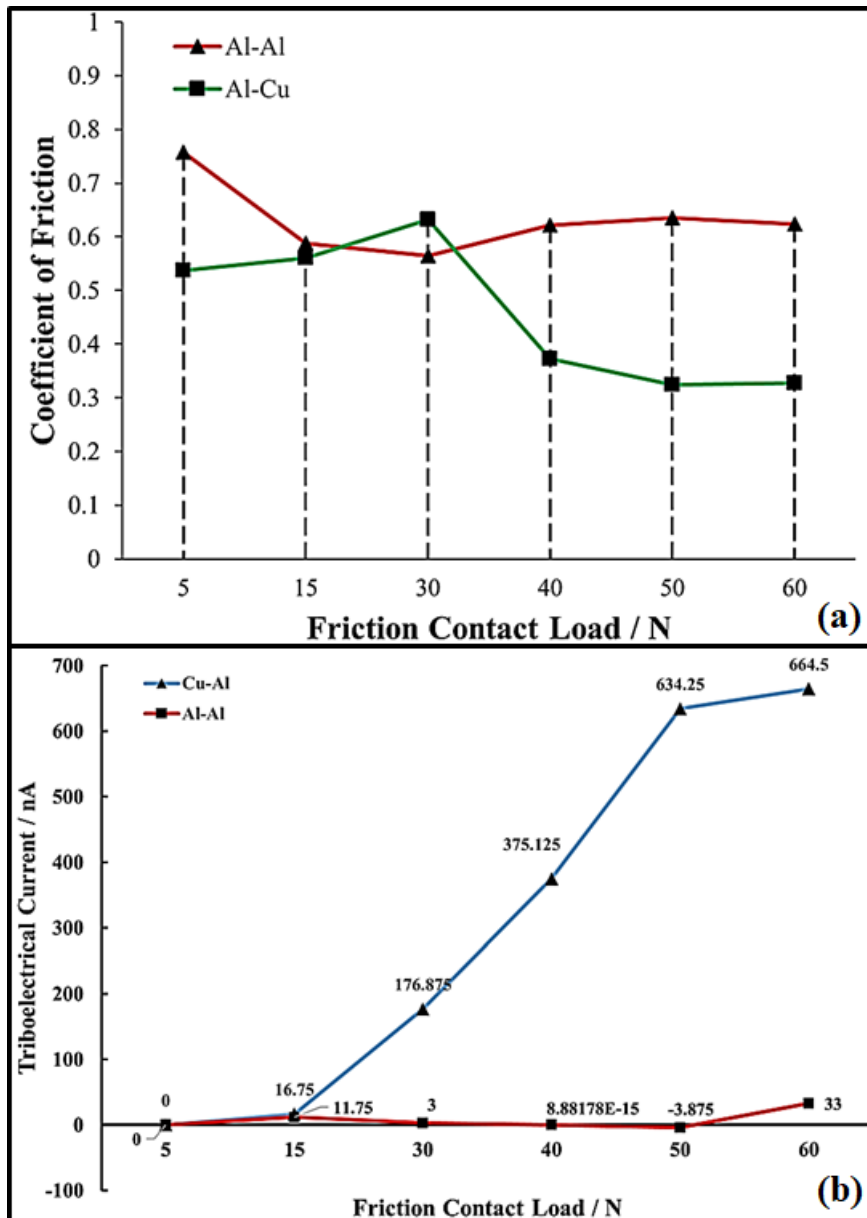
Figure 1.6: (a) Coefficient of friction of Al-Al and Al-Cu contact pairs, (b) triboelectric current of Al-Al and Al-Cu contact pairs. (Shuaihang Pan et al., 2018)

From the literature, the coefficient of friction and wear rate of materials depends on several factors such as material, type of reinforcement, amount of reinforcement, type of coating, normal load, sliding speed etc. The trends in coefficient of friction, wear rate, wear mechanism and formation of tribo-layer changed dramatically with change in contact pair material and loading parameters.

1.3.3   Wear in metallic contacts

Wear is defined as loss of material from sliding surfaces as a result of mechanical action (Morton Antler, 1981). Adhesion, abrasion, delamination, brittle fracture and fretting are the common wear mechanisms occurring in metallic interfaces. Any of these mechanisms may be the reason for the wear of metallic interfaces which depends on the materials of contact pairs, loading parameters (normal load at contact interface, sliding speed), contact interface condition (dry or lubricated), geometry of contact interface, temperature etc. Adhesive wear mechanism can be identified from the prow formation at contact interface. Adhesive wear occurs commonly in ductile materials and its severity depends on surface condition and contact pressure. Aurum, Silver, Lead, Tin etc. are some of the ductile metals where severe adhesive wear can be observed (Morton Antler, 1981). Abrasive wear can be observed when materials slide against harder counter body or interaction of contact interface with harder material particles. Both higher hardness materials and ductile materials can resist material fracture during abrasion. Delamination wear mechanism starts due to surface crack formation and loosening of surface material. Delamination is the common wear mechanism in metal composites. Fretting wear is defined as the loss of material at contact interface when the contact interface is subjected to high contact stress and nano-scale relative sliding (Bill, 1983). The fretting wear may lead to formation of surface cracks at contact interface and sudden failure of components.

Sarmistha Das et al., (2007) worked on wear characteristics of aluminium-silicon alloy and steel contacts to study the wear mechanisms of cylinder and piston in automobile engine. Dry sliding experiments were conducted under 1 MPa -100 MPa contact pressure and sliding speed of 0.2 m/s. The authors adopted a range of normal contact pressure from literature which exists between cylinder and piston. Ultra-low

wear was observed up to 10 MPa applied contact pressure and the wear process changed to mild wear (up to 70 MPa contact pressure) and severe wear.

Al-Qutub et al. (2013) observed improvement in wear resistance of Al 6061 alloy due to addition of carbon nanotubes at lower normal load (5 N to 15 N). At higher normal loads (20 N to 30 N), the monolithic alloys showed better wear resistance than carbon nanotube reinforced Al 6061 alloy. The sharp change in wear rate indicates the change in wear mechanism. In carbon nanotube reinforced Al 6061 components wear mechanism changed from mild to severe at 15 N normal load. But, in monolithic Al 6061 alloy wear mechanism changed from mild to severe at 25 N normal load. The pores present in the reinforced alloy initiate cracks at higher normal load which leads to poor wear resistance of carbon nanotube reinforced Al 6061 alloy. Similar effect was observed by Lee et al. (1992) in SiC reinforced Al 6061 alloy. Many researchers (Wang et al., 2001; Korkut, 2003; Sudarshan and Surappa, 2008) concluded that the reinforcement in aluminium metal matrix composites results in positive effect on wear resistance at lower normal loading conditions whereas at negative effect at higher normal loading conditions. Abrasive wear mechanism was characterized by appearance of small delaminated flakes. Appearance of large delaminated flakes represents the change of wear mechanism to delamination wear and severe wear. Adhesion and oxidation were dominant wear mechanisms in monolithic Al 6061 alloy. Excessive surface fracturing and delamination were dominant in reinforced Al 6061 alloy.

Zhou et al., (2007) observed oxidation as the main wear mechanism in carbon nanotube reinforced aluminium alloy which was characterized by identifying the formation of aluminium layer on the contact surface and delamination wear mechanism. They also observed the addition of carbon nanotube reinforcement, improves the surface hardness and wear resistance, decreases the surface friction coefficient. Kim et al. (2009) found adhesive and abrasive wear mechanisms in carbon nanotube reinforced aluminium alloy composites whereas Choi et al. (2010) reported micro ploughing and delamination were the dominant wear mechanisms in carbon nanotube reinforced aluminium alloy composites.

From the literature, various researchers differentiated the wear in aluminium alloys as mild wear, moderate wear and severe wear. Adhesion, abrasion and delamination are the main wear mechanisms in aluminium alloys. During sliding test, wear of small metal particles from the metal surface represents mild wear, appearance of small delaminated flakes represents moderate wear and appearance of large delaminated flakes represents severe wear. Oxidation of metal surfaces during sliding is one of the main causes for both abrasive and delaminated wear mechanism. Softening of metal matrix due to frictional heat or other reasons during sliding is the main cause for adhesive wear mechanism. Strengthening of aluminium alloys with various reinforcing particles resulted in improvement of friction and wear characteristics of alloy at lower normal loads but showed negative impact on the same at higher normal loads.

1.3.4 Frictional heat generation

Friction between two bodies transforms the mechanical energy into thermal energy or heat. Most of the energy dissipation is in the form of frictional heat (Day and Newcomb, 1984; Lim and Ashby, 1987; Majcherczak et al., 2007). The energy dissipation at contact interface during sliding process may occur due to atomic-scale interactions of contact pair materials (Sergey and Frenken, 2014) or plastic deformation of surface layers of contact pair (Rubtsov and Kolubaev, 2009). The frictional heat at contact interface changes both physical properties and chemical properties of contact surfaces. As a result, it influences the tribological properties (friction and wear) of contact pair. In some practical applications the frictional heat may exceed melting point of contacting materials, e.g. brass bullet surface melts when it travels through gun barrel during firing (Adrian Bejan, 1994) leading to decrease in coefficient of friction. Similar phenomenon was observed between steel and ice contacts during bobsleighing (Matthias Scherge et al., 2018). Temperature at contact interface leads to thermal softening and shear failure of materials. The instantaneous rise in temperature at contact asperities is known as flash temperature (Lim and Ashby, 1987). In metals, at higher sliding speeds, the flash temperature at contact interface reaches several hundred degree Celsius which promotes the oxidation of contact interface (Stachowiak and Batchelor, 1993; Zhang et al., 2012). The oxide

15

layer formation on the contact surfaces changes both friction and wear properties of base materials. The average of these flash temperatures in the contact area is called bulk temperature. In some practical cases, the flash temperatures are much higher than the bulk temperatures (Piotr Grzes, 2019). The present study concentrated on the estimation of bulk temperature.

Wang et al., (1995) measured the contact temperatures by using thermocouple located at 1.5 mm from the contact surface. The temperature of sliding Al6061 reinforced with SiCw contacts increased with increase in applied load and sliding distance. Sharma (2001) derived an equation to calculate the frictional heat which is a function of normal load (L), sliding distance (l_b), sliding velocity (v), area of contact (A), thermal conductivity (K_m) and coefficient of friction (μ). The buck temperature (T_b) at contact surface is given in equation 1.1; where α is fraction of heat and T_0 is sink temperature.

$$T_b = T_0 + \frac{\alpha \mu L v l_b}{A K_m}$$

(1.1)

Inverse heat transfer methods were invented to predict the temperature at the heat source locations where measurement of temperature at the same location is not feasible. The temperature at heat source location can be estimated from the measured temperature at possible locations away from the heat source. Zhizhong Sun et al. (2011) investigated the effect of casting mould pressure on Interfacial Heat Transfer Coefficient (IHTC) during casting of magnesium alloy. From this study, authors observed that the peak value of IHTC increased with increase in moulding pressure. The heat flux at mould interface and temperate distribution in mould wall were estimated using inverse heat transfer method. IHTC obtained from the inverse heat transfer method was more accurate than that obtained by extrapolated fitting methods.

Liping Chen et al. (2014) calculated interfacial heat transfer coefficient (IHTC) during casting of magnesium alloy using silica sand mould. The heat flux and temperature transfer from the molten magnesium alloy to the silica sand mould were calculated using inverse heat transfer algorithms. The temperature at selected locations, away from the inner surface of mould, was measured during casting process of magnesium

alloy. The measured temperature history data was analyzed using Beck's nonlinear evolution theory to estimate the heat flux at interface of metal alloy and cast mould.

1.3.5 Thermoelectric Effect Sensors (Thermocouples)

Thermocouples are the thermoelectric sensors which rely on principal states that when two different metals are connected together, the Electromotive Force (EMF) generated at junction of metals is a function of temperature.

$$EMF = a_1T + a_2T^2 + a_3T^3 + \ldots\ldots + a_nT^n \qquad (1.2)$$

EMF is a nonlinear function of temperature. The higher order terms (a_2T^2, a_3T^3, ..., a_nT^n) are approximately equal to zero for certain pairs of materials. So the approximate EMF can be written as:

$$EMF = a_1T \qquad (1.3)$$

Wires of such materials connected together is called thermocouple. Thermocouples are the most commonly used devises to measure temperature in various industries. Thermocouples are manufactured using different material pairs such as Chromel-constantan, Iron-constantan, Copper-constantan, Chromel-alumel, Nicrosil-nisil, Platinum/13% rhodium-platinum and Platimum/10% rhodium-platinum. The standard combinations of thermocouples are internationally represented with type letters, example type K is a thermocouple made with chromel-alumel.

Chromel-constantan (type E), iron-constantan (type J), chromel-alumel (type K), nicrosil-nisil (type N) and copper-constantan (type T) are the five standard base metal thermocouples. These five types of thermocouples are relatively cheap to manufacture but become inaccurate with time and have short life span. The performance of thermocouple may affect through contamination by the working environment. To overcome the affect of working environment on thermocouple, a protective sheath can be provided on thermocouple. The protective sheath makes the thermocouple slow to respond the temperature changes. Therefore thermocouples should be used without protective cover as far as possible. Along with these five type thermocouple Iron-constantan thermocouples (type J), Nickel/molybdenum-nickel-cobalt thermocouples (type M), Platinum thermocouples (type B, type R and type S), Tungsten thermocouples (type C) and Chrom-legold/iron thermocouples are also available in market.

E-type thermocouples have the highest measurement sensitivity (68 µV/°C) with an accuracy of ±0.5%. These thermocouples can be used to measure temperatures, in the range from -200 °C to 900 °C, at oxidizing environment even without protective sheath. The performance and life of these thermocouples affect by reducing environment. J-type thermocouples have sensitivity of 55 µV/°C and preferred to measure the temperature ranging from -40 °C to +750 °C with an accuracy of ±0.75%. The oxidizing and reducing environments shows less affect on performance of J-type thermocouple. T-type thermocouples have measuring sensitivity of 45 µV/°C and preferred to measure sub-zero temperature down to -200 °C with an accuracy of ±0.75%. They can be used in oxidizing and reducing environments to measure temperatures up to 350 °C. K-type thermocouples are widely used for general purpose with measurement sensitivity of 41 µV/°C and measurement accuracy of ±0.75%. These thermocouples can be used to measure the temperatures ranging from -200 °C to 1300 °C and suitable for oxidizing environment but not in reducing atmosphere. N-type thermocouples are developed with the intension of improving the life time of K-type thermocouples. Therefore N-type thermocouples are having similar thermoelectric characteristics of K-type thermocouple with long term stability. These thermocouples can be used to measure the temperatures up to 1300 °C with accuracy of ±0.75%. N-type thermocouples are having measuring sensitivity of 39 µV/°C (Brookes, 1985). M-type thermocouples are made from nickel-18% molybdenum alloy and nickel-0.8% cobalt alloy. They can be used to measure the temperatures up to 1400 °C which is highest possible measuring devise using metallic thermocouple. Oxidation affect these thermocouples vary severely so these thermocouples generally uses for special application like vacuum furnaces.

Thermocouples made from noble metals are highly stable and lost long but they are expensive. They can be used at high temperatures but not in reducing atmospheres. B-type thermocouples are made from platinum-rhodium alloy, one wire made with 30% rhodium and another wire made with 6% rhodium. These thermocouples have measurement sensitivity of 10 µV/°C and can be used to measure temperatures ranging from 50 °C to 1800 °C. R-type thermocouples are also made from platinum-rhodium alloy but one wire made with pure platinum and another wire with 13% rhodium. These can be used to measure the temperatures ranging from 0 °C to 1700

°C with the accuracy of ±0.5%. These thermocouples are having measurement sensitivity of 10 µV/°C. S-type thermocouples are made from platinum-rhodium alloy, one wire made with pure platinum and another wire made with 10% rhodium. The temperature range can be measured is 0 °C to 1750 °C. C-type thermocouples are having one wire made with pure tungsten and the other wire made from tungsten/rhenium alloy. These thermocouples can be used to measure temperatures up to 2300 °C in vacuum furnaces.

In the present study, K-type thermocouples were used due to its wide range of temperature measuring capability, accuracy of measurements, measuring sensitivity and relatively low cost. K-type thermocouples are most commonly used temperature measurement devises in various industries.

1.3.6 Effect of temperature on coefficient of friction and wear

Singh and Alpas (1995) studied wear of Al6061 alloy with and without Al_2O_3 reinforcement at temperatures ranging from 25 °C to 500 °C. Transition from mild wear to severe wear was observed in Al6061 alloy at 150 °C whereas in Al_2O_3 reinforced Al6061 alloy the transition was observed at 250 °C. Al_2O_3 reinforced Al6061 showed better wear resistance, when compared to Al6061 alloy at higher temperatures. In mild wear regime, reduction in wear rate was due to oxidation of counter face material (iron) and deposition of oxides on contact surfaces.

Wang et al., (2010) observed coefficient of friction between aluminium and steel metal at different temperature to develop Finite Element Model. The coefficient of friction varied from 0.1 to 1 in the temperature range of 23 °C - 450 °C. Wear tests were conducted using ball on disk type testing machine with aluminium as disk specimen and steel as ball specimen. Authors observed increase in coefficient of friction with increase in temperature due to increase in plowing mechanism at higher temperatures. Wang et al., (2009) observed the increase in coefficient of friction with sliding distance was due to increase in real contact area during sliding.

Pujante et al., (2013) investigated different wear mechanisms occurring in aluminium-steel tribopair at different temperatures of 30 °C, 150 °C, 250 °C, 350 °C and 450 °C.

At room temperature (30 °C), moderate abrasive wear, low and stable coefficient of friction observed in aluminium-steel tribopair. Material transfer from pin to disk surface and unstable coefficient of friction were observed at temperatures from 150 °C to 250 °C. Oxide formation was observed at 350 °C which resulted in abrasive wear on steel disk surface.

Kouami Auxence Melardot Aboua et al., (2019) presented a survey on change in frictional characteristics of Diamond-like Carbon (DLC) coatings at different temperatures. Experiments were conducted at different temperatures of 80 °C, 100 °C and 120 °C. Decrease in coefficient of friction was observed with increase in temperature.

From the literature review, it was observed that temperature showed significant effect on coefficient of friction and wear of different materials. The temperature at contact interface occurs due to frictional heat and environment where that particular component was used. So, estimation of frictional heat and its effect on tribological properties is important. In the present study, frictional heat was estimated at different experimental parameters and effect of temperature on coefficient of friction and wear of Al 6061-T6 alloy was observed.

1.4 RESEARCH GAP

From the literature, researcher studied the friction and wear characteristics of aluminum alloys under different normal load, sliding speed and temperature conditions. Most of the researchers (Wang et al., 2010; Viktoria Westlund et al., 2018) have studied the wear and friction characteristics of aluminium alloys by considering steel as a counter-face material, having a flat on flat contact configuration, during the experiments. Few researchers (Dewan and Mohammad 2012; Shuaihang Pan et al., 2018) focused on the friction behaviour of aluminium-to-aluminium metal alloy during full sliding. In the present study, special emphasis has been given to the effect of temperature on tribological properties of Al 6061-T6 alloy. Dry sliding experiments were conducted by considering the aluminium-to-aluminium contact pair, having a cylinder on flat contact configuration. The influence of

temperature, normal load and sliding speed on coefficient of friction was investigated by conducting experiments under full sliding conditions.

1.5 AIM AND OBJECTIVES

The objectives of the study are as follows:

- To study the effect of normal load and sliding speed on frictional heat in Al 6061-T6 alloy contacts during dry sliding.
- To study initial, stabilized, steady-state and unsteady state coefficient of friction of Al 6061-T6 alloy at different normal loads, sliding speeds and temperatures.
- To study wear characteristics of Al 6061-T6 alloy at different normal loads, sliding speeds and temperatures.

1.6 STRUCTURE OF THE THESIS

Chapter 1 provides introduction to aluminium alloys and friction. This chapter contains motivation for the present study, literature review on full sliding experimental setups, literature review on effect of normal load and sliding speed on coefficient of friction, literature review on wear of metallic contacts, literature review on frictional heat measuring techniques and it's estimation methods, literature review on effect of temperature on coefficient of friction and wear, research gap and objectives of this study.

Chapter 2 gives the details of materials used, properties of materials, specimen preparation, experimental parameters considered and detailed procedure to conduct dry sliding experiments using pin on disk tribometer at different temperature conditions.

Chapter 3 explains detailed procedure to estimate the contact interface temperatures using inverse heat transfer technique. This chapter also explains the effect of loading parameters (normal load and sliding speed) on frictional heat in dry sliding Al 6061-T6 alloy contacts.

Chapter 4 contains preliminary test results of Al 6061-T6 and Al 6082-T6 alloy which gives details of oxidation effect during dry sliding of metal contacts. The oxidation of metal surfaces was confirmed using Scanning Electronic Microscopy with Energy Dispersive X-ray Spectroscopy analysis.

Chapter 5 describes the coefficient of friction and wear characteristics of Al 6061-T6 alloy. Evolution of coefficient of friction and coefficient of friction at different stages of dry sliding process of Al 6061-T6 alloy are presented in detail. Wear rate and wear mechanisms observed in dry sliding of Al 6061-T6 alloy are discussed in detail using optical micrographs.

Chapter 6 presents conclusions drawn from this study, limitations of present study and scope for future work. This will be followed by references.

CHAPTER 2

DRY SLIDING EXPERIMENTS

This chapter explains materials used for conducting dry sliding experiments, characterization of materials used, fabrication of specimens, experimental procedures and design of experiments.

2.1 MATERIALS AND SPECIMEN PREPARATION

Aluminium alloy (Al 6061-T6), having a chemical composition of Si 0.682%, Mg 0.927%, Fe 0.175%, Cu 0.204%, Mn 0.039%, Cr 0.062%, Zn 0.009%, Ti 0.028%, B 0.003%, Bi 0.003%, Sn 0.004%, V 0.001%, Z 0.001% and remaining aluminium (in wt. %) was used for the investigation. The mechanical properties of Al 6061-T6 are yield strength 276 MPa, Poisson's ratio 0.33, elastic modulus 69 GPa and Brinell hardness 95. The chemical composition and mechanical properties of Al 6061-T6 alloy were provided by the material supplier. The phases present in a material can be found through X-ray Diffraction Analysis. Figure 2.1 (a) shows the different peak intensities of aluminium at different plane angles. The maximum peak intensity was observed at 37° (2θ). The observed X-ray diffraction results are comparable with the results observed by Suresh et al. (2014) for Al 6061-T6 alloy. Scanning Electron Microscopy (SEM) was carried out with Energy Dispersive X-Ray Spectroscopy (EDS) to confirm the elements present in Al 6061-T6 alloy. The EDS spectrum revealed presence of 95.76 % Al, 0.51 % Mg, 0.11 % Si and 3.63 % O on the surface of Al 6061-T6 alloy (Figure 2.1 (b)). A 170 mm diameter cylindrical bar of Al 6061-T6 alloy was utilised for specimen fabrication. The disk specimens were fabricated from the cylindrical bar by cutting 8 mm thick circular plates (Figure 2.2 (a)). The pin specimens were fabricated by cutting the pins from the disk specimen, as shown in Figure 2.2 (b). The disk specimen's surface roughness (Ra) of 0.3 μm - 0.5 μm was achieved using CNC milling operation (Manoj and Mahender, 2016).
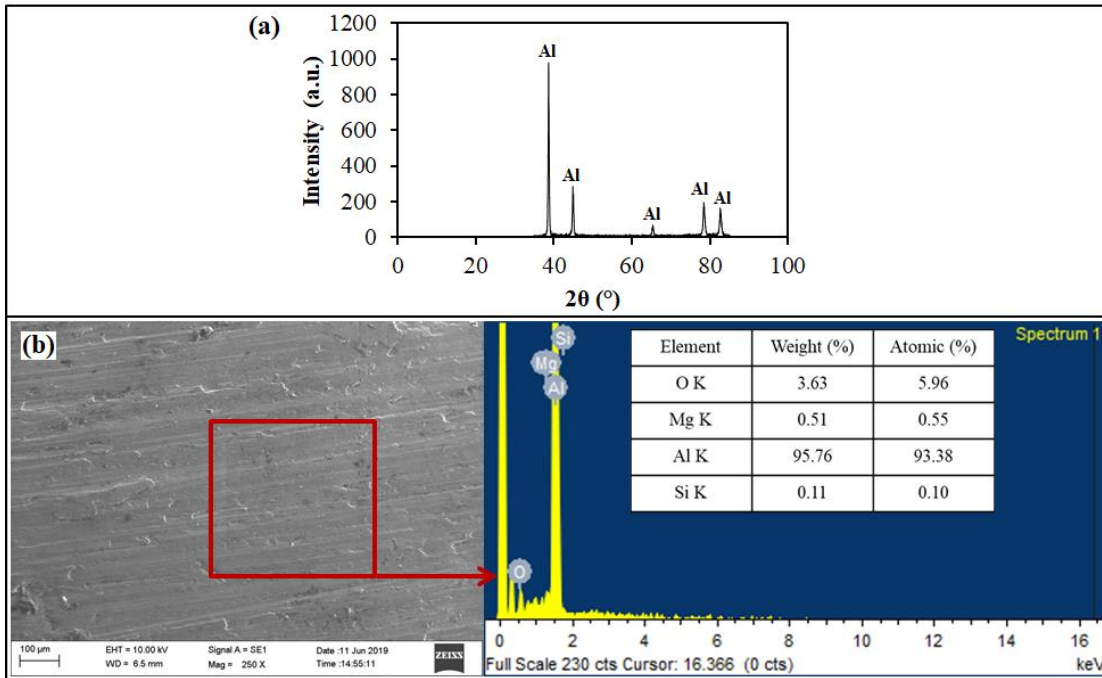
Figure 2.1: (a) X-ray diffraction pattern of Al 6061-T6 alloy and (b) EDS analysis of Al 6061-T6 alloy.

Element	Weight (%)	Atomic (%)
O K	3.63	5.96
Mg K	0.51	0.55
Al K	95.76	93.38
Si K	0.11	0.10
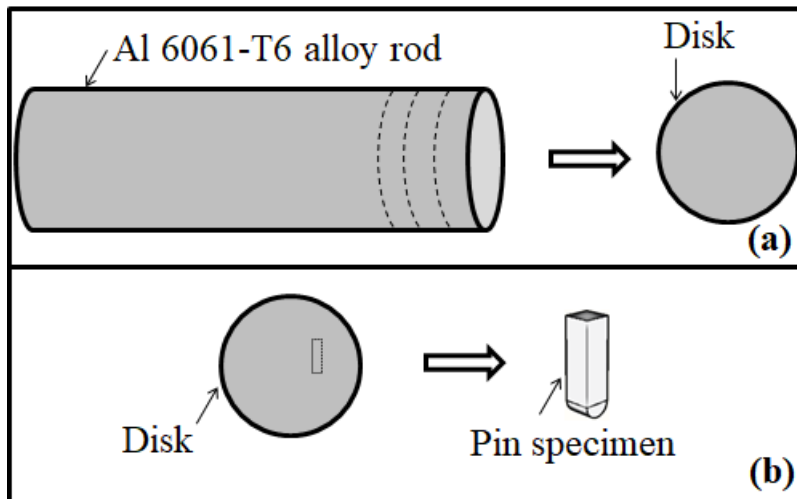
Figure 2.2: Fabrication of disk and pin specimen from the Al 6061-T6 metal rod.

2.2 PIN ON DISK EXPERIMENTS

Experiments were performed using pin on disk type tribometer (DUCOM make). Pins were fabricated as prismatic bars having a length of 30 mm, cross section of 6 mm × 6 mm and a cylindrical contact radius of 3 mm (Figure 2.3 (a)). A cylinder on flat contact configuration was used for conducting experiments. Experiments were conducted by applying three different normal loads (1 kg, 1.5 kg and 2 kg) and three different sliding speeds (1.25 m/s, 2m/s and 3 m/s) at different temperatures of room temperature (31 ± 1 °C), 60 °C, 100 °C and 150 °C. The normal loads applied were considered by ensuring that the contact configuration was in an elastic limit (Johnson, 1985). The maximum contact pressure at cylindrical pin and flat disk surfaces was calculated using Hertzian type contact (cylinder on flat contact) formula (equation 2.1) and given in Table 2.1. All experiments were performed up to a sliding distance of 600 m. A heating chamber was used to conduct experiments at higher temperatures. After arranging the disk and the pin, the experimental setup was closed with a heating chamber (Figure 2.3 (b)) and the materials (disk and pin) were allowed for 15 minutes to attain uniform temperature before the start of the experiment. The chamber temperature was monitored using a thermocouple inserted in the heating chamber, as shown in Figure 2.3 (b).

Table 2.1: The maximum contact pressures applied at the contact for experimentation.

Normal load (kg)	Maximum contact pressure (MPa)	% of yield strength
1	82	30
1.5	100.4	36.4
2	115.9	42

$$P_{max} = \sqrt{\frac{NE}{2\pi R\left(1-\upsilon^2\right)}} \qquad (2.1)$$

Where, P_{max} is the maximum pressure at contact interface

N is the normal load per unit thickness of specimen

E is the Young's modulus of the pin and disk specimens (69 GPa)

R is the radius of the cylindrical pin specimen (3 mm)

υ is the Poison's ratio of the material (0.3)
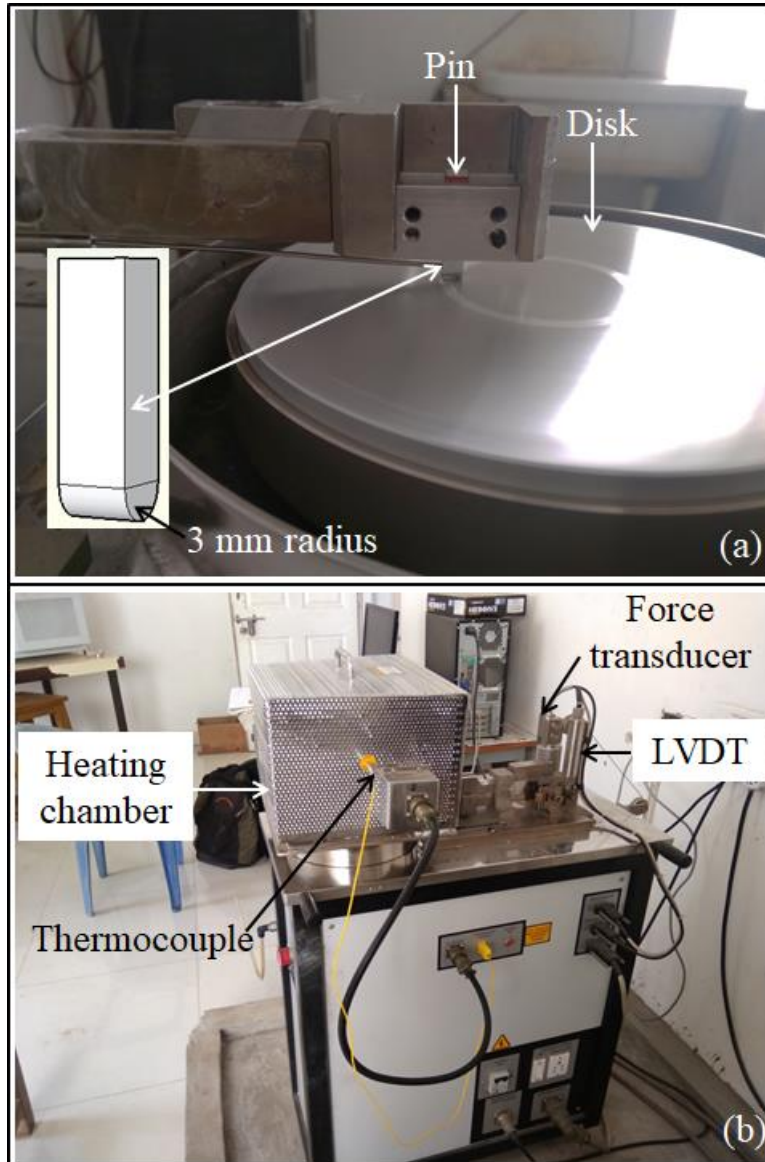
Figure 2.3: (a) Pin and disk arrangement and (b) pin on disk tribometer used for the study.

The contacting surfaces of the two specimens (pin and disk) were cleaned before the experiment by using a cotton cloth and by applying acetone solution ((CH3)2CO). The arrangement of pin on disk surface is shown in Figure 2.3 (a). Precautions were taken to maintain the line contact (cylinder on flat contact) before starting the experiment. The weight of the pin samples was noted before and after the experiments using weighing machine of accuracy 0.001 g. The pin on disk tribometer consisted of

frictional force transducer with an accuracy 0.01 N and wear sensor with an accuracy of 0.01 μm. Friction force and wear sensor (Linear variable differential transformer (LVDT)) readings were initialized before the start of every experiment. The frictional forces and wear depth data measured during the experiments were acquired using a personal computer. The friction force was measured using force couple mechanism (Figure 2.4). The wear sensor attached to the loading arm measures the cumulative wear depth (wear of both pin and disk surfaces) during the experiment. The schematic representation of frictional force measurement and wear depth measurement are given in Figure 2.4 and Figure 2.5 respectively. Friction coefficient (μ) was calculated as the ratio of friction force (F) to applied normal load (L). The experimental parameters considered for the present study are given in Table 2.2. The methodology used for this study is given in Figure 2.6.
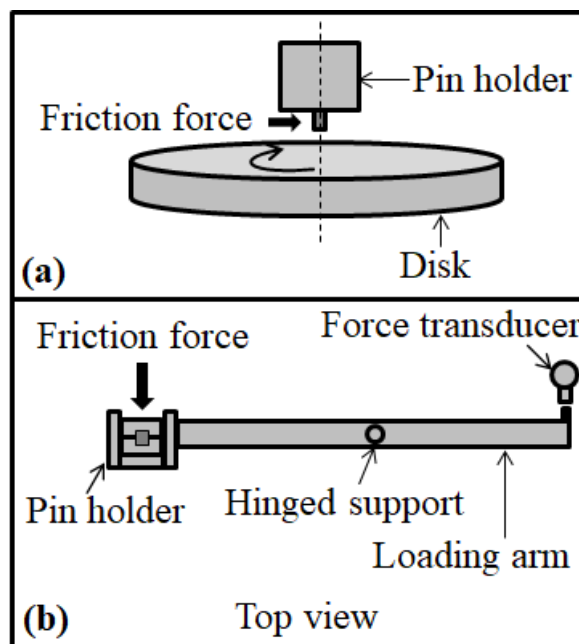
Figure 2.4: Friction force transfer from (a) disk to pin and (b) pin to force transducer.
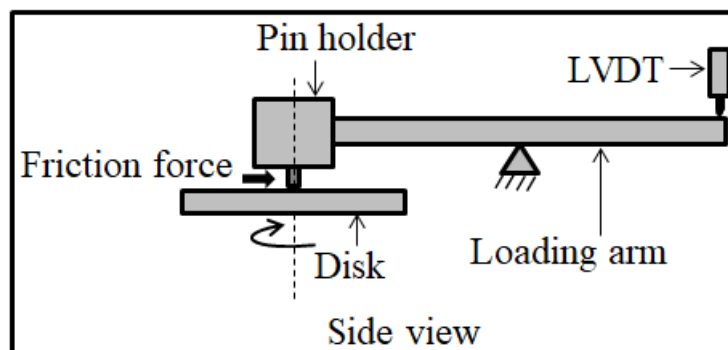
Figure 2.5: Schematic picture of wear depth measurement using LVDT during pin on disk experiment.

Table 2.2: Test conditions.

Parameter	Value
Normal load	1 kg, 1.5 kg and 2 kg
Sliding speed	1.25 m/s, 2 m/s and 3 m/s
Temperature	Room temperature (31 ± 1) °C, 60 °C, 100 °C and 150 °C
Atmosphere	Atmospheric air
Humidity	80 %
Roughness of disk surface	R_a = 0.3 μm - 0.5 μm
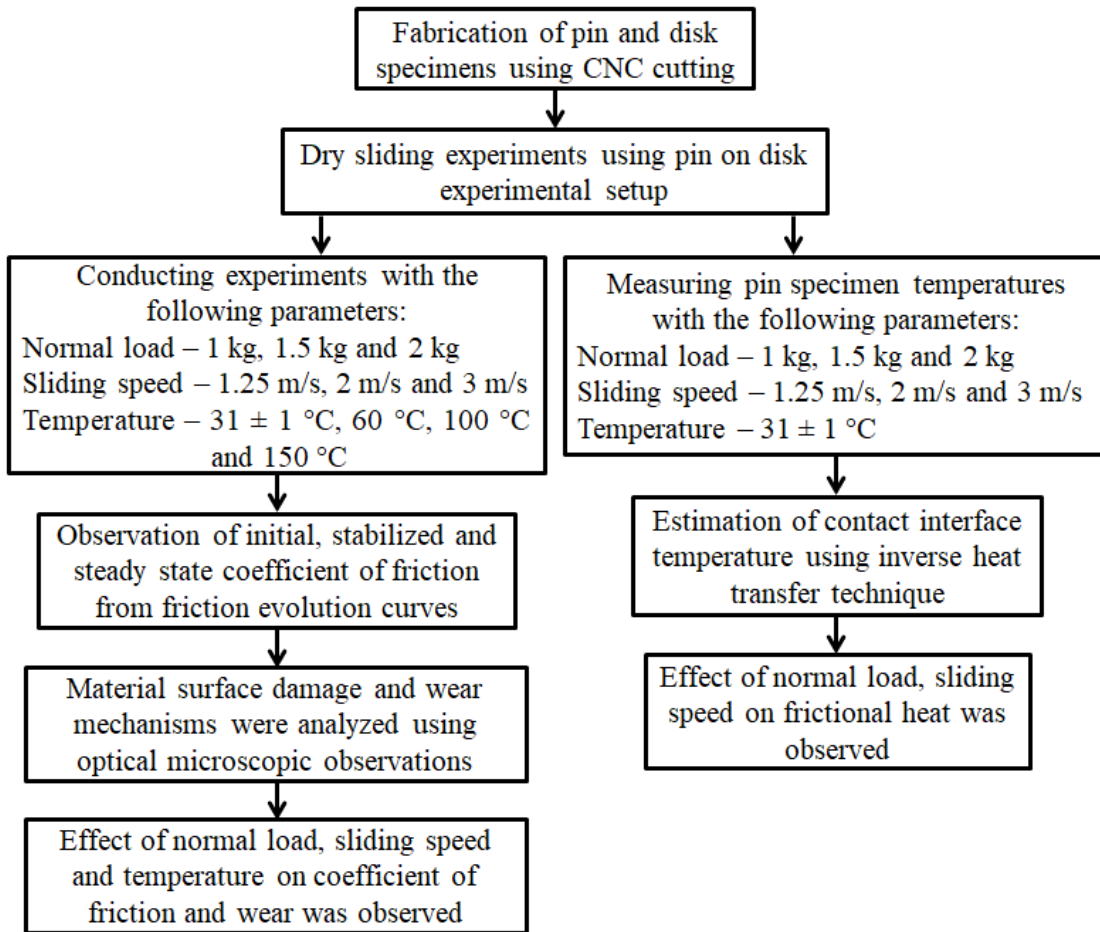
Figure 2.6: Flow chart of research methodology.

CHAPTER 3

FRICTIONAL HEAT ESTIMATION DURING DRY SLIDING

Temperature is one of major parameters effecting the coefficient of friction and wear of metallic contacts. The temperature at sliding contact interface exists due to frictional heat generation and from the surrounding environment. The temperature at contact interface promotes the oxidation of surfaces of contact interface materials. So, it is important to study the temperature at contact interface due to frictional heat and effect of loading parameters on frictional heat. This chapter focuses on one-dimensional inverse heat transfer model using Finite Element Approach and validation of the same. Preliminary experiments were conducted using two different materials (Al 6061-T6 and SS304) to check the performance of proposed inverse heat transfer technique. This investigation focuses on estimation of frictional heat at contact interface during dry sliding of metal contacts. Temperatures at 3 mm and 7 mm locations from contact interface were measured during dry sliding of metal surfaces using pin on disk experimental setup. One dimensional inverse heat transfer model was developed using Finite Element Method and Beck's algorithm. Transient thermal analysis was conducted using *ANSYS* workbench to validate the results.

3.1 INTRODUCTION TO FRICTIONAL HEAT ESTIMATION

Inverse heat transfer models are being used to estimate the temperature at locations where there are practical difficulties to measure temperature. Industrial processes like metal casting and welding in automobile industries and aerospace industries (Antonino Repaci, 1991) use inverse heat transfer models to estimate the source temperature. During casting of metal bodies, heat transfer coefficient between molten metal to body of metal cast is important to understand the metal solidification process, this can be estimated using inverse heat transfer methods. Friction stir welding, sliding of brake pad-disc contact of automobile produces heat at the contact interfaces. Direct measurement of contact temperatures is not feasible experimentally. Estimating these temperatures is important for engineering design of components.

Beck et al., (1985) had done extensive studies on inverse heat conduction problems. They had derived different approaches to estimate the unknown heat source temperatures from the measured temperature data at selected points away from the heat source. Aweda and Adeyemi (2009) calculated heat transfer coefficients between steel mould and cast aluminium metal during squeeze casting of aluminium metal. They observed increase in heat transfer coefficient with increase in squeezing pressure and decrease in heat transfer coefficient with fall in solidification temperatures. The heat transfer coefficients were estimated using Beck's non-linear solution as mentioned in Krishnan and Sharma (1996). Ana Paula Fernandes et al., (2015) developed analytical model, based on Green's function, to solve the inverse heat conduction problems. The model was used to estimate the interface temperature of tool-work-piece during machining process. The quality of resistance spot weld depends on dimension of nugget, which depends on the temperature at weld spot. Chunfeng Zhao et al., (2016) developed inverse heat conduction model based on conjugate gradient method to estimate the temperatures at weld spot to estimate nugget dimension. Zhang et al., (2017) worked on estimation of interfacial heat transfer coefficient at metal-sand mould interface during low-pressure casting using nonlinear inverse methods. In their investigation, they found the accuracy of results can be improved by considering temperature-dependent thermo-physical properties of materials rather than considering the constant thermo-physical properties of materials. Shoubin Wang et al., (2018) solved two-dimensional unsteady inverse heat conduction problem using boundary element method. The model proposed by the authors showed accurate results even though the measuring points are far away from the heat source. Raghavendra et al., (2019) worked on estimation of temperature rise due to dry sliding friction of aluminium metal against EN-32 steel. The temperatures were estimated using finite element method and validated using *ANSYS* simulation. Zhizhong Sun et al., (2011), Liping Chen et al., (2014) and Zhang et al., (2017) used finite difference method to develop inverse heat transfer algorithms. Borut Cerne et al., (2019) used semi-analytical methods to estimate flash temperatures and bulk temperatures at the contact of gear teeth. Toshio Yoshimura & Kazushige Ikuta (1985); Srinivasa Raju et al., (2016); Christian Zeller et al., (2018) used Finite Element Method for transient thermal analysis. Researchers (Gupta et al., (2017);

30

Vishweshwara et al., (2019) and Vishweshwara et al., (2020)) also used artificial intelligence to estimate heat flow in materials for inverse heat transfer problems.

In the present study, efforts have been made to estimate the frictional heat at contact interface when two materials slide against each other; at such locations direct measurement of frictional heat is not practical. So, the temperature away from the contact interface due to frictional heat was measured to estimate the contact temperature. Inverse heat conduction model, using Finite Element Method and Beck's theorem, was developed and explained in this study.

3.2 MATERIALS USED FOR HEAT FRICTIONAL HEAT EXPERIMENTS

3.2.1 Materials

Two different materials (Al 6061-T6 and SS304) having large difference in thermo-physical properties are considered for the study. The thermo-physical properties of Al 6061-T6 and SS304 materials, provided by material supplier, are given in Table 3.1. For each experiment pin and disk specimens are fabricated with same materials. Pin specimens having dimension 30 mm length, 6 mm x 6 mm cross-section and 3 mm radius cylindrical finish at one end of the pin were fabricated with both the alloys. The photographic pictures of pin specimen and temperature measurement systems are shown in Figure 3.1. Two perpendicular faces of the pin specimen were drilled to a depth of 3 mm with 1.5 mm diameter drill bit. The drill locations are 3 mm (point 'A' in Figure 3.2) and 7 mm (point 'B' in Figure 3.2) from the cylindrical contact interface.

Table 3.1: Thermo-physical properties of Al 6061-T6 and SS304 alloys.

Material	Thermal conductivity (W m^{-1} °C^{-1})	Specific heat (J kg^{-1} °C^{-1})	Density (kg m^{-3})
Al 6061-T6	167	896	2700
SS304	16.2	500	8000

3.2.2 Experimental details

Dry sliding experiments were conducted using pin on disk experimental setup. Experiments were conducted with cylinder on flat contact configuration having same

material of contact pair. The experimental parameters (normal load and sliding speed) used for both the alloys are given in Table 3.2. While conducting experiment, the friction between the sliding bodies generates heat at the contact interface. Direct measurement of temperature at contact interface is not possible using thermocouples. So, temperature at 3 mm and 7 mm locations were measured using K-type thermocouples. The thermocouples were inserted in the drilled holes to measure temperature at mid-section of the pin. The temperature data was measured at 5 data samples per second. The measured temperatures at 3 mm location and 7 mm location are given in Figure 3.3 and Figure 3.4.
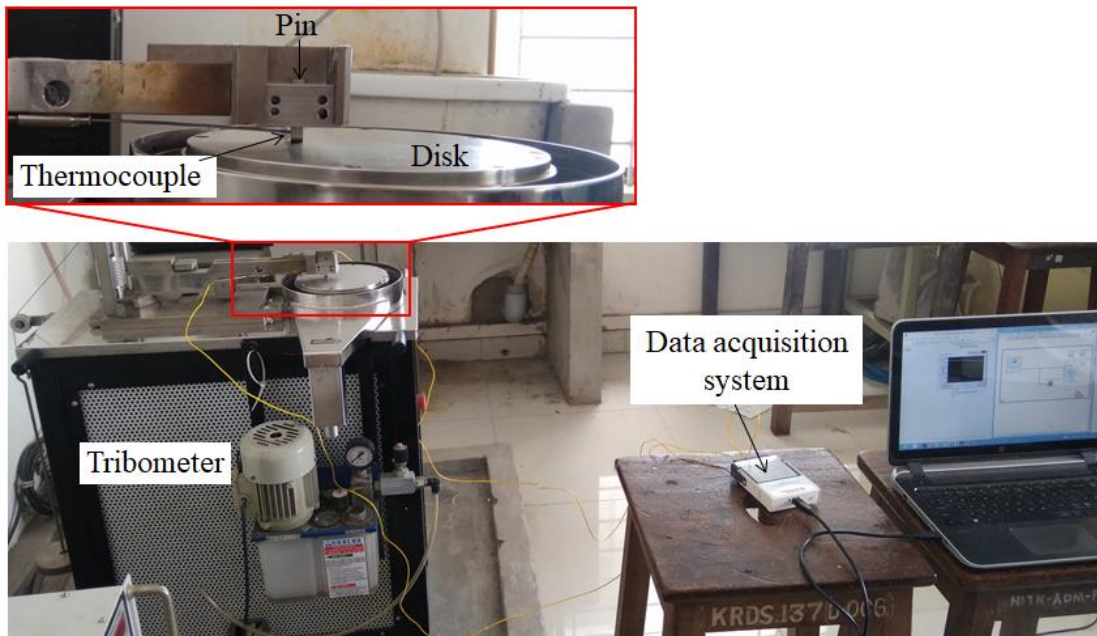
Figure 3.1: Pin on disk setup during experiment along with temperature data acquisition system.
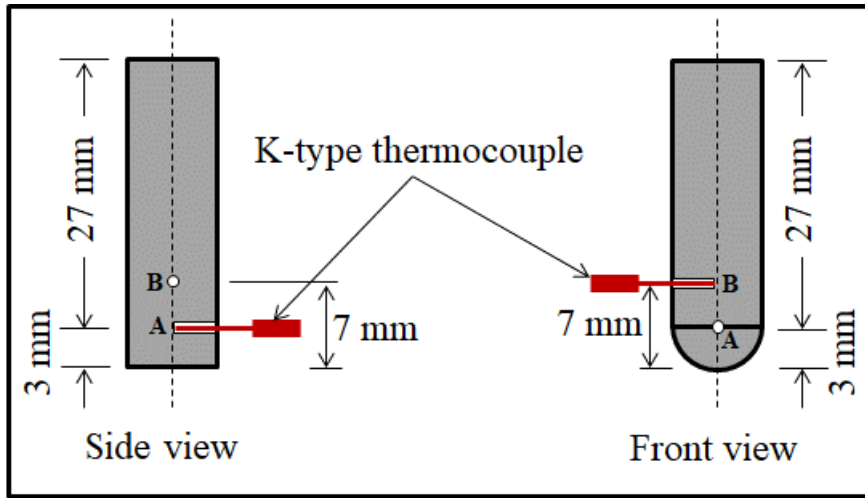
Figure 3.2: Schematic of temperature measurement points with thermocouples in pin specimen.

Table 3.2 Experimental parameters used for dry sliding pin on disk experiments.

Material	Normal load (kg)	Sliding speed (m/s)
Al 6061-T6	1	1.25
SS304	2	1
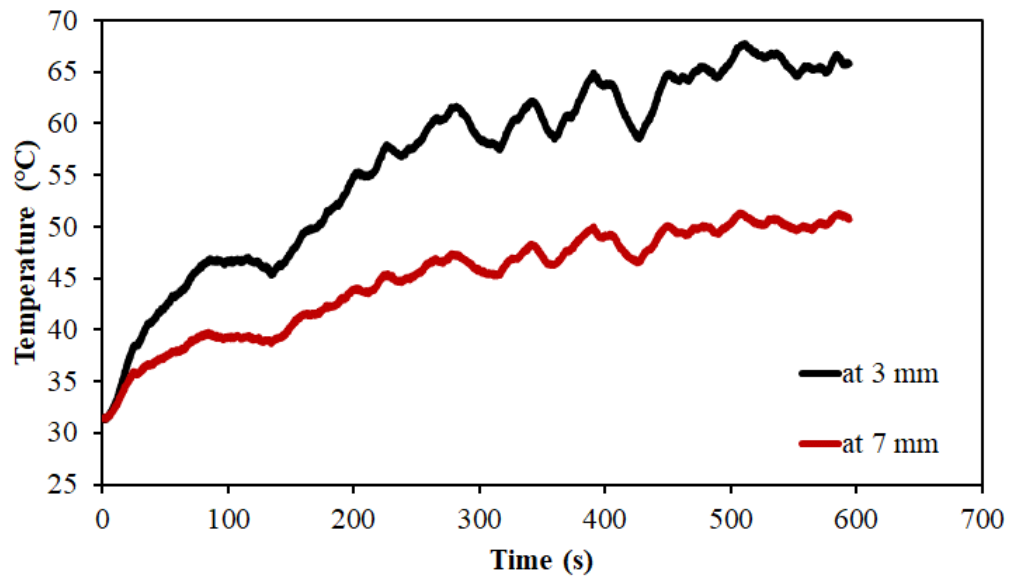
Figure 3.3: Temperatures measured at 3 mm and 7 mm from contact interface during dry sliding experiments on SS304 alloy.
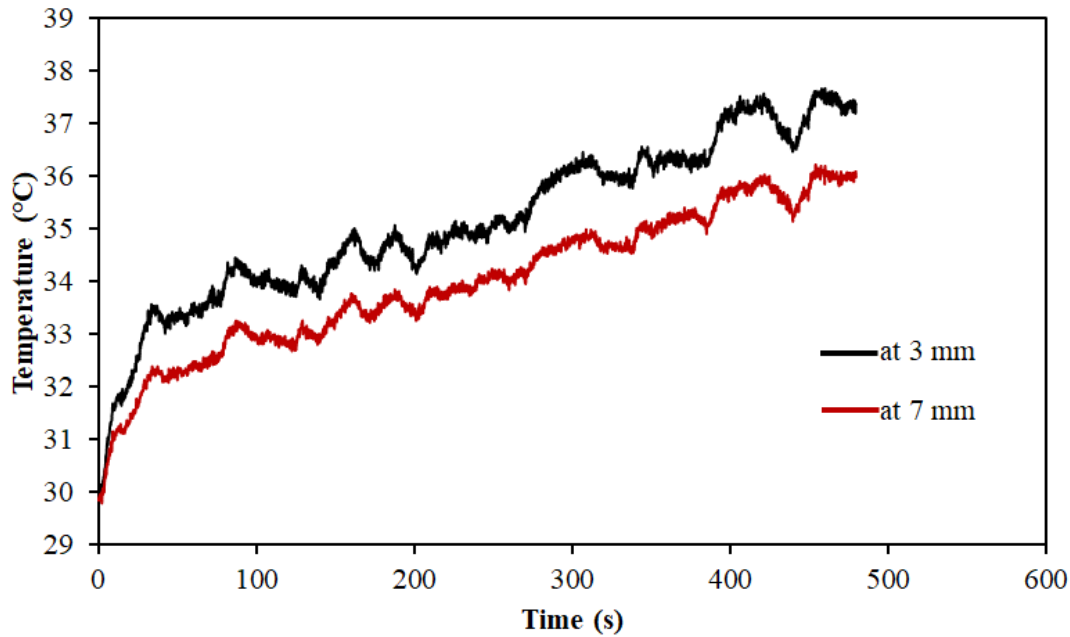
Figure 3.4: Temperatures measured at 3 mm and 7 mm from contact interface during dry sliding experiments on Al 6061-T6 alloy.

3.2.3 Methodology

The temperatures measured at 3 mm and 7 mm from the contact interface were used as base data to estimate the temperature at contact interface. One-dimensional conductive heat transfer model was formulated using Finite Element Method. Consequently, inverse heat transfer model was developed using Beck's algorithm. Heat flux at contact interface and temperature distribution along the pin was estimated using proposed inverse heat transfer model. The estimated heat flux data at contact interface and measured temperature at 7 mm location was used to validate the proposed model. The validation of proposed model was done using *ANSYS* workbench. Methodology to estimate the contact interface temperatures is given in Figure 3.5.
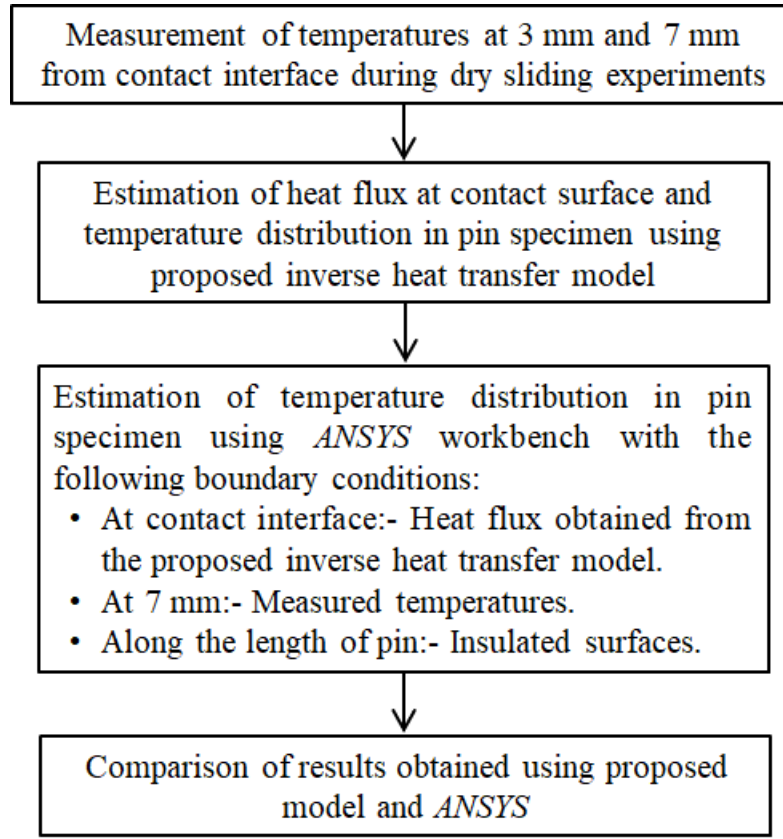
Figure 3.5: Methodology for estimation of contact interface temperatures.

3.3 FINITE ELEMENT FORMULATION FOR INVERSE HEAT TRANSFER

In the present study, the temperature measurements were taken at mid-plane of the pin (plane 'abcd' in Figure 3.7) to develop one-dimensional conductive heat transfer model. Heat transfer analysis was performed on the same plane 'abcd'. The assumptions are heat conduction is one dimensional and change in length of pin due to wear is negligible. The temperature measurement points are taken nearer to the contact interface to minimize heat loss due to convection; the present model is developed for pure conduction case. The governing equation for one-dimensional heat conduction is given as:

$$\frac{\partial}{\partial x}\left(k\frac{\partial \mathrm{T}}{\partial x}\right) = \rho c \frac{\partial \mathrm{T}}{\partial t} \qquad \text{at } 0 < x < \mathrm{L} \text{ and } t = 0; \qquad (3.1)$$

Where, x is distance from the contact interface, k is thermal conductivity, ρ is density of material, c is specific heat, T is temperature, t is time and L is length of pin considered for analysis (7 mm).

The initial conditions and boundary conditions used in this study are,

Initial conditions:

$$T(x, 0) = T_{mea}(x = 3 \text{ mm}, 0 \text{ s});$$ (3.2a)

$$\text{Heat flux, } q(0, 0) = 0;$$ (3.2b)

Boundary conditions:

$$T(x = 7 \text{ mm}, t) = T_{mea}(x = 7 \text{ mm}, t); \text{ at } t > 0;$$ (3.2c)

$$q(x = 0 \text{ mm}, t) = q(t); \text{ at } t > 0;$$ (3.2d)

The temperature is assumed to vary linearly between two nodes of the element (Figure 3.6). Thus,
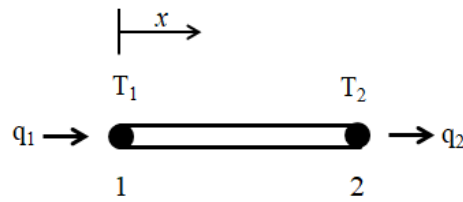
Figure 3.6: Schematic of two node linear element.

$$T(x) = a_0 + a_1 x$$ (3.3a)

$$T_1 = a_0 + a_1 x_1$$ (3.3b)

$$T_2 = a_0 + a_1 x_2$$ (3.3c)

$$T(x) = \left(\frac{x_2 - x}{x_2 - x_1} \quad \frac{x - x_1}{x_2 - x_1} \right) \left\{ \begin{matrix} T_1 \\ T_2 \end{matrix} \right\} = \begin{bmatrix} N_1 & N_2 \end{bmatrix} \left\{ \begin{matrix} T_1 \\ T_2 \end{matrix} \right\} = N^T T$$ (3.3d)

$$T'(x) = \left(\frac{-1}{x_2 - x_1} \quad \frac{1}{x_2 - x_1} \right) \left\{ \begin{matrix} T_1 \\ T_2 \end{matrix} \right\} = \begin{bmatrix} N_1' & N_2' \end{bmatrix} \left\{ \begin{matrix} T_1 \\ T_2 \end{matrix} \right\} = B^T T$$ (3.3e)

$$\frac{\partial T(x)}{\partial t} = \left(\frac{x_2 - x}{x_2 - x_1} \quad \frac{x - x_1}{x_2 - x_1} \right) \left\{ \begin{matrix} \frac{\partial T_1(x)}{\partial t} \\ \frac{\partial T_2(x)}{\partial t} \end{matrix} \right\} = \begin{bmatrix} N_1 & N_2 \end{bmatrix} \left\{ \begin{matrix} \frac{\partial T_1(x)}{\partial t} \\ \frac{\partial T_2(x)}{\partial t} \end{matrix} \right\} = N^T \dot{T}$$ (3.3f)

The weak form for the equation (1) can be written using Galerkin Method. The Galerkin weighted residual is:

36

$$\int_{x_1}^{x_2} W_i E(x)\,dx = 0$$

(3.4a)

Where, $E(x)$ is residual, W_i is weight function or interpolation function (N_i)

$$E(x) = \frac{\partial}{\partial x}\left(k\frac{\partial T}{\partial x}\right) - \rho c \frac{\partial T}{\partial t}$$

(3.4b)

$$\int_{x_1}^{x_2} N_i \left(\frac{\partial}{\partial x}\left(k\frac{\partial T}{\partial x}\right) - \rho c \frac{\partial T}{\partial t}\right)dx = 0$$

(3.4c)

$$\int_{x_1}^{x_2} N_i \left(\frac{\partial}{\partial x}\left(k\frac{\partial T}{\partial x}\right)\right)dx - \int_{x_1}^{x_2} N_i \left(\rho c \frac{\partial T}{\partial t}\right)dx = 0$$

(3.4d)

Using integration by parts

$$k\int_{x_1}^{x_2} \frac{\partial N_i}{\partial x}\left(\frac{\partial T}{\partial x}\right)dx + \int_{x_1}^{x_2} N_i\left(\rho c \frac{\partial T}{\partial t}\right)dx = \left(k\,N_i\big|_{x_2}\frac{\partial T(x_2)}{\partial x}\right) - \left(k\,N_i\big|_{x_1}\frac{\partial T(x_1)}{\partial x}\right)$$

(3.5a)

$$k\int_{x_1}^{x_2} N_i' T' dx + \rho c \int_{x_1}^{x_2} N_i N_i^T \dot{T} dx = N_i\big|_{x_2} q_2 + N_i\big|_{x_1} q_1$$

(3.5b)

Incorporating natural boundary conditions (heat flux)

For i = 1;

$$k\int_{x_1}^{x_2} N_1' T' dx + \rho c \int_{x_1}^{x_2} N_1 N_1^T \dot{T} dx = N_1\big|_{x_2} q_2 + N_1\big|_{x_1} q_1$$

(3.6a)

$$N_1\big|_{x_1} = 1; N_1\big|_{x_2} = 0; N_2\big|_{x_1} = 0; N_2\big|_{x_2} = 1$$

(3.6b)

$$k\int_{x_1}^{x_2} N_1' T' dx + \rho c \int_{x_1}^{x_2} N_1 N_1^T \dot{T}_1 dx = q_1$$

(3.6c)

$$k\int_{x_1}^{x_2} N_2' T' dx + \rho c \int_{x_1}^{x_2} N_2 N_2^T \dot{T}_2 dx = q_2$$

(3.6d)

Writing equations in matrix form

$$k\int_{x_1}^{x_2} \begin{bmatrix} N_1' \\ N_2' \end{bmatrix} \begin{bmatrix} N_1' & N_2' \end{bmatrix} \begin{Bmatrix} T_1 \\ T_2 \end{Bmatrix} dx + \rho c \int_{x_1}^{x_2} \begin{bmatrix} N_1 \\ N_2 \end{bmatrix} \begin{bmatrix} N_1 & N_2 \end{bmatrix} \begin{Bmatrix} \dot{T}_1 \\ \dot{T}_2 \end{Bmatrix} dx = \begin{Bmatrix} q_1 \\ q_2 \end{Bmatrix}$$

(3.7a)

$$k\int_{x_1}^{x_2} BB^T \begin{Bmatrix} T_1 \\ T_2 \end{Bmatrix} dx + \rho c \int_{x_1}^{x_2} NN^T \begin{Bmatrix} \dot{T}_1 \\ \dot{T}_2 \end{Bmatrix} dx = \begin{Bmatrix} q_1 \\ q_2 \end{Bmatrix}$$

(3.7b)

$$\frac{k}{l}\begin{bmatrix} 1 & -1 \\ -1 & 1 \end{bmatrix}\begin{Bmatrix} T_1 \\ T_2 \end{Bmatrix} + \frac{\rho c l}{6}\begin{bmatrix} 2 & 1 \\ 1 & 2 \end{bmatrix}\begin{Bmatrix} \dot{T}_1 \\ \dot{T}_2 \end{Bmatrix} = \begin{Bmatrix} q_1 \\ q_2 \end{Bmatrix}$$

(3.7c)

$$\frac{\rho c l}{6}\begin{bmatrix} 2 & 1 \\ 1 & 2 \end{bmatrix}\begin{Bmatrix} \dfrac{\partial T_1}{\partial t} \\ \dfrac{\partial T_2}{\partial t} \end{Bmatrix} + \frac{k}{l}\begin{bmatrix} 1 & -1 \\ -1 & 1 \end{bmatrix}\begin{Bmatrix} T_1 \\ T_2 \end{Bmatrix} = \begin{Bmatrix} q_1 \\ q_2 \end{Bmatrix}$$

(3.7d)

Where, i is node number (1, 2, ….7) and n is time step number (2, 3, …. n_{max})

By using forward difference for time discretization

$$\frac{\rho c l}{6}\begin{bmatrix} 2 & 1 \\ 1 & 2 \end{bmatrix}\begin{Bmatrix} \dfrac{T_i^n - T_i^{n-1}}{\Delta t} \\ \dfrac{T_{i+1}^n - T_{i+1}^{n-1}}{\Delta t} \end{Bmatrix} + \frac{k}{l}\begin{bmatrix} 1 & -1 \\ -1 & 1 \end{bmatrix}\begin{Bmatrix} T_i^n \\ T_{i+1}^n \end{Bmatrix} = \begin{Bmatrix} q_i^n \\ q_{i+1}^n \end{Bmatrix}$$

(3.8a)

$$\frac{\rho c l}{6}\begin{bmatrix} 2 & 1 \\ 1 & 2 \end{bmatrix}\begin{Bmatrix} T_i^n - T_i^{n-1} \\ T_{i+1}^n - T_{i+1}^{n-1} \end{Bmatrix} + \frac{(\Delta t)k}{l}\begin{bmatrix} 1 & -1 \\ -1 & 1 \end{bmatrix}\begin{Bmatrix} T_i^n \\ T_{i+1}^n \end{Bmatrix} = (\Delta t)\begin{Bmatrix} q_i^n \\ q_{i+1}^n \end{Bmatrix}$$

(3.8b)

The temperature at two nodes of an element at time 'n' is,

$$\left[\frac{\rho c l}{6}\begin{bmatrix} 2 & 1 \\ 1 & 2 \end{bmatrix} + \frac{(\Delta t)k}{l}\begin{bmatrix} 1 & -1 \\ -1 & 1 \end{bmatrix} \right]\begin{Bmatrix} T_i^n \\ T_{i+1}^n \end{Bmatrix} = \frac{\rho c l}{6}\begin{bmatrix} 2 & 1 \\ 1 & 2 \end{bmatrix}\begin{Bmatrix} T_i^{n-1} \\ T_{i+1}^{n-1} \end{Bmatrix} + (\Delta t)\begin{Bmatrix} q_i^n \\ q_{i+1}^n \end{Bmatrix}$$

(3.8c)
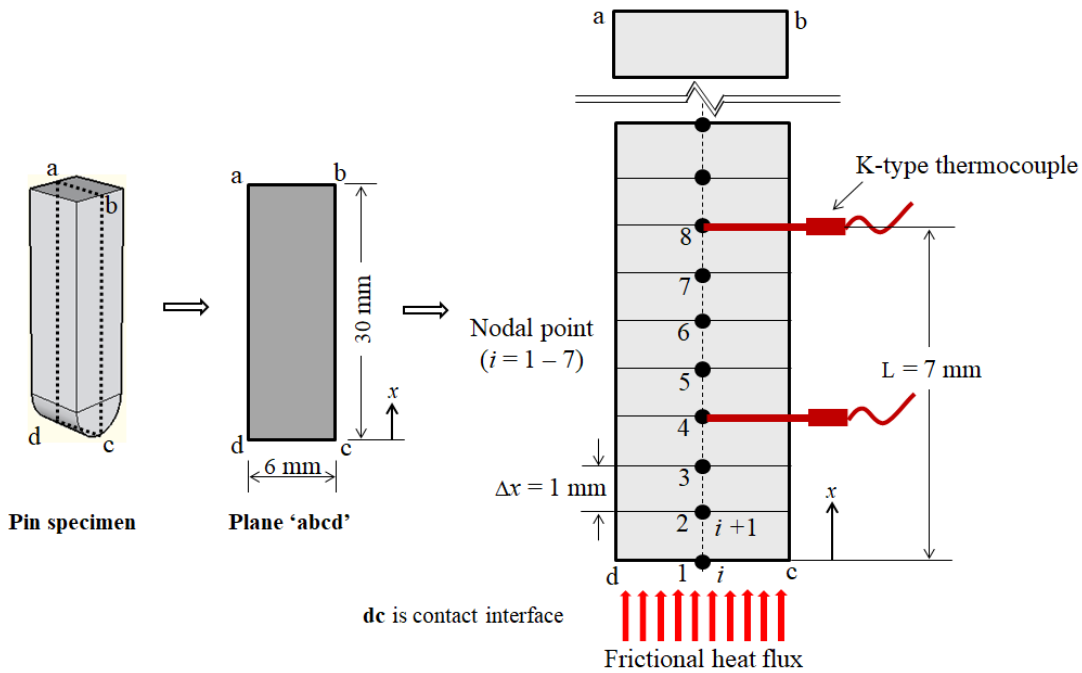
Figure 3.7: Nodal discretization and boundary conditions of pin specimen.

38

At a particular time, to calculate temperature at contact interface using equation (3.8c), heat flux data at contact interface is needed which is unknown in this study. The temperature distribution in the pin can be calculated by assuming the heat flux at the contact interface and by correcting the assumed heat flux using the known (measured) temperature at selected locations in the pin. Beck et al., (1985) developed non-linear estimation method by forming relationship between temperature in the body and source heat flux. They used least square technique to develop non-linear estimation method. In the present study, one-dimensional Finite Element Method was used along with Beck's non-linear estimation method to develop inverse heat transfer model. To determine heat flux at the contact interface for particular time step (node i = 1 and at time t), initial heat flux 'q' is assumed as 1 for t > 0 and it was maintained constant for certain time steps 'u' (u = 2 - 5) (Zhizhong Sun et al., 2011), in the present study 'u' is considered as 4. While estimating temperature at every time step, temperatures in subsequent future 'u' time steps were estimated with assumed heat flux 'q'. The assumed heat flux was changed by 'εq', where 'ε' is a small fraction, and new set of temperatures were calculated with heat flux 'q + εq'. The effect of change in heat flux on nodal temperature was formulated using equation (3.9), here ϕ is called sensitivity coefficient. The error in the assumed heat flux was calculated using equation (3.10) and heat flux was corrected using equation (3.11). The same process was repeated for a particular time step until the equation (3.12) satisfied and the process is repeated for future time steps.

$$\phi_i^{n+j-1} = \frac{\left. \mathrm{T}_{est@i}^{n+j-1} \right|_{q+\varepsilon q} - \left. \mathrm{T}_{est@i}^{n+j-1} \right|_{q}}{\varepsilon \mathrm{q}} ; j = 1, 2, ... \mathrm{u}$$

(3.9)

$$\mathrm{dq}^n = \frac{\sum_{i=1}^{m} \sum_{j=1}^{u} \left(\left(\left. \mathrm{T}_{mea}^{n+j-1} \right|_i - \left. \mathrm{T}_{est}^{n+j-1} \right|_i \right) \phi_i^{n+j-1} \right)}{\sum_{i=1}^{m} \sum_{j=1}^{u} \left(\phi_i^{n+j-1} \right)^2} ; i = 4, j = 1, 2, ... \mathrm{u}$$

(3.10)

$$\mathrm{q}_{cor}^n = \mathrm{q}^n + \mathrm{dq}^n$$

(3.11)

$$\frac{\mathrm{dq}^n}{\mathrm{q}^n} \leq \varepsilon ; \varepsilon = 0.0001$$

(3.12)

Where, T_{est} is estimated temperature, T_{mea} is measured temperature, q_{cor} is corrected heat flux, dq is change in heat flux. The flow chart given in Figure 3.8 explains complete process of proposed inverse heat transfer model. The proposed inverse heat transfer model starts by considering initial conditions given in equations (3.2a) and (3.2b). The proposed model can predict the heat flux correctly if the assumed heat flux is less than the actual heat flux. So, at every time step the assumed heat flux is considered as $q = 1$ W/m^2. The temperature distribution in the 7 mm length of the pin was calculated using equation (3.8c) with known boundary conditions, $T(7, t) = T_{mea}(7, t)$ and $q^n = q^{n+1} \ldots q^{n+j+1}$, where n is present time step, $j = 1, 2, \ldots u$. The correction in assumed heat flux was calculated by comparing the measured temperatures at 3 mm location (node 4 in Figure 3.7) and the estimated temperature at the same location for a particular time step as given in equation (3.10). The corrected heat flux (q_{cor}) was assigned to the assumed heat flux until the accuracy of the model was attained at particular time step as given in equation (3.12). The heat flux at contact interface and temperature distribution in the pin for all the time steps were calculated as given in Figure 3.8 by writing *MATLAB* program.
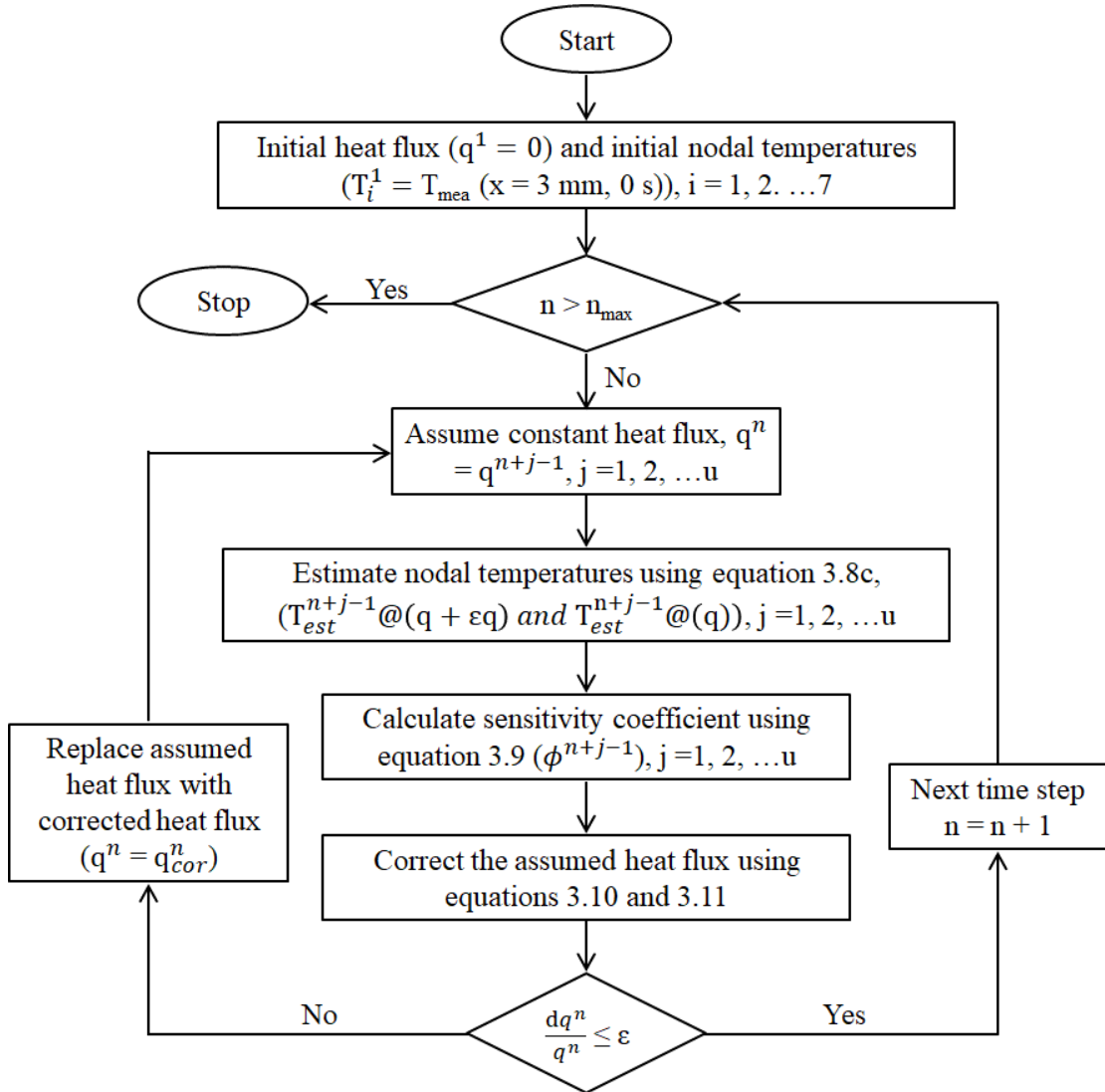
Figure 3.8: Flow chart of proposed inverse heat transfer model.

The flowchart contains the following elements:

- **Start**
- Initial heat flux ($q^1 = 0$) and initial nodal temperatures ($T_i^1 = T_{mea}$ (x = 3 mm, 0 s)), i = 1, 2. …7
- Decision: $n > n_{max}$ → **Yes** → **Stop**; → **No**
- Assume constant heat flux, $q^n = q^{n+j-1}$, j =1, 2, …u
- Estimate nodal temperatures using equation 3.8c, (T_{est}^{n+j-1}@(q + εq) *and* T_{est}^{n+j-1}@(q)), j =1, 2, …u
- Calculate sensitivity coefficient using equation 3.9 (ϕ^{n+j-1}), j =1, 2, …u
- Correct the assumed heat flux using equations 3.10 and 3.11
- Decision: $\dfrac{dq^n}{q^n} \leq \varepsilon$ → **No** → Replace assumed heat flux with corrected heat flux ($q^n = q_{cor}^n$); → **Yes** → Next time step n = n + 1
- Next time step n = n + 1 loops back to $n > n_{max}$

3.4 RESULTS AND DISCUSSION

3.4.1 Temperature distribution and heat flux from inverse method

The measured temperature data at 3 mm and 7 mm from the contact interface were taken as base data, for *MATLAB* programming, to estimate heat flux at contact interface and temperature distribution in pin specimen. The temperature data was measured at time interval of 0.2 s, so the required parameters were estimated at time step size (Δt) of 0.2 s. The time for estimation of temperature distribution in pin depends on the element size. The temperatures in pin were calculated with element length of 1 mm and 0.1 mm. Figure 3.9 shows the estimated contact interface

temperatures with 1 mm and 0.1 mm element size in SS304 alloy specimen. There were no considerable changes in estimated temperature with element lengths of 1 mm and 0.1 mm; the difference is of order 10^{-3} °C. Similar observation was made in Al 6061-T6 alloy. Thus element size of 1 mm was considered for both estimation and validation of the present study. The *MATLAB* program written for this study is given in Annexure I.
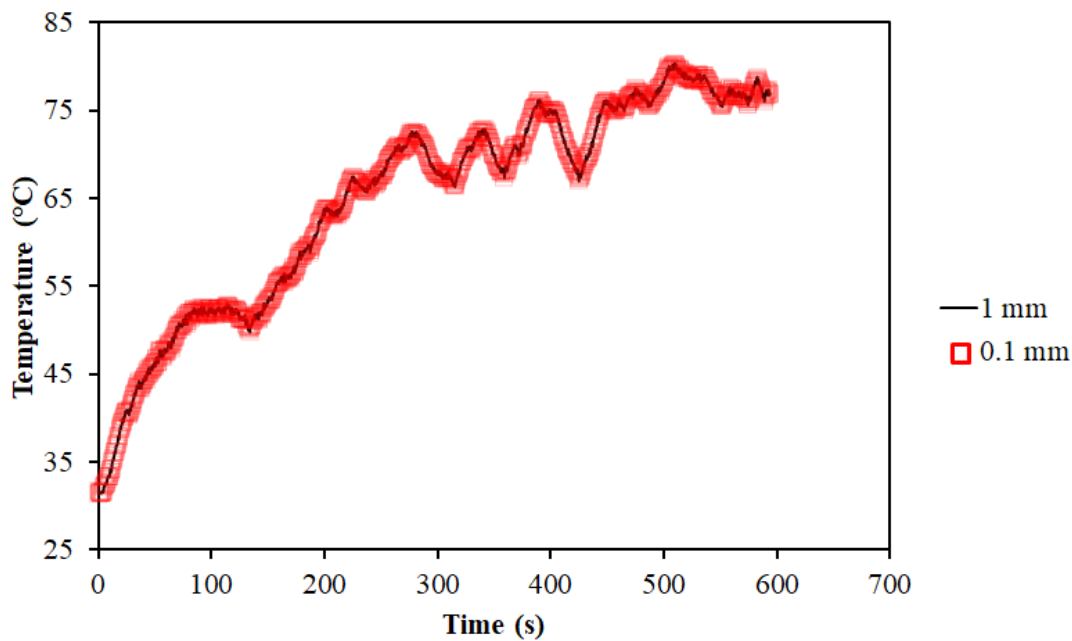
Figure 3.9: Estimated contact interface temperature of SS304 contact pair at element size of 1 mm (black line) and element size of 0.1 mm (red box).

When two metal bodies slide against each other, the friction between two surfaces develops high contact stresses which leads to plastic deformation of contact surface and thereby generates frictional heat. SS304 alloy, on applying normal load of 2 kg and sliding speed of 1 m/s, showed increase in heat flux and temperature at contact interface with increase in sliding time. The estimated heat flux at contact interface in SS304 alloy is given in Figure 3.10 (a). The increase in heat flux in the first 300 s of sliding was due to increase in coefficient of friction between pin and disk specimen. The stable heat flux was due to stabilized friction coefficient. The estimated temperature at each node of the pin specimen is given in Figure 3.12 (a). The pin contact surface temperature is important to understand the friction process at contact

42

interface. In the present study, to understand the stability of the proposed inverse heat transfer model, the estimated temperature at all the nodes of both the alloys (SS304 and Al 6061-T6) are given in detail. In Figure 3.11, T_1, T_2…. T_8 represents nodal temperatures at node 1, 2….8 as given in Figure 3.7. The surface plot of temperature distribution in SS304 pin during the full sliding experiment is presented in Figure 3.13 (a). Similarly, estimated heat flux at contact interface of full sliding Al 6061-T6 contact on applying 1 kg normal load and sliding speed of 1.25 m/s is given in Figure 3.10 (b). In Al 6061-T6 alloy, rapid increase in heat flux was observed within 40 s of sliding time and then heat flux stabilized. The estimated temperature values at each node of Al 6061-T6 alloy pin is given in Figure 3.12 (b), the surface plot of the estimated temperatures is given in Figure 3.13 (b). In both the alloys, the temperature at contact interface increased with increase in sliding time. Similar observations were done by Francis E. Kennedy et al., (2015) and Odabas (2018). From Figure 3.14 and Figure 3.15, continuous increase in contact interface temperature was observed when continuous increase in coefficient of friction occurred. The contact interface temperature stabilized when the fluctuation in coefficient of friction was more, which occurs due to removal of contact asperities and rolling effect of removed metal asperities at the contact interface. The stabilized coefficient of friction leads to increase in contact interface temperature.
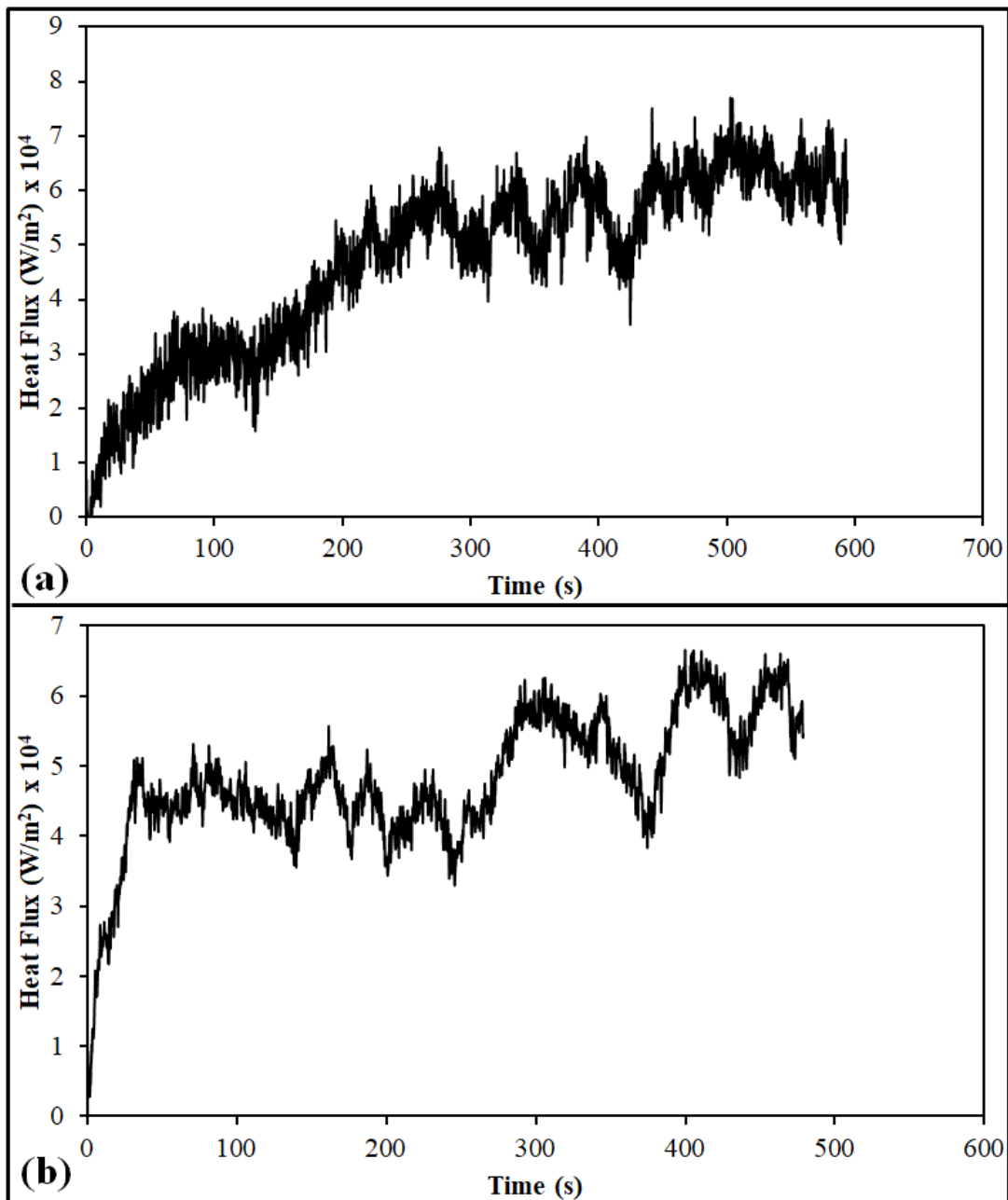
Figure 3.10: Estimated heat flux at contact interface of (a) SS304 alloy and (b) Al 6061-T6 alloy.
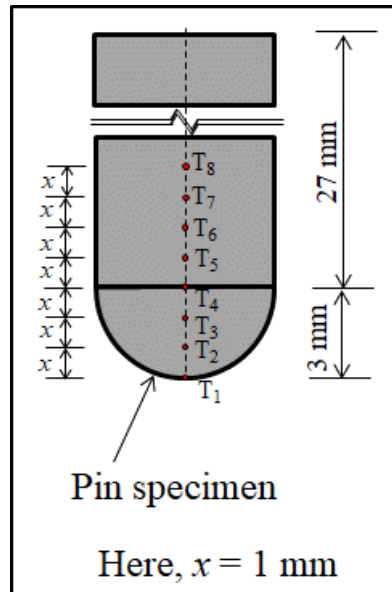
Figure 3.11: Nodal positions in pin specimen.
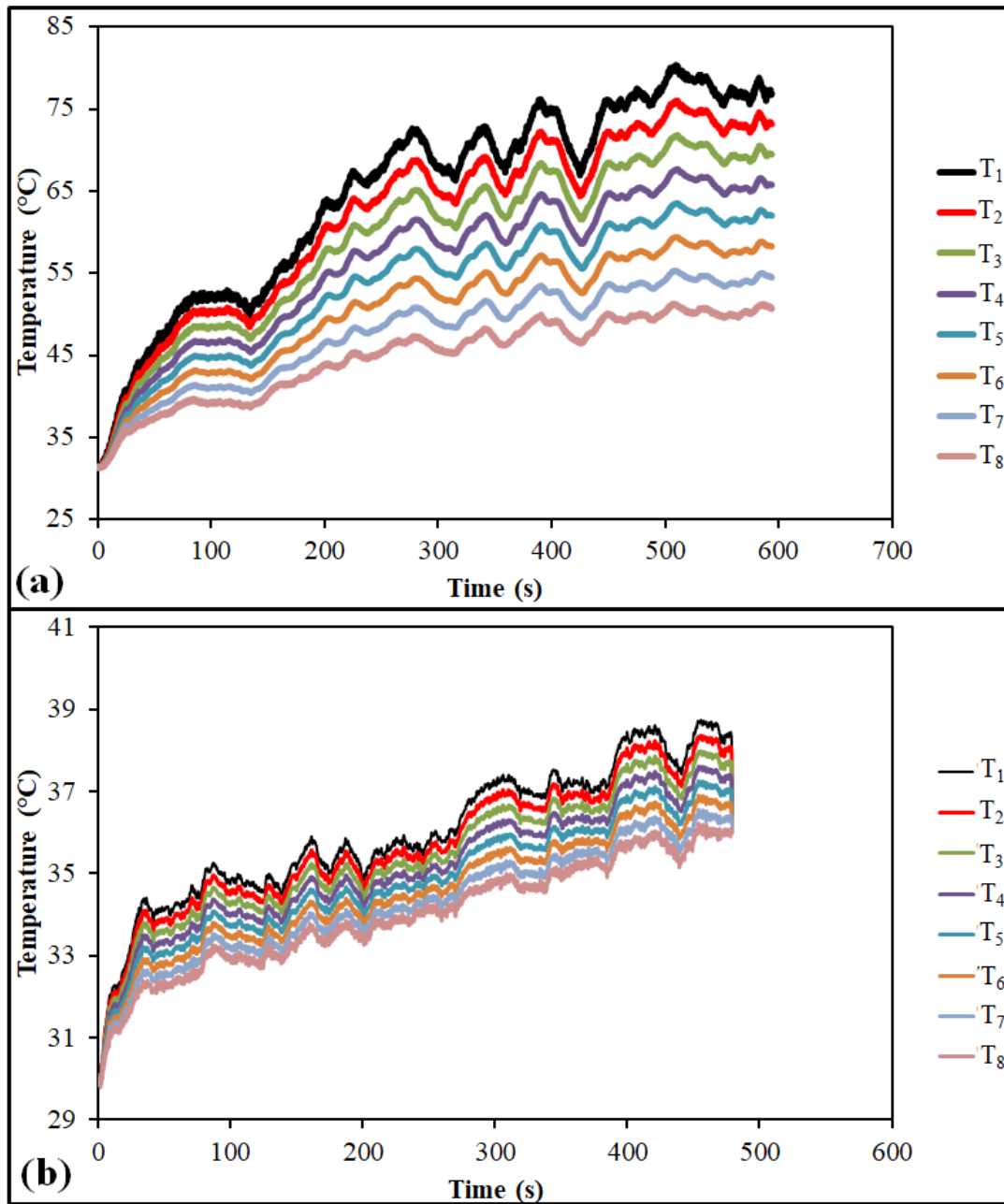
Figure 3.12: (a) Estimated nodal temperatures in SS304 alloy and (b) estimated nodal temperatures in Al 6061-T6 alloy.
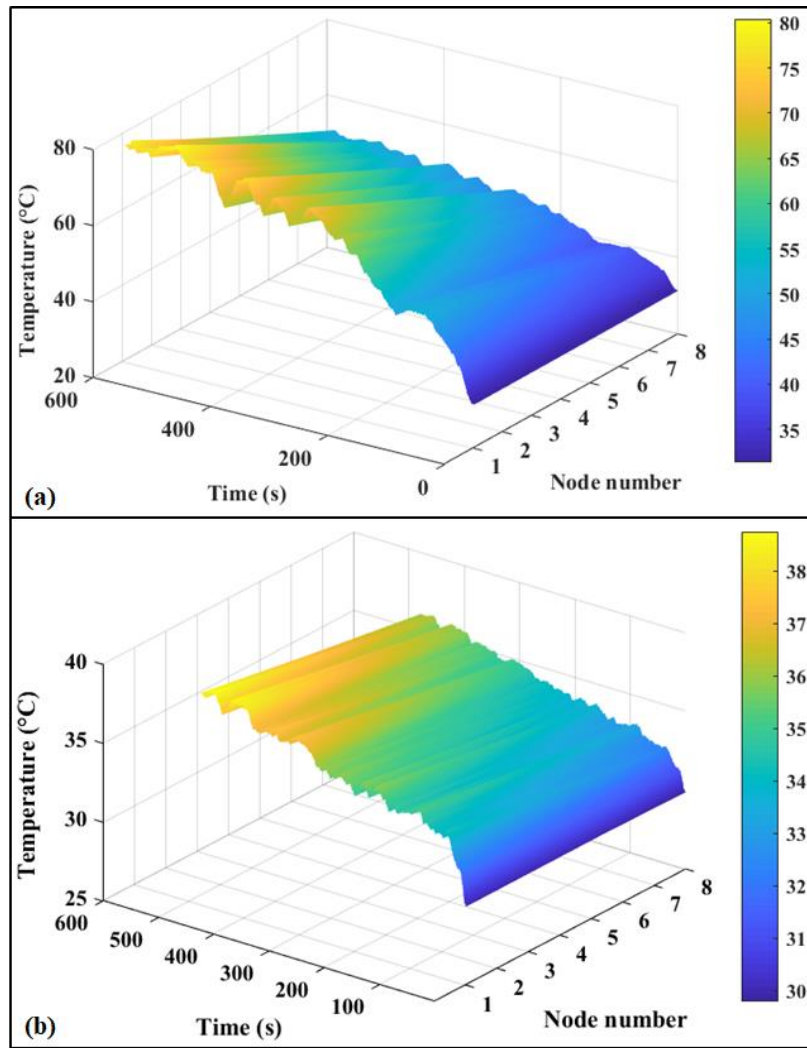
Figure 3.13: Surface plots of nodal temperatures in (a) SS304 alloy and (b) Al 6061-T6 alloy.
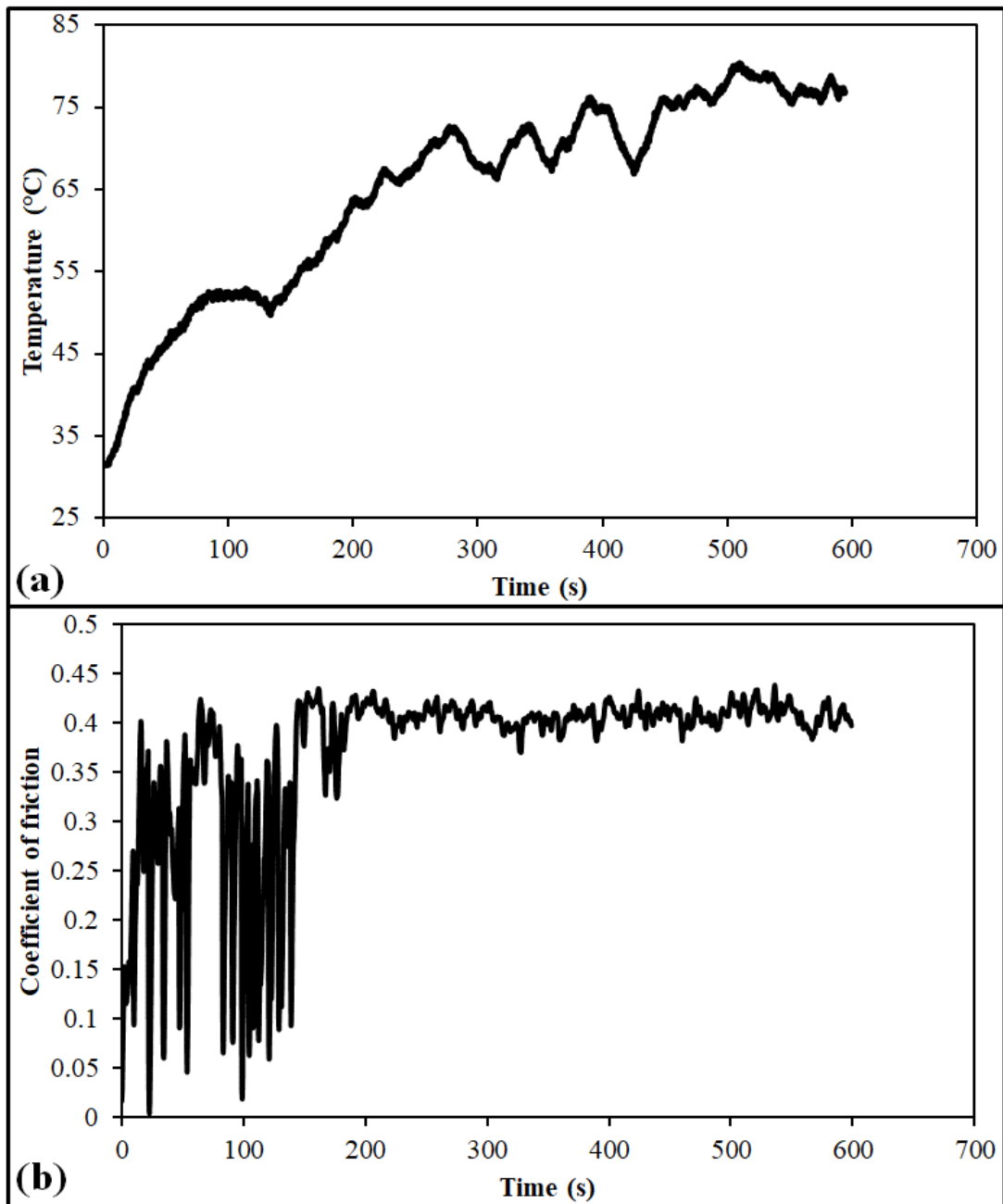
Figure 3.14: (a) Evolution of contact interface temperature and (b) evolution of coefficient of friction in SS304 alloy.

48
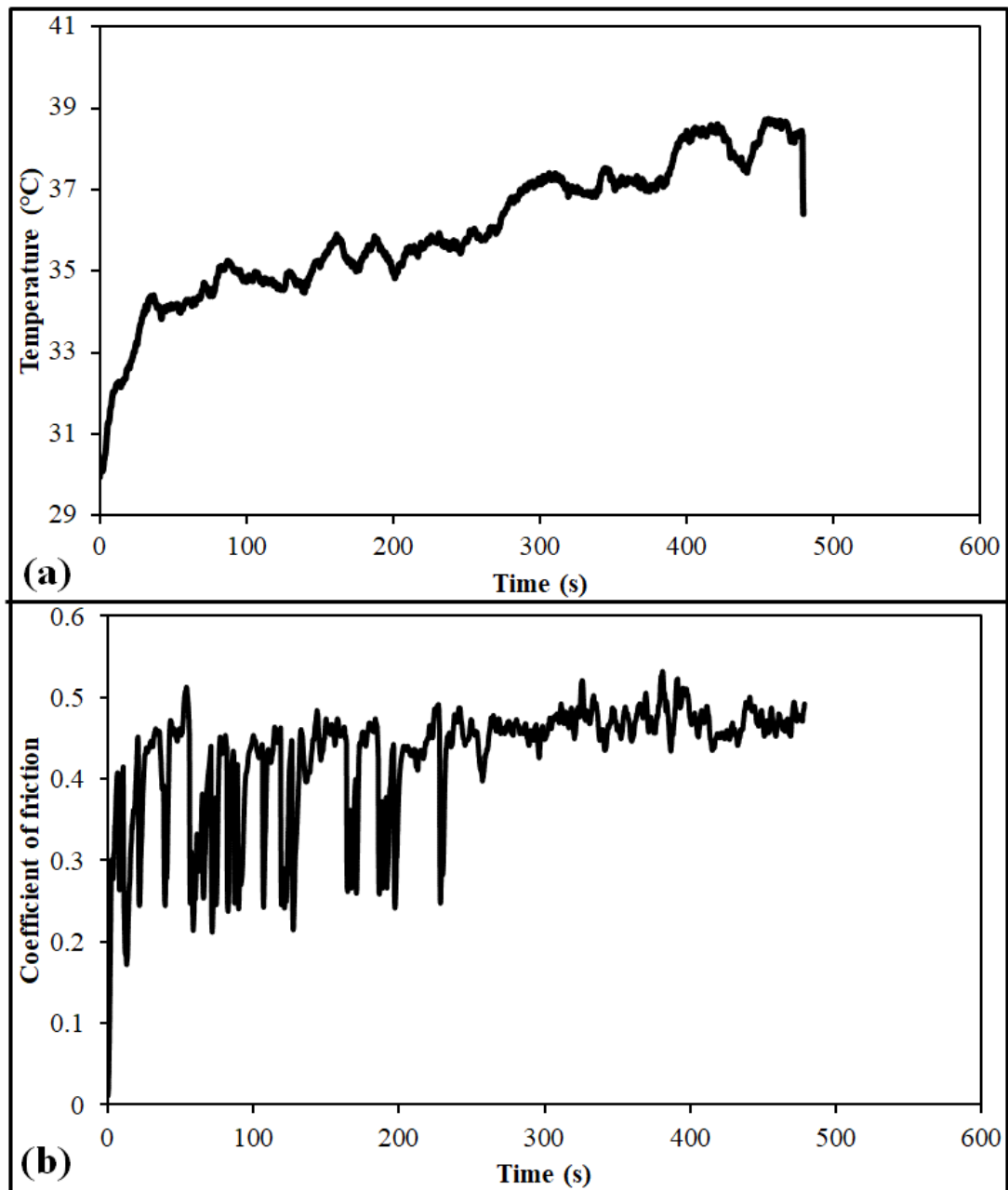
Figure 3.15: (a) Evolution of contact interface temperature and (b) evolution of coefficient of friction in Al 6061-T6 alloy.

3.4.2 Validation of inverse method

The estimated heat flux data at contact interface of SS304 alloy and Al 6061-T6 alloy, which is presented in Figure 3.10, was used to validate proposed inverse heat transfer model. Pin length of 7 mm from the contact interface was analyzed using *ANSYS* workbench to validate the results obtained from proposed inverse heat transfer model. PLANE77 element with element size of 1 mm was considered for analysis. PLANE77 is a, two dimensional, eight-node element having one degree of freedom (temperature) at each node (Figure 3.16 (b)). Two-dimensional transient thermal analysis was performed by assigning boundary conditions as heat flux at contact interface (side 'dc' in Figure 3.16 (a)), measured temperatures at 7 mm from contact interface of the model (side 'ab' in Figure 3.16 (a)) and other two boundaries were insulated (side 'ad' and 'bc' in Figure 3.16 (a)). The modeled temperature distribution, at a particular time, using *ANSYS* in pins of both the alloys at a particular time is given in Figure 3.17. The temperature data at each node (according to Figure 3.7) of the pin from *ANSYS* analysis was noted and compared with the data obtained from the inverse heat transfer model. The difference in temperatures between proposed inverse heat transfer model and *ANSYS* model at each node are plotted in Figure 3.18 and Figure 3.19. Mean and standard deviation of error between models is given in Table 3.3 and Table 3.4. In SS304 alloy, the initial few seconds of the experiment showed maximum difference (0.4 °C) between the models where the mean value of difference is around 0.03 °C at T1 location. In Al 6061-T6 alloy, the difference between the models showed mean value around 0.006 °C. From Table 3.3 and Table 3.4, the standard deviation values are almost equal to zero, which represents the deviation of errors is less from the mean value. The temperature at 3 mm location of pin obtained from *ANSYS* analysis was compared with the measured temperature data at the same location of specimen for both the alloys. The difference between *ANSYS* analysis and measured data in SS304 alloy and Al 6061-T6 alloy is presented in Figure 3.20 (a) and Figure 3.20 (b) respectively. The mean value of error between *ANSYS* results and experimental data is 0.05 °C and 0.04 °C in SS304 alloy and Al 6061-T6 alloy respectively.
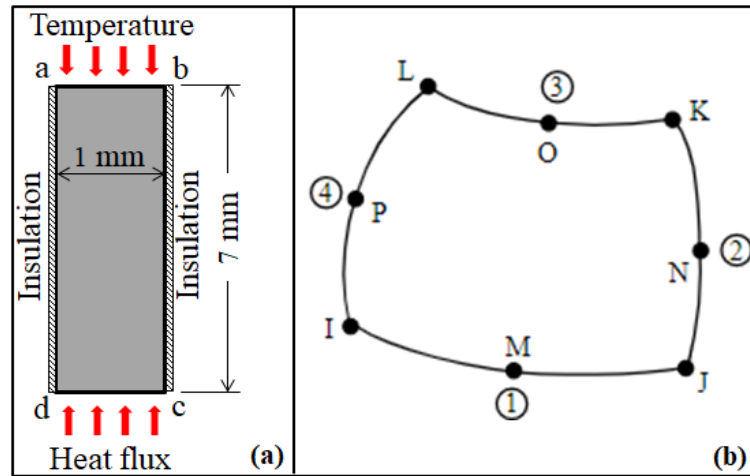
Figure 3.16: (a) Boundary conditions applied on central plane 'abcd' of pin specimen and (b) schematic of PLANE77 element (*ANSYS* Help, 2019).
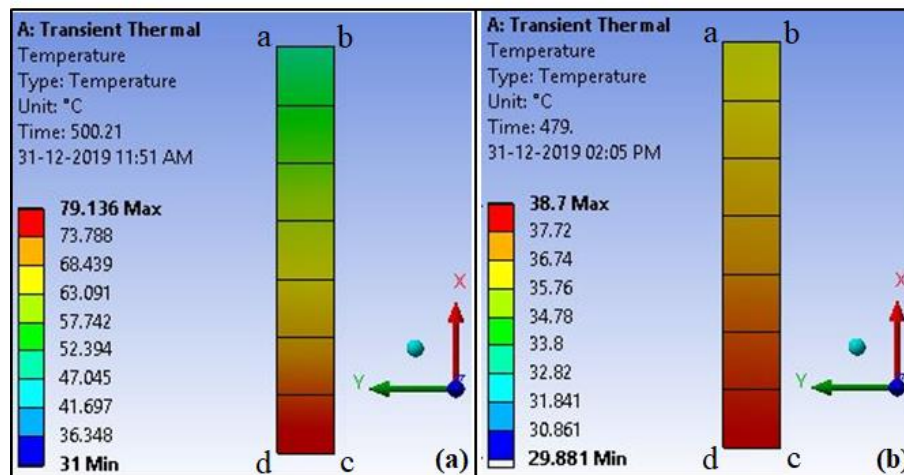
Figure 3.17: (a) Temperature distribution in SS304 alloy pin specimen at 500.2 s and (b) temperature distribution in Al 6061-T6 alloy pin specimen at 479 s.

Table 3.3: Mean and standard deviation of difference between *ANSYS* results and proposed model at different nodes in SS304 alloy pin specimen.

SS304	T_1	T_2	T_3	T_4	T_5	T_6	T_7
Mean (°C)	0.0293	0.0168	0.0119	0.0092	0.0073	0.0058	0.0055
Standard deviation (°C)	0.0387	0.0307	0.0278	0.0251	0.0215	0.0167	0.0113

Table 3.4: Mean and standard deviation of difference between *ANSYS* results and proposed model at different nodes in Al 6061-T6 alloy pin specimen.

Al 6061-T6	T_1	T_2	T_3	T_4	T_5	T_6	T_7
Mean (°C)	0.0067	0.0063	0.0059	0.0057	0.0057	0.0058	0.0063
Standard deviation (°C)	0.0067	0.0063	0.0060	0.0059	0.0061	0.0065	0.0075
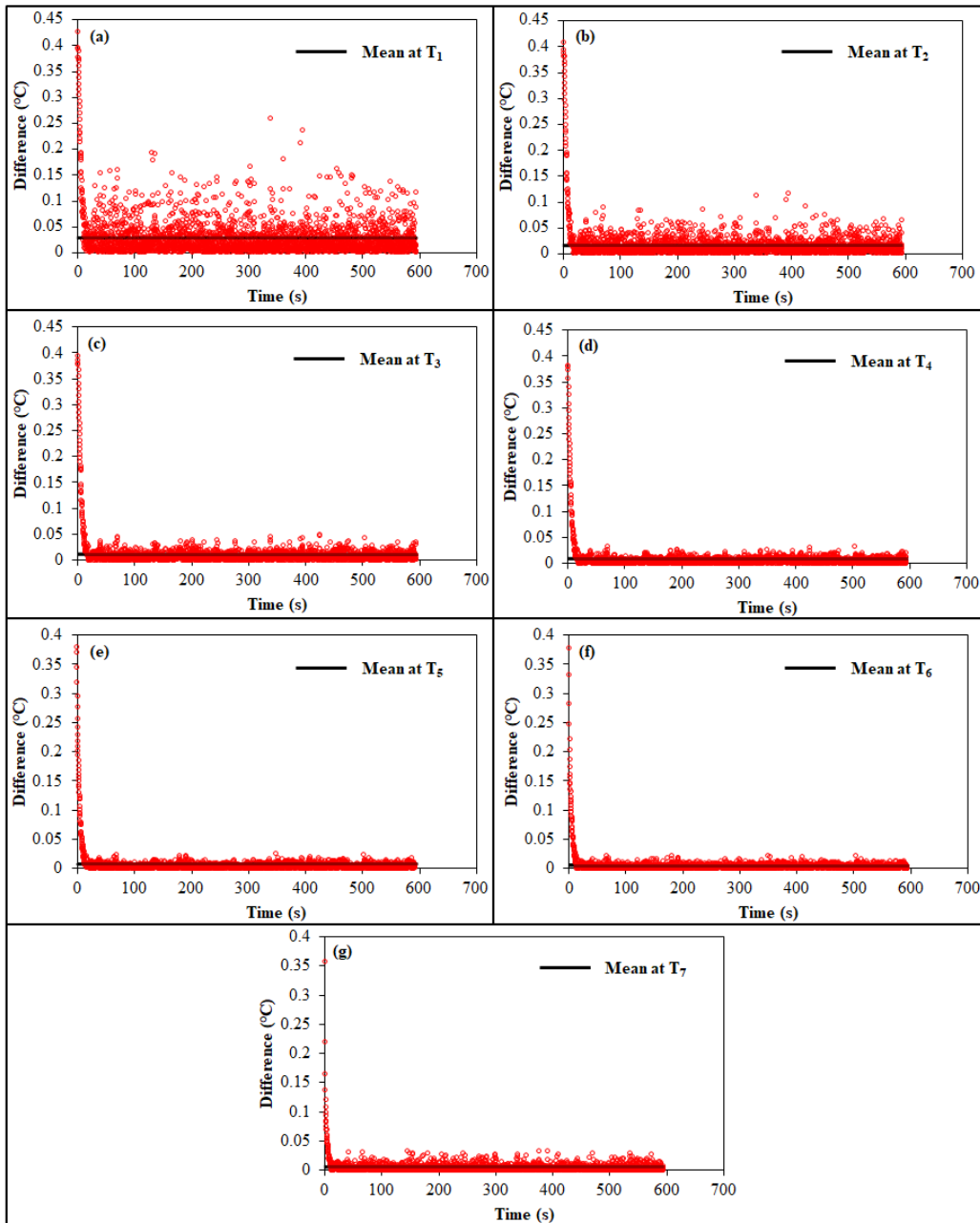
Figure 3.18: Difference between *ANSYS* results and proposed model at different nodes in SS304 alloy pin specimen.

52
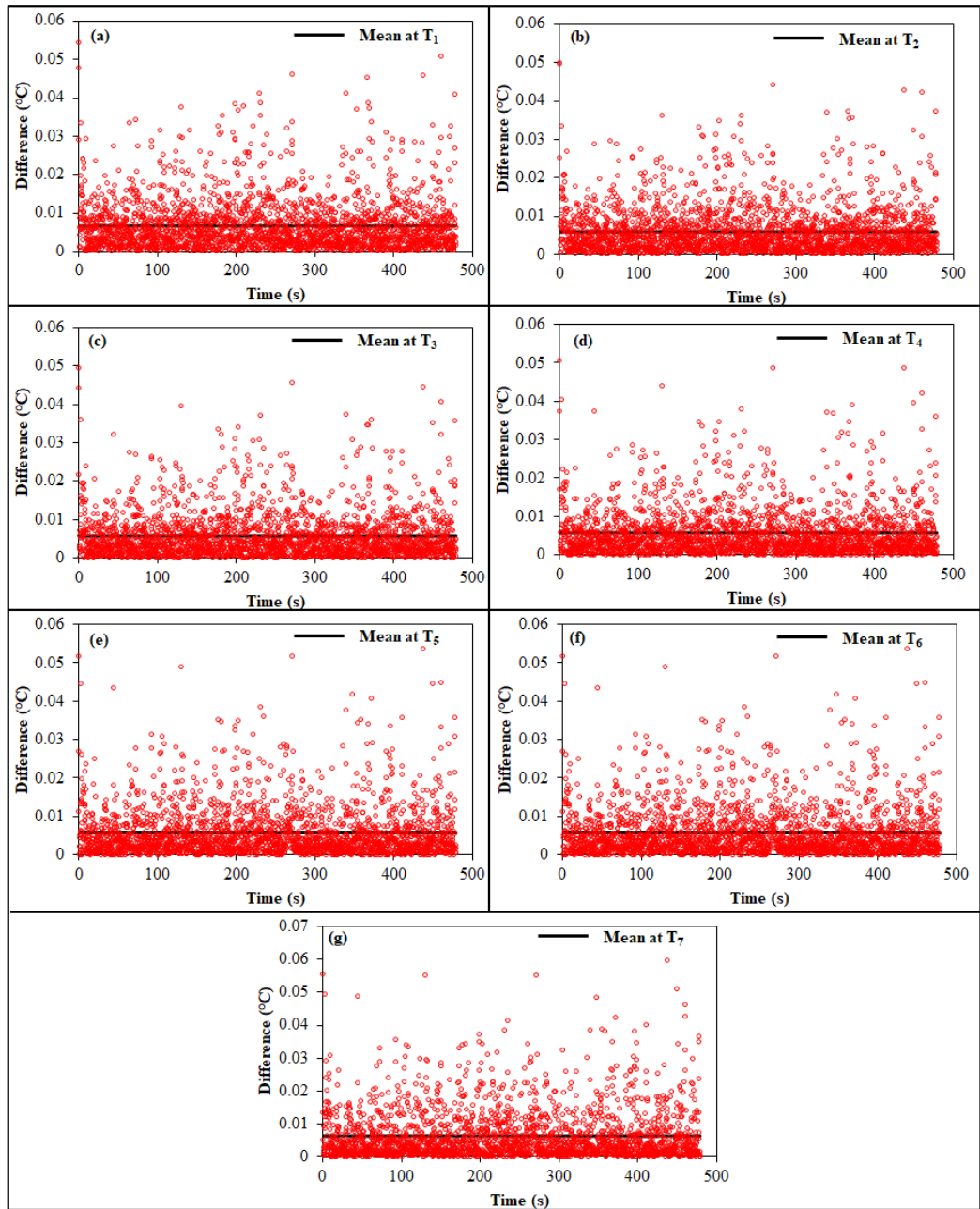
Figure 3.19: Difference between *ANSYS* results and proposed model at different nodes in Al 6061-T6 alloy pin specimen.
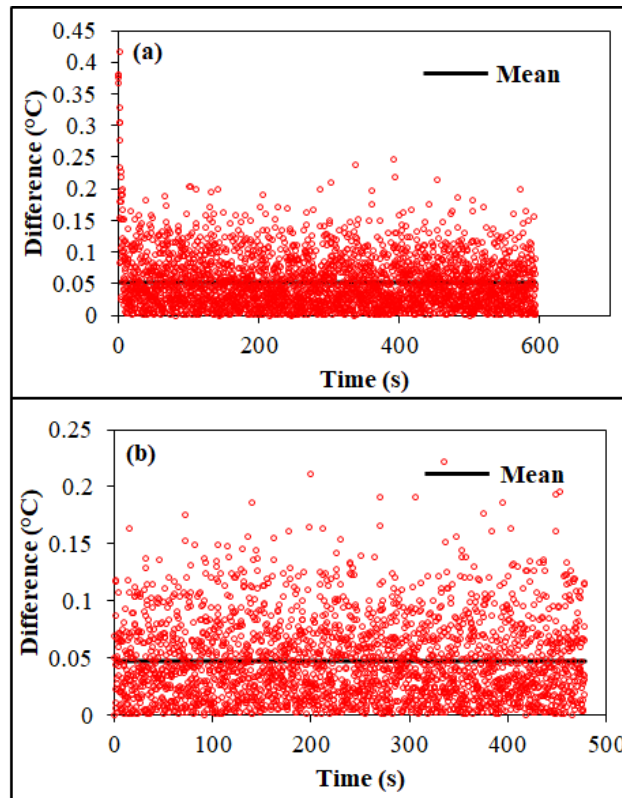
Figure 3.20: Difference between *ANSYS* results and measured temperature at 3 mm location in (a) SS304 alloy and (b) Al 6061-T6 alloy.

3.5 FRICTIONAL HEAT IN DRY SLIDING AL 6061-T6 ALLOY

Experiments were conducted by applying normal loads of 1 kg, 2 kg and 3 kg; sliding speeds of 1.25 m/s, 2 m/s and 3 m/s to understand the influence of loading parameters on frictional heat. Temperatures at 3 mm and 7 mm from the contact surface of pin specimen were measured using K-type thermocouple. The temperatures measured during experiments conducted under specified loading parameters are given in Figure 3.21. The measured temperature data was used to estimate the temperature at contact surface as explained in section 3.3. The estimated heat flux using inverse heat transfer analysis is given in Figure 3.22. The heat flux increased with increase in normal load, sliding speed and sliding distance. Highest heat flux was observed at normal load of 2 kg and sliding speed of 3 m/s experimental condition.
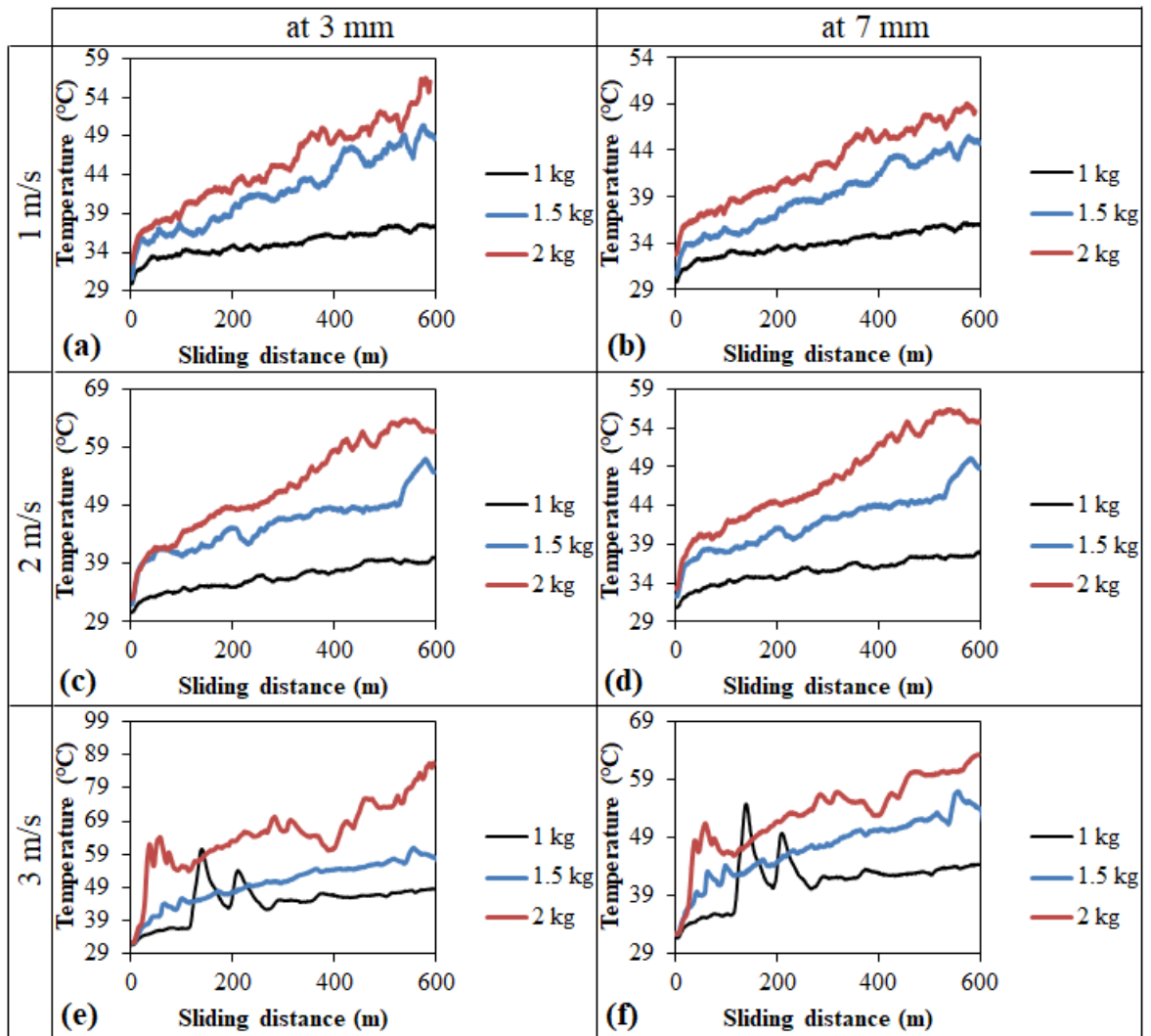
Figure 3.21: Measured temperatures at 3 mm and 7 mm from the contact surface at different normal loads and different sliding speeds.
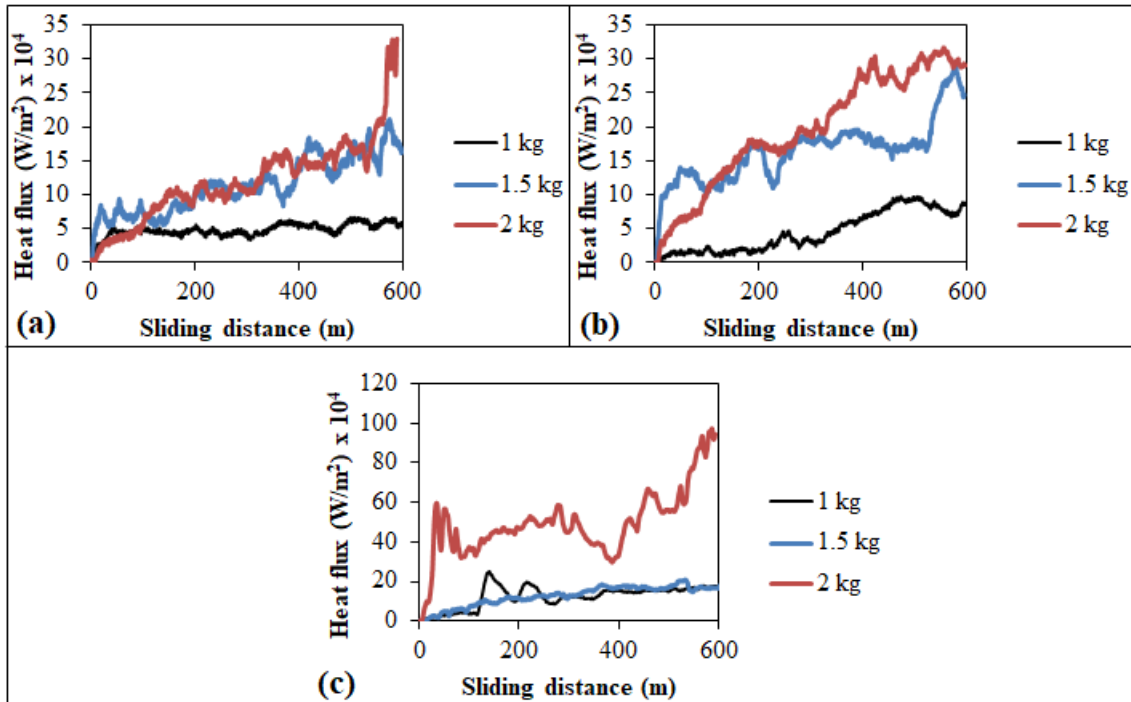
Figure 3.22: Estimated heat flux at sliding speed of (a) 1.25 m/s, (b) 2 m/s and (c) 3 m/s.
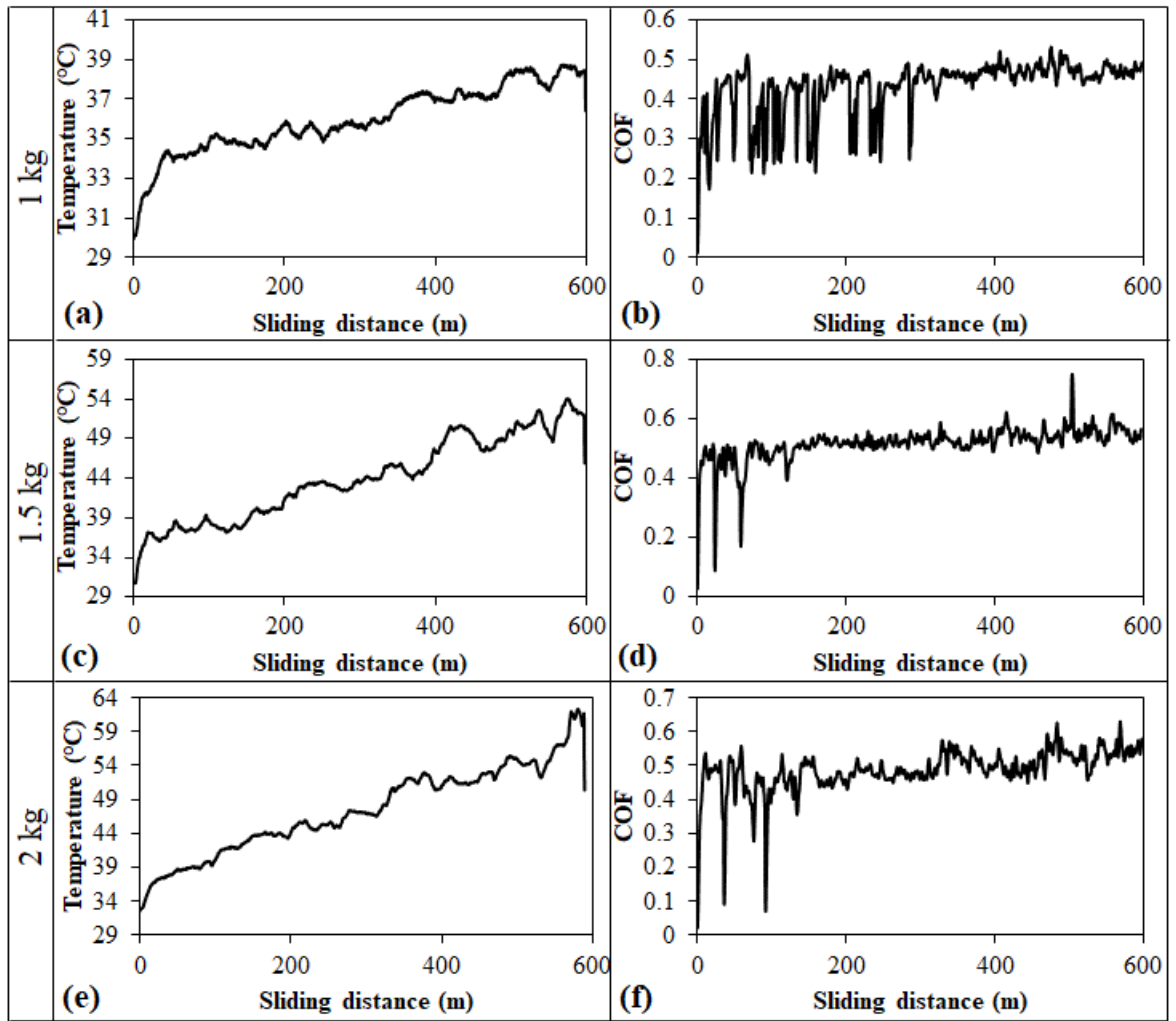
Figure 3.23: Estimated contact interface temperature (a, c and e) and measured coefficient of friction (b, d and f) under 1.25 m/s sliding speed.

At sliding speed of 1.25 m/s experimental conditions, the contact interface temperature increased with increase in sliding distance. The temperature increased suddenly in first few meters of sliding distance due to flattening of asperities, removal of oxide layer and increase in real contact area. From Figure 3.23, contact interface temperature increased with increase in normal load. From the comparison of evolution of coefficient of friction and evolution of contact interface temperature, rate of increase in temperature was less at unsteady state region of coefficient of friction. The maximum contact interface temperatures attained at end of the experiment were 38 °C, 53 °C and 62 °C at normal of 1 kg, 1.5 kg and 2 kg respectively.
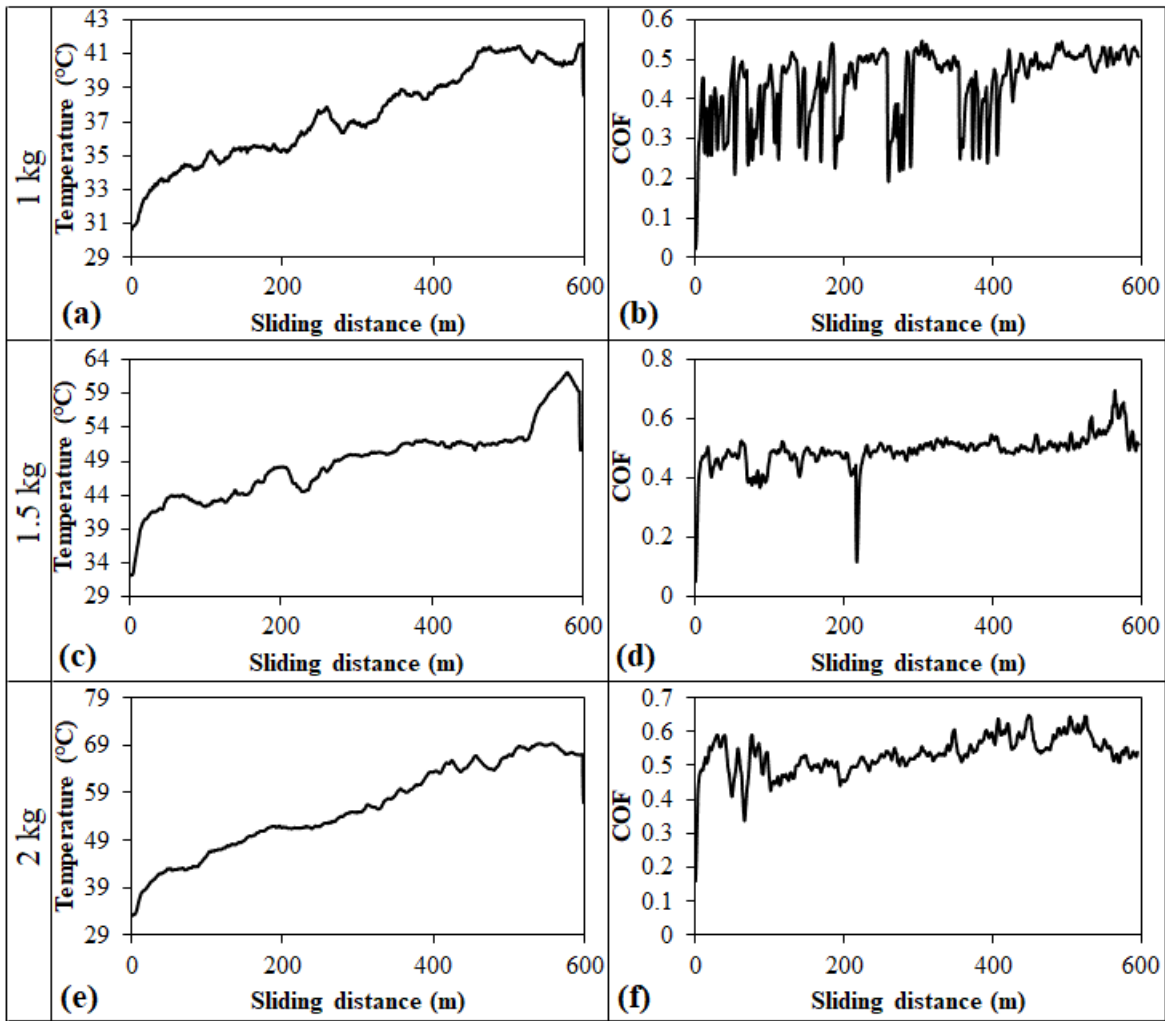
Figure 3.24: Estimated contact interface temperature (a, c and e) and measured coefficient of friction (b, d and f) under 2 m/s sliding speed.

At sliding speed of 2 m/s experimental conditions, the evolution of contact interface temperatures was similar to that observed in experiments conducted at sliding speed of 1 m/s. The frictional heat generated was more at 2 m/s experimental conditions when compared to that at similar normal load at sliding speed of 1 m/s. From Figure 3.24 it was observed that contact interface temperature increased with increase in normal load. The maximum contact interface temperatures attained at end of the experiment were 41 °C, 60 °C and 68 °C at normal of 1 kg, 1.5 kg and 2 kg respectively.
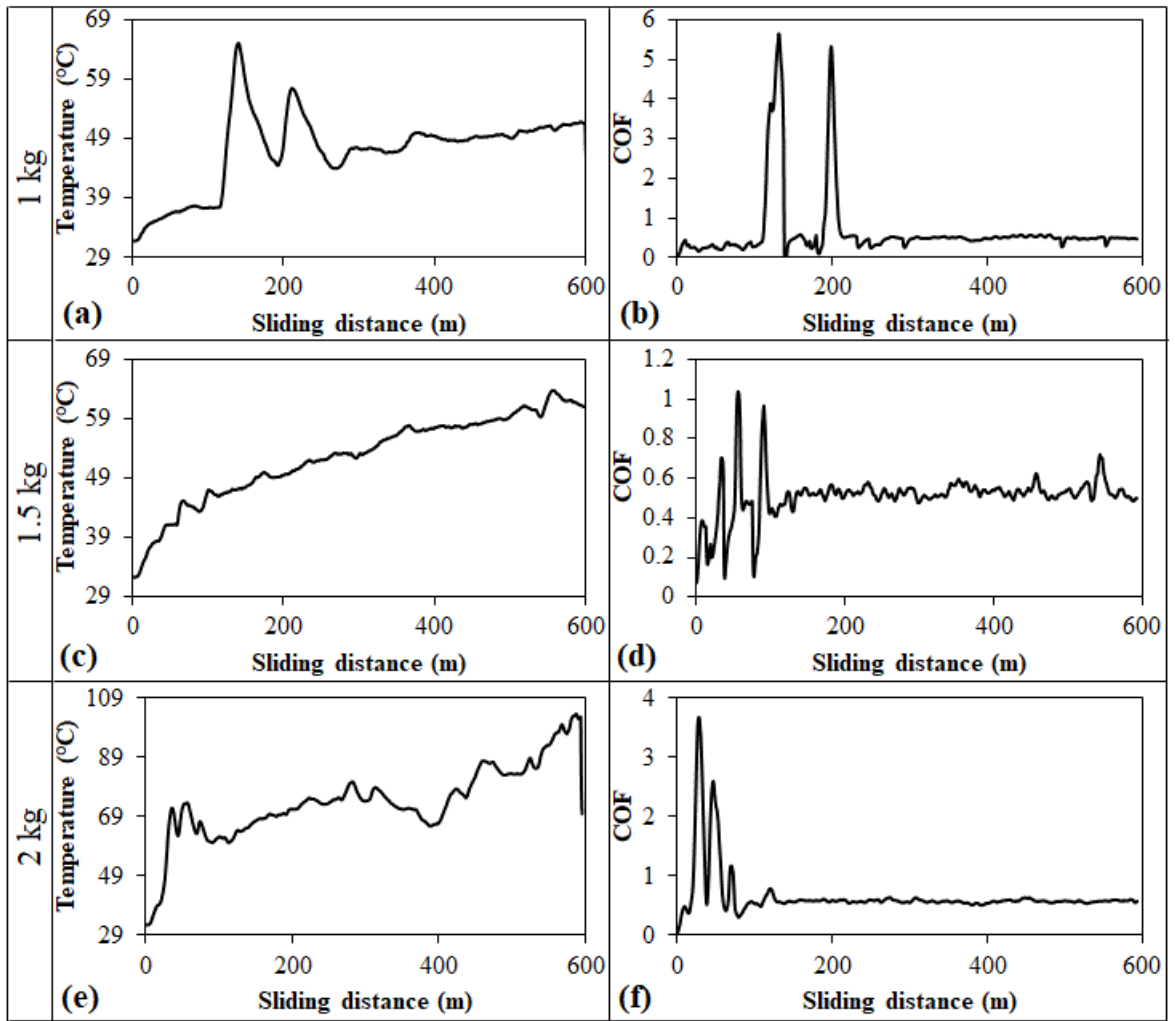
Figure 3.25: Estimated contact interface temperature (a, c and e) and measured coefficient of friction (b, d and f) under 3 m/s sliding speed.

At sliding speed of 3 m/s experimental conditions, the sudden increase in evolution of contact interface temperatures was due to severe plastic deformation of contact surfaces. The sudden increase in coefficient of friction resulted due to severe plastic deformation. When the evolution of coefficient of friction reached steady state the evolution of contact interface temperature curves became smoother. From Figure 3.25, contact interface temperature increased with increase in normal load and combined effect of normal load sliding speed resulted in highest contact temperature. The maximum contact interface temperatures attained at end of the experiment were 52 °C, 64 °C and 100 °C at normal of 1 kg, 1.5 kg and 2 kg respectively. The

maximum contact temperatures at end of each experiment are summarized in Figure 3.26.
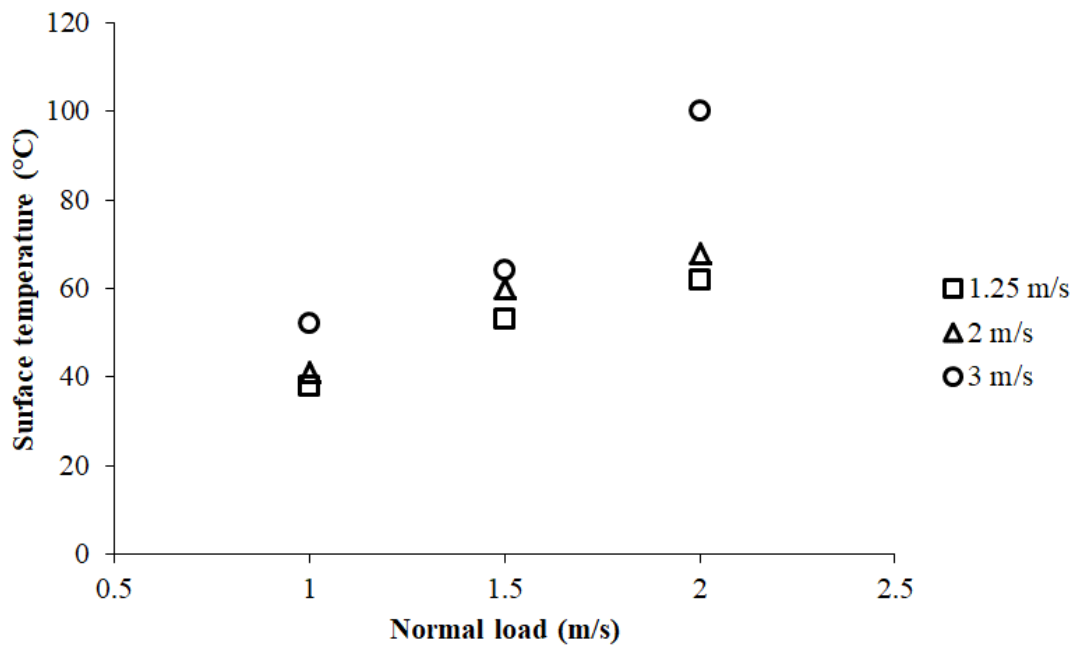
Figure 3.26: Maximum contact interface temperature of Al 6061-T6 alloy during dry sliding.

In this study, temperatures at 3 mm and 7 mm location from contact interface of pin specimen and disk were measured using K-type thermocouples. From this study, it is concluded that the proposed inverse heat transfer model is suitable for different type of materials where the physical problem having less convection losses. The contact interface temperature increases with increase in coefficient of friction. The contact interface temperature increased even after the coefficient of friction stabilized. The proposed inverse heat transfer model can also be used to estimate the heat transfer coefficient during metal casting process and weld spot temperatures during welding process.

OXIDATION OF ALUMINIUM CONTACTS DURING DRY SLIDING

This chapter describes the preliminary experiments conducted to understand the variation of coefficient of friction over a period of time and effect of oxidation on sliding contacts. Friction tests were conducted using Aluminium alloys (Al 6061 and Al 6082) with 1 kg constant normal load and at sliding speed of 1.5 m/s. The detailed friction results have been presented and discussed to understand the influence of coefficient of friction on the contact tractions at the interface. The obtained friction results are compared with the results mentioned in literature, where reciprocating sliding experiments were conducted. From this comparison, it is concluded that the formation of oxide and nitride layers are dominant when the friction tests are conducted using pin on disc setup.

4.1 EXPERIMENTAL DETAILS

The materials used for the study (Al 6061 and Al 6082) are under T6 heat-treated condition. The mechanical properties of the raw materials used for the study are given in Table 4.1. Pin on disk type tribometer (Hegadekatte et al., 2006 and Douglas Godfrey, 1995) was used to conduct experiments. A circular disk of 8 mm thick and 160 mm diameter was used as rotating disk and a cylindrical pin of 6 mm diameter was used as a stationary pin specimen in the tribometer. Pin and disk specimens were fabricated as per required dimensions using CNC cutting machine. Experiments were conducted at room temperature (33℃) and humidity of 86 %. Tests were conducted to observe the variations in coefficient of friction at normal load of 1 kg and 1.5 m/s sliding speed.

Table 4.1: Mechanical properties of the materials.

Material	Ultimate strength (MPa)	Tensile strength (MPa)	Elastic modulus (GPa)	Hardness (Brinell)
Al 6061	310	276	69	95
Al 6082	310	260	69	90

4.2 RESULTS AND DISCUSSION

When two metal surfaces are sliding against each other and exposed to the atmosphere results in oxidation of material surfaces. For example haematite (Fe_2O_3) in steel contacts forms on the surface of the metal during sliding. The fluctuations in coefficient of friction over a period of time are due to the formation of this oxide layer on the contacting surface during sliding. The oxide layer fails due to tangential tractions at the contact surface during sliding and acts like a lubricant which leads to decreasing coefficient of friction. Hosung Kong et al. (1995) observed the influence of oxide layer formation on coefficient of friction by conducting the friction experiments in air, medium vacuum (1.3 Pa) and high vacuum (5×10^{-3} Pa) at steel contacts. The authors observed higher coefficient of friction in high vacuum environmental condition than the coefficient of friction in medium vacuum and air environmental condition (Roamer Predmore et al., 1970). In vacuum the contact configuration is metal to metal whereas in air the contact configuration is metal oxide to metal oxide which leads to decrease in coefficient of friction.

In the present study experiments were conducted in air under dry sliding condition. The frictional force was recorded during sliding continuously using data acquisition system connected to the tribometer. A constant normal load of 1 kg was applied during sliding for all the experiments. The ratio of recorded frictional force to the constant normal force applied at an instance of time gives the coefficient of friction at that instance of time (Peter J. Blau, 2008). The coefficient of friction was calculated over a period of time using frictional forces obtained from the data acquisition system and plotted in Figure 4.1.
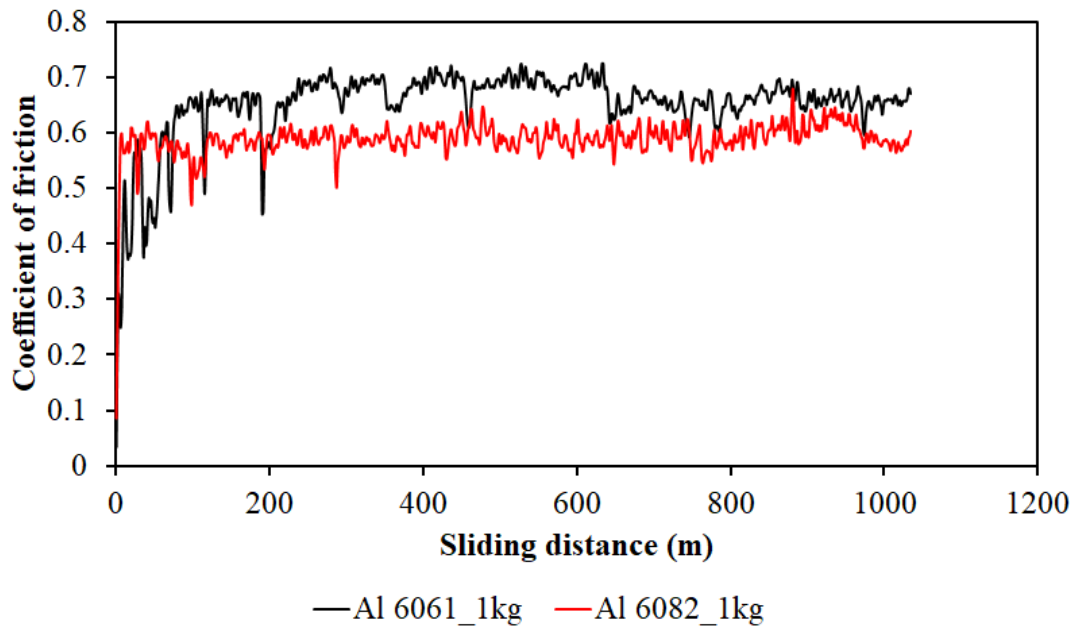
Figure 4.1: Friction coefficient versus sliding distance of aluminium alloys.
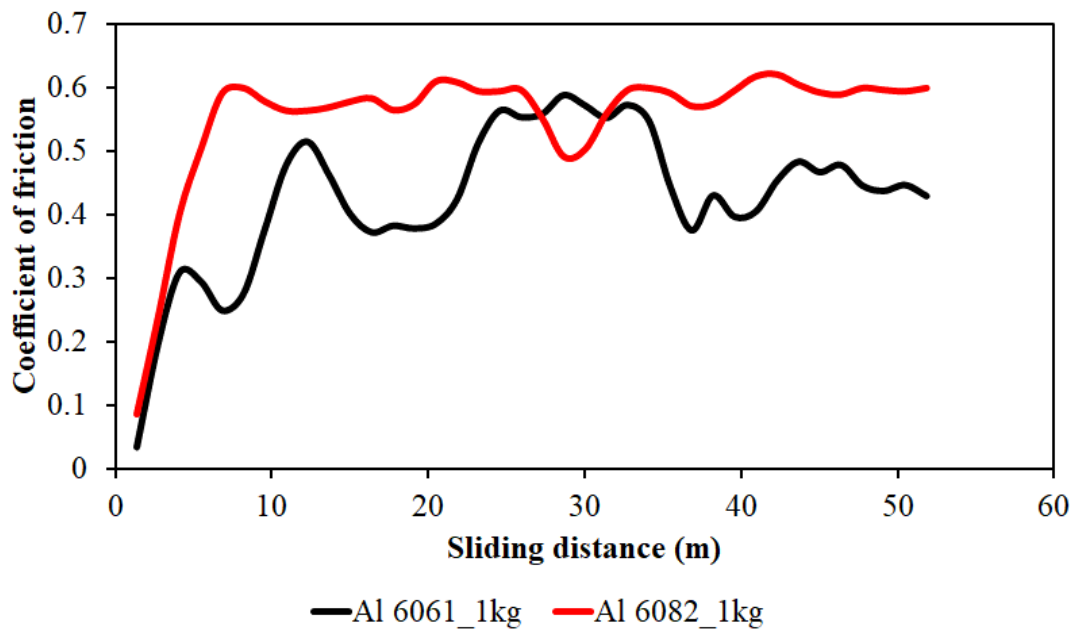
Figure 4.2: Friction coefficient in first 50 m of sliding distance.

The coefficient of friction of Al 6061 increased linearly to 0.52 up to the sliding distance of 12 m (Figure 4.2) and with lot of fluctuations it stabilized around 0.65 from sliding distance of 70 m to 200 m. Later the fluctuating coefficient of friction

was increased to 0.68 from sliding distance of 200 m to 650 m. At sliding distance of 650 m drop in the coefficient of friction was observed and it was fluctuating around 0.65 till the end of the test. Murthy H. and Vadivuchezhian K. (2017) have conducted reciprocating dry and full sliding experiments on Al 6061 T6 alloy. The authors have observed that the coefficient of friction of Al 6061 T6 alloy was varying from 0.6 to 0.65. The model frictional curve of the reciprocating test conducted at normal load per unit depth of 0.8 MN/m, sliding amplitude 0.07 mm and frequency of 0.5 Hz is given in Figure 4.3. The coefficient of friction of Al6061 alloy observed from the present study (unidirectional full sliding) is giving good agreement with the coefficient of friction obtained by the reciprocal full sliding test results obtained by H. Murthy and K. Vadivuchezhian (2017).
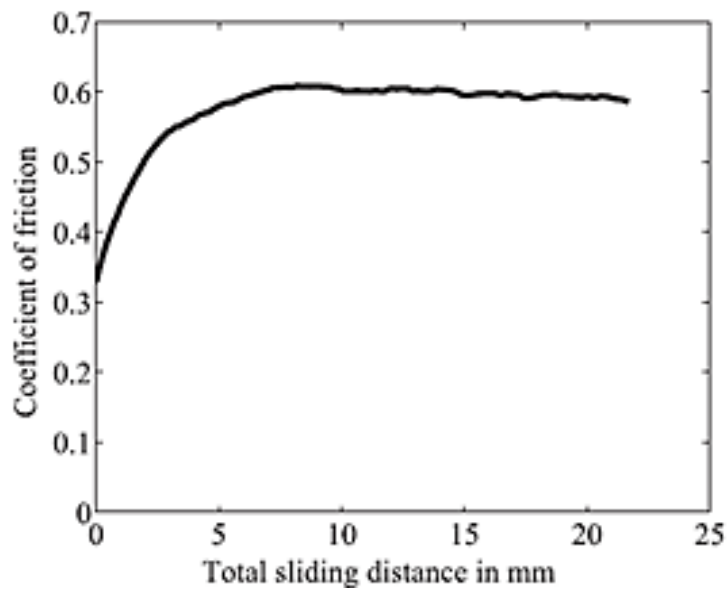
Figure 4.3: Friction coefficient obtained from full sliding tests (Murthy and Vadivuchezhian, 2017).
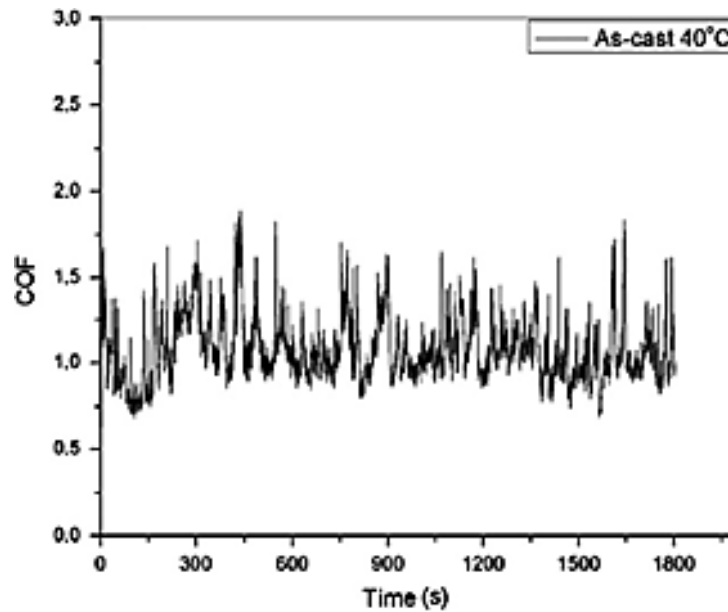
Figure 4.4: Friction coefficient as a function of time for AA6082 alloy at 40℃ (Sanjeev Das et al., 2013).

The coefficient of friction of Al 6082 is increased linearly to 0.6 up to 7 m of sliding distance and fluctuated around the value of 0.6 till the end of the test (Figure 4.1). Sanjeev Das et al. (2013) have studied the friction and wear characteristics of Al 6082 alloys by conducting the reciprocating full sliding tests. Tests were conducted at 10 N normal load, sliding amplitude 2 mm, and frequency of 13 Hz. They have observed the continuous repetition of increase and decrease of coefficient of fiction as shown in Figure 4.4.

The linear increase in coefficient of friction for the both alloys (Al 6061 and Al 6082) at initial stage of the experiments is due to the presence of oxide layer on the contact pairs (Figure 4.5 (a) and Figure 4.6 (a)). The initial sliding cycles remove the oxide layer (Giovanni Straffelini, 2015) and the contact configuration shifts to metal to metal contact which promotes the increase in the coefficient of friction. The fluctuations in the coefficient of friction during the length of the experiment are due to the abrasive effect of the removed oxide layer particles on the wear track. Energy Dispersive X-ray (EDX) analysis was carried out on disk samples before and after the wear experiments. Figure 4.5 shows the Scanning Electron Micrographs with EDX analysis of Al6061 alloy. From the EDX analysis, the oxygen content on the surface

65

of the wear track was increased after the full sliding experiments due to oxidation of material during the experiment. When the materials slide against each other frictional heat generates at the contact interface due to plastic deformation of contact asperities. The generated heat varies along the length of contact and depends on the stress concentration at the contact location during sliding. The generated heat at micro-level contact area may exceed 1000 °C and this temperature is called flash temperature (Suttera and Ranc, 2010). Some spots on the wear track will get oxidized due to generated flash temperatures. The oxidization of wear track in both Al 6061 and Al 6082 alloy was identified by the EDX analysis and given in Figure 4.5 and Figure 4.6. Oxide layer of about 200 μm thickness was formed on the surface of cylindrical pin specimen (Figure 4.7). The cross-section of cylindrical pin surface was analysed using EDX and oxidation of pin surface was conformed as given in Figure 4.7.

Element	Weight (%)	Atomic (%)
O K	3.63	5.96
Mg K	0.51	0.55
Al K	95.76	93.38
Si K	0.11	0.10

Element	Weight (%)	Atomic (%)
O K	6.66	10.74
Mg K	0.37	0.40
Al K	92.44	88.38
Si K	0.53	0.48
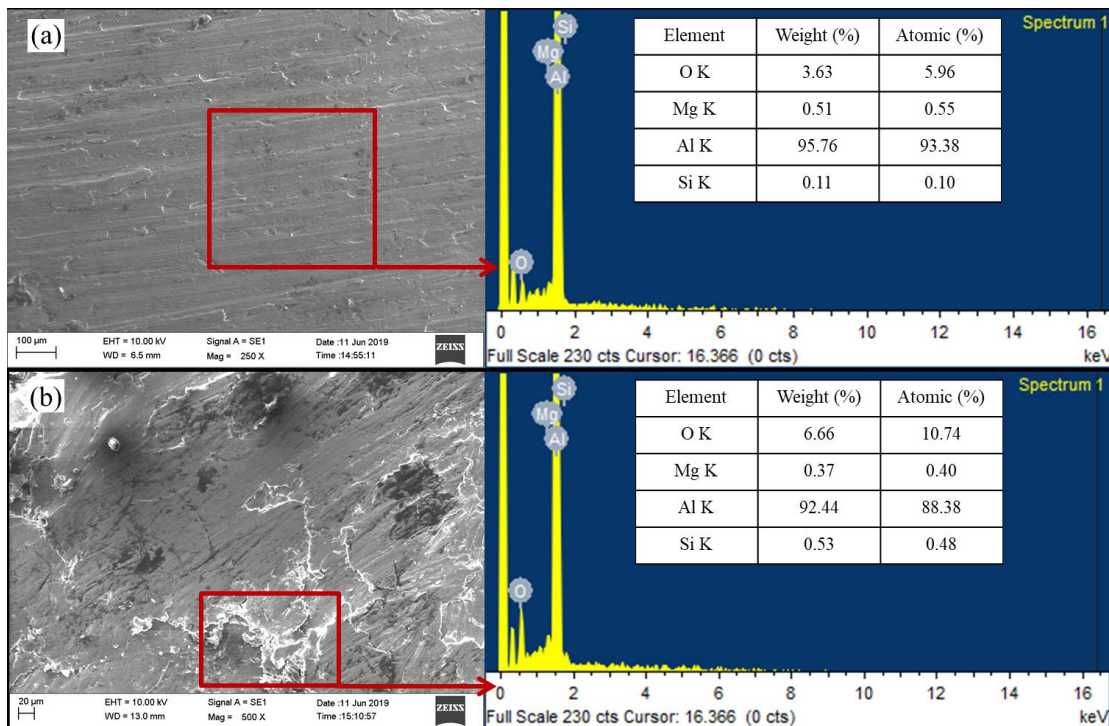
Figure 4.5: Scanning Electron Micrograph and EDX analysis of Al 6061 alloy disk specimen surface (a) before the experiment and (b) after the experiment.
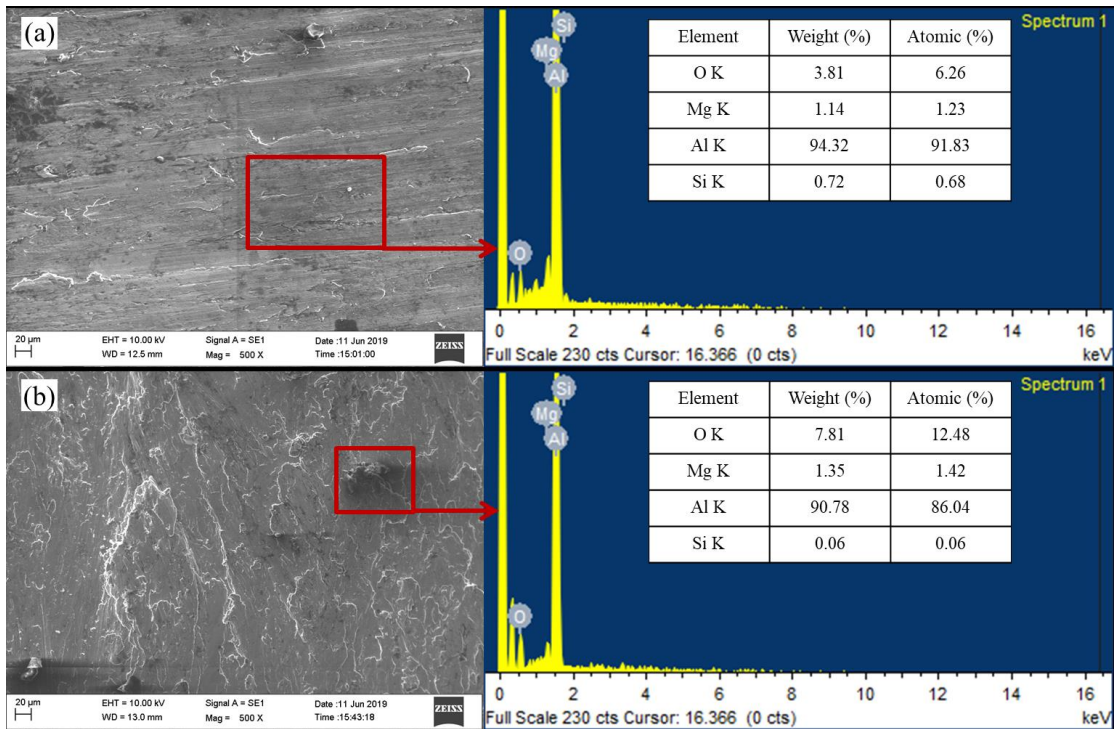
Figure 4.6: Scanning Electron Micrograph and EDX analysis of Al 6082 alloy disk specimen surface (a) before the experiment and (b) after the experiment.
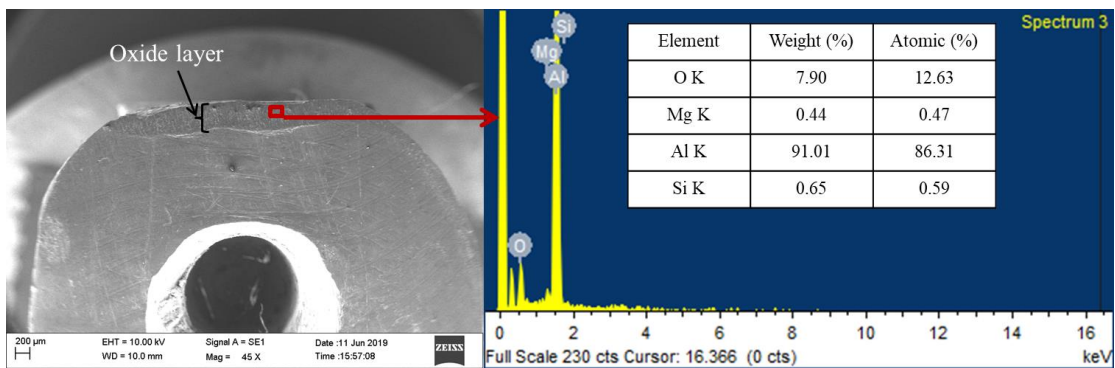
Figure 4.7: Scanning Electron Micrograph and EDX analysis of Al 6061 alloy cylindrical pin specimen after the experiment.

From the preliminary experiments of this study the following conclusions are drawn:

- The coefficient of friction obtained from the pin on disk experiments have given lower values than the coefficient of friction obtained from the reciprocating sliding experiments.

67

- The coefficient of friction of Al 6061 is greater than that of the same of Al 6082 under similar loading conditions.
- The fluctuations in coefficient of friction during the length of the test are due to the abrasive effect of oxide layer present on the contact surfaces.
- The repetition of sudden fall and gradual increase of coefficient of friction is due to failure of oxide layer and the gradual increase in metal to metal contact.
- Formation of oxide layer is dominant in pin on disk tribometer test.

CHAPTER 5

COEFFICIENT OF FRICTION AND WEAR OF AL 6061-T6 ALLOY

5.1 INTRODUCTION

The present study focuses on the effect of normal load, sliding speed and temperature on the coefficient of friction of Al 6061-T6 alloy under dry sliding conditions. Dry sliding experiments were conducted using rotary type pin on disk tribometer. Pins with 3 mm radius of contact and circular disks of 165 mm diameter were fabricated to simulate Hertzian contact configuration. Experiments were conducted by applying three different normal loads (1 kg, 1.5 kg and 2 kg) and three different sliding speeds (1.25 m/s, 2 m/s and 3 m/s) at different temperatures (room temperature (31 ± 1 °C), 60 °C, 100 °C and 150 °C). Coefficient of friction at end of the first cycle of sliding, stabilized stage, unsteady state and steady state are reported elaborately in this study. Adhesive and abrasive wear mechanisms were observed in the dry sliding of Al 6061-T6 alloy contacts from the microscopic analysis of worn contact surfaces. The coefficient of friction and wear rate were more influenced by the increase in normal load than increase in sliding speed and temperature. Under normal load of 1 kg and 1.5 kg, Al 6061-T6 ally showed better wear resistance at higher temperatures when compared to wear at room temperature. This study reveals the coefficient of friction of aluminium-to-aluminium (Al 6061-T6 alloy) contacts under cylinder on flat contact configuration.

The efficiency of mechanical systems in the automobile industry can be improved by reducing the weight of system components or by enhancing the properties of materials (Uyyuru et al., 2007). Aluminium alloys are regarded as the emerging materials in the automobile and aerospace industries, due to their resistance to corrosion and high strength to weight ratio (Siva Sankara Raju et al., 2019). Characterization of aluminium alloys at higher temperatures is important, as these alloys are utilized extensively in automobile engine components, such as piston, liner and cylinder head (Alpas and Zhang, 1992). Many researchers (Nakanishi et al., 2002; Blau and Meyer,

2003) have studied the applicability of aluminium alloys in automobile brake components due to their properties, such as lightweight, low thermal expansion and high thermal conductivity, which enhance the system efficiency. Liliang Wang et al. (2009) observed the effect of temperature and normal pressure on the coefficient of friction between aluminium surface and steel surface. They conducted the experiments under the maximum contact pressure of 120 MPa and maximum temperature of 500 °C. The coefficient of friction increased with the increase in temperature; and it increased up to 1.9 at higher temperatures. Ramesh et al. (2010) observed a decrease in the coefficient of friction with an increase in normal load up to 80 N in Al 6061 alloy and silicon nitrate-reinforced Al 6061 composite. However, the coefficient of friction increased with the increase in sliding speed. The reinforced silicon nitrate particles act as a solid lubricant, resulting in the decrease of coefficient of friction and wear. Adhesive wear mechanism between aluminium surface and steel surface was studied at different temperatures by Vilaseca et al. (2011). Pujante et al. (2013) reported that the wear mechanism in aluminium alloy AA2017 was extremely dependent on the system temperature. Abrasive wear and adhesive wear mechanisms were observed at different temperatures, ranging from room temperature to 450 °C.

5.2 EVOLUTION OF COEFFICIENT OF FRICTION

The typical evolution of coefficient of friction during the full sliding of Al 6061-T6 contacts is given in Figure 5.1. The evolution of coefficient of friction at 1 kg normal load and 1.25 m/s sliding speed and at room temperature is shown in Figure 5.1. Full sliding of Al 6061-T6 alloy exhibits different stages in the evolution of coefficient of friction, which increases linearly in the first few meters of sliding distance (till point 'A' in Figure 5.1) and reaches a stabilized state. The coefficient of friction at this stage is called stabilized coefficient of friction. Later, the fluctuations increase in the coefficient of friction, which is called the unsteady state of coefficient of friction. When the coefficient of friction graph exhibits minor fluctuations, it is called as a steady state coefficient of friction. In this study, initial coefficient of friction, stabilized coefficient of friction, steady state coefficient of friction and unsteady state coefficient of friction of Al 6061-T6 alloy contacts are discussed in detail.
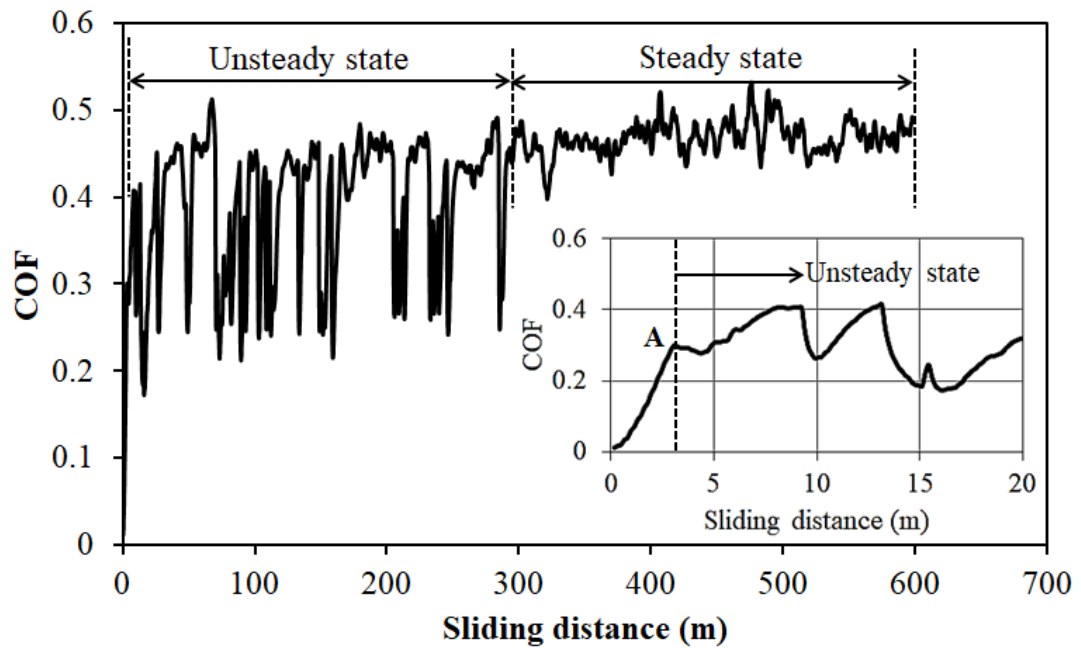
Figure 5.1: Coefficient of friction evolution at, room temperature, 1 kg normal load and 1.25 m/s sliding speed.

Figure 5.2 illustrates the formation of debris and its deposition on the pin surface during the full sliding experiments. Grooves of micro-depth were observed along the length of the contact in the first few meters of sliding distance. Debris formed due to the grooving effect on the metal surface was trapped on the front side of the pin (Stage 1, Figure 5.2). Resultantly, the wear process transforms to severe wear due to the high contact stresses developed by the trapped metal debris. The fluctuation in coefficient of friction was more after the interaction of debris at the contact surface. The deposition of metal debris was observed on the front side of the pin at a lower normal load under room temperature. The deposition of metal debris was also observed on the transverse side of the pin (Stage 2, Figure 5.2) and on the surface of the wear track, at higher normal loads and higher temperatures.
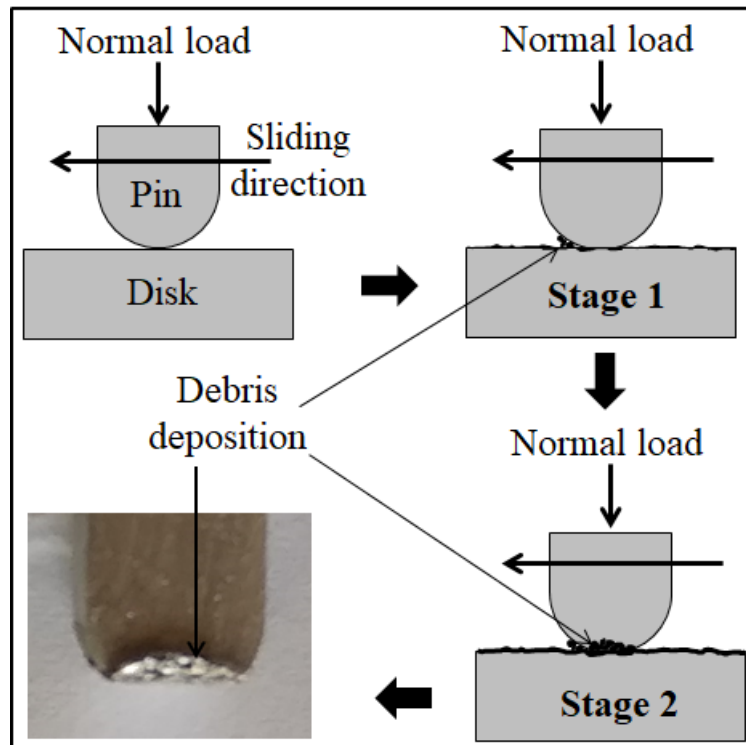
Figure 5.2: Schematic of wear debris formation and debris deposition on pin and disk during sliding.

5.2.1 At sliding speed of 1.25 m/s

Figure 5.3 – 5.6 shows the evolution of coefficient of friction during the full sliding of aluminium-to-aluminium contacts on applying 1 kg, 1.5 kg and 2 kg normal loads at different temperatures. The evolution of coefficient of friction up to the initial stabilisation (before the initialisation of severe material damage), steady state and unsteady state coefficient of friction is discussed in this study. Initially, the coefficient of friction increased linearly up to the sliding distance of 5 m – 10 m; after which it stabilised before the severe material damage began. The sliding of the contact pair resulted in the increment of the actual contact area due to the flattening of contact asperities in the first few cycles (Shuaihang Pan, 2018). The resulting increase in adhesion between the contact pairs led to a linear increment in the coefficient of friction. Later, it resulted in the failure of material due to the plastic deformation of asperities. The failed asperities were trapped on the front side of the pin (Figure 5.2), which resulted in undulations in friction evolution curves. The stabilisation of coefficient of friction curves at higher normal loads was consistent when compared to

lower normal load, due to the flattening of surface asperities at higher normal loads. Similar observations were mentioned by Shuaihang Pan et al. (2018) in aluminium-to-aluminium contact pairs under a full sliding condition. However, the oscillations in coefficient of friction were observed at higher temperatures and during the stabilisation stage. This may be due to material softening and earlier plastic deformation of contact asperities. The metal deposition on the wear track increased with the increase in normal load and temperature. This metal deposition was due to the transformation of material from pin to disk. Metal softening and severe plastic deformation occur at higher normal loads because of the increase in frictional heat (Chen and Li, 2005; Rusin et al., 2016). Figure 5.7 (j and l) depicts severe plastic deformations on the wear track, caused by the combined effect of contact pressure and temperature. Coefficient of friction varied throughout the experiment because of the formation and removal of metal layers, which changed the area of contact and adhesion between the contact pairs during the experiment. It was physically observed that noise at the contact interface increased with the increase in normal load and temperature. More noise and vibration in the loading arm of pin was observed on the disk setup at 2 kg normal load and 150 °C temperature. Experiments conducted with temperatures of 60 °C and 150 °C and a normal load of 2 kg were stopped at 250 m sliding distance, due to the vibrations caused in the pin on disk tribometer.

Coefficient of friction evolved in two states (steady state and unsteady state) at 1.25 m/s sliding speed and at 1 kg normal load; whereas, it was in a steady state at 1.5 kg and 2 kg normal load. As the temperature increased, a steady state in friction evolution was observed at an earlier stage of the experiment. Adhesion between the metal surfaces resulted in more fluctuations in the coefficient of friction (unsteady state) at lower normal loads. Removal of tribolayer and the formation of metal-to-metal contact resulted in a steady state coefficient of friction, which was higher than the unsteady state coefficient of friction. When normal load was increased, the wear mechanism between metal surfaces transformed from adhesion to mixed wear (adhesion and abrasion) at an early stage of the experiment, resulting in a steady state coefficient of friction. The region of unsteady state decreased with the increase in normal load (Odabas, 2018).

Figure 5.3: Coefficient of friction evolution under sliding speed of 1.25 m/s and room temperature.

Figure 5.4: Coefficient of friction evolution under sliding speed of 1.25 m/s and at 60 °C temperature.

Figure 5.5: Coefficient of friction evolution under sliding speed of 1.25 m/s and at 100 °C temperature.

Figure 5.6: Coefficient of friction evolution under sliding speed of 1.25 m/s and at 150 °C temperature.
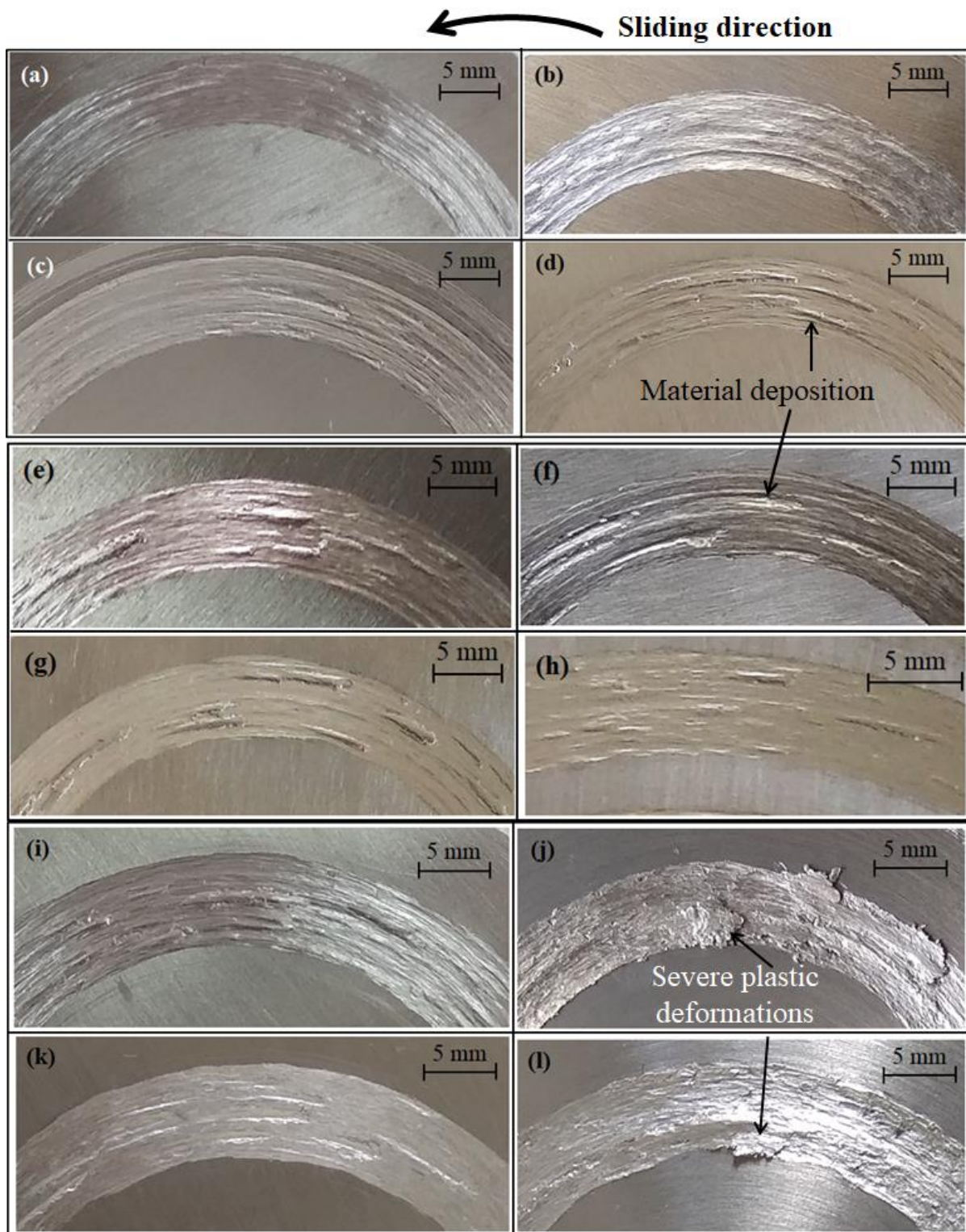
Figure 5.7: Worn surfaces of wear track at sliding speed of 1.25 m/s and, at 1 kg normal load (a-d), at 1.5 kg normal load (e-h) and at 2 kg normal load (i-l); under room temperature (a, e, i), 60 °C (b, f, j), 100 °C (c, g, k) and 150 °C (d, h, l).

5.2.2 At sliding speed of 2 m/s

A linear increase in the coefficient of friction at an early stage (5 m – 10 m sliding distance) of the experiment and stabilization of coefficient of friction was observed in each set of the experiments (Figure 5.8 - Figure 5.11). The evolution of friction coefficient showed both unsteady state and steady state zones at room temperature and under 1 kg normal load condition (Figure 5.8). Under all other loading conditions and at 2 m/s sliding speed, a steady state coefficient of friction zone was shown with a sudden fall in coefficient of friction. This sudden fall in coefficient of friction is attributed to the action of metal debris as solid lubricants (Rusin et al., 2016). Fluctuations in friction evolution curves reduced with the increase in normal load. This may be due to the softening of material at the contact interface, frictional heat generated during sliding and easy removal of metal debris from the contact interface (Wang et al., 2010). The experiments were stopped at 70 m of sliding distance, at 2 kg normal load and under temperatures of 60 °C and 150 °C, because of vibrations in tribometer caused by severe plastic deformation in the wear track during the initial stage of the experiments (Figure 5.12 (j and l)). Similarly, at 1 kg normal load and 100 °C temperature, the coefficient of friction increased suddenly to 3.7 during the initial stage of the experiment because of severe plastic deformation and accumulation of metal debris at the contact interface. The material deposition on the disk surface is shown in Figure 5.12 for all experimental conditions at 2 m/s sliding speed. Metal deposition on disk surface increased with the increase in normal load and temperature. Metal depositions are metal oxides that have a higher hardness than metal matrix.
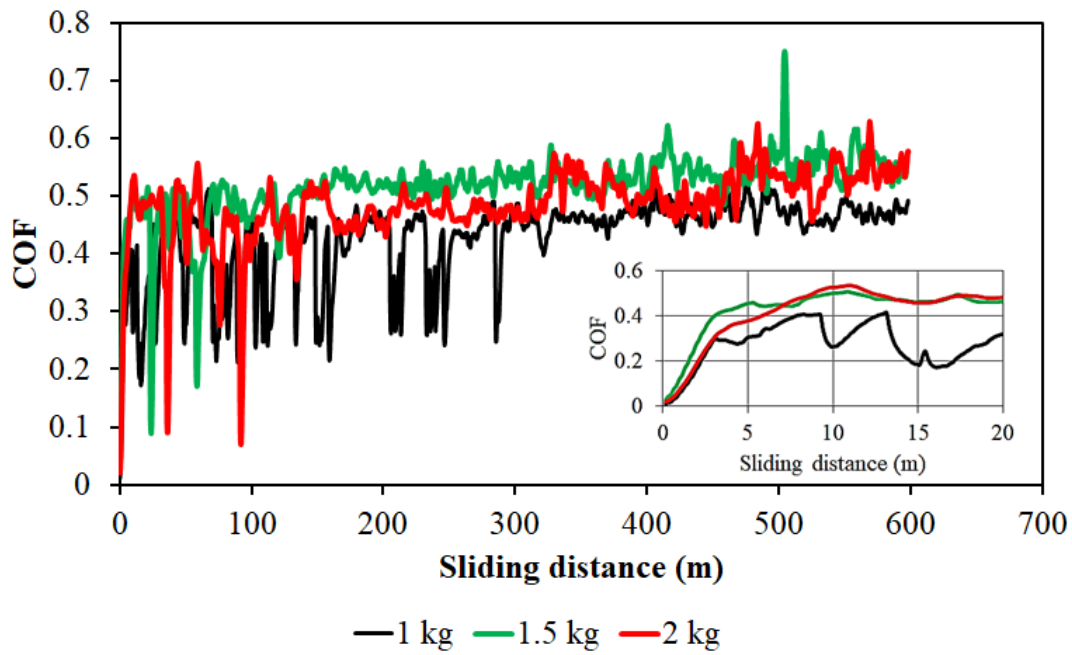
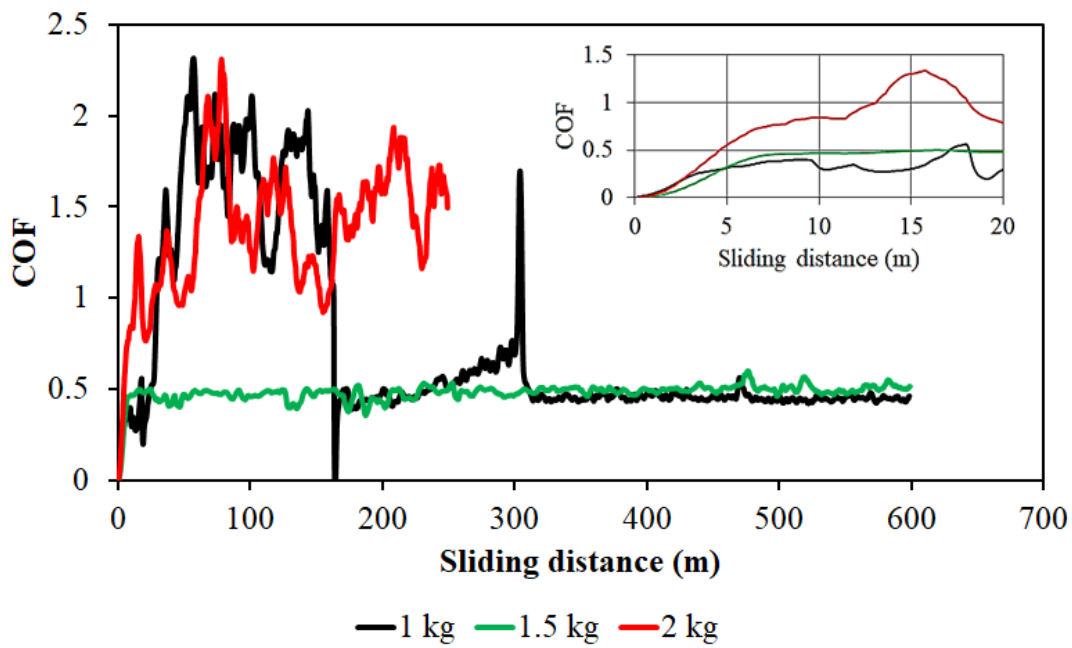Figure 5.8: Coefficient of friction evolution under sliding speed of 2 m/s and at room temperature.

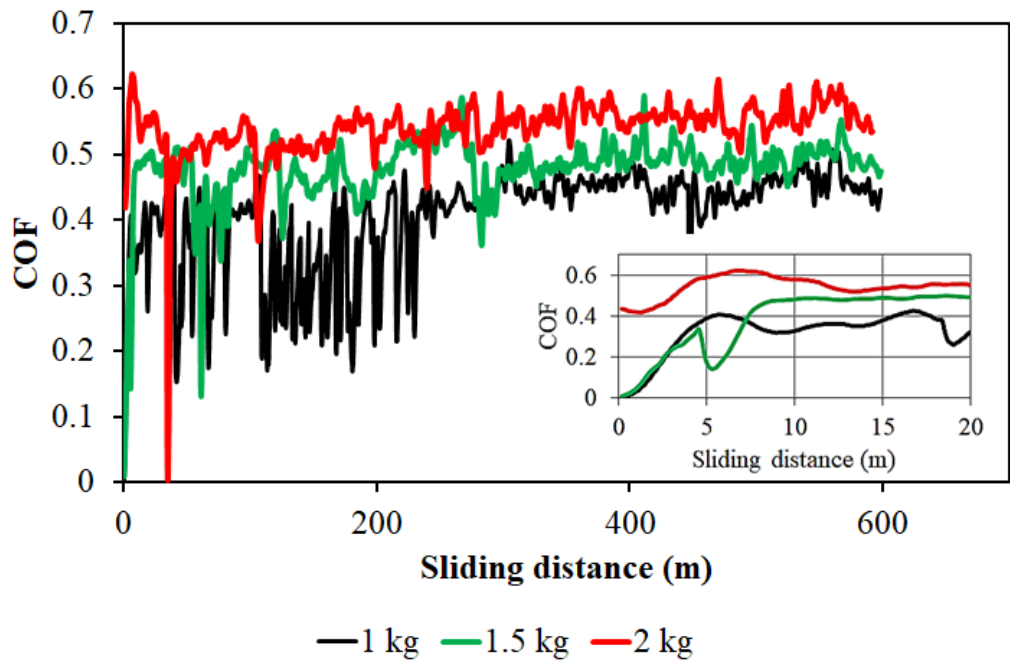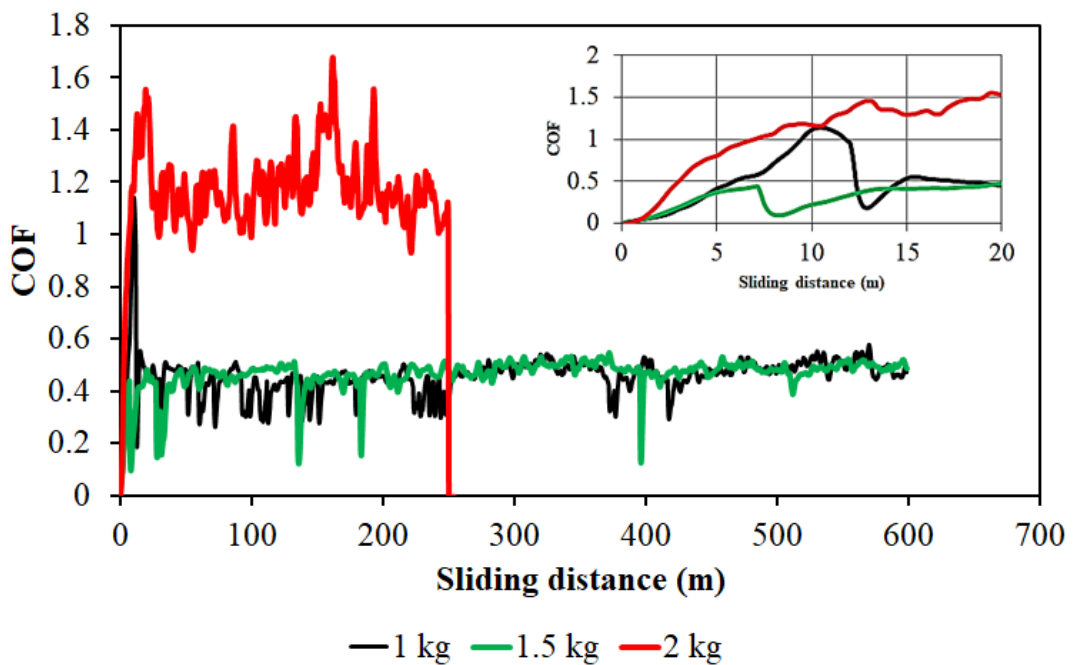Figure 5.9: Coefficient of friction evolution under sliding speed of 2 m/s and at 60 °C temperature.

Figure 5.10: Coefficient of friction evolution under sliding speed of 2 m/s and at 100 °C temperature.

Figure 5.11: Coefficient of friction evolution under sliding speed of 2 m/s and at 150 °C temperature.

Figure 5.12: Worn surfaces of wear track at sliding speed of 2 m/s and, at 1 kg normal load (a-d), at 1.5 kg normal load (e-h) and at 2 kg normal load (i-l); under room temperature (a, e, i), 60 °C (b, f, j), 100 °C (c, g, k) and 150 °C (d, h, l).

5.2.3 At sliding speed of 3 m/s

Coefficient of friction increased linearly and stabilized around 5 m to 10 m of sliding distance. Even at room temperature, the evolution of coefficient of friction was smooth and showed a steady state condition (Figure 5.13 - Figure 5.16). Frictional heat generation at higher sliding speeds, higher normal loads and applied temperatures caused the steady state coefficient of friction. The coefficient of friction curves were more stable at 3 m/s sliding speed condition when compared with those at 1.25 m/s and 2 m/s sliding speed conditions. A sudden increase in coefficient of friction at the initial stage of experiments was due to the easy removal of wear debris from the contact interface and the wear debris being stuck on the front side of the pin specimen at a higher sliding speed. Experiment conducted with 2 kg normal load and at 60 °C temperature was stopped at 60 m of sliding distance, because of more vibrations in the experimental setup. Material deposition on the wear track was more at 3 m/s sliding speed when compared to that at 1.25 m/s and 2 m/s sliding speeds (Figure 5.17). Experiment was not conducted with 2 kg normal load and at 150 °C temperature because of vibrations in tribometer at the initial stage.
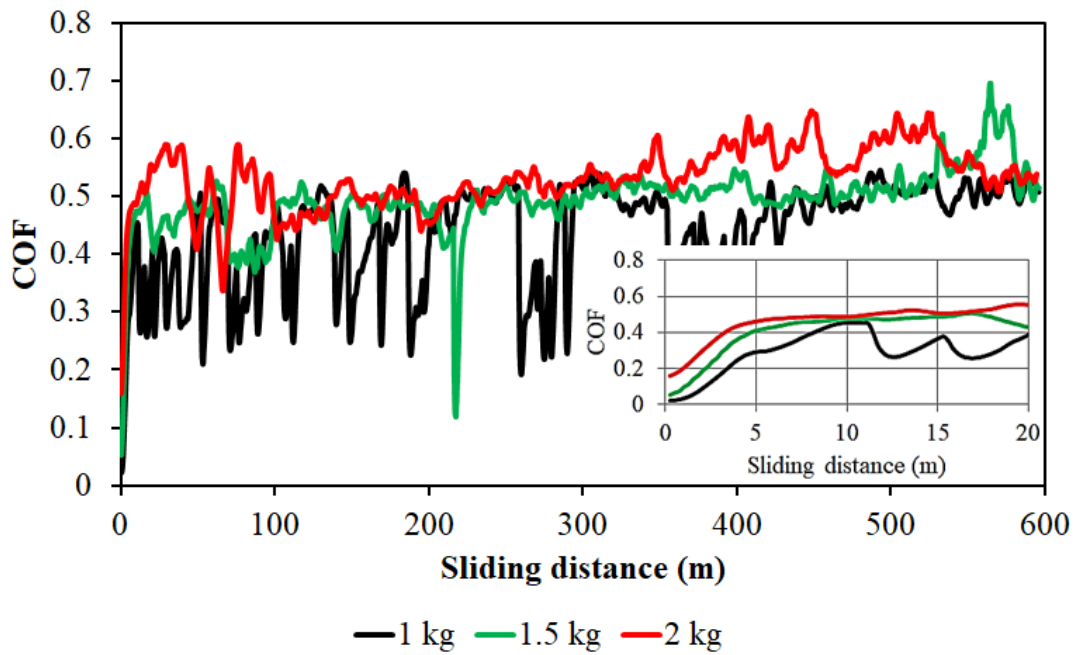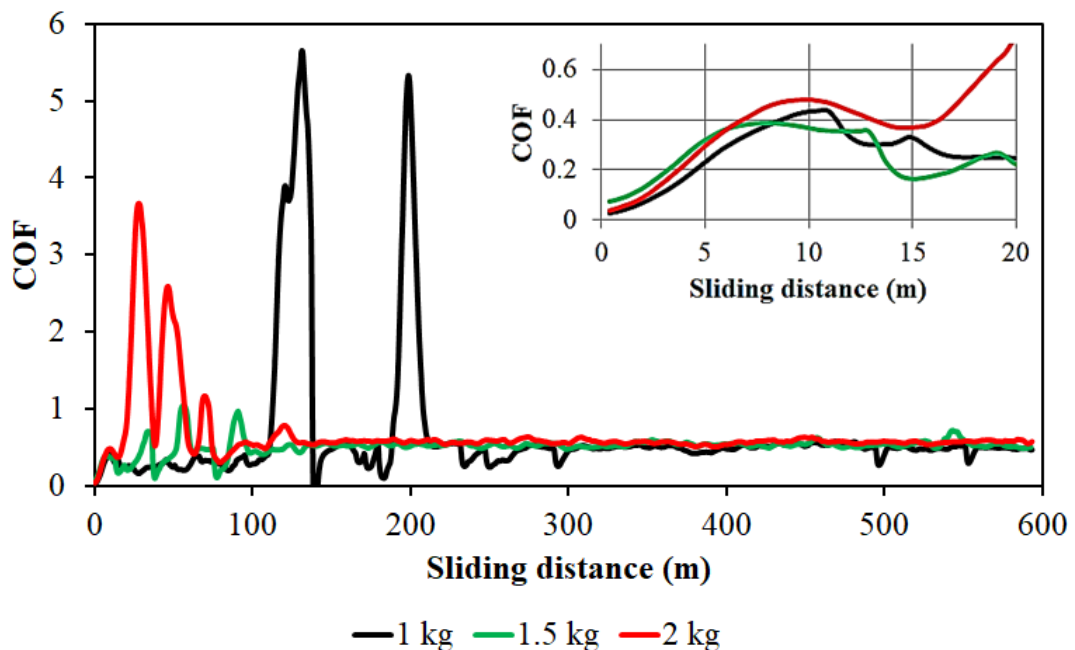

Figure 5.13: Coefficient of friction evolution under sliding speed of 3 m/s and at room temperature.
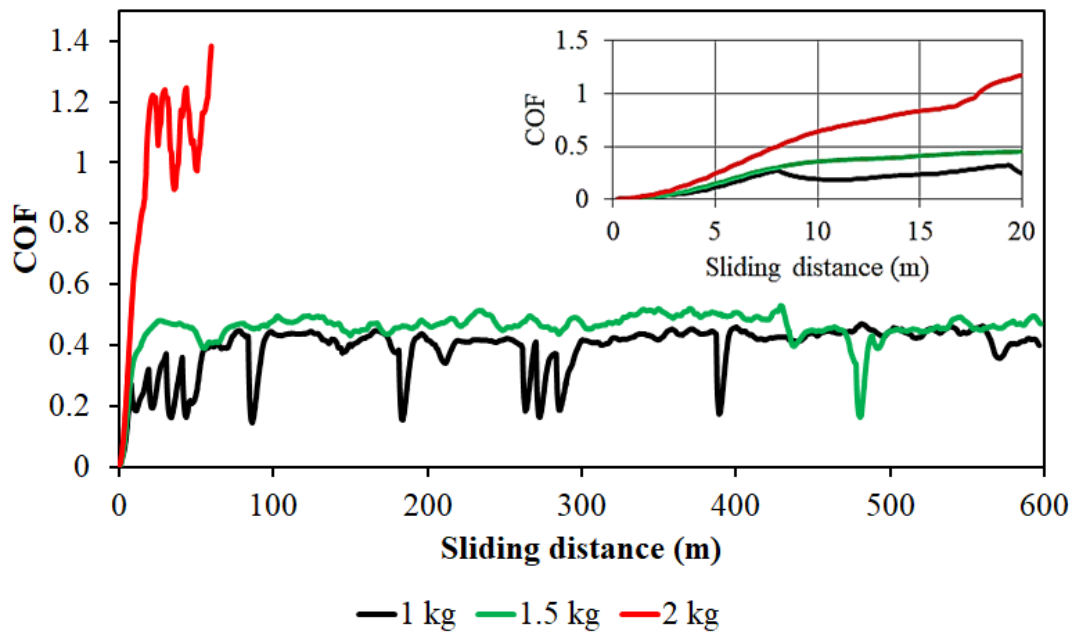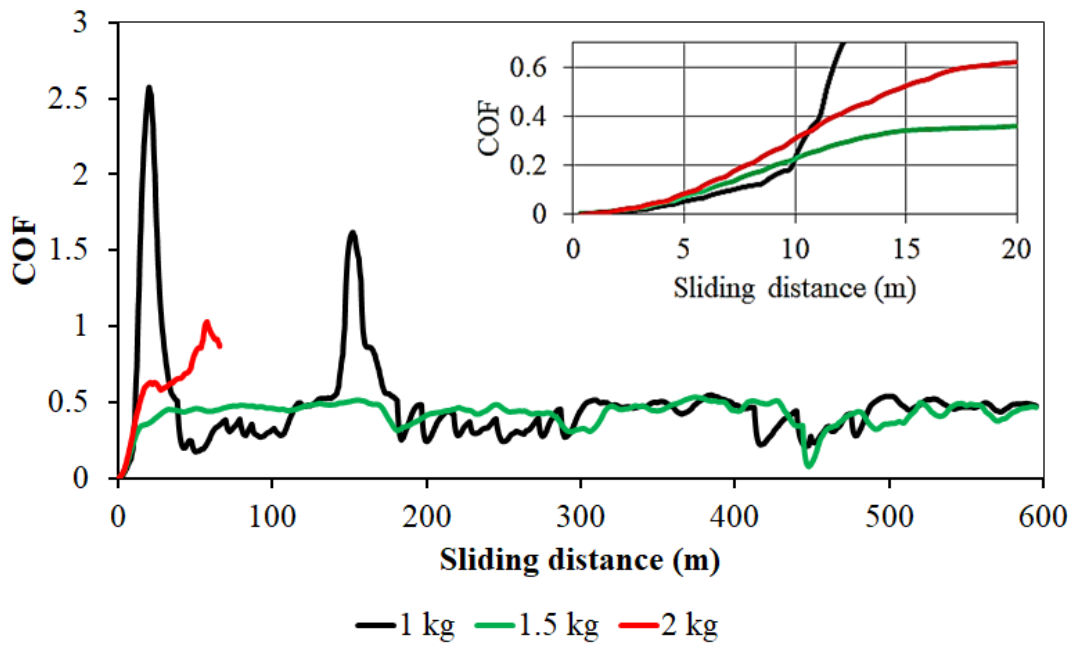
Figure 5.14: Coefficient of friction evolution under sliding speed of 3 m/s and at 60 °C temperature.
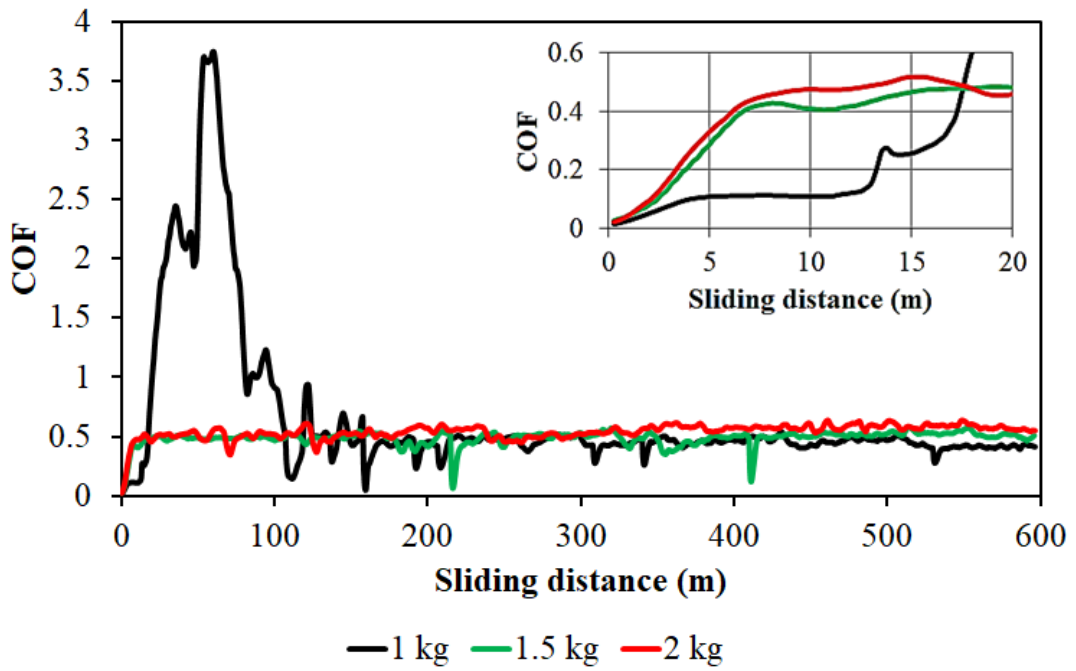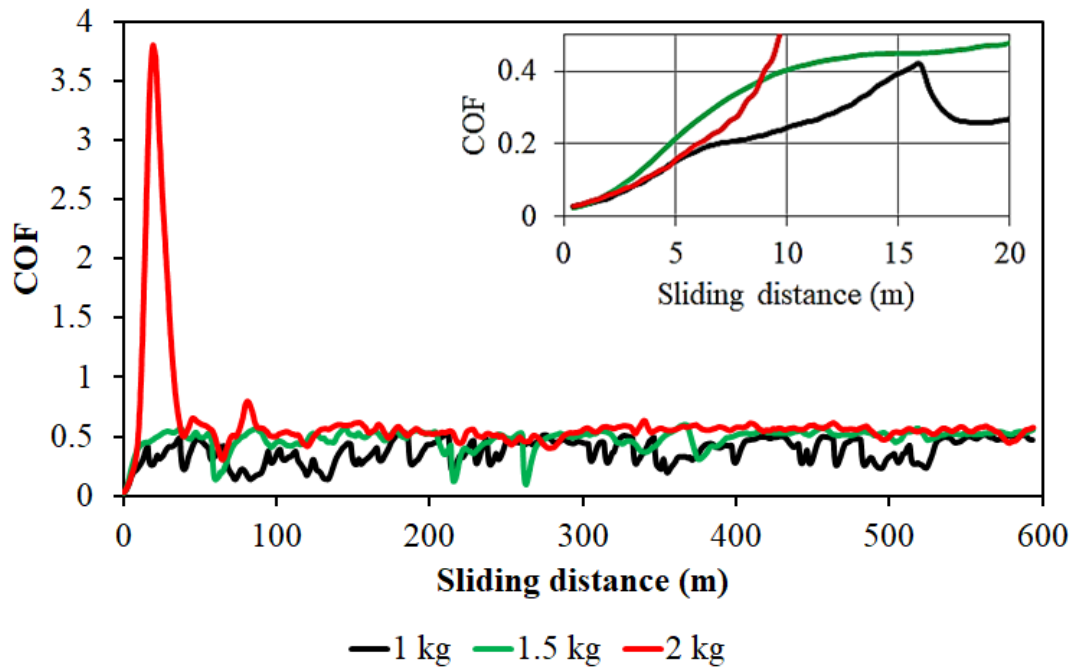

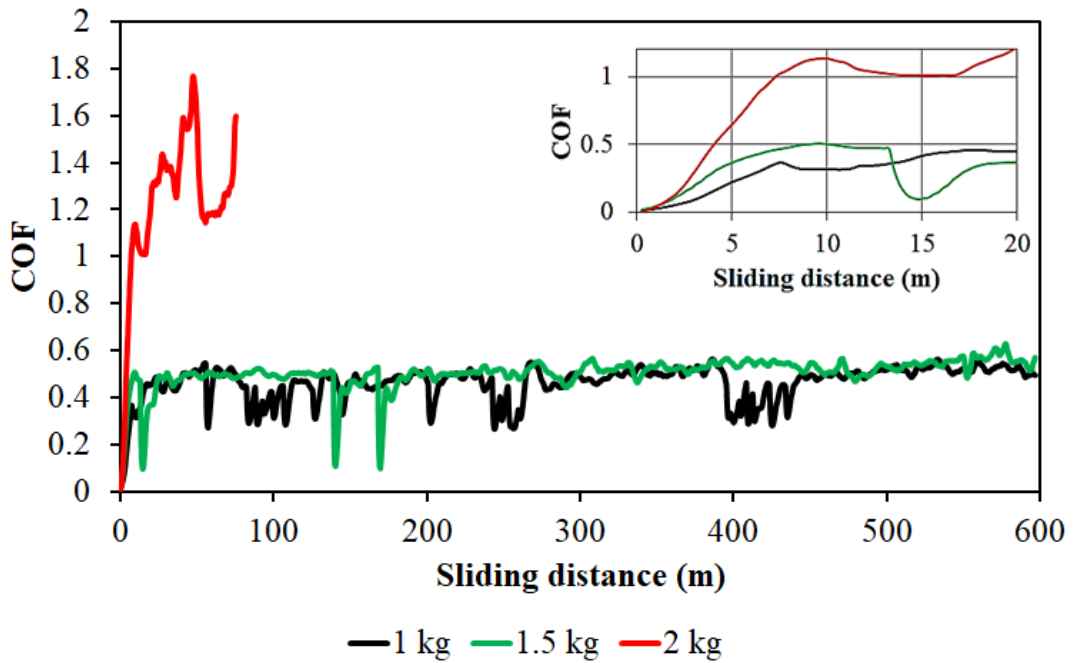Figure 5.15: Coefficient of friction evolution under sliding speed of 3 m/s and at 100 °C temperature.
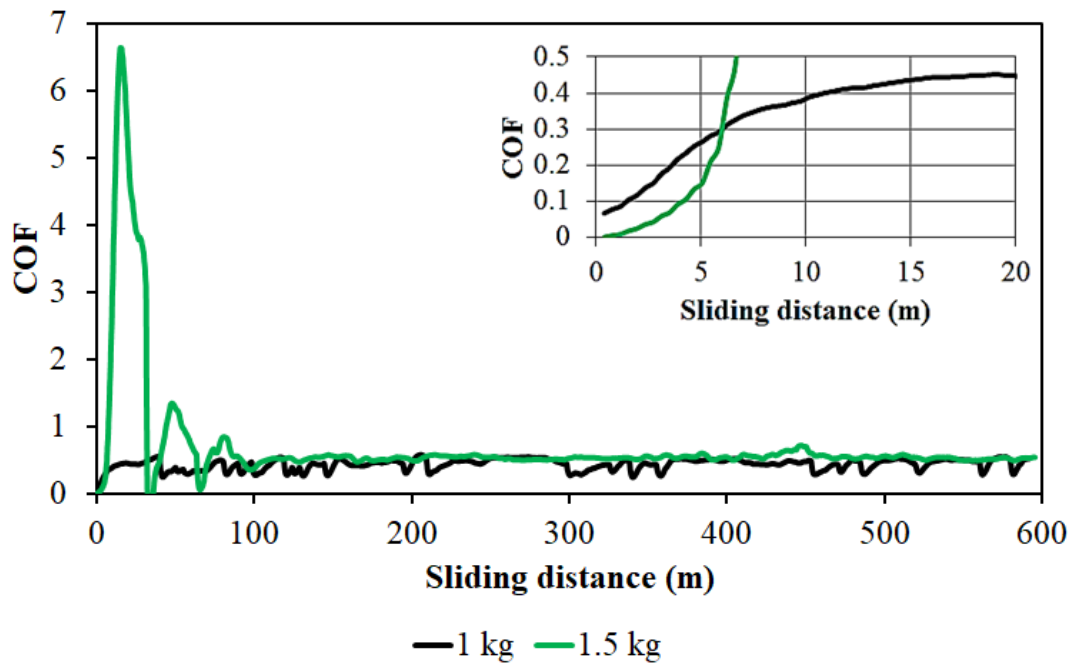
Figure 5.16: Coefficient of friction evolution under sliding speed of 3 m/s and at 150 °C temperature.
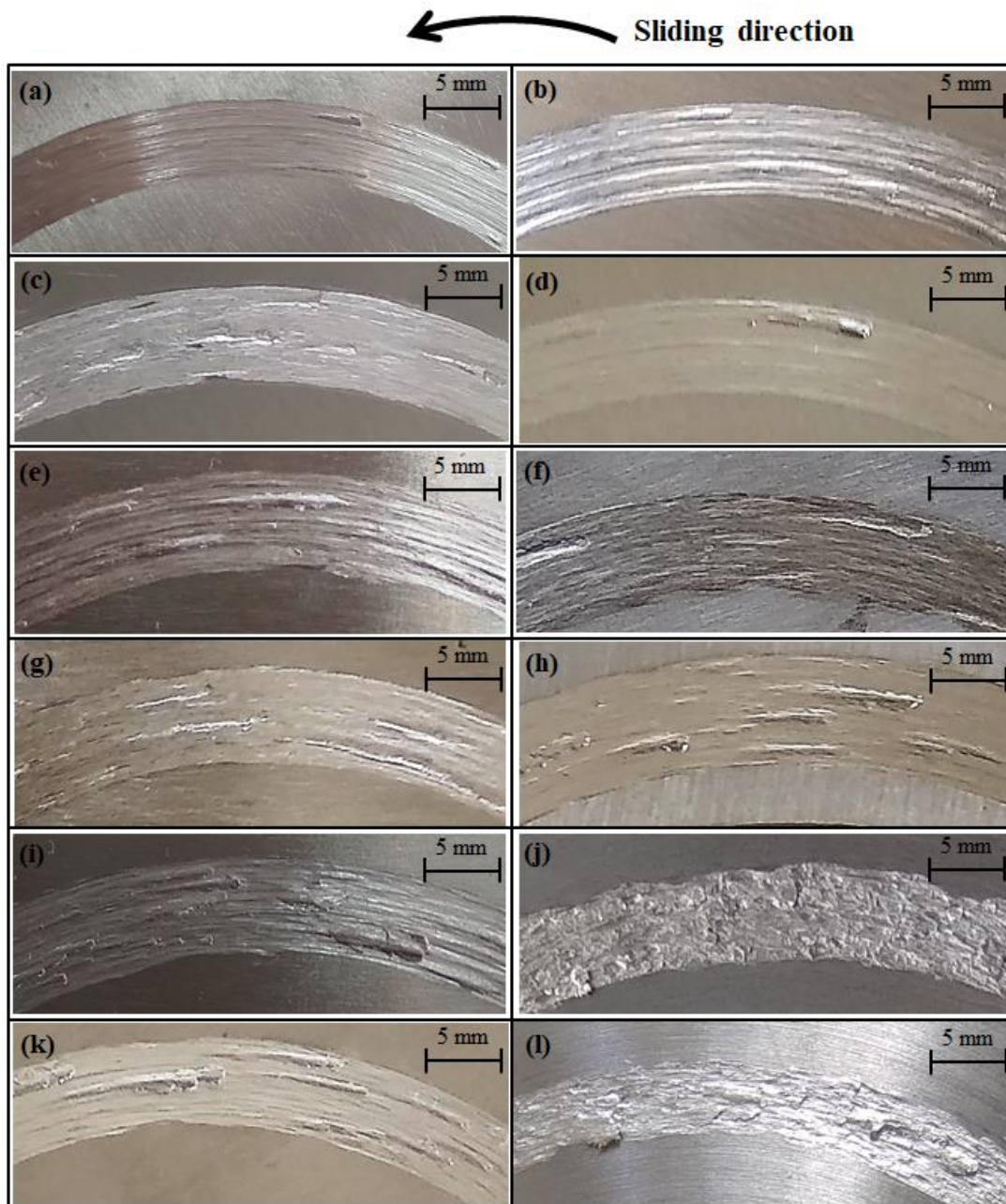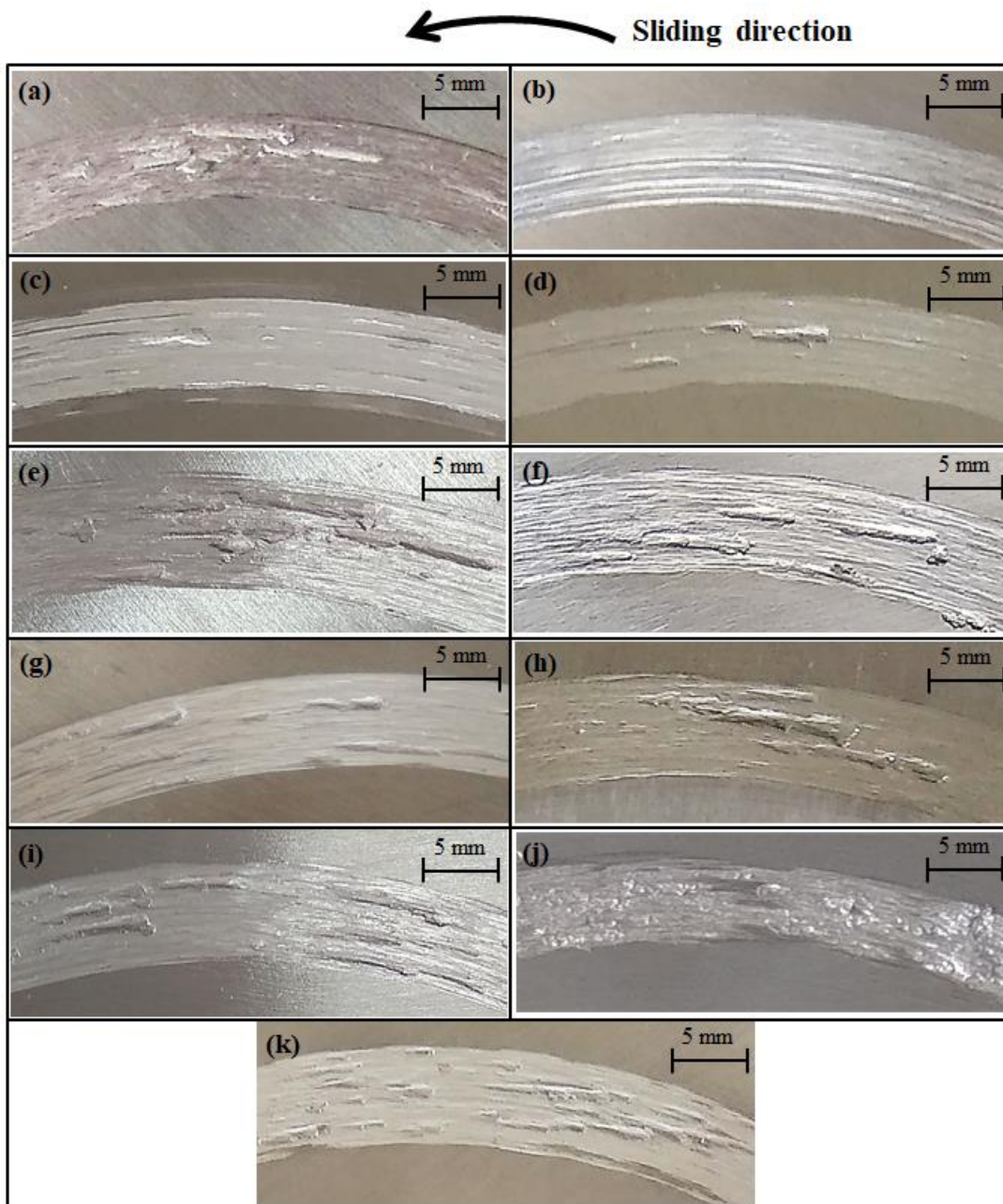
Figure 5.17: Worn surfaces of wear track at sliding speed of 3 m/s and, at 1 kg normal load (a-d), at 1.5 kg normal load (e-h) and at 2 kg normal load (i-k); under room temperature (a, e, i), 60 °C (b, f, j), 100 °C (c, g, k) and 150 °C (d, h).

5.3 RESULTS AND DISCUSSION

5.3.1 Coefficient of friction

Coefficient of friction at the end of first cycle of all experimental conditions is summarized as the initial coefficient of friction in Figure 5.18 - Figure 5.21. The initial coefficient of friction occurs due to the deformation of asperities present on the contact surfaces at the initial stage of sliding. The initial coefficient of friction varied from 0.01 to 0.16 at room temperature. Lower initial coefficient of friction was observed when lower normal load was applied and higher initial coefficient of friction was observed when higher normal load was applied. The surface of pin and disk specimens oxidized more at higher temperatures, resulting in lower initial coefficient of friction when compared with the initial coefficient of friction at room temperature. The initial coefficient of friction showed variations in the range of 0.001 - 0.01, 0.002 - 0.03 and 0.001 - 0.07 at temperatures of 60 °C, 100 °C and 150 °C, respectively. Normal load and sliding speed showed a directly proportional relationship with the initial coefficient of friction, whereas temperature showed an inversely proportional relationship with the initial coefficient of friction.
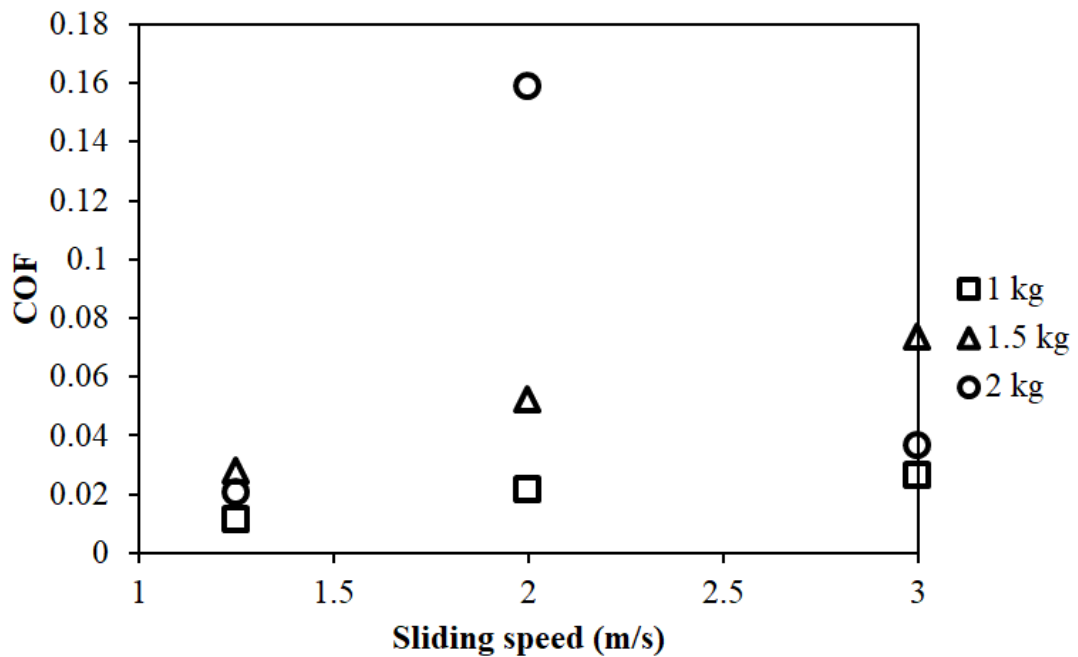
Figure 5.18: Variation of initial coefficient of friction under different normal loads, sliding speeds and at room temperature.
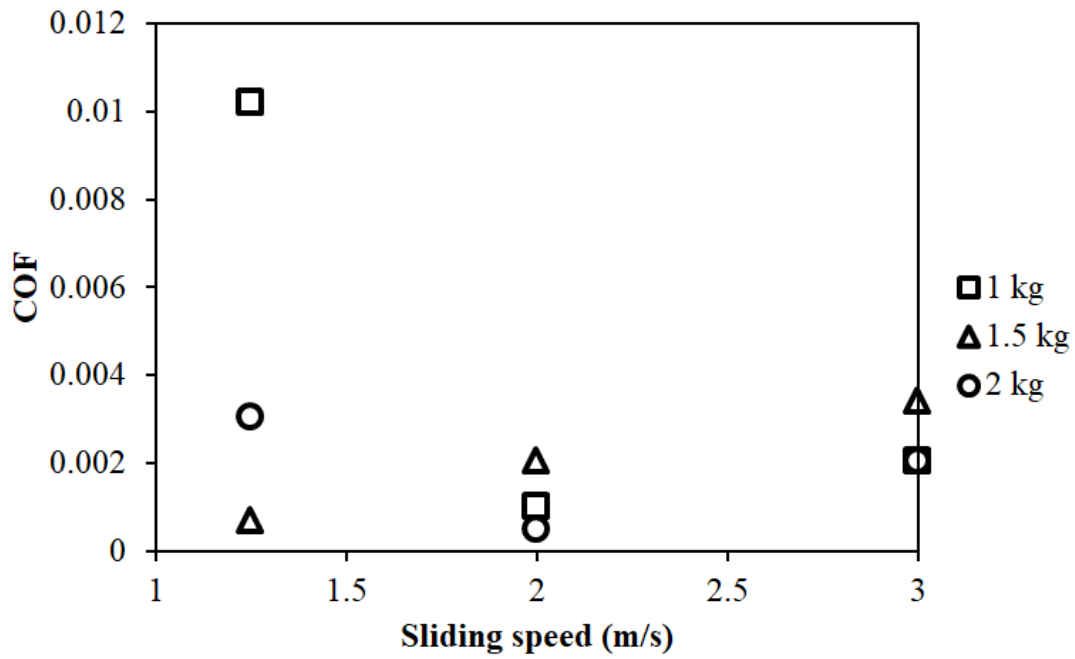
Figure 5.19: Variation of initial coefficient of friction under different normal loads, sliding speeds and at 60 °C temperature.
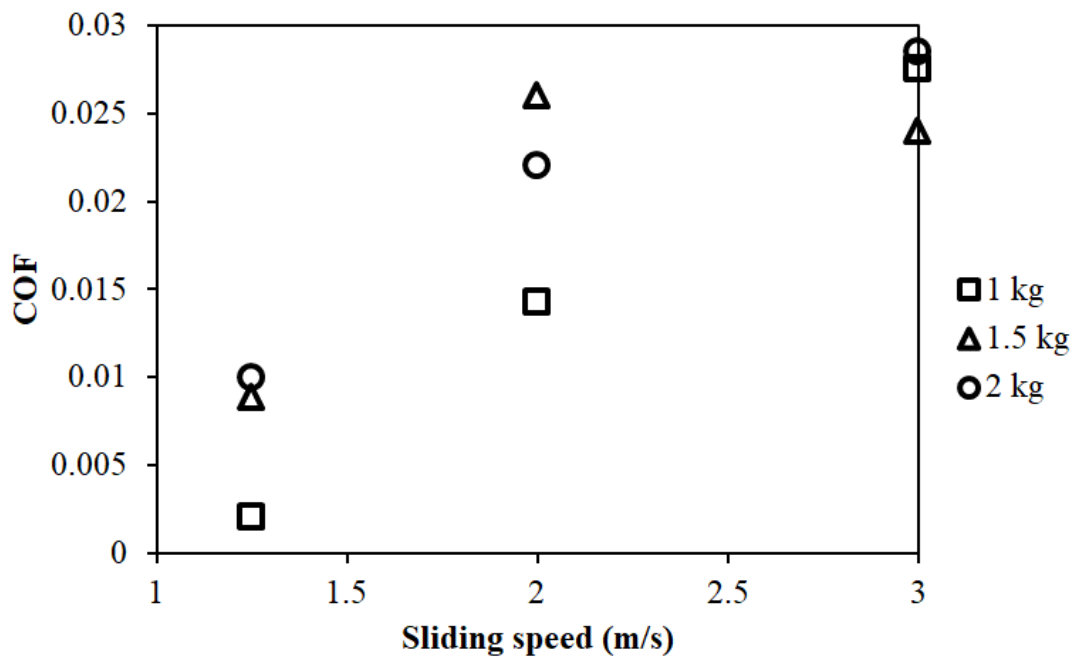
Figure 5.20: Variation of initial coefficient of friction under different normal loads, sliding speeds and at 100 °C temperature.
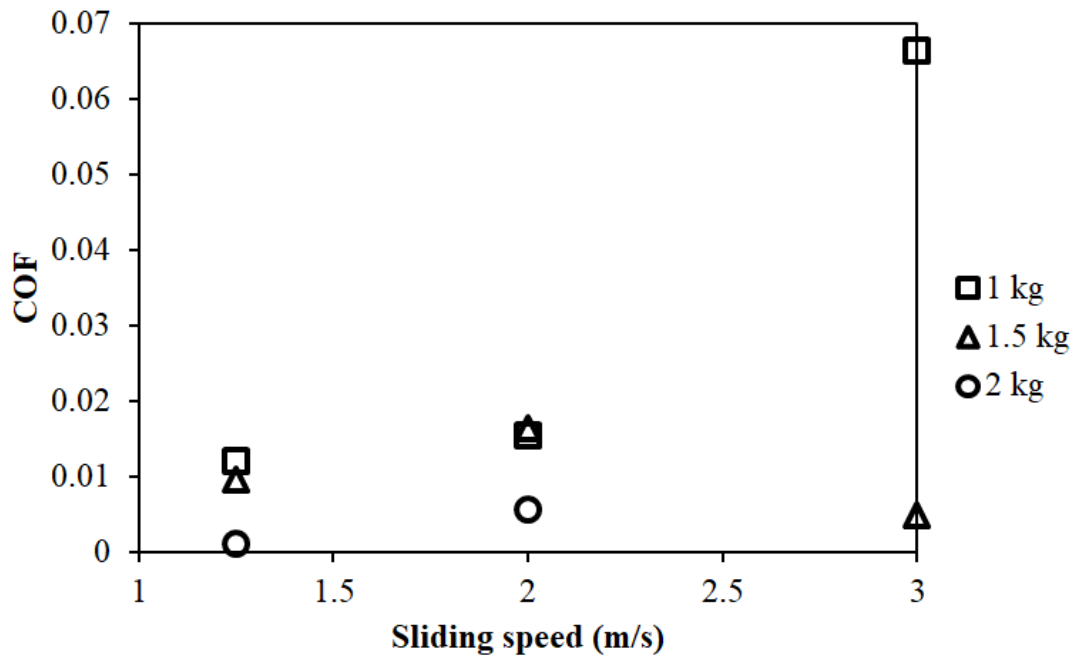
Figure 5.21: Variation of initial coefficient of friction under different normal loads, sliding speeds and at 150 °C temperature.

In all experimental conditions, the coefficient of friction increased linearly with the sliding distance (5 m – 10 m) and stabilized later. The linear increase in coefficient of friction was due to the flattening of contact asperities and removal of initial oxide layer on the contact surfaces. The coefficient of friction stabilized when the contact surfaces attained the maximum contact area. The stabilized coefficient of friction of Al 6061-T6 alloy at various experimental conditions is presented in Figure 5.22 - Figure 5.25. The stabilized coefficient of friction increased with the increase in normal load and sliding speed at room temperature (31 ± 1 °C). It can be gauged from Figure 5.22 that the lowest coefficient of friction (0.3) was observed at a normal load of 1 kg and sliding speed of 1.25 m/s and the highest coefficient of friction (0.5) was observed at a normal load of 2 kg and sliding speed of 3 m/s. At 60 °C temperature, stabilized coefficient of friction increased with the increase in normal load and it decreased with the increase in sliding speed. Normal load showed a significant effect on the change in stabilized coefficient of friction when compared to the sliding speed. The stabilized coefficient of friction varied in the range of 0.26 - 2.5 (Figure 5.23). The highest value of coefficient of friction (2.5) at 1 kg normal load and at 3 m/s

sliding speed was due to the severe plastic deformation of contact surfaces during the initial stages of the experiment. At 100 °C temperature, both sliding speed and normal load showed a significant effect on stabilized coefficient of friction. At 1 kg and 2 kg normal load conditions, stabilized coefficient of friction decreased when sliding speed increased from 1.25 m/s to 2 m/s; stabilized coefficient of friction further increased when sliding speed increased to 3 m/s. The stabilized coefficient of friction varied in the range of 0.1 - 0.6 (Figure 5.24). A significant increase in stabilized coefficient of friction was observed at 150 °C temperature and at normal load of 2 kg, due to the severe plastic deformation of contact interfaces, as shown in Figure 5.25. Stabilized coefficient of friction varied in the range of 0.15 - 1.2 (Figure 5.25). The resultant higher coefficient of friction at higher temperatures was due to the material softening and increase in contact area, which increased the material deformation (Deuis et al., 1997).

Figure 5.22: Variation of stabilized coefficient of friction at room temperature.

Figure 5.23: Variation of stabilized coefficient of friction at 60 °C temperature.

Figure 5.24: Variation of stabilized coefficient of friction at 100 °C temperature.

Figure 5.25: Variation of stabilized coefficient of friction at 150 °C temperature.

The average of coefficient of friction in a steady state region was considered as a steady state coefficient of friction, as shown in Figure 5.26 - Figure 5.29. Coefficient of friction increased at room temperature with the increase in normal load and sliding speed, but the increase in coefficient of friction was insignificant. Coefficient of friction increased from 0.47 (at 1 kg normal load and 1.25 m/s sliding speed) to 0.57 (at 2 kg normal load and 3 m/s sliding speed).The normal load and sliding speed did not change coefficient of friction (which was around 0.45) significantly at 1 kg and 1.5 kg normal loads and at 60 °C temperature. However, the application of a 2 kg normal load resulted in the coefficient of friction being significantly decreased from 1.5 to 0.75 with the increase in sliding speed from 1.25 m/s to 3 m/s. The significant increase in coefficient of friction at a higher normal load was due to the removal of tribolayer at contact interface and the formation of metal to metal contact (Ramesh et al., 2010). The worn pin surfaces (Figure 5.30), due to the adhesive wear at 2 kg normal load and 60 °C temperature, are evidences of higher coefficient of friction, as reported in Figure 5.27. The frictional heat generated at higher sliding speeds resulted in the formation of oxide layer on the contact interface, which led to a decrease in coefficient of friction with an increase in sliding speed (Uyyuru et al., 2007). At 100 °C temperature, coefficient of friction showed a directly proportional relationship

with normal load, and the sliding speed showed an insignificant effect on coefficient of friction. The steady state coefficient of friction converged around 0.48 and 0.53 under normal loads of 1.5 kg and 2 kg, respectively. At 1 kg normal load, steady state coefficient of friction increased from 0.35 to 0.45 and then decreased to 0.38 with the increase in sliding speed from 1.5 m/s to 3 m/s. At 150 °C temperature, the steady state coefficient of friction increased with the increase in normal load and sliding speed; but the increments were not significant at normal loads of 1 kg and 1.5 kg. Steady state coefficient of friction varied in the range of 0.42 - 0.53 for all sliding speeds and applied normal load of 1 kg and 1.5 kg, at 150 °C temperature. When a 2 kg normal load was applied, the coefficient of friction varied in the range of 1.19 - 1.31. The higher coefficient of friction at 2 kg normal load condition was due to the adhesive wear at the contact interface (Figure 5.31, Figure 5.62 and Figure 5.65)).

Across the temperatures observed, the insignificant change in stabilized coefficient of friction and the decrease in stabilized coefficient of friction with an increase in sliding speed were due to the formation of stable oxide layers on the surface of interfaces (Odabas, 2018). However, at higher normal load conditions, the stability of oxide layer decreased due to the high contact stresses, which led to the removal of oxide layer and the formation of metal to metal contact. Stabilized coefficient of friction increased at this stage due to the adhesion between contact surfaces (Huttunen-Saarivirta et al., 2018).

Dewan and Mohammad (2012) and Shuaihang Pan et al. (2018) observed the coefficient of friction of aluminium to aluminium and flat on flat contact pairs. Cylindrical pin specimens of 6 mm diameter were used in their studies. Dewan and Mohammad (2012) observed an increase in steady state coefficient of friction from 0.2 to 0.3, with an increase in normal load from 5 N to 10 N. They observed an increase in steady state coefficient of friction from 0.22 to 0.26, with an increase in sliding speed from 0.5 m/s to 1 m/s. Shuaihang Pan et al. (2018) conducted experiments at 25 °C temperature and 0.04 m/s sliding speed. They observed steady state coefficient of friction of 0.75, 0.6, 0.57 and 0.6 at normal loads of 5 N, 15 N, 30 N and 40 N, respectively.
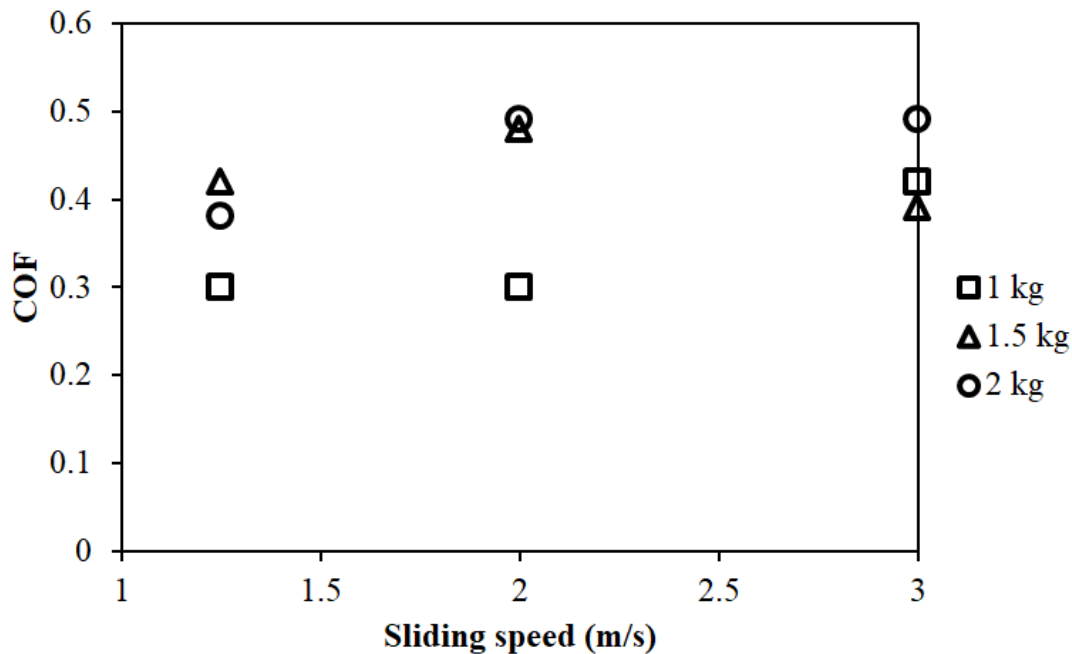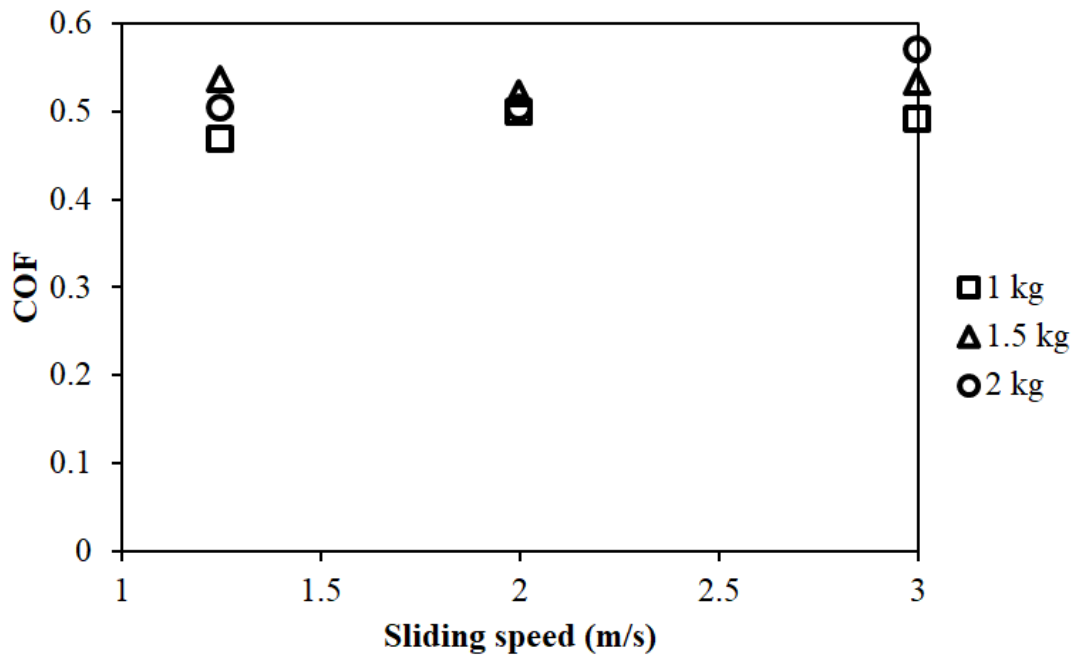
Figure 5.26: Variation of steady state coefficient of friction at room temperature.
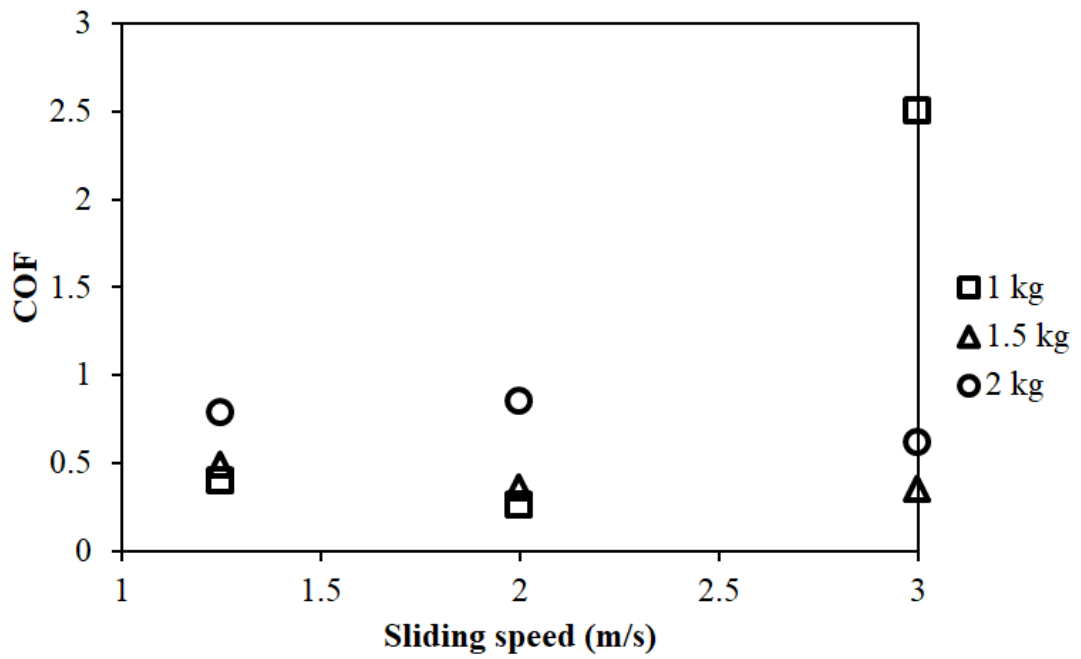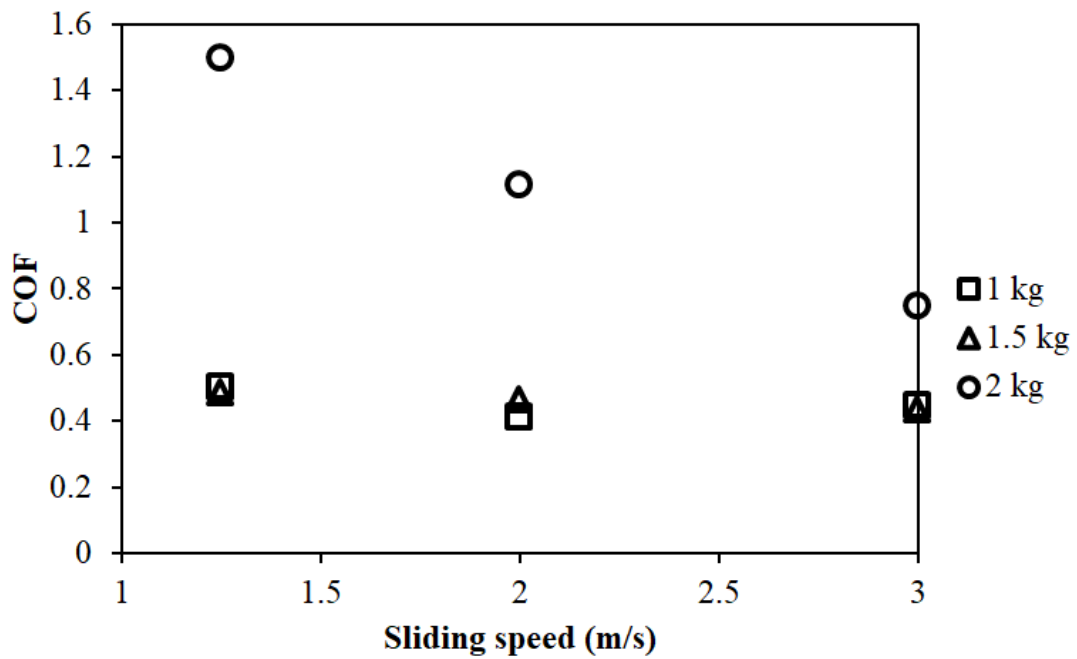

Figure 5.27: Variation of steady state coefficient of friction at 60 °C temperature.
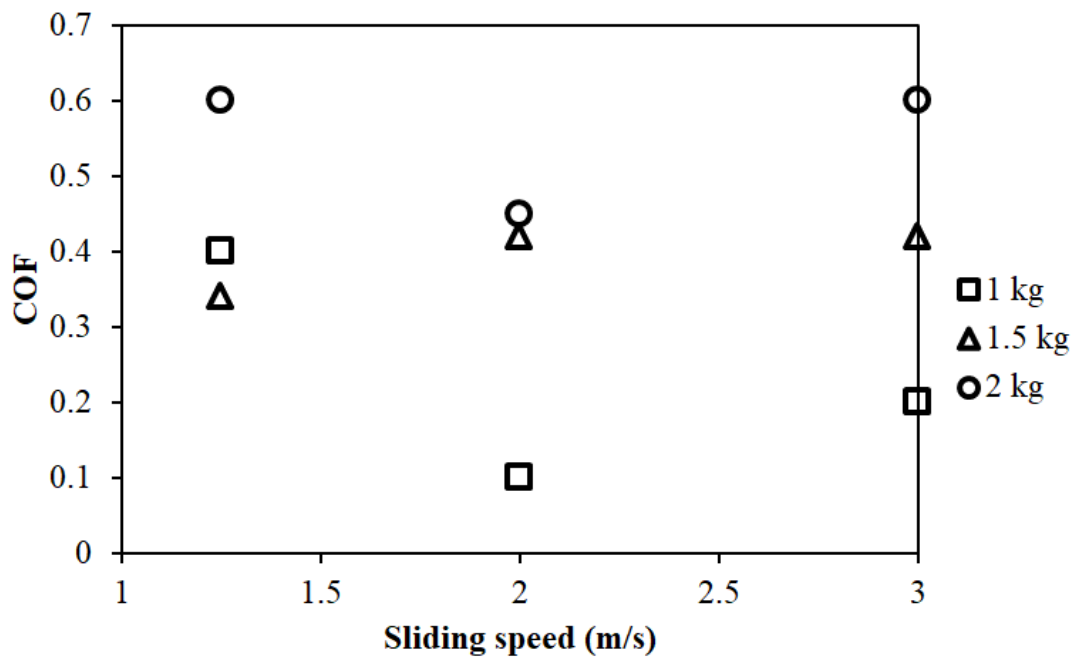
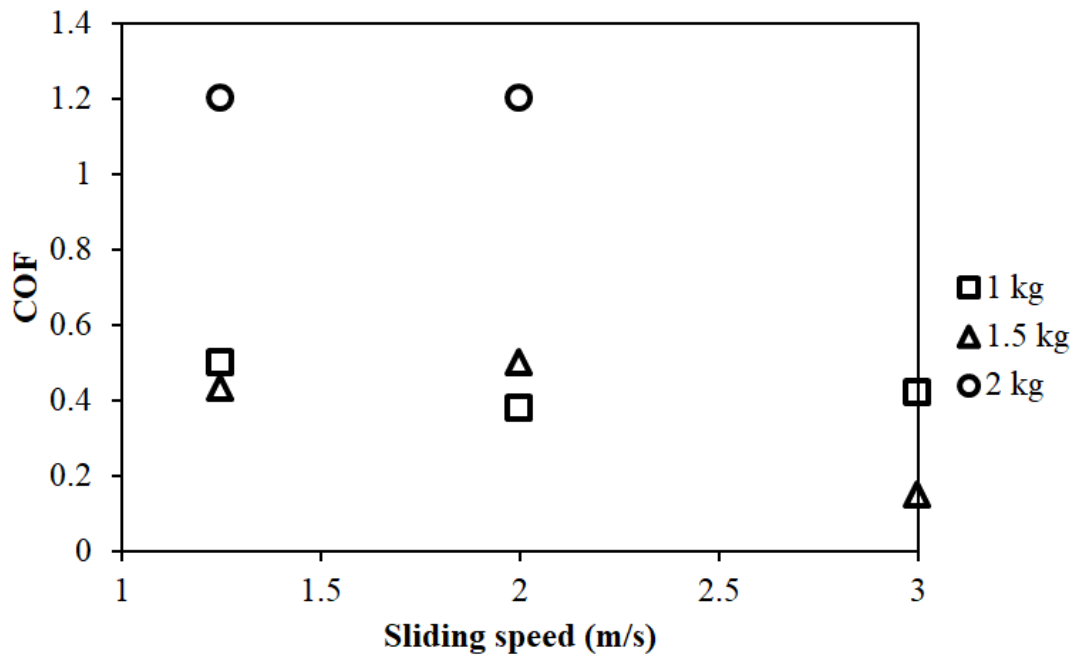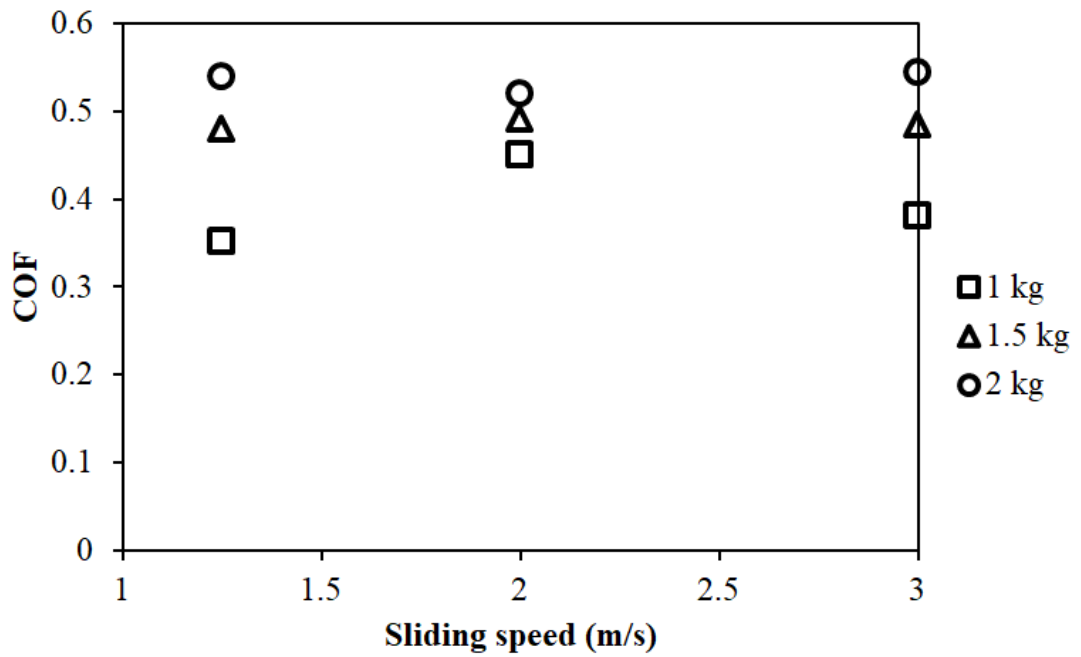Figure 5.28: Variation of steady state coefficient of friction at 100 °C temperature.
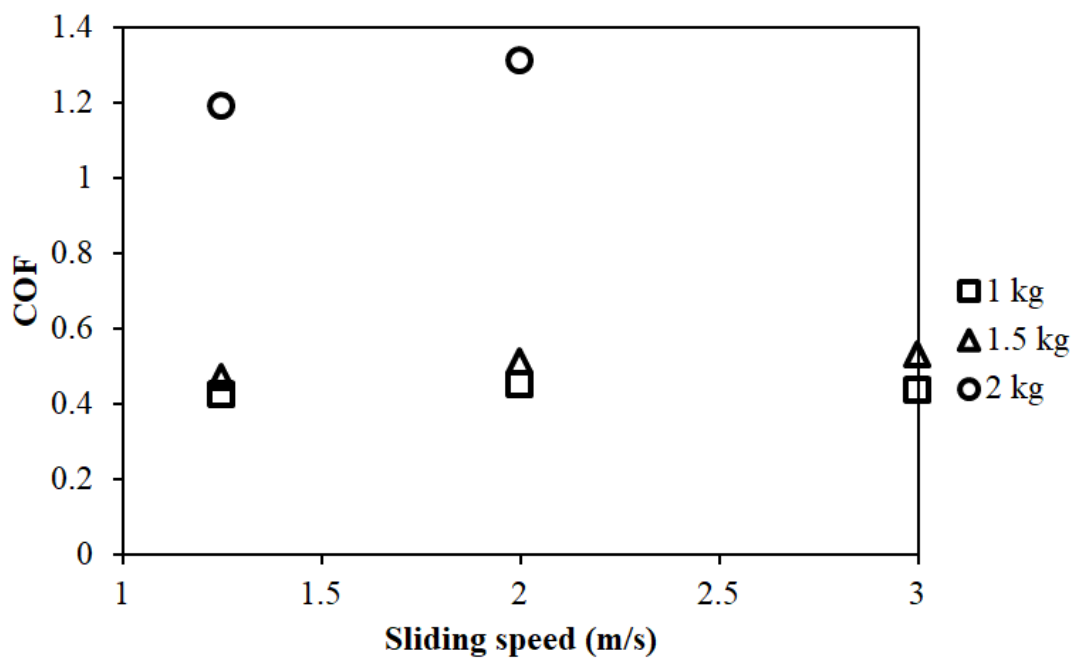
Figure 5.29: Variation of steady state coefficient of friction at 150 °C temperature.
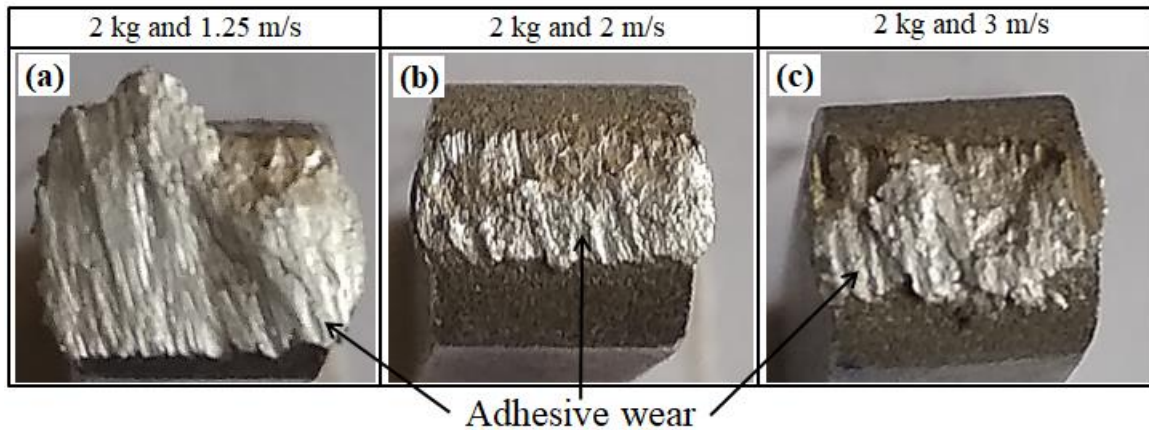
Figure 5.30: Adhesive wear on worn surfaces of pin specimen under 60 °C temperature.
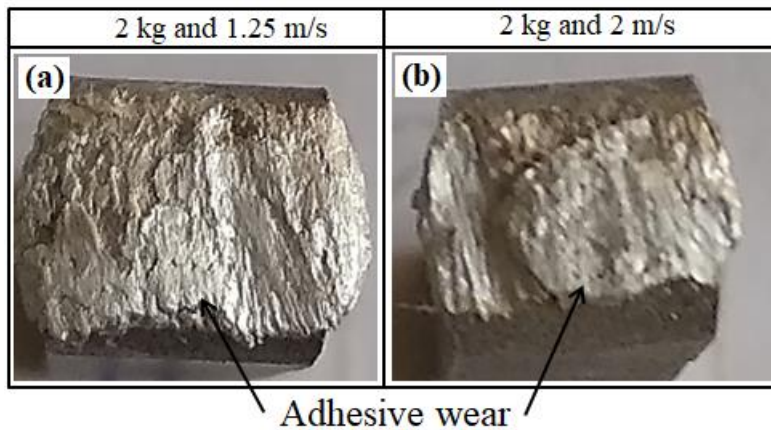
Figure 5.31: Adhesive wear on worn surfaces of pin specimen under 150 °C temperature.

An unsteady state was observed in the evolution of coefficient of friction during experiments conducted at room temperature. The average of coefficient of friction in unsteady state region is given in Figure 5.32. The unsteady state coefficient of friction converged around 0.45 at all sliding speeds considered for 1.5 kg normal load. At 1 kg normal load, unsteady state coefficient of friction decreased from 0.39 to 0.28 with an increase in sliding speed from 1.25 m/s to 3 m/s. At 2 kg normal load, unsteady state coefficient of friction increased from 0.44 to 0.99 with an increase in sliding speed from 1.25 m/s to 3 m/s. The initial, stabilized, steady state and unsteady state coefficients of friction of Al 6061-T6 alloy observed at room temperature, 60 °C temperature, 100 °C temperature and 150 °C temperature are summarized in Table 5.1, Table 5.2, Table 5.3 and Table 5.4, respectively.

94
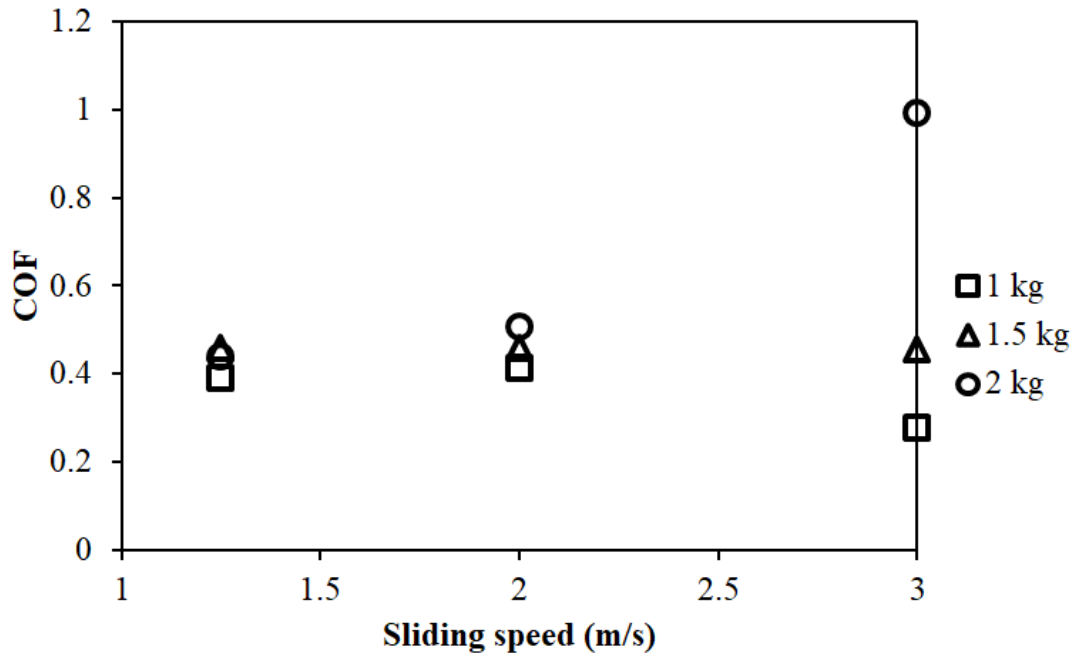
Figure 5.32: Variation of unsteady state coefficient of friction under different normal loads and sliding speeds at room temperature.

Table 5.1: Summary of coefficient of friction at room temperature.

Normal load (kg)	Sliding speed (m/s)	Coefficient of Friction			
		Initial	Stabilized	Steady state	Unsteady state
1	1.25	0.011	0.3	0.47	0.39
1	2	0.021	0.3	0.5	0.41
1	3	0.027	0.42	0.49	0.28
1.5	1.25	0.028	0.42	0.54	0.46
1.5	2	0.052	0.48	0.52	0.46
1.5	3	0.073	0.39	0.53	0.45
2	1.25	0.02	0.38	0.5	0.44
2	2	0.159	0.49	0.5	0.51
2	3	0.037	0.49	0.57	0.99

Table 5.2: Summary of coefficient of friction at 60 °C temperature.

Normal load (kg)	Sliding speed (m/s)	Coefficient of Friction		
		Initial	Stabilized	Steady state
1	1.25	0.01	0.4	0.5
1	2	0.001	0.26	0.41
1	3	0.002	2.5	0.44
1.5	1.25	0.001	0.49	0.48

1.5	2	0.002	0.36	0.47
1.5	3	0.003	0.35	0.43
2	1.25	0.003	0.79	1.5
2	2	0.001	0.85	1.12
2	3	0.002	0.62	0.75

Table 5.3: Summary of coefficient of friction at 100 °C temperature.

Normal load (kg)	Sliding speed (m/s)	Coefficient of Friction		
		Initial	Stabilized	Steady state
1	1.25	0.002	0.4	0.35
1	2	0.014	0.1	0.45
1	3	0.028	0.2	0.38
1.5	1.25	0.009	0.34	0.48
1.5	2	0.026	0.42	0.49
1.5	3	0.024	0.42	0.49
2	1.25	0.01	0.6	0.54
2	2	0.022	0.45	0.52
2	3	0.029	0.6	0.54

Table 5.4: Summary of coefficient of friction at 150 °C temperature.

Normal load (kg)	Sliding speed (m/s)	Coefficient of Friction		
		Initial	Stabilized	Steady state
1	1.25	0.012	0.5	0.42
1	2	0.015	0.38	0.45
1	3	0.066	0.42	0.43
1.5	1.25	0.01	0.43	0.47
1.5	2	0.016	0.5	0.51
1.5	3	0.005	0.15	0.53
2	1.25	0.001	1.2	1.19
2	2	0.006	1.2	1.31

5.3.2 Analysis of worn surfaces

The worn surface images of disk specimen were captured using an optical microscope. The observed wear mechanisms are discussed in this section. Adhesive wear mechanism was predominant at room temperature (31 ± 1 °C), at 1 kg normal load and 1.25 m/s sliding speed (Figure 5.33). Wear mechanism changed from adhesive wear to abrasive wear when normal load and sliding speed increased due to

frictional heat generation. During wear process, the oxide debris was stuck on the front side of the pin and its hardness was greater than the hardness of the metal matrix (e.g., Pan et al., 2017). The formation and removal of oxide layer at higher sliding speed was easy because of the frictional heat, which was authenticated by the presence of wear grooves on the disk surface. Figure 5.36 shows shallow grooves and crater formation on the disk specimen, due to abrasive wear. As the normal load increased, higher frictional tractions resulted in debris compaction on disk surface (Figure 5.34), deeper grooves (Figure 5.37) and crater formation (Figure 5.40). At 2 kg normal load, (Figure 5.35, Figure 5.38 and Figure 5.41) the depth and width of abrasive grooves and craters were more than those observed at lesser normal loads. This shows that higher normal loads result in higher wear losses (Jerina and Kalin, 2014). Abrasive wear mechanism was dominant when 2 kg normal load was applied.

Figure 5.33: Micrograph of worn disk specimen tested at 1 kg normal load, 1.25 m/s sliding speed and at room temperature.

Figure 5.34: Micrograph of worn disk specimen tested at 1.5 kg normal load, 1.25 m/s sliding speed and at room temperature.

Figure 5.35: Micrograph of worn disk specimen tested at 2 kg normal load, 1.25 m/s sliding speed and at room temperature.

Figure 5.36: Micrograph of worn disk specimen tested at 1 kg normal load, 2 m/s sliding speed and at room temperature.

Figure 5.37: Micrograph of worn disk specimen tested at 1.5 kg normal load, 2 m/s sliding speed and at room temperature.

Figure 5.38: Micrograph of worn disk specimen tested at 2 kg normal load, 2 m/s sliding speed and at room temperature.

Figure 5.39: Micrograph of worn disk specimen tested at 1 kg normal load, 3 m/s sliding speed and at room temperature.

Figure 5.40: Micrograph of worn disk specimen tested at 1.5 kg normal load, 3 m/s sliding speed and at room temperature.

Figure 5.41: Micrograph of worn disk specimen tested at 2 kg normal load, 3 m/s sliding speed and at room temperature.

Adhesive wear mechanism was dominant at 60 °C temperature and at 1 kg and 1.5 kg normal loading conditions. Abrasive grooves were observed on a wide area at 1 kg normal load and 1.25 m/s sliding speed (Figure 5.42). The width of wear grooves increased with the increase in sliding speed (Figure 5.45 and Figure 5.48). Wider grooves (Figure 5.43 and Figure 5.49)) and cracks (Figure 5.46) were observed on the disk surface at 1.5 kg normal load, as the sliding speed increased. Surface cracks led to the failure of unstable oxide layers. The high contact stress at 2 kg normal load caused the failure of oxide layer on the metal surface and the formation of metal to metal contact (Ramesh et al., 2010). Severe adhesive wear was observed at 2 kg normal load (Figure 5.44, Figure 5.47 and Figure 5.50) and these adhesive forces caused the high coefficient of friction observed at 2 kg normal load conditions.
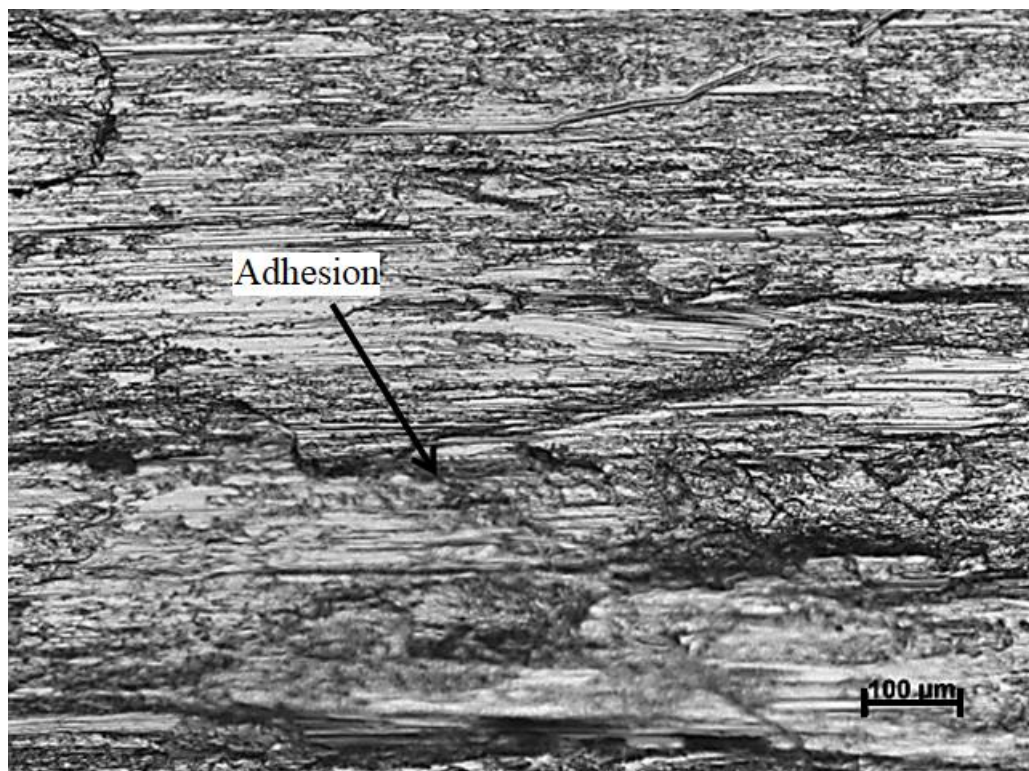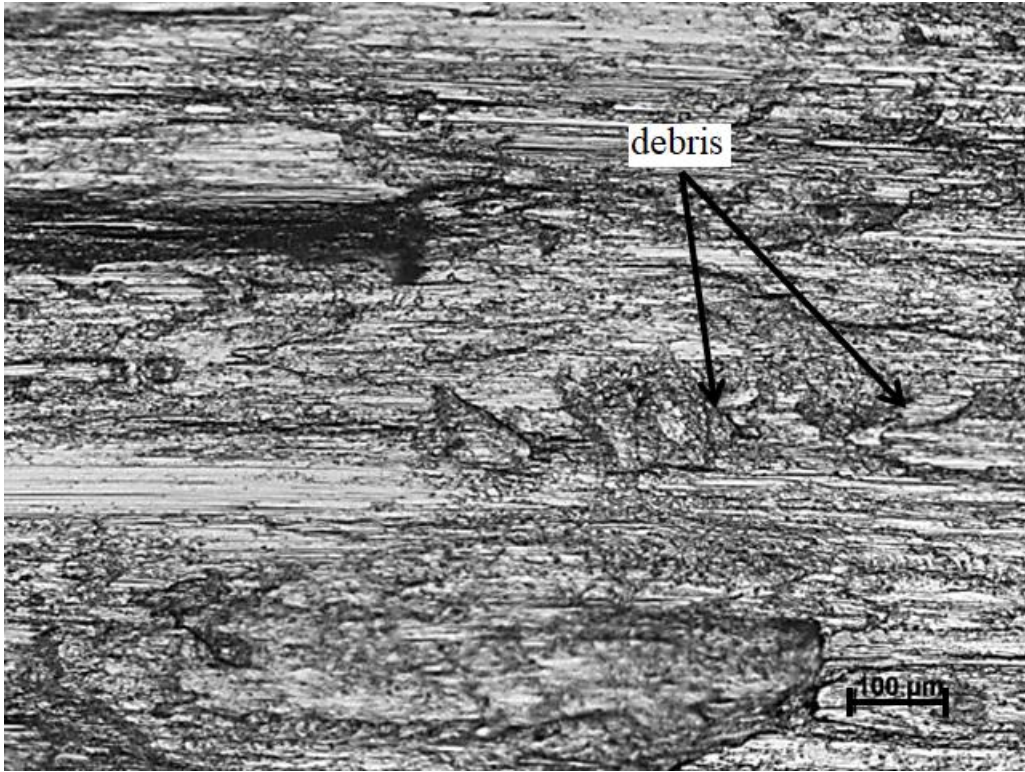

Figure 5.42: Micrograph of worn disk specimen tested at 1 kg normal load, 1.25 m/s sliding speed and at 60 °C temperature.

Figure 5.43: Micrograph of worn disk specimen tested at 1.5 kg normal load, 1.25 m/s sliding speed and at 60 °C temperature.
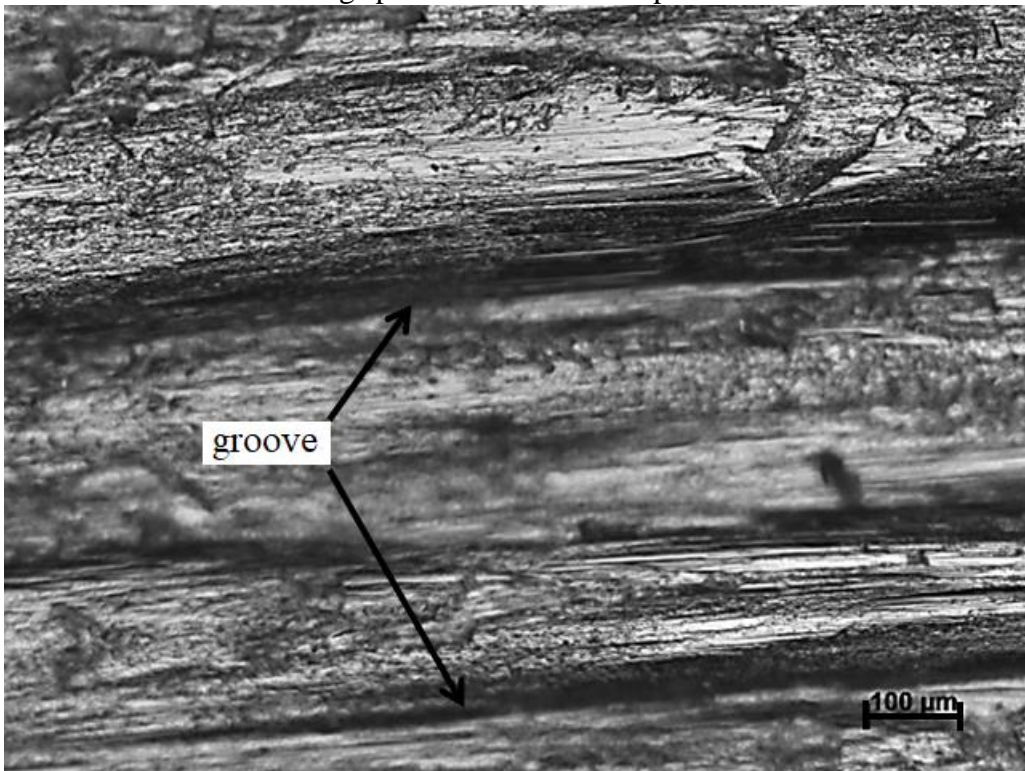

Figure 5.44: Micrograph of worn disk specimen tested at 2 kg normal load, 1.25 m/s sliding speed and at 60 °C temperature.
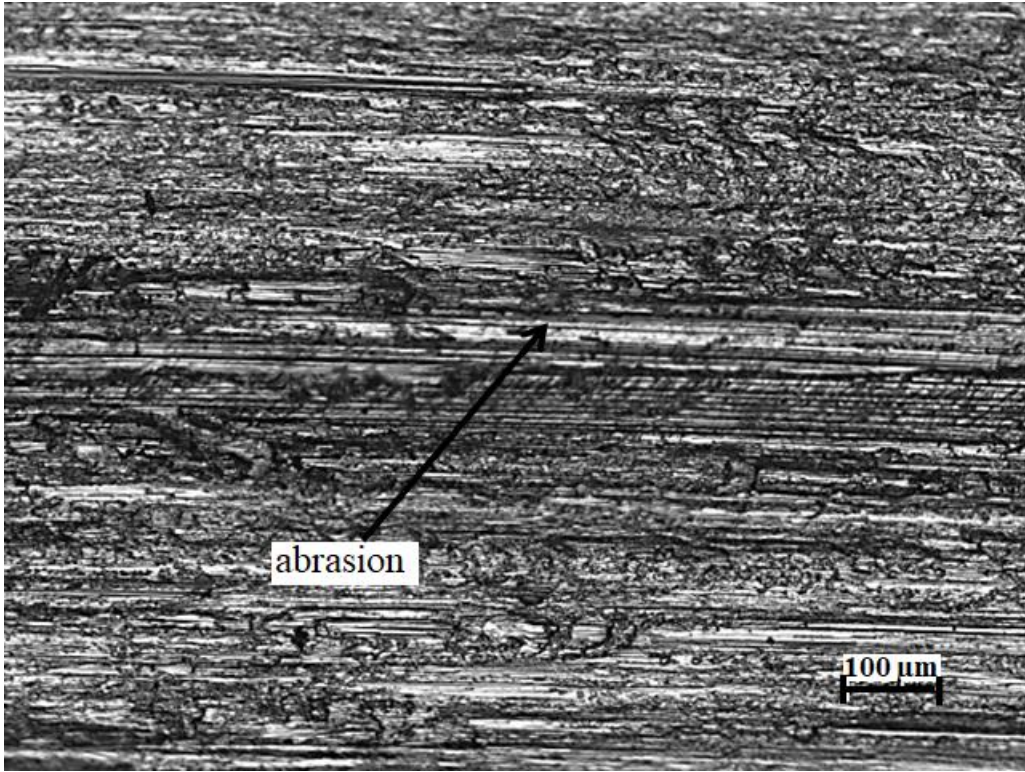
Figure 5.45: Micrograph of worn disk specimen tested at 1 kg normal load, 2 m/s sliding speed and at 60 °C temperature.

Figure 5.46: Micrograph of worn disk specimen tested at 1.5 kg normal load, 2 m/s sliding speed and at 60 °C temperature.
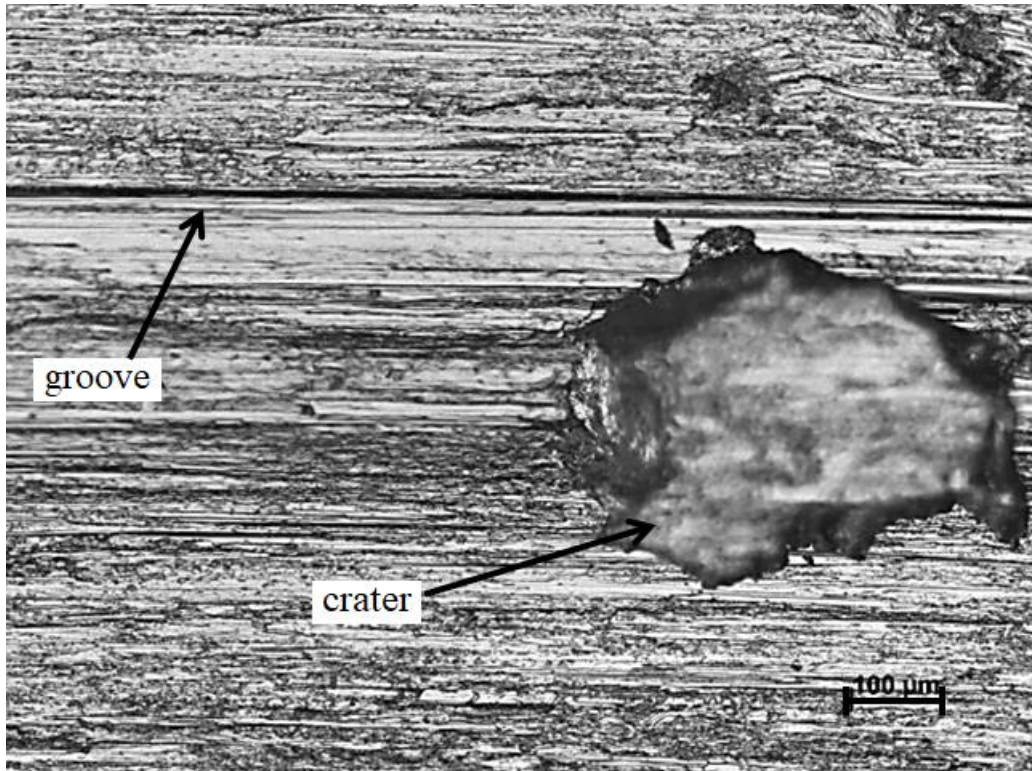
Figure 5.47: Micrograph of worn disk specimen tested at 2 kg normal load, 2 m/s sliding speed and at 60 °C temperature.

Figure 5.48: Micrograph of worn disk specimen tested at 1 kg normal load, 3 m/s sliding speed and at 60 °C temperature.
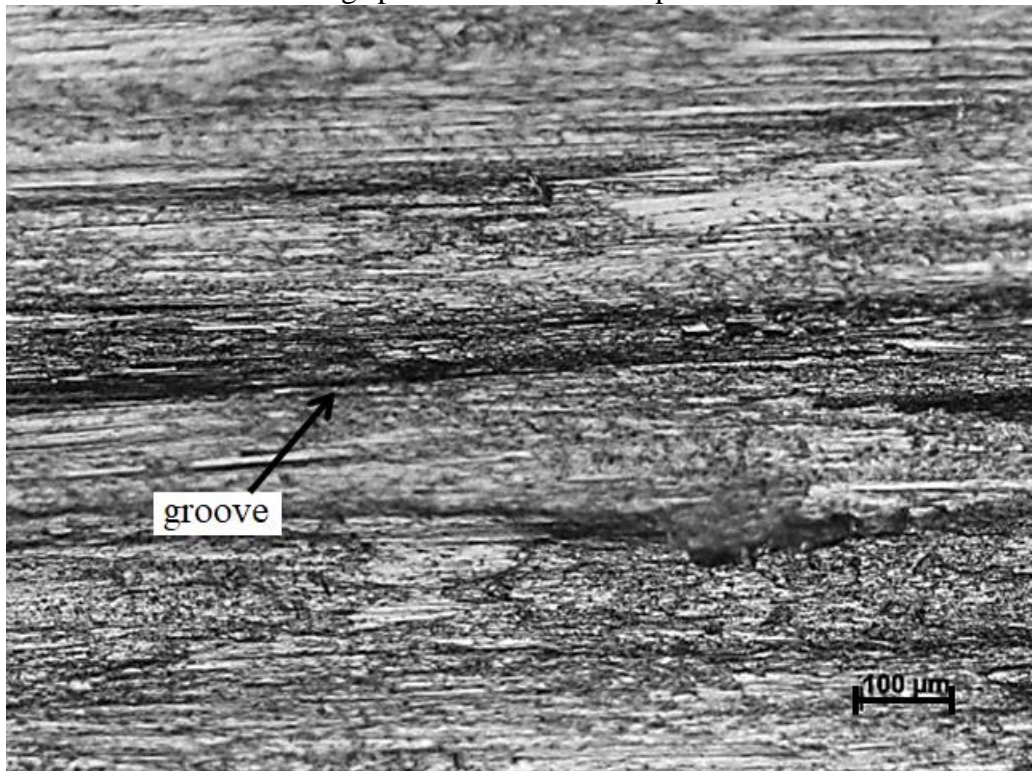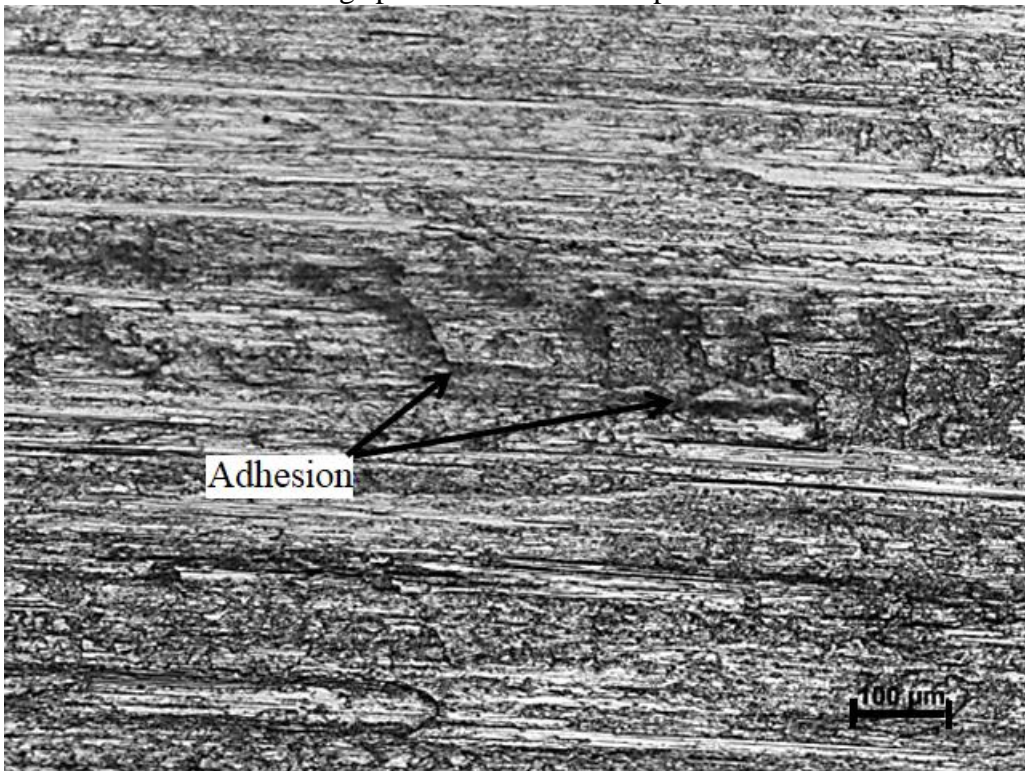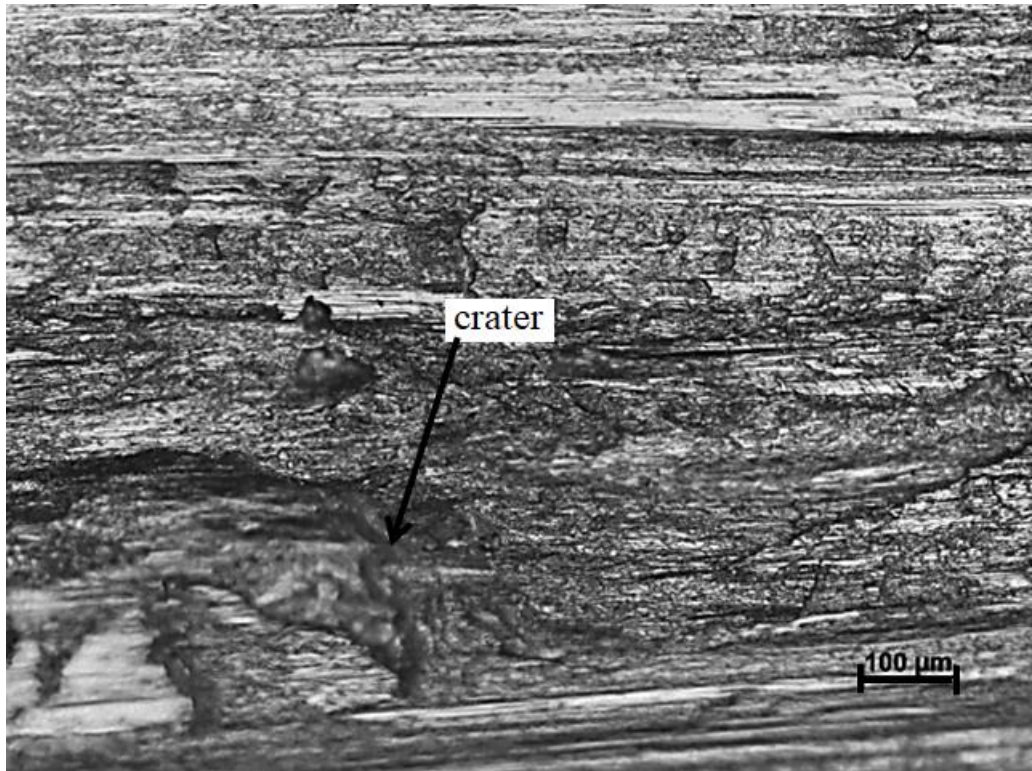
Figure 5.49: Micrograph of worn disk specimen tested at 1.5 kg normal load, 3 m/s sliding speed and at 60 °C temperature.

Figure 5.50: Micrograph of worn disk specimen tested at 2 kg normal load, 3 m/s sliding speed and at 60 °C temperature.

Mixed wear mechanism (abrasive and adhesive) was observed at 100 °C temperature (Figure 5.51 - Figure 5.59). Abrasive wear scars were observed on a wider area of disk surface. Voids were observed on the disk surface and the area of void surface increased with the increase in normal load and sliding speed. Removal of oxide particles from the disk surface at higher normal load and sliding speed and at higher temperatures caused the formation of voids on the disk surface. Abrasive wear mechanism was dominant at 1 kg normal load and 3 m/s sliding speed (Figure 5.57). When 2 kg normal load was applied, the adhesive wear mechanism resulted in severe plastic deformation of material (Figure 5.53, Figure 5.56 and Figure 5.59).

Figure 5.51: Micrograph of worn disk specimen tested at 1 kg normal load, 1.25 m/s sliding speed and at 100 °C temperature.

Figure 5.52: Micrograph of worn disk specimen tested at 1.5 kg normal load, 1.25 m/s sliding speed and at 100 °C temperature.

Figure 5.53: Micrograph of worn disk specimen tested at 2 kg normal load, 1.25 m/s sliding speed and at 100 °C temperature.
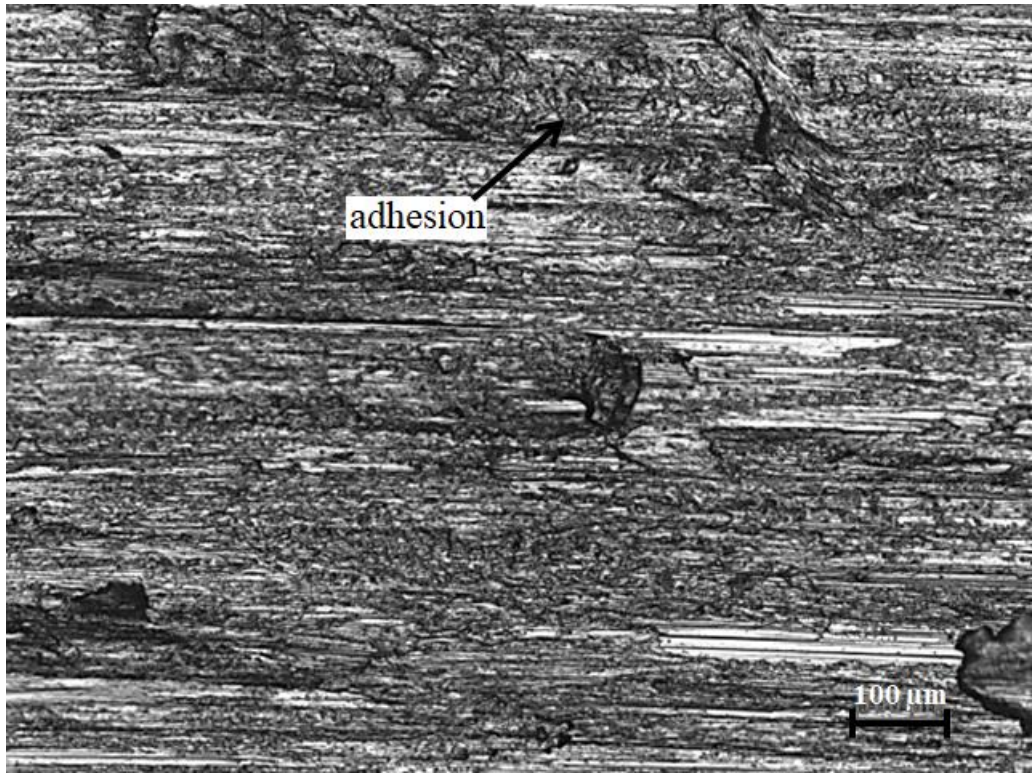
Figure 5.54: Micrograph of worn disk specimen tested at 1 kg normal load, 2 m/s
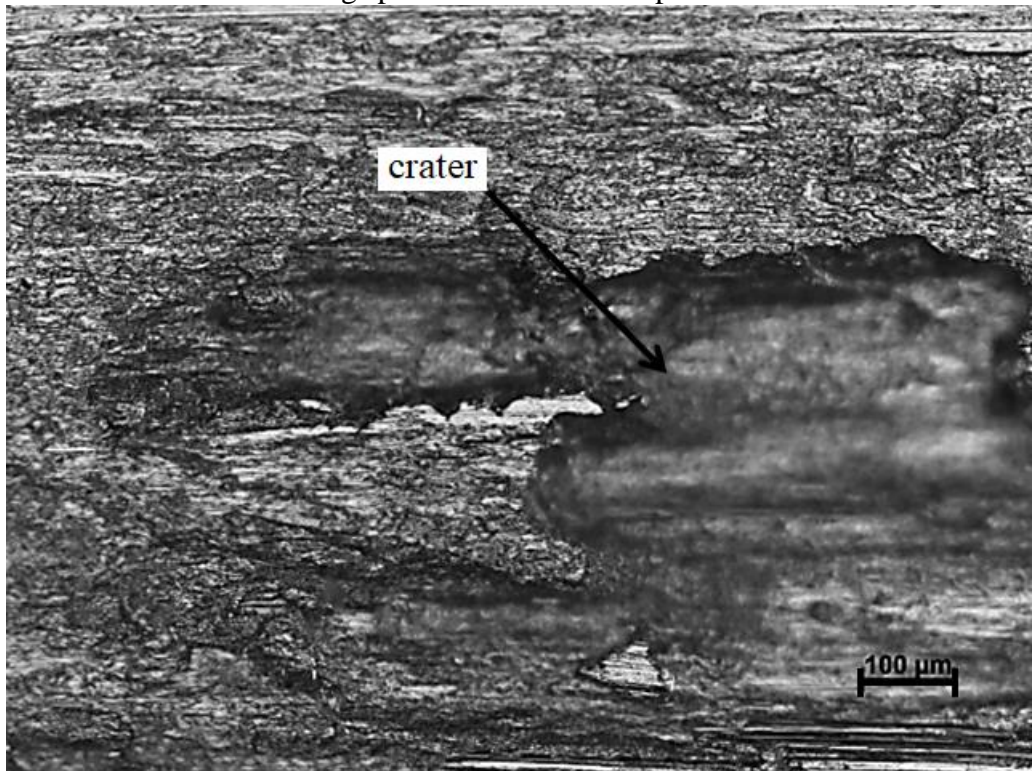sliding speed and at 100 °C temperature.
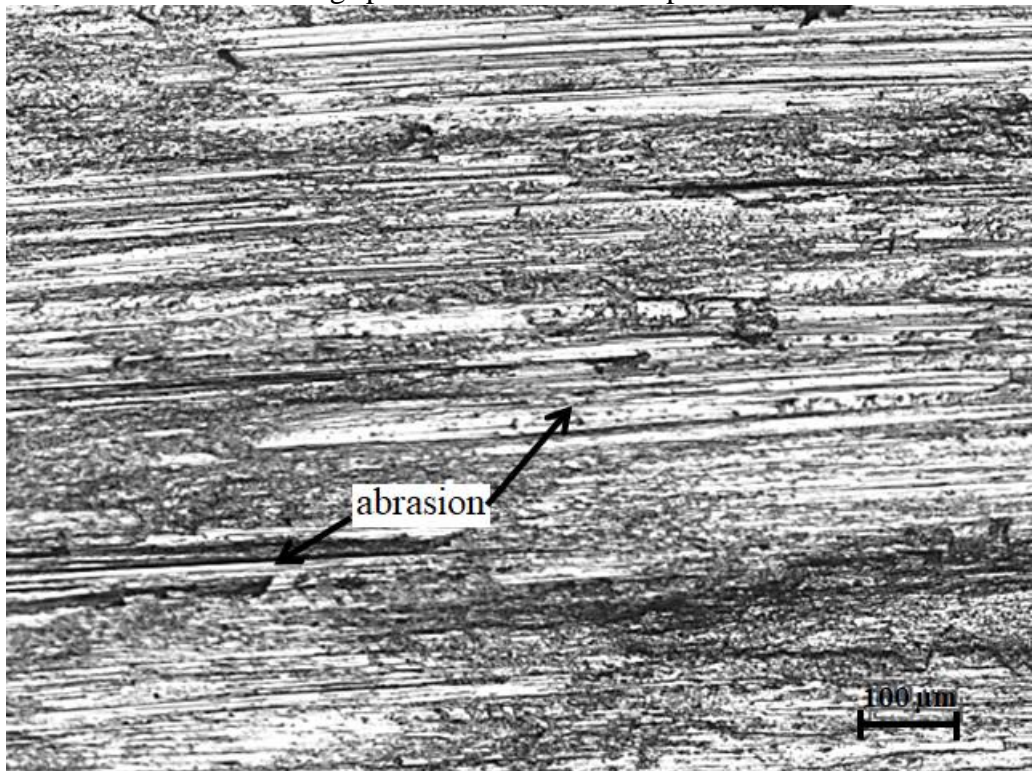
Figure 5.55: Micrograph of worn disk specimen tested at 1.5 kg normal load, 2 m/s
sliding speed and at 100 °C temperature.
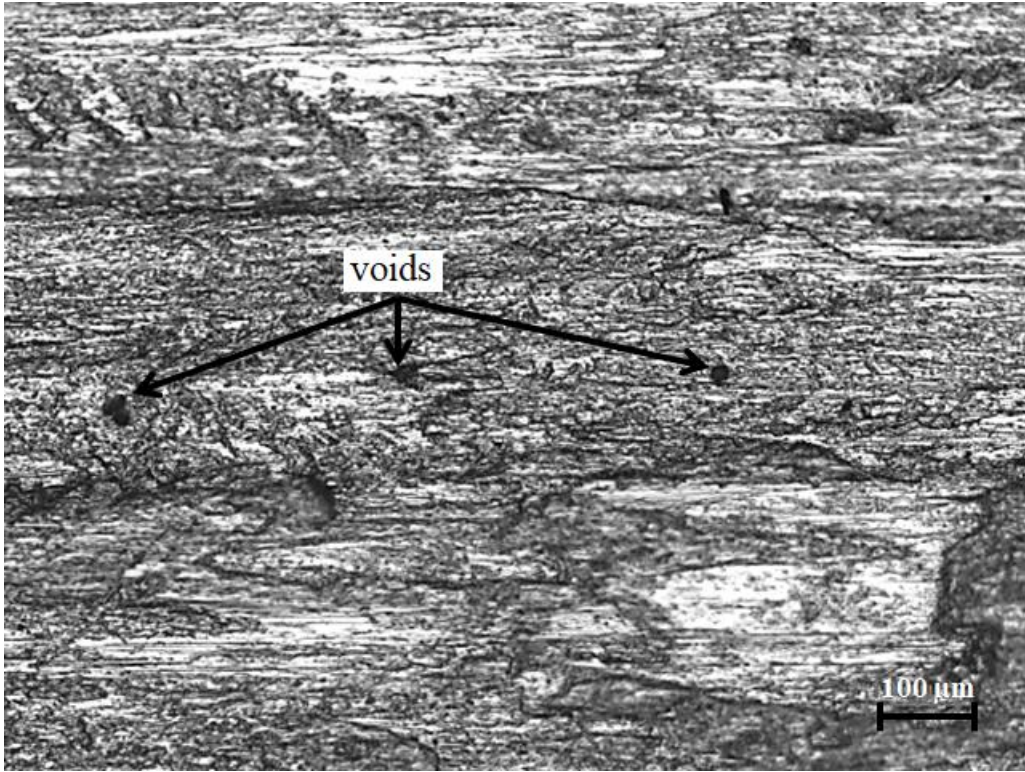
Figure 5.56: Micrograph of worn disk specimen tested at 2 kg normal load, 2 m/s
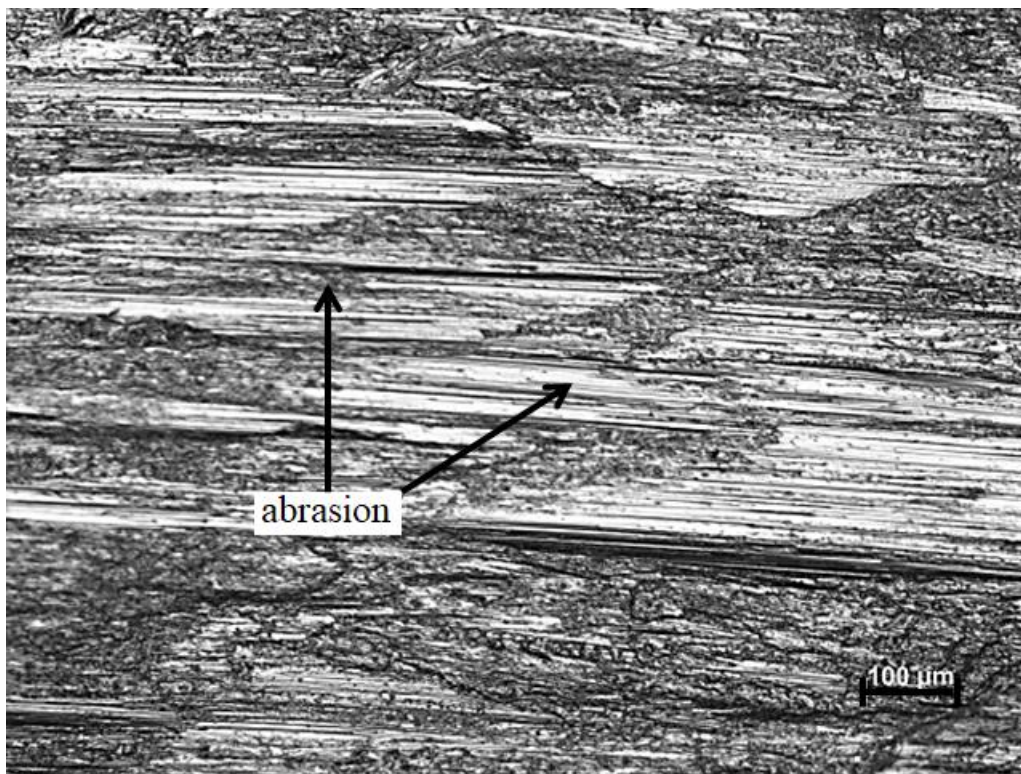sliding speed and at 100 °C temperature.
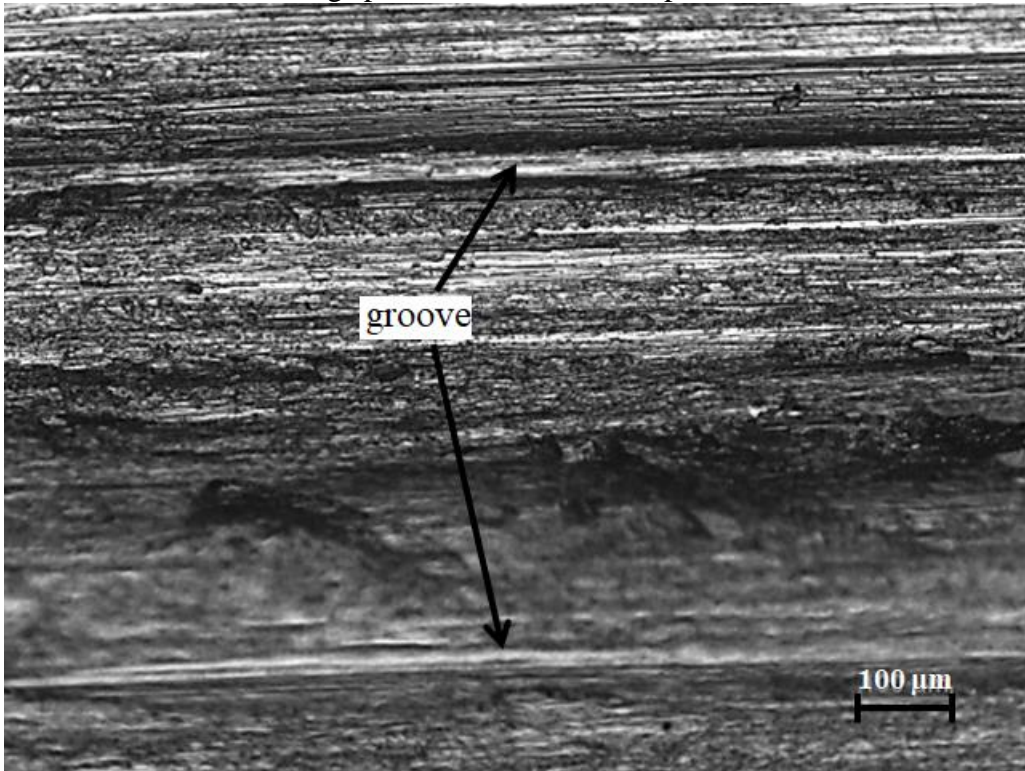
Figure 5.57: Micrograph of worn disk specimen tested at 1 kg normal load, 3 m/s
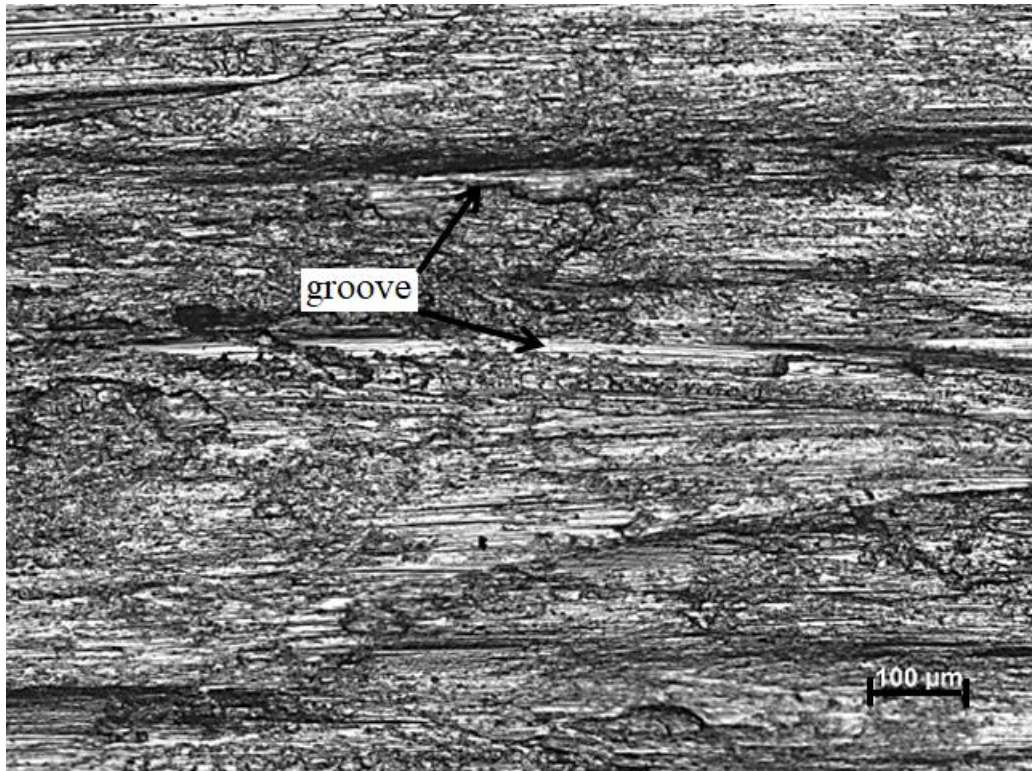sliding speed and at 100 °C temperature.
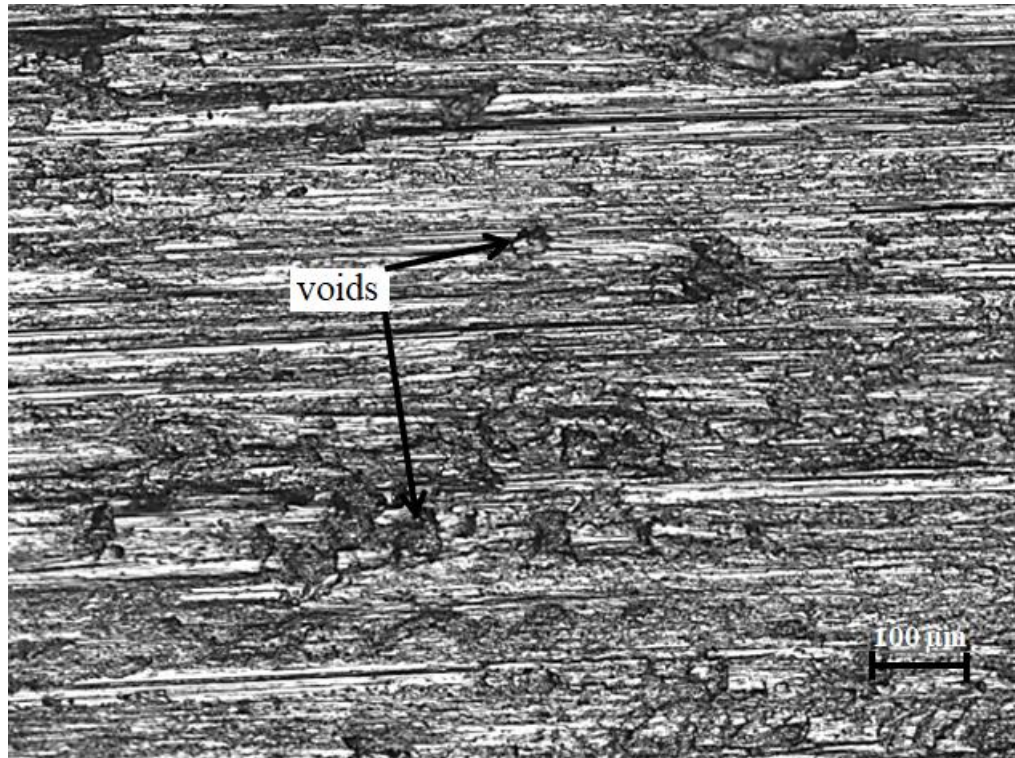
Figure 5.58: Micrograph of worn disk specimen tested at 1.5 kg normal load, 3 m/s sliding speed and at 100 °C temperature.
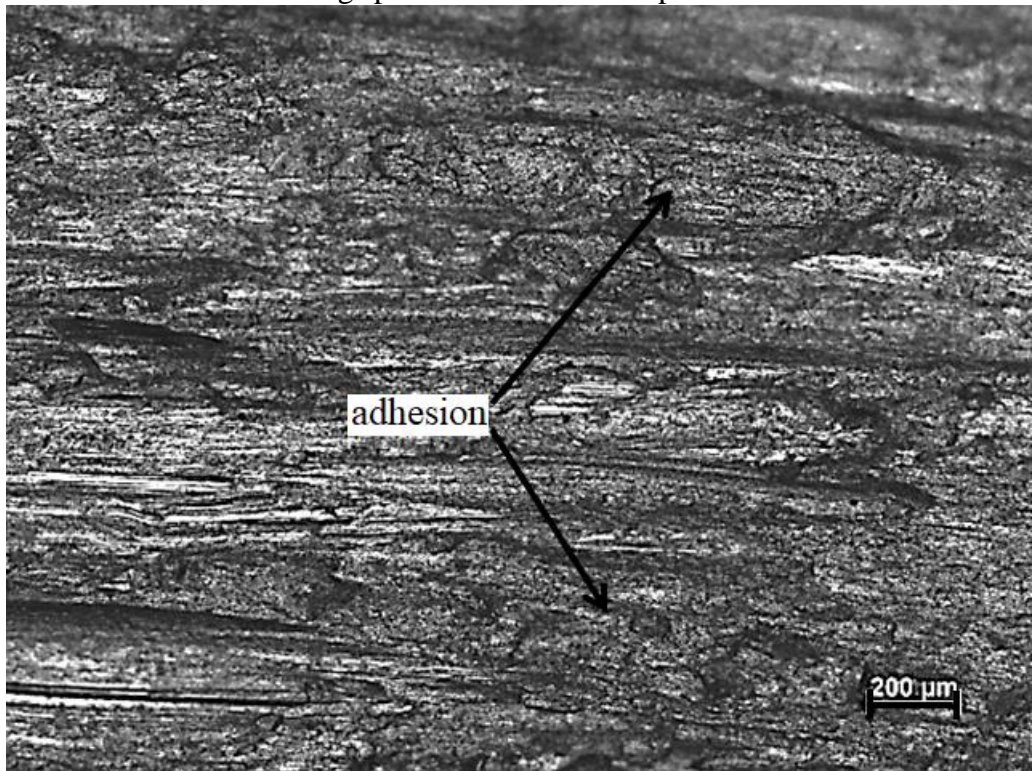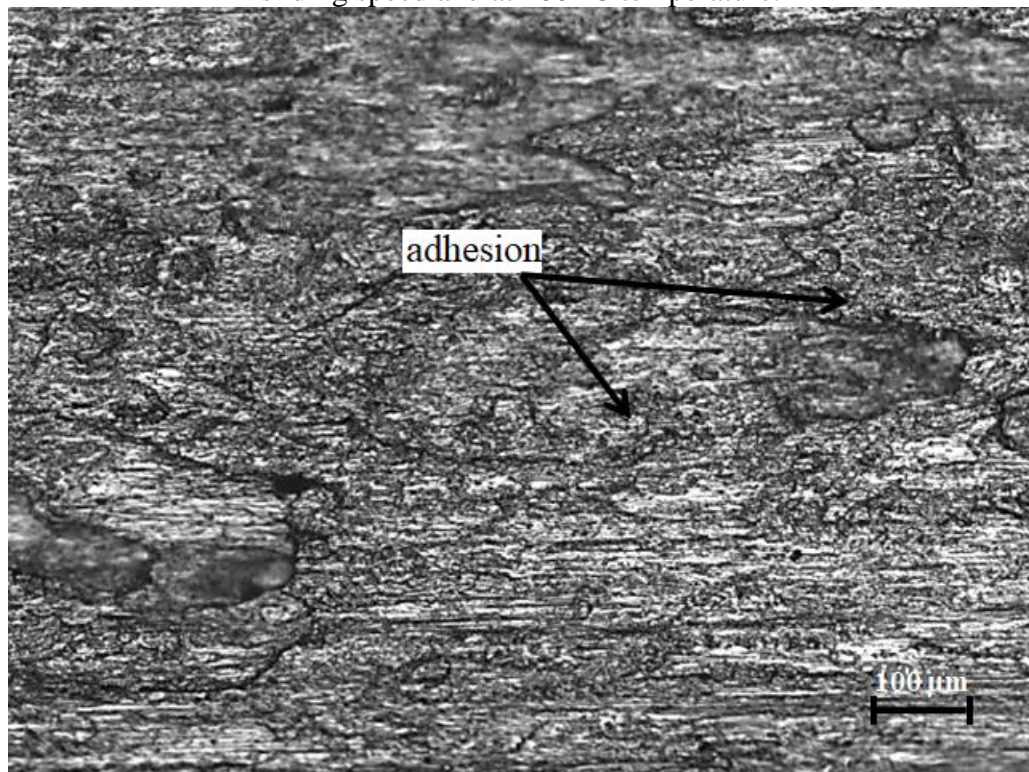

Figure 5.59: Micrograph of worn disk specimen tested at 2 kg normal load, 3 m/s sliding speed and at 100 °C temperature.

Abrasive wear mechanism was dominant at lower normal load (1 kg) conditions at 150 °C temperature (Figure 5.60, Figure 5.63 and Figure 5.66). Voids were observed on the disk surface at a normal load of 1.5 kg and at a sliding speed of 1.25 m/s (Figure 5.61), cracks formed along the sliding direction at 2 m/s sliding speed (Figure 5.64), and craters were formed because of the failure of unstable oxide layers at a sliding speed of 3 m/s (Figure 5.67). The oxide layer on the metal surface was unstable at 2 kg normal load condition, leading to severe adhesive wear mechanism. The adhesive forces at normal load of 2 kg resulted in a stick-slip phenomenon (Vilaseca et al., 2011), which caused more vibrations in tribometer. Consequently, the experiment was untimely stopped at normal load of 2 kg, because of such vibrations in tribometer.
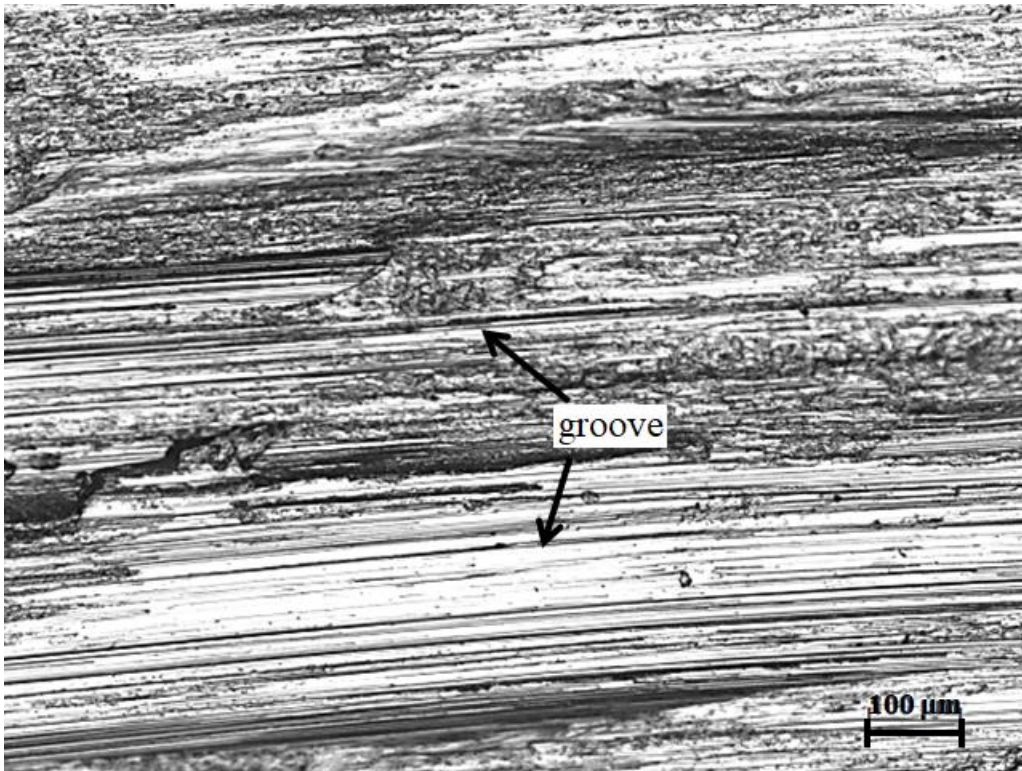
Figure 5.60: Micrograph of worn disk specimen tested at 1 kg normal load, 1.25 m/s sliding speed and at 150 °C temperature.
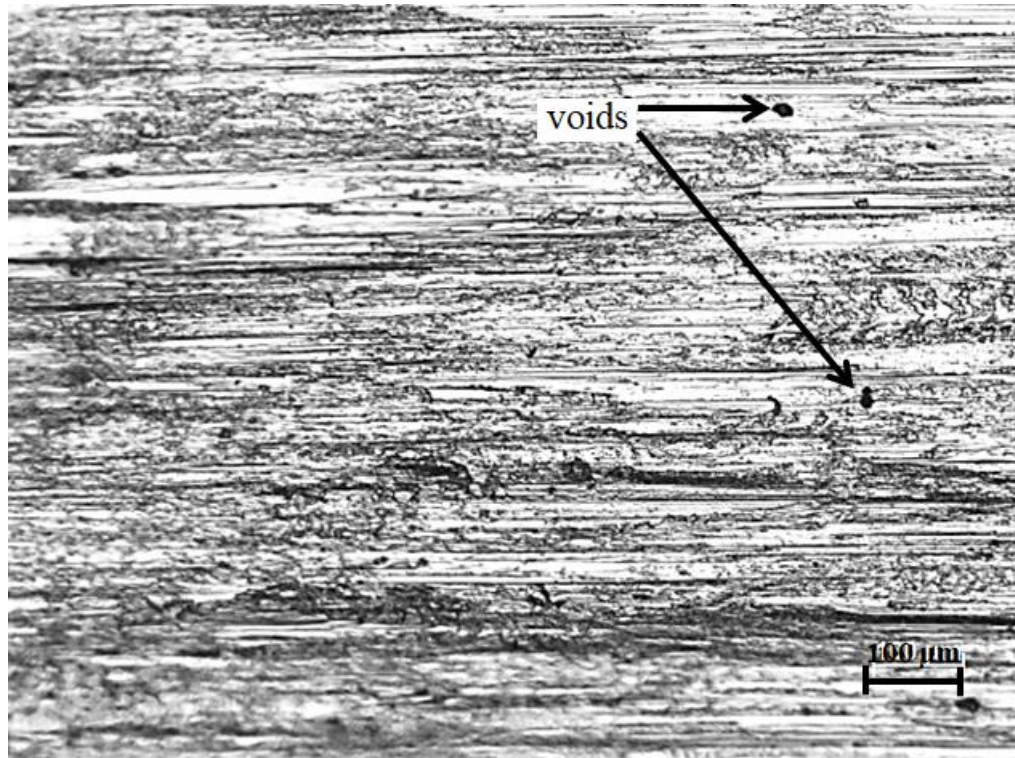
Figure 5.61: Micrograph of worn disk specimen tested at 1.5 kg normal load, 1.25 m/s sliding speed and at 150 °C temperature.
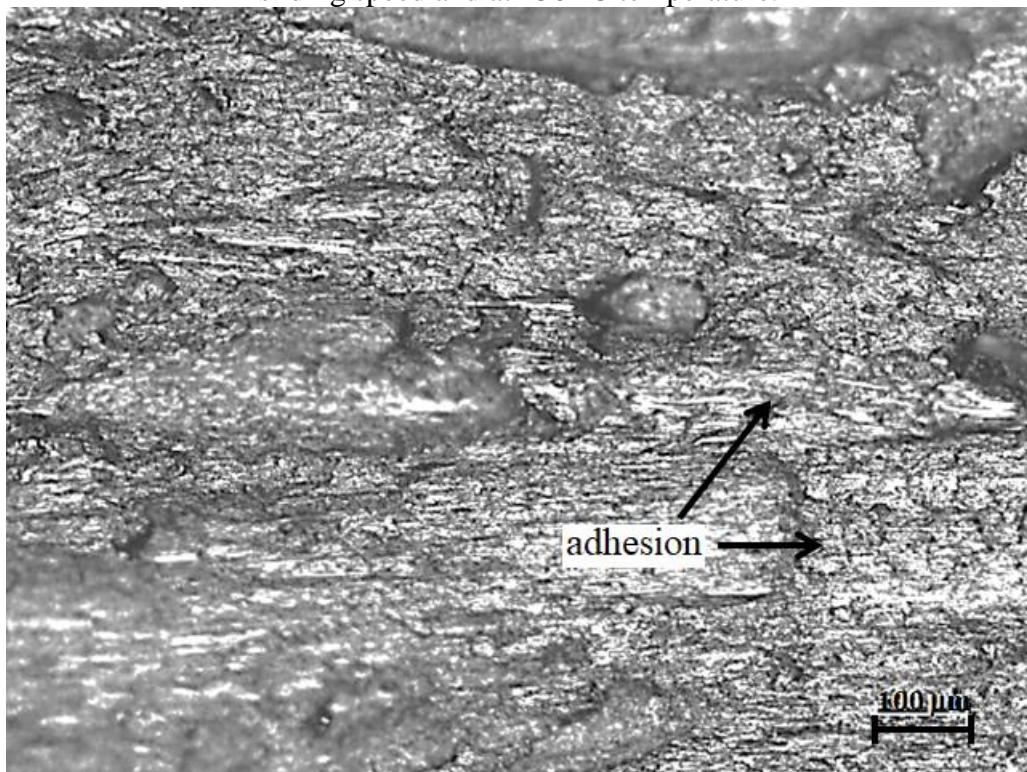
Figure 5.62: Micrograph of worn disk specimen tested at 2 kg normal load, 1.25 m/s sliding speed and at 150 °C temperature.
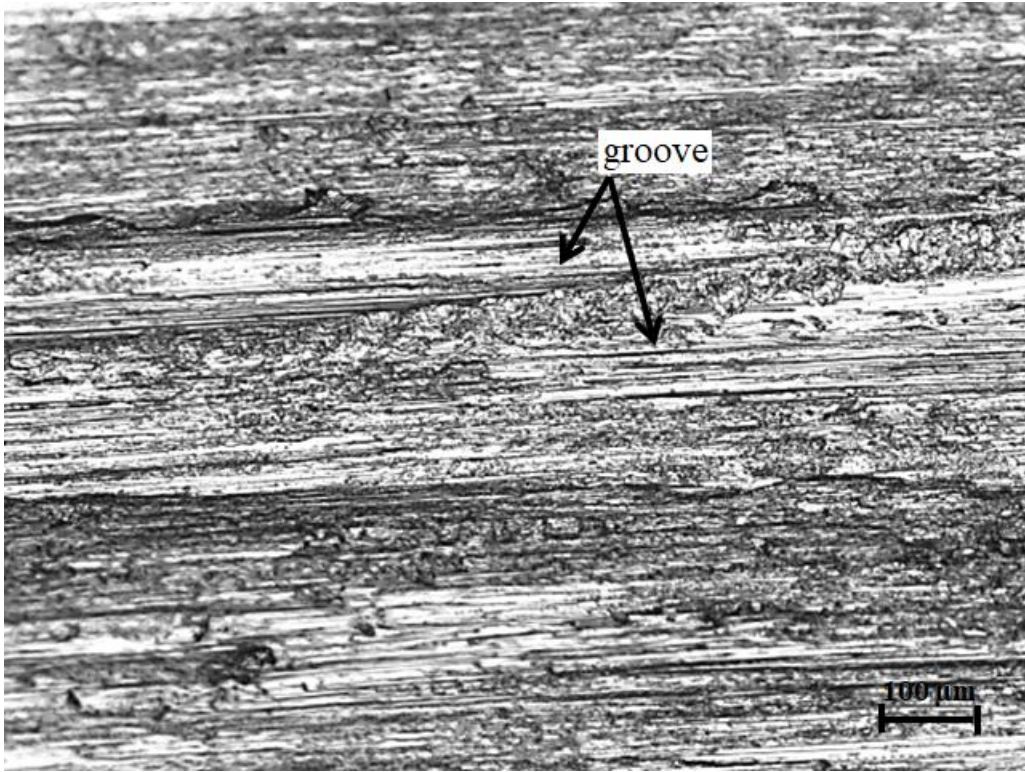
Figure 5.63: Micrograph of worn disk specimen tested at 1 kg normal load, 2 m/s sliding speed and at 150 °C temperature.
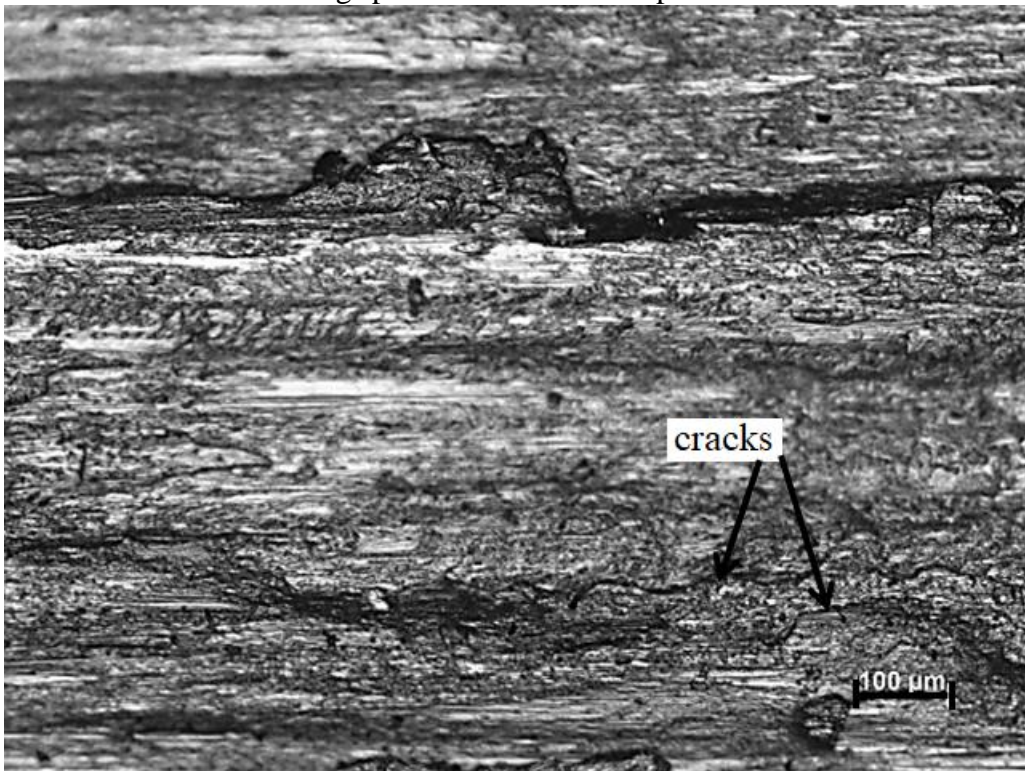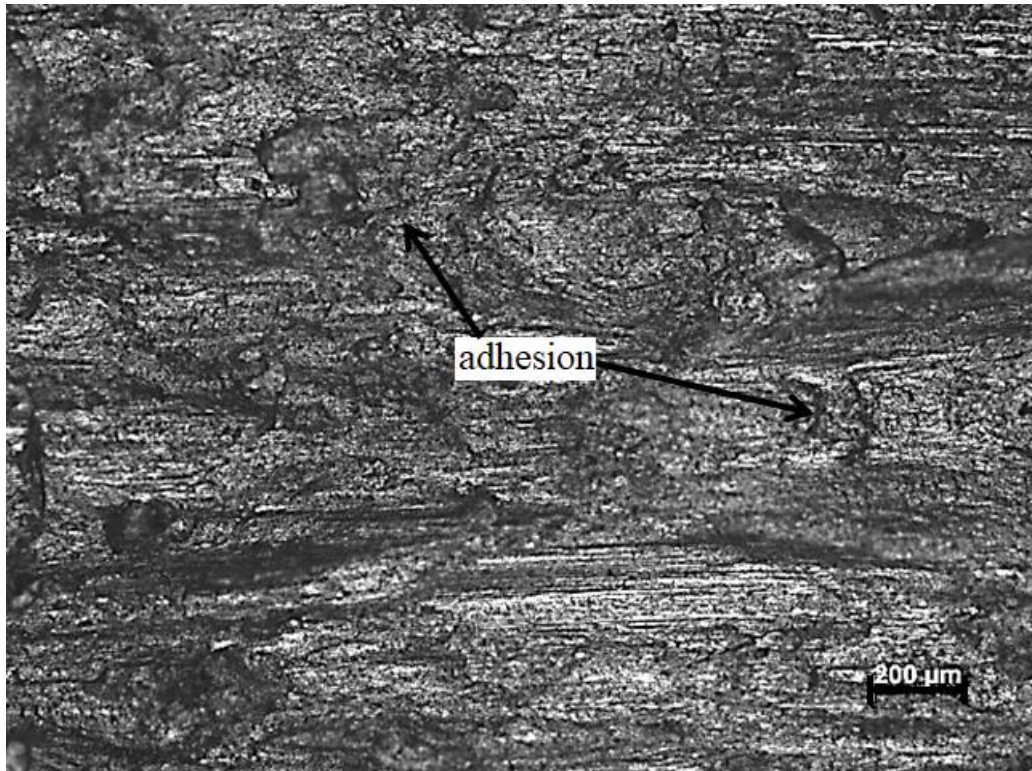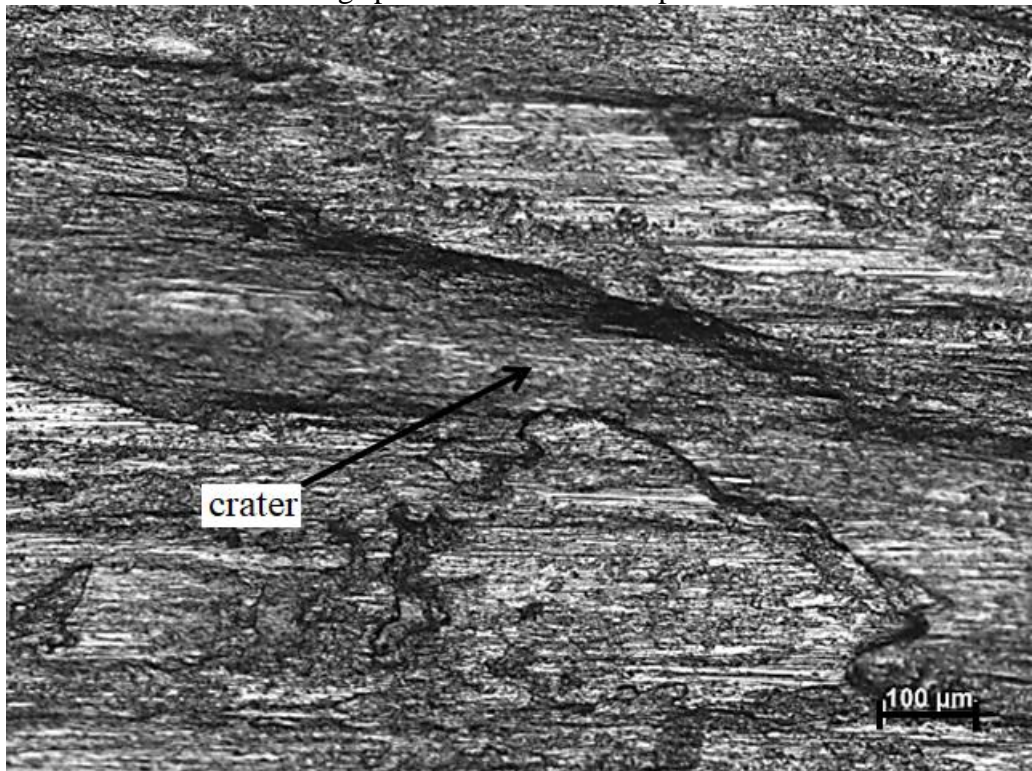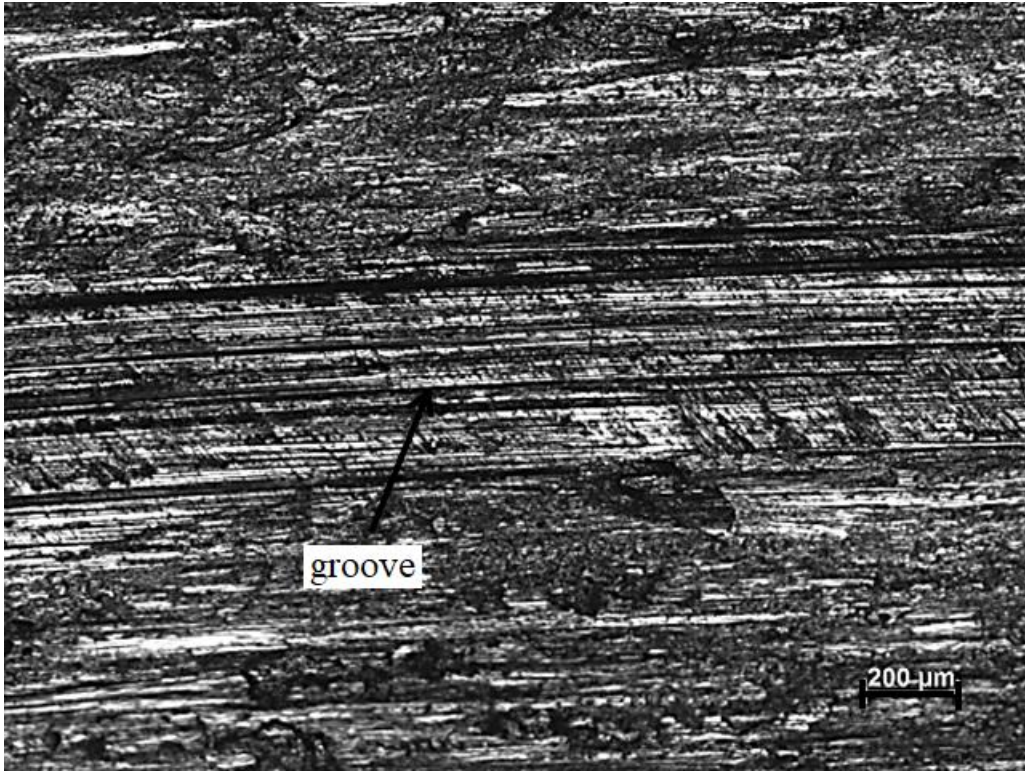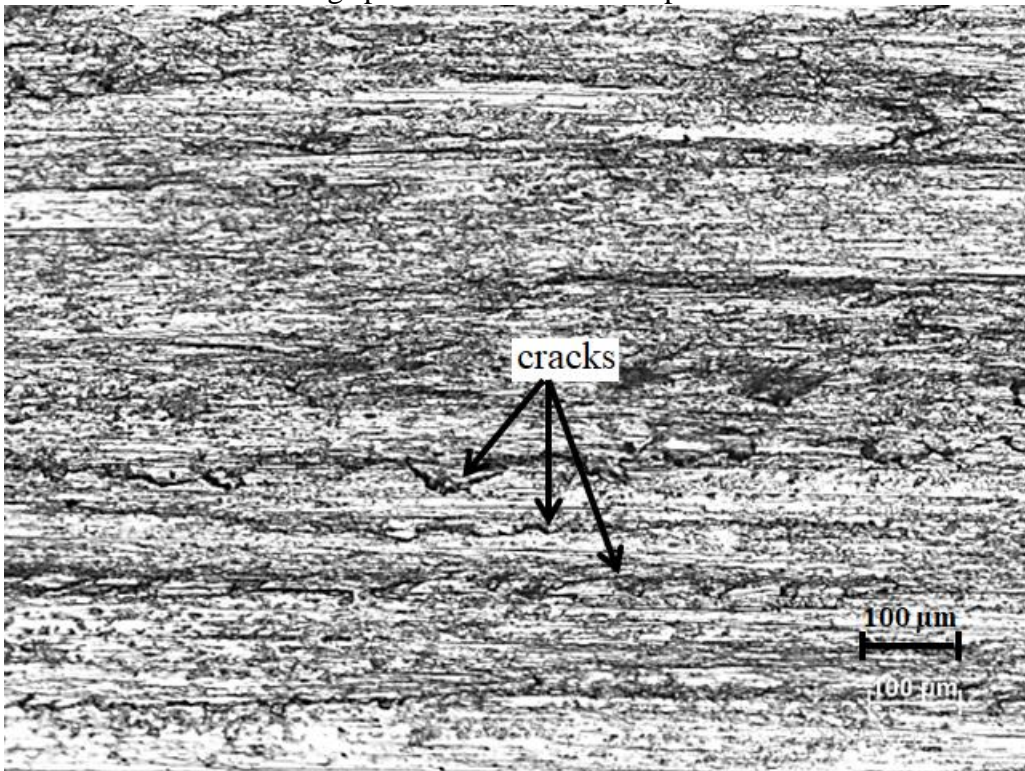

Figure 5.64: Micrograph of worn disk specimen tested at 1.5 kg normal load, 2 m/s sliding speed and at 150 °C temperature.

114
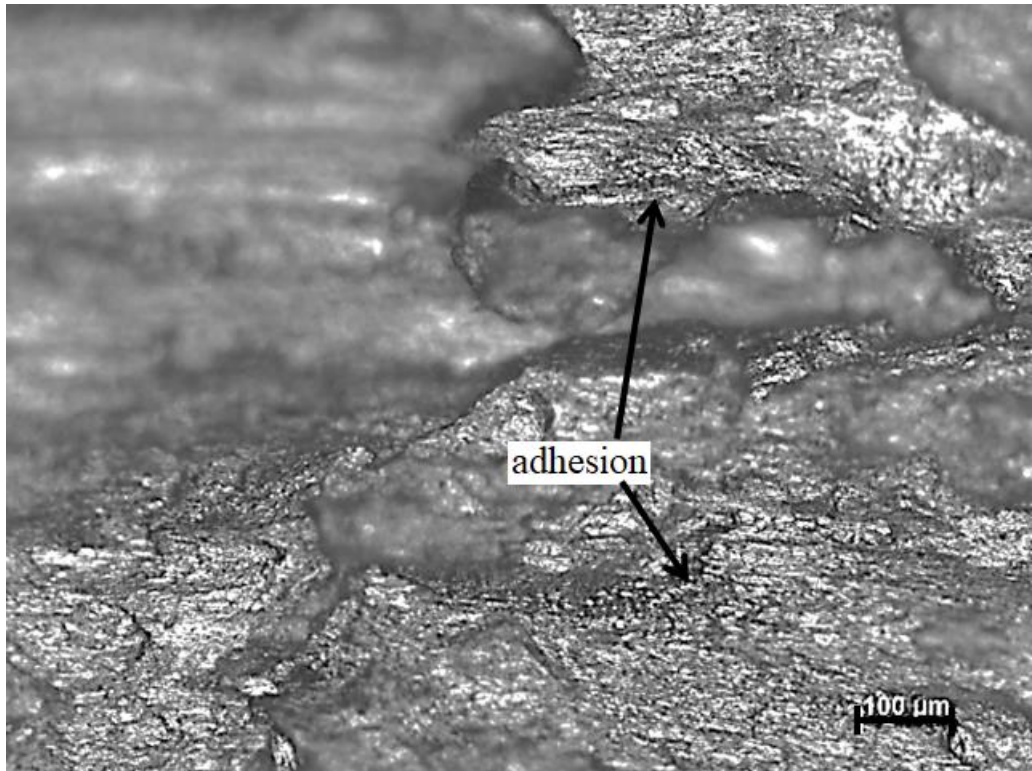
Figure 5.65: Micrograph of worn disk specimen tested at 2 kg normal load, 2 m/s sliding speed and at 150 °C temperature.
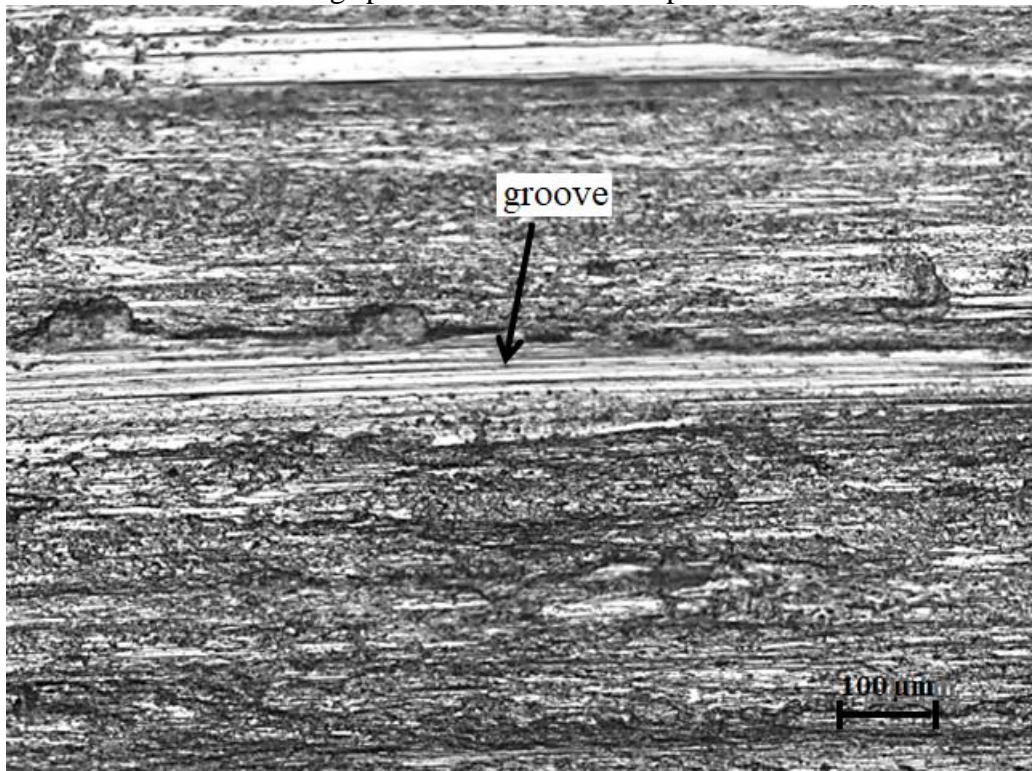
Figure 5.66: Micrograph of worn disk specimen tested at 1 kg normal load, 3 m/s sliding speed and at 150 °C temperature.
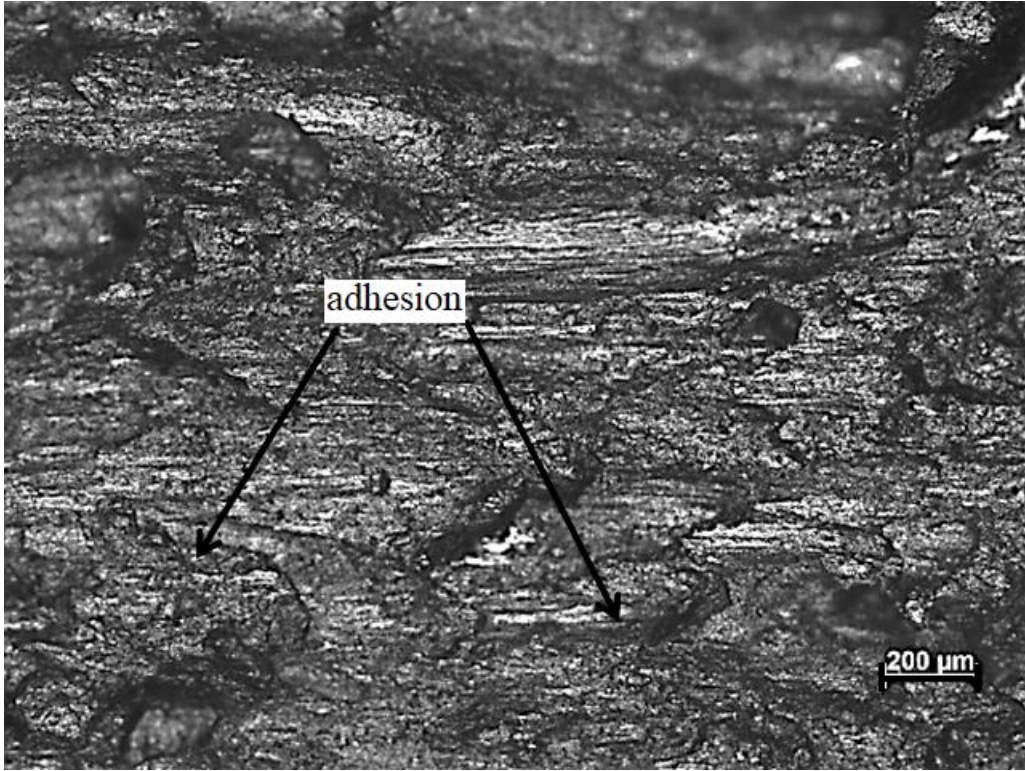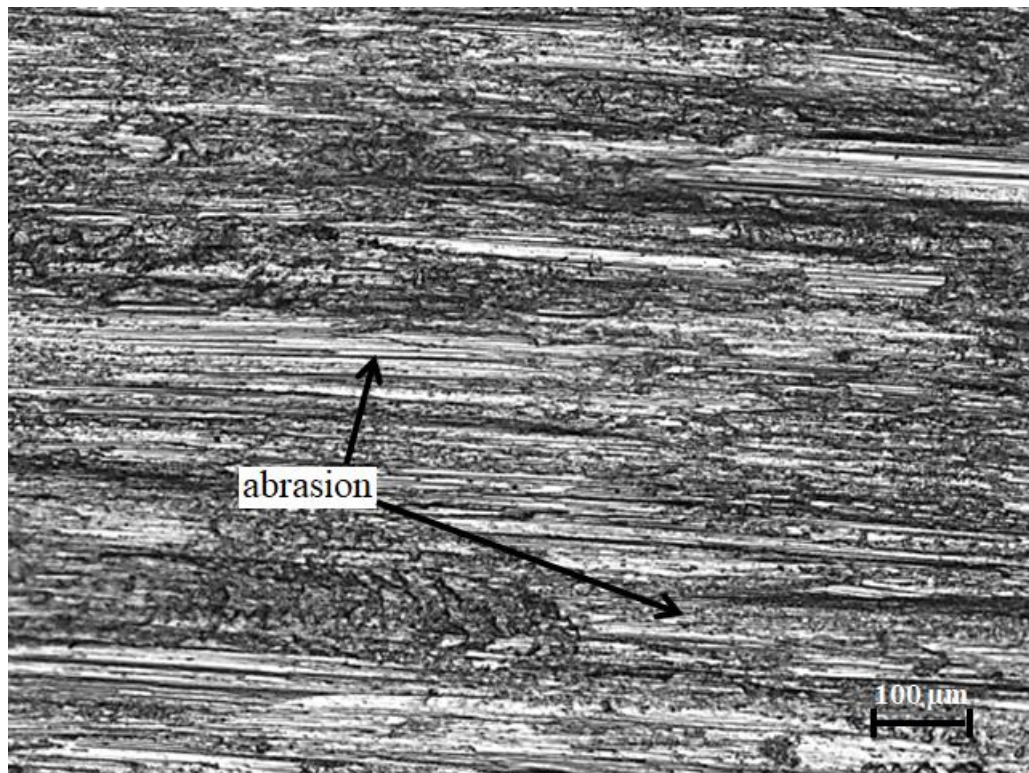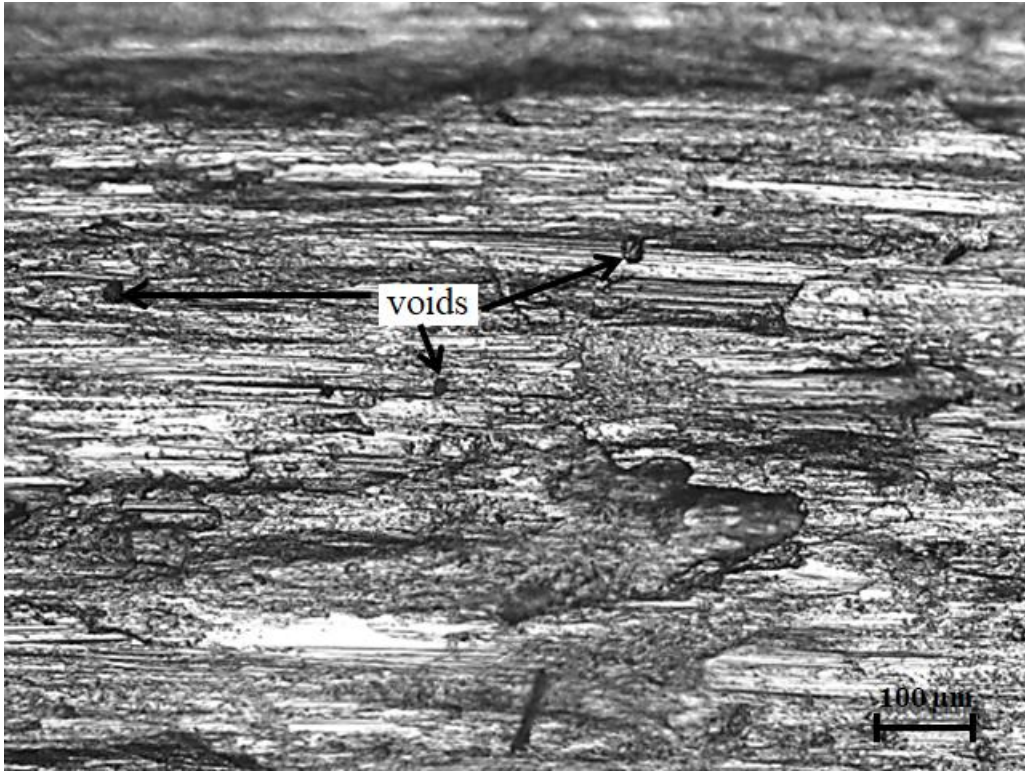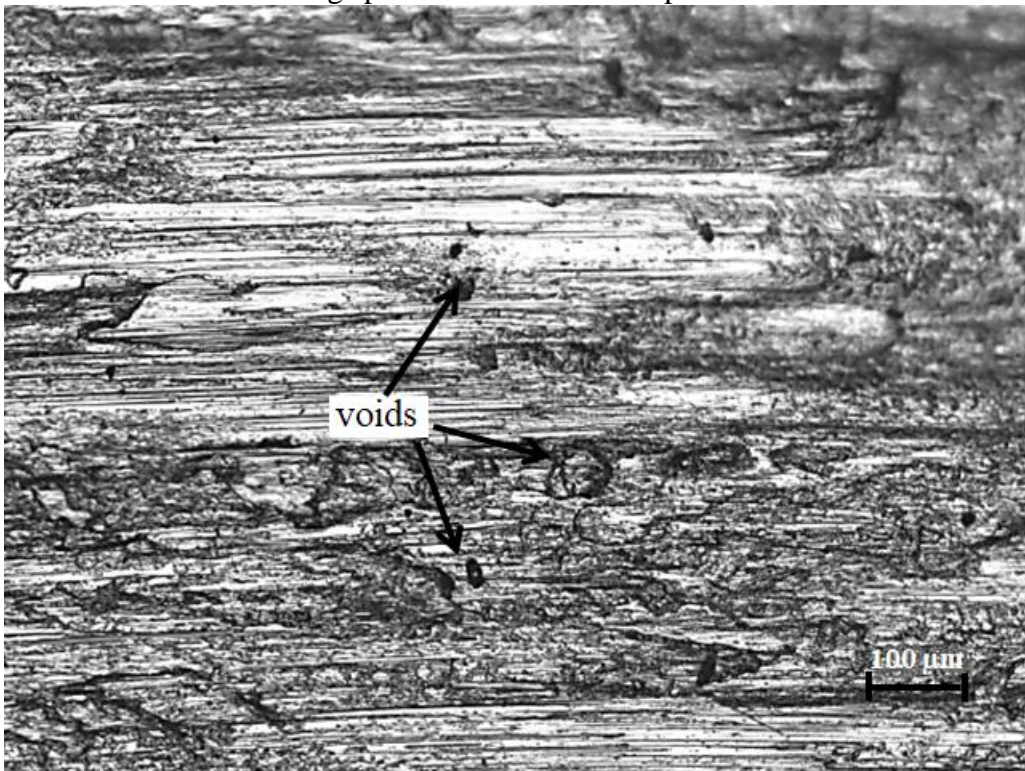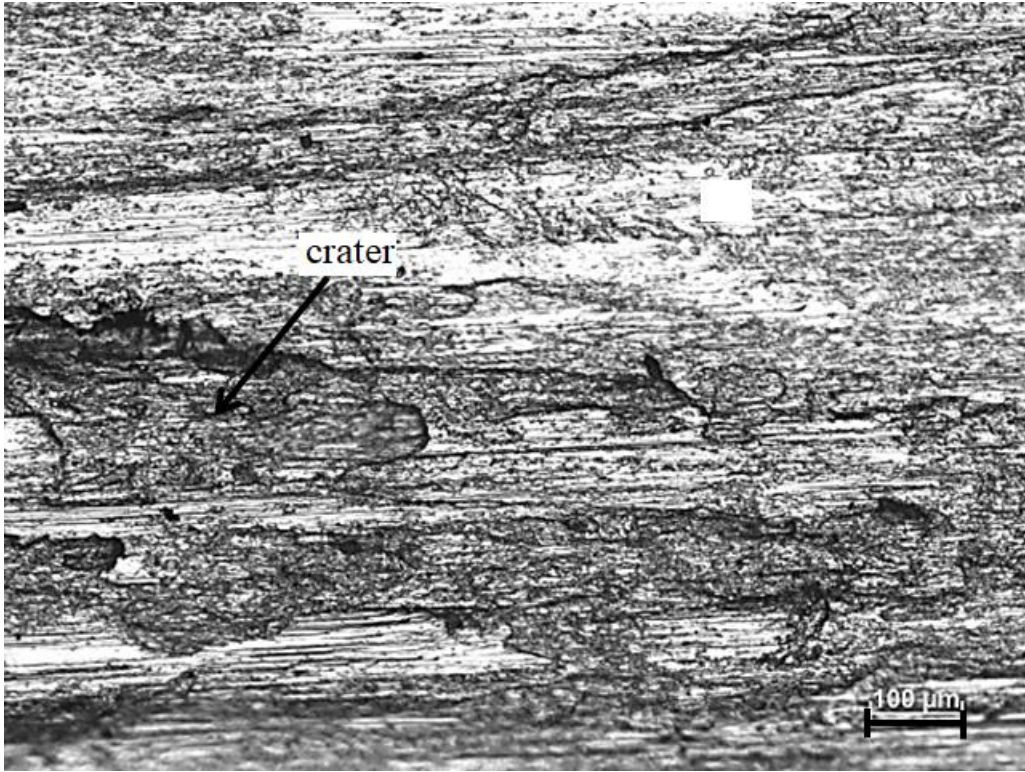
Figure 5.67: Micrograph of worn disk specimen tested at 1.5 kg normal load, 3 m/s sliding speed and at 150 °C temperature.

5.3.3 Wear of Al 6061-T6

In ductile materials like Aurum, Silver, Lead, Tin etc. adhesive wear mechanism was dominant and the abrasive wear mechanism was due to interaction of harder material particles at contact interface (Morton Antler, 1981). From the microscopic observations of worn surfaces of disk specimen, major wear mechanisms involved in dry sliding of Al 6061-T6 alloy were adhesive wear and abrasive wear. Adhesive wear was identified by deposition of transferred material from one body to another body or severe plastic deformation of contact surface (Figure 5.39). The contact surface oxidizes due to higher frictional heat or environment temperature at contact interface. During sliding of contact surfaces the oxide layer losses its stability due to contact tractions and results in metal oxide debris. The harder metal oxide debris compacts into the contact surfaces during sliding. The compacted metal oxide debris results in formation of grooves on disk surfaces which was identified as abrasive wear. Figure 5.66 represents the grooves on disk specimen due to abrasive wear at

116

150 °C temperature condition. In this study, wear process in Al 6061-T6 alloy contacts is explained using prow mechanism and the schematic picture of prow process in ductile materials is given in Figure 5.68. When two fresh metal surfaces are sliding against each other, prow at contact interface grows due to plastic deformation of contact asperities and accumulation of removed contact asperities from contact surfaces at front side of sliding contact. Over a period of sliding, the prow grows to several micrometres thickness and removes from the contact interface due to lack of resistance of prow layer to shear tractions at contact interface. The removed prow results in debris formation and fresh metal contacts at contact interface. The cycle of prow process repeats and wear at contact interface progresses. The wear of metallic contacts depends on several parameters like normal load, sliding speed, surface condition, temperature etc.
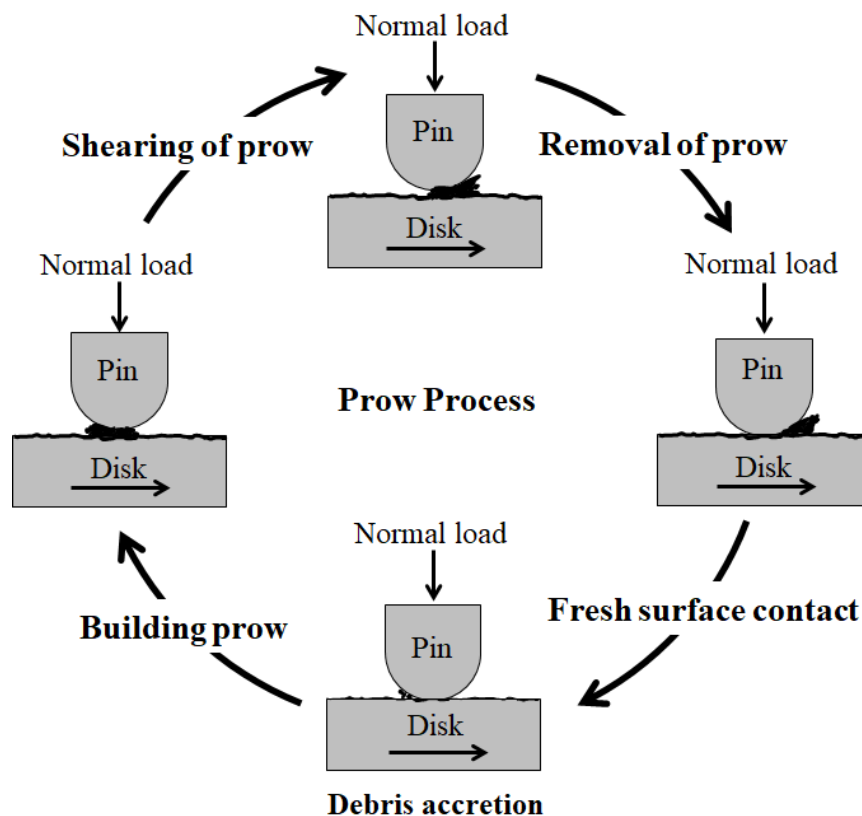
Figure 5.68: Schematic of prow formation process. Horizontal arrow represents direction of disk movement.

Researchers (Giovanni Straffelini & Alberto Molinari, 2011; Uthayakumar et al., 2013) calculated the wear volume from the wear height data measured using LVDT in

117

wear testing machine and the cross-section area of pin specimen. Most of the researchers used softer material as pin specimen and harder material (steel) as disk specimen. The present study focused on wear characteristics of aluminium to aluminium contacts, so the pin and disk specimens were fabricated using Al 6061-T6 alloy. Due to prow formation and deposition of wear material on contact surfaces of both pin and disk the wear height data obtained from LVDT attached to tribometer resulted in negative wear in all the experimental cases. Figure 5.69 shows the wear height (in microns) data measured using LVDT during the experiments conducted at room temperature. At room temperature condition, no significant change in the wear height data was observed up to 400 m of sliding distance at 1 kg normal load and 1.25 m/s sliding speed as the wear rate and deposition of wear debris remained same. After 400 m of sliding speed, the sudden drop in wear height was due to higher wear debris deposition rate at contact interface. At normal load of 1.5 kg & 2 kg and sliding speed of 2 m/s & 3 m/s, both increasing and decreasing trends of wear height were observed due to oxidation and removal of oxide layer from metal surfaces over a period of time. In Figure 5.69 (d), flattening of wear height data at 350 m sliding distance was due to limitation of LVDT, the LVDT can measure wear height data ranging from +2000 µm to -2000 µm. At sliding speed 3 m/s and normal loads 1.5 kg & 2 kg, positive wear height was observed due to severe plastic deformation and removal of material from contact surfaces. Figure 70, Figure 71 and Figure 72 show the wear height data at 60 °C temperature, 100 °C temperature and 150 °C temperature experimental conditions respectively. At higher temperatures, increasing and decreasing trends in wear height was due to formation and removal of oxide layers during sliding. At 60 °C temperature & 150 °C temperature and 2 kg normal load conditions wear experiments were stopped at early stage due to more vibration in loading arm of wear testing machine. The more vibration in loading arm was due to severe plastic deformation of contact surfaces.
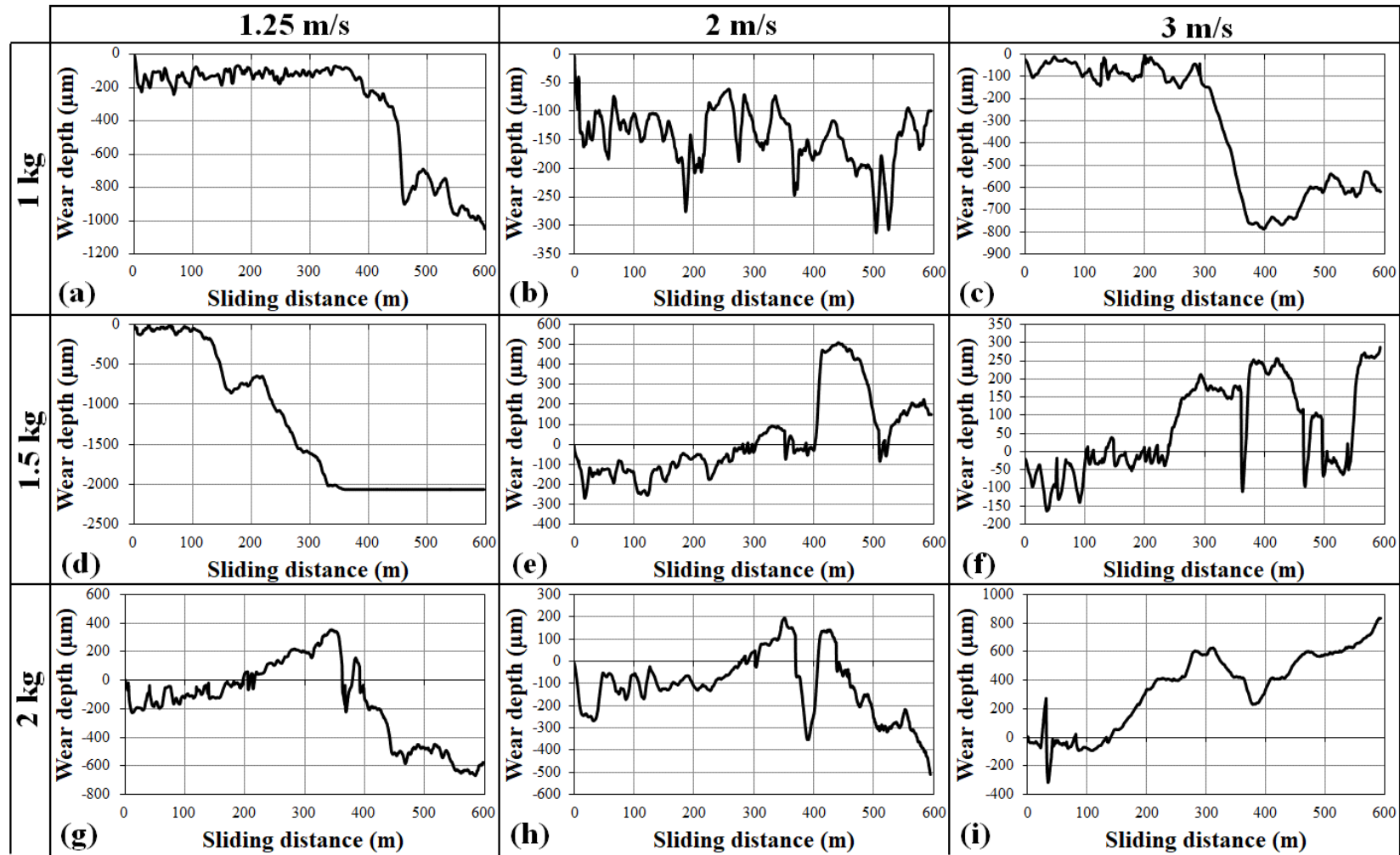
Figure 5.69: Wear of Al 6061-T6 alloy at room temperature under different loading conations.
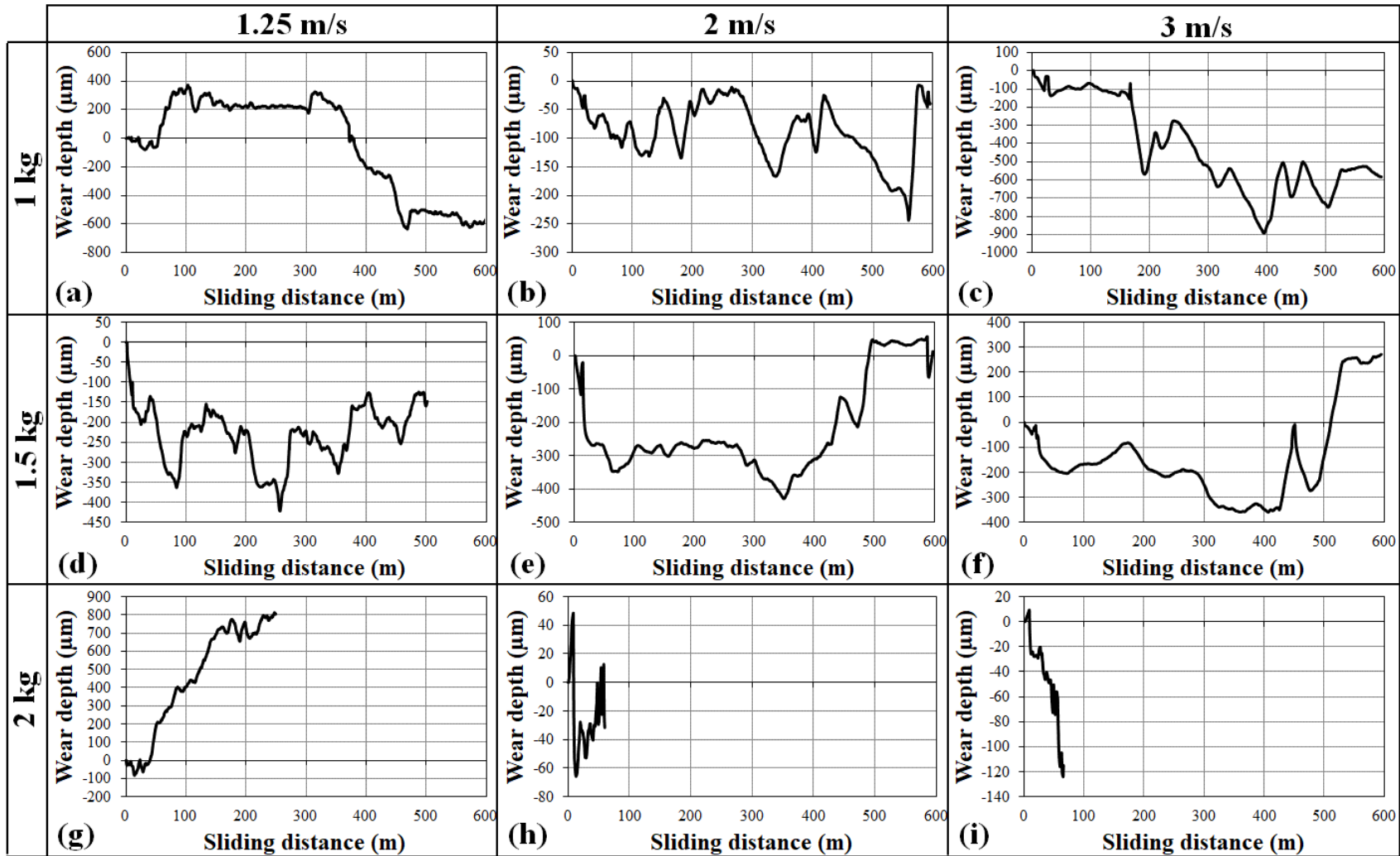
Figure 5.70: Wear of Al 6061-T6 alloy at 60 °C temperature under different loading conations.
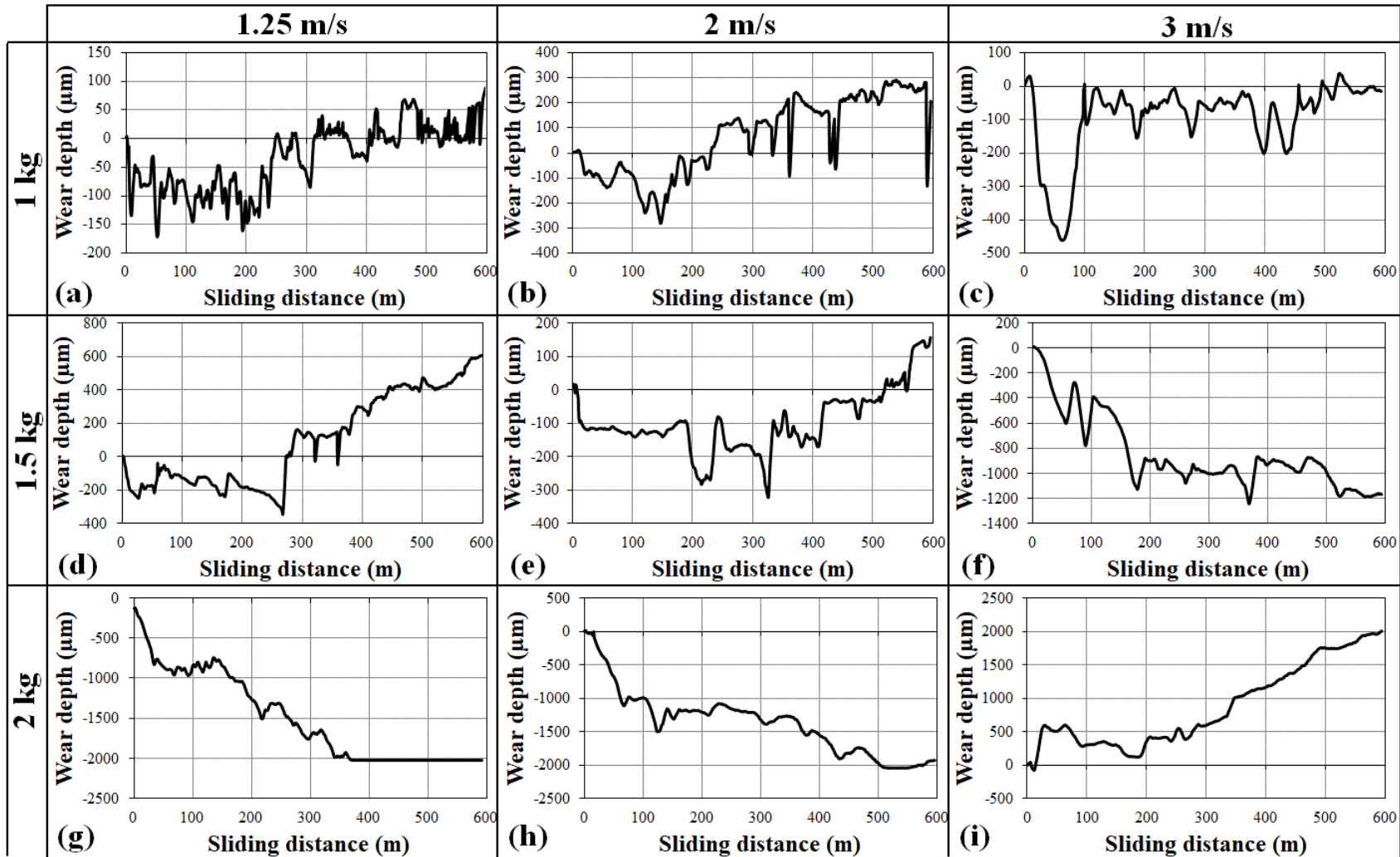
Figure 5.71: Wear of Al 6061-T6 alloy at 100 °C temperature under different loading conations.

121
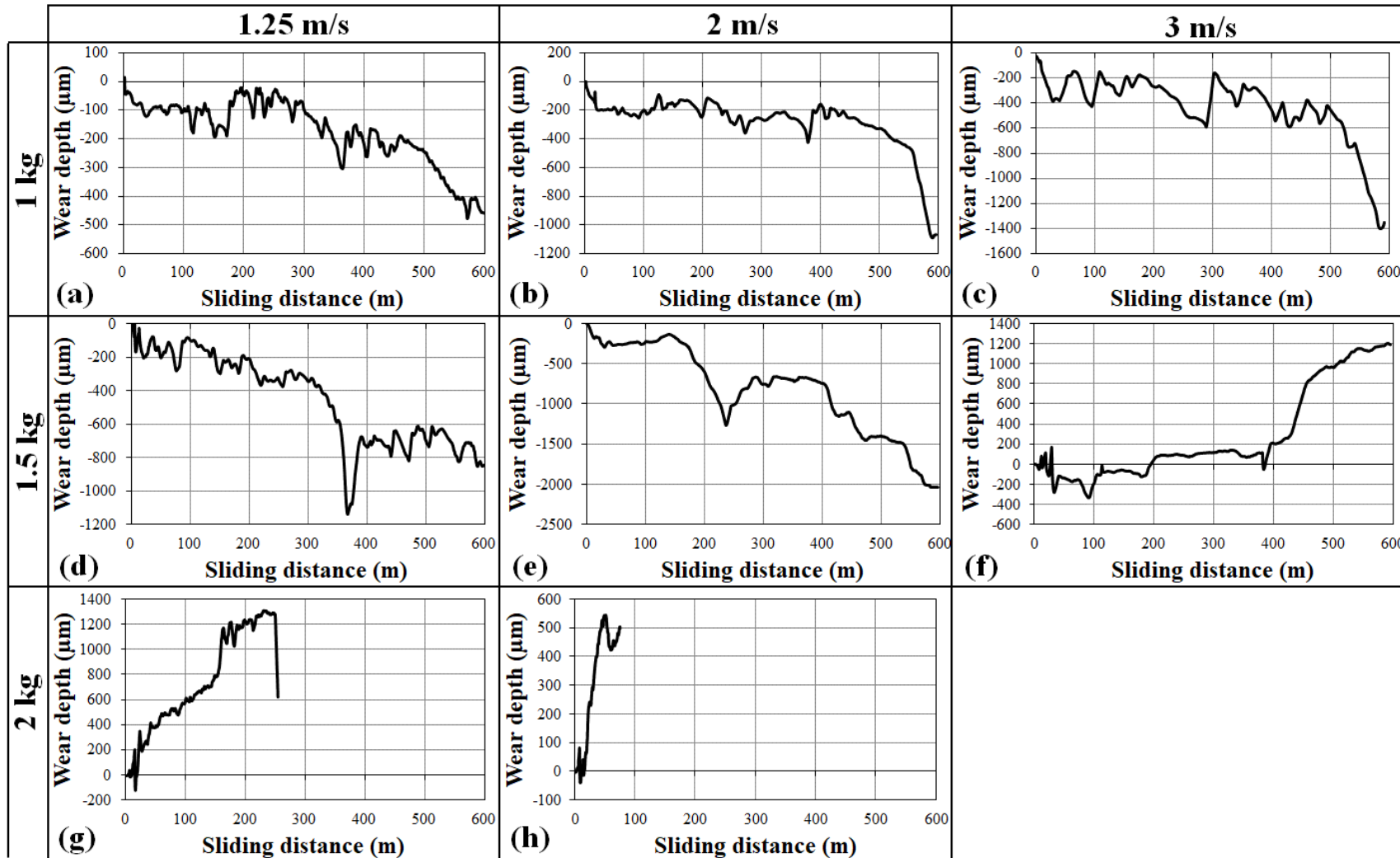
Figure 5.72: Wear of Al 6061-T6 alloy at 150 °C temperature under different loading conations.

The weight of pin specimens was measured before conducting experiments and after the experiments to calculate mass loss due to wear. Weighing machine having least count of 0.001 g was used for the study. The ratio of weight loss of pin and sliding distance of pin during each experiment is considered as wear rate (mass/unit distance) in this study. The wear rate of Al 6061-T6 alloy at room temperature, 60 °C temperature, 100 °C temperature and 150 °C temperature conditions are given in Figure 8. At room temperature, at a particular sliding speed wear rate increased with increase in normal load (Figure 5.73). From the wear debris obtained from the experiments conducted at room temperature, size of the wear debris increased with increase in normal load (Figure 5.77 – Figure 5.85). The larger wear debris is the evidence for the higher wear rate at a 2 kg normal load condition (Al-Qutub, 2013; Wen Gao et al., 2018). At higher normal load, wear rate was more due to direct metal to metal contact which is having less hardness than the metal oxides (Like Pan et al., 2017). Wear rate decreased with increase in sliding speed from 1.25 m/s to 2 m/s and the wear rate increased at sliding speed 3 m/s. At 1 kg normal load and 2 m/s sliding speed, zero wear rate was observed due to deposition of wear debris on pin specimen. The cross-section of wear pins at room temperature conditions are given in Figure 5.86 (a-c).
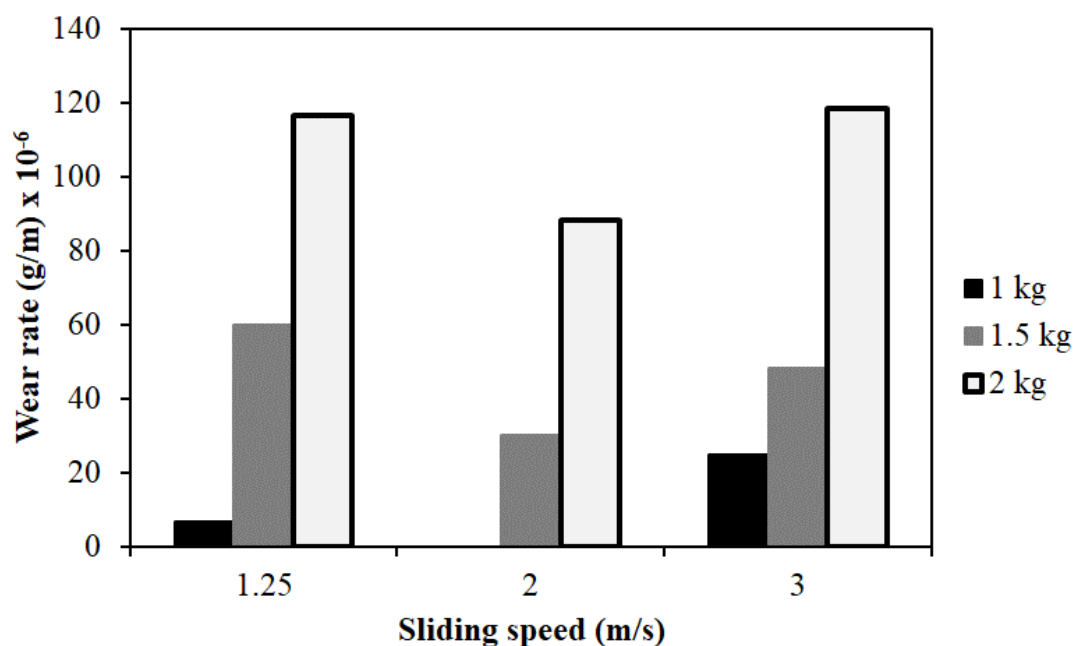
Figure 5.73: Wear rate of Al 6061-T6 alloy at room temperature.
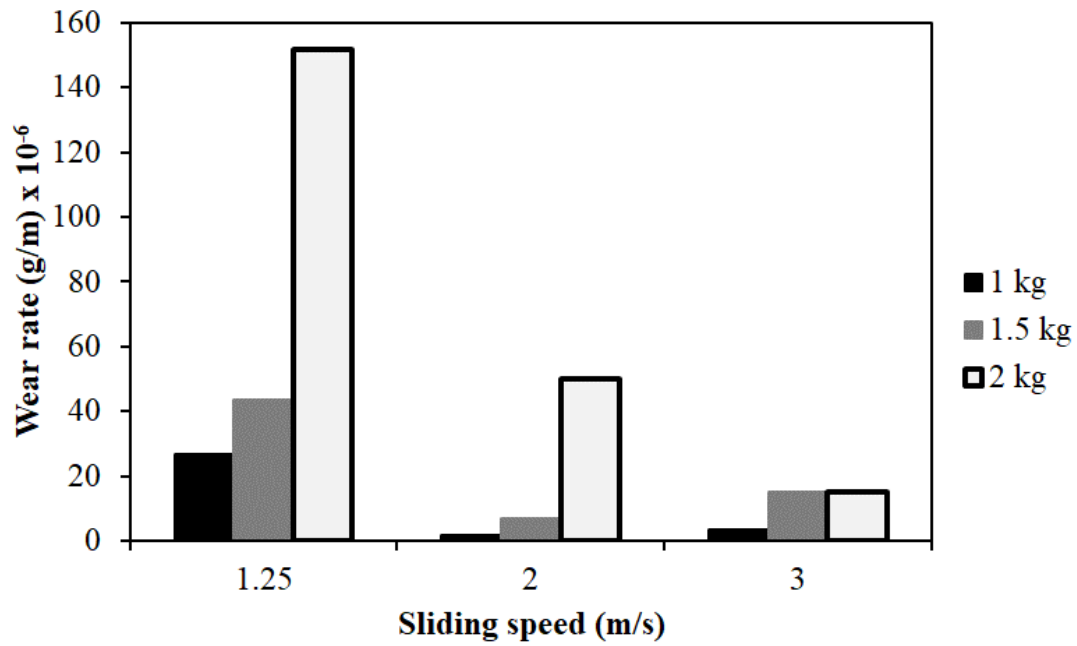
Figure 5.74: Wear rate of Al 6061-T6 alloy at 60 °C temperature.
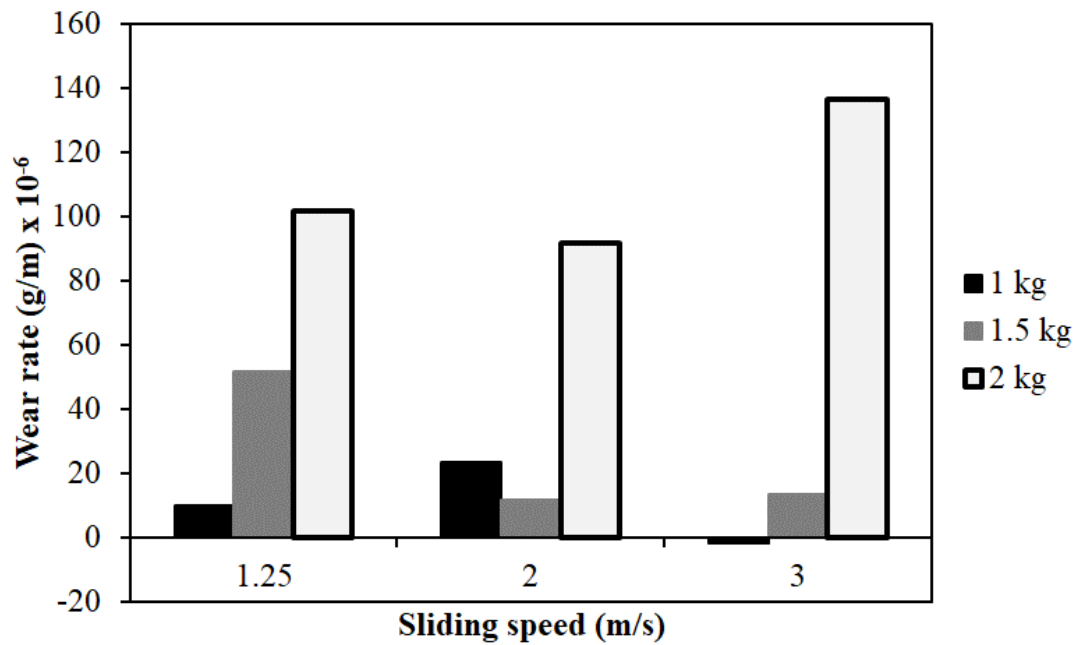
Figure 5.75: Wear rate of Al 6061-T6 alloy at 100 °C temperature.
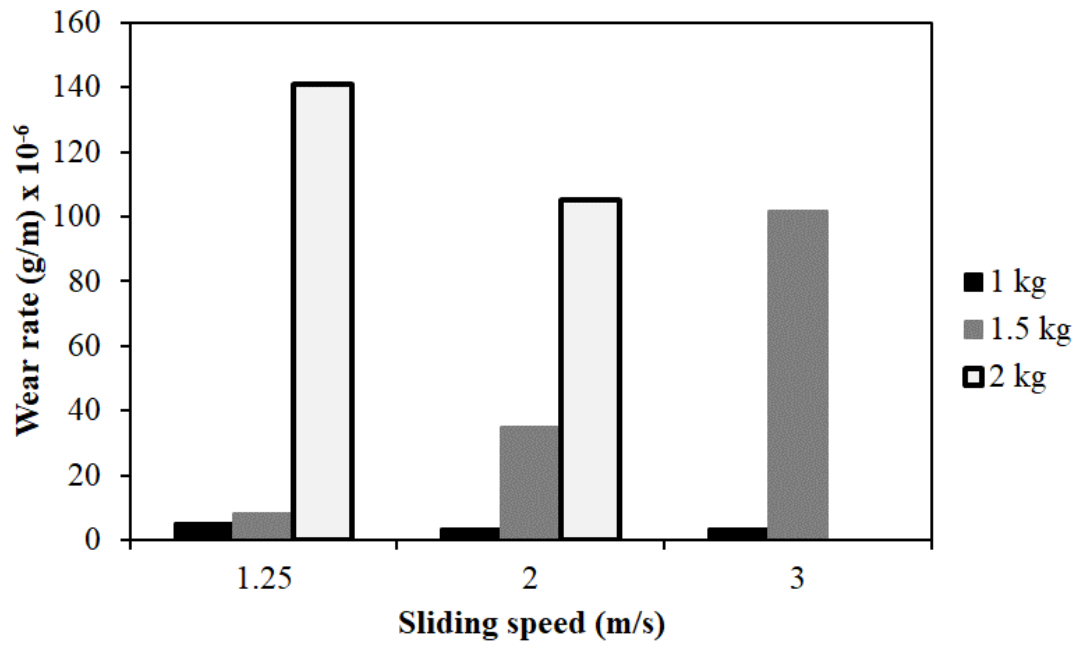
Figure 5.76: Wear rate of Al 6061-T6 alloy at 150 °C temperature.
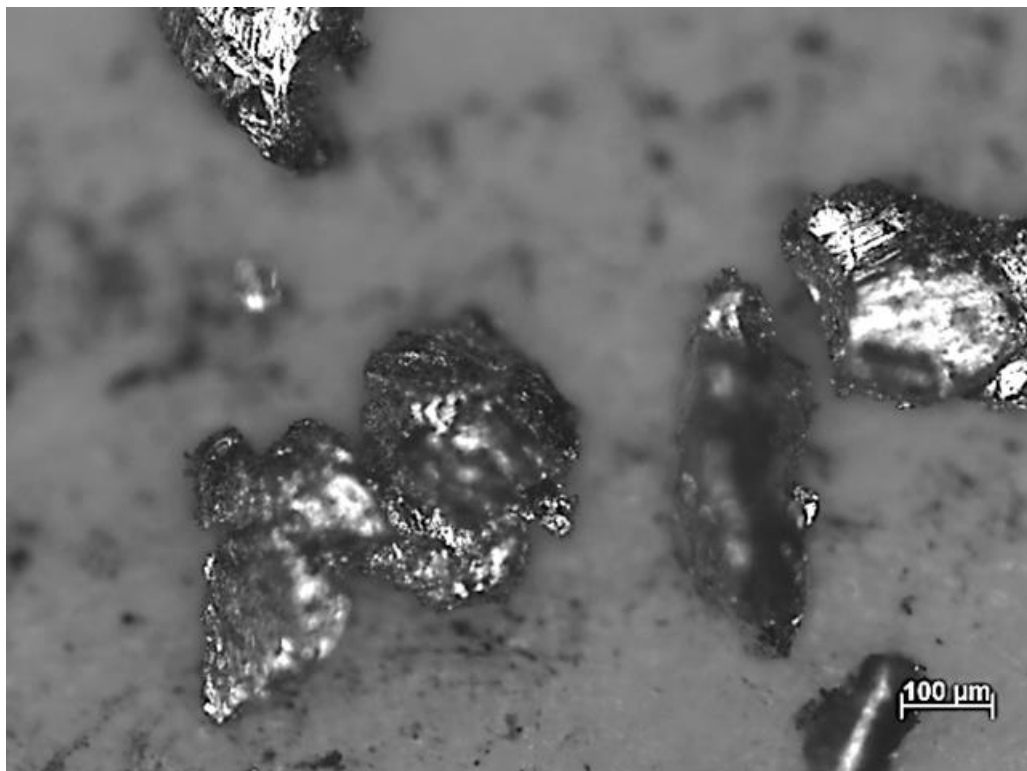
Figure 5.77: Micrograph of wear debris collected from experiments conducted at 1 kg normal load, 1.25 m/s sliding speed and at room temperature.
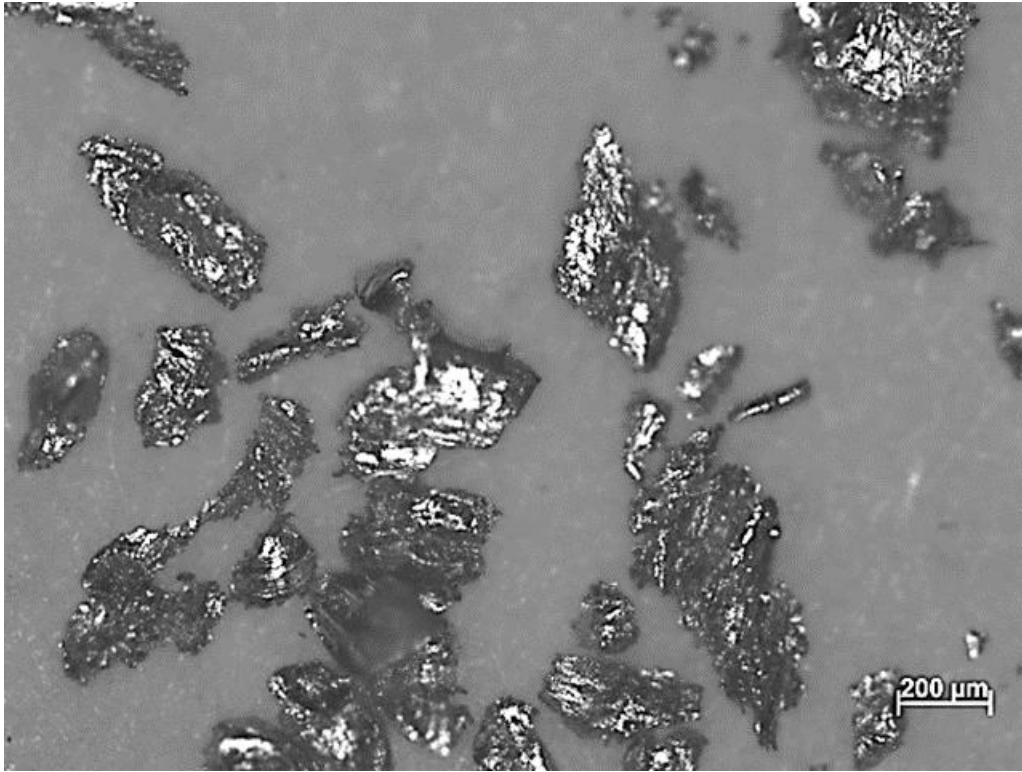
Figure 5.78: Micrograph of wear debris collected from experiments conducted at 1.5 kg normal load, 1.25 m/s sliding speed and at room temperature.
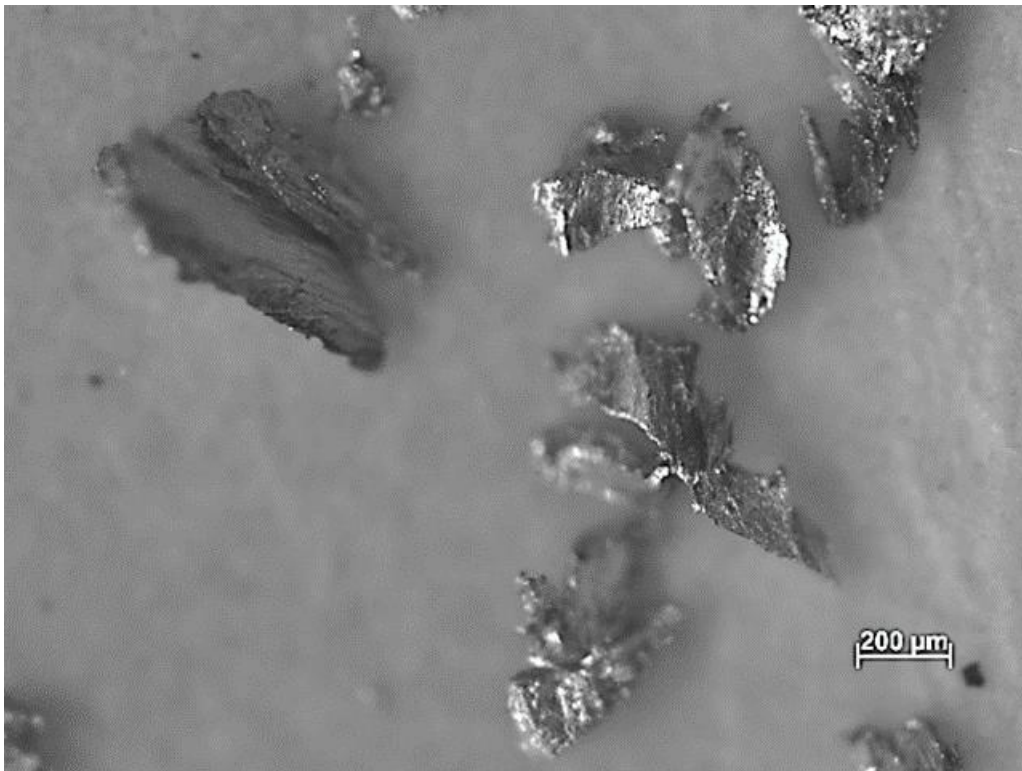
Figure 5.79: Micrograph of wear debris collected from experiments conducted at 2 kg normal load, 1.25 m/s sliding speed and at room temperature.
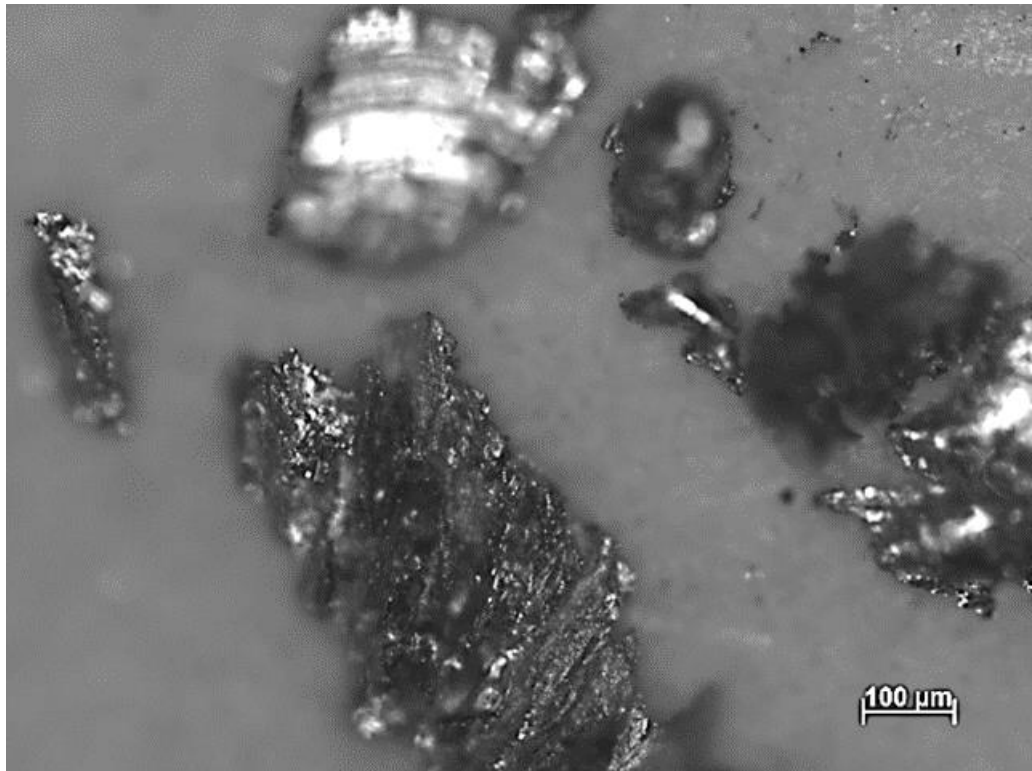
Figure 5.80: Micrograph of wear debris collected from experiments conducted at 1 kg normal load, 2 m/s sliding speed and at room temperature.
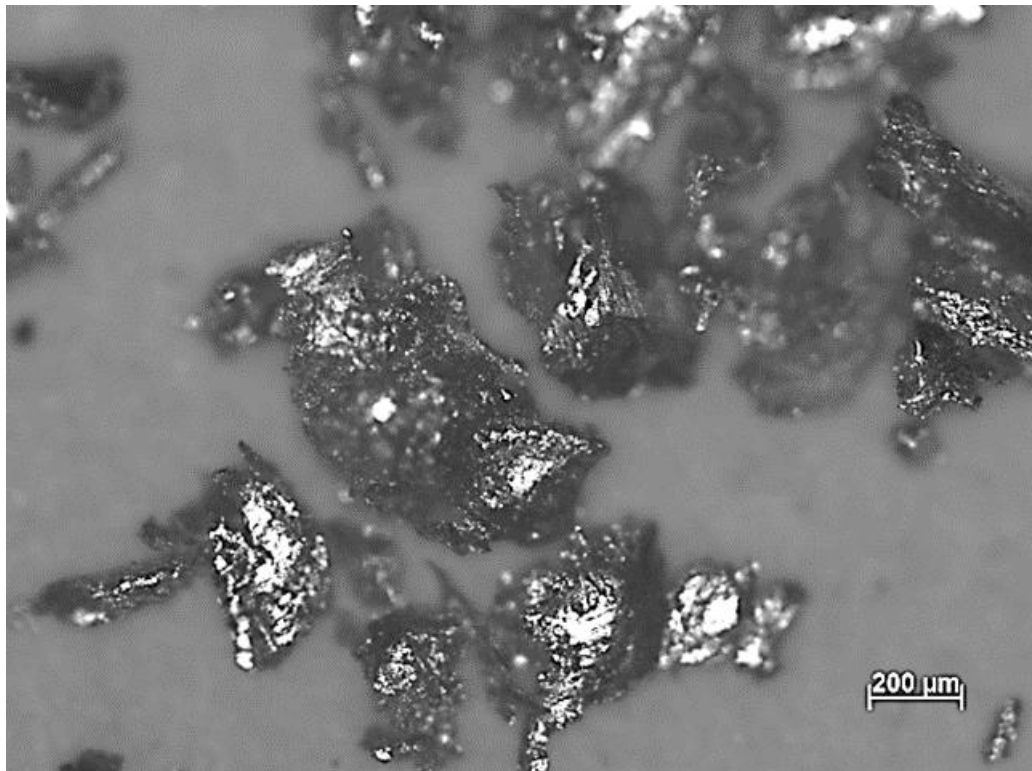
Figure 5.81: Micrograph of wear debris collected from experiments conducted at 1.5 kg normal load, 2 m/s sliding speed and at room temperature.
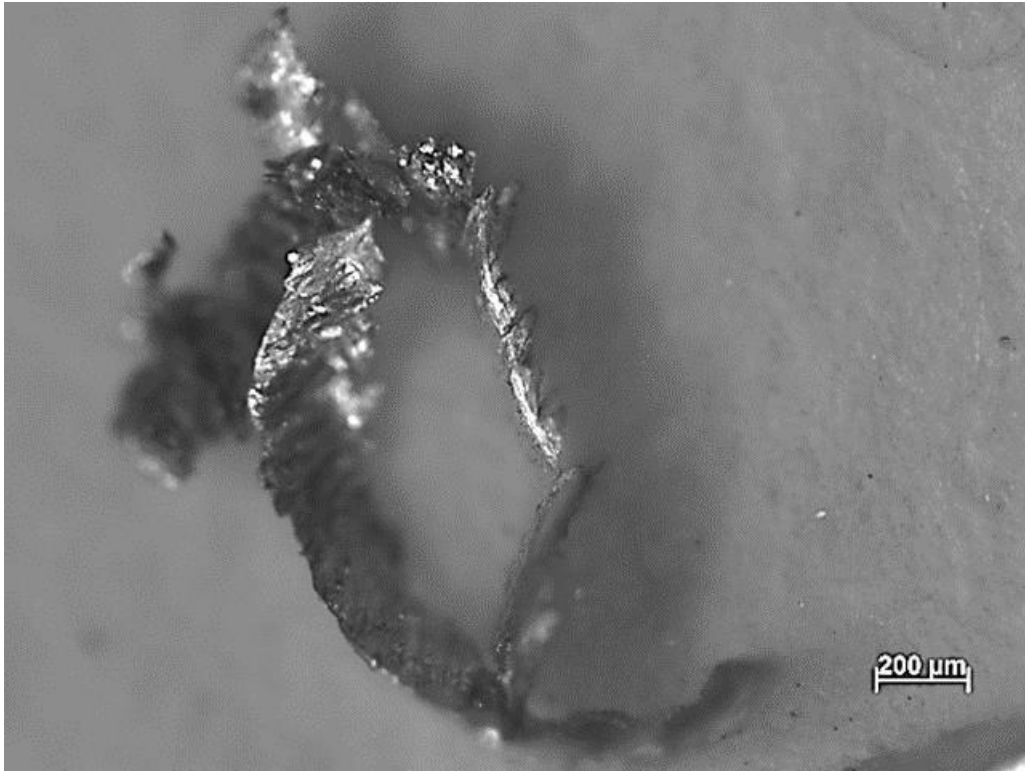
Figure 5.82: Micrograph of wear debris collected from experiments conducted at 2 kg normal load, 2 m/s sliding speed and at room temperature.
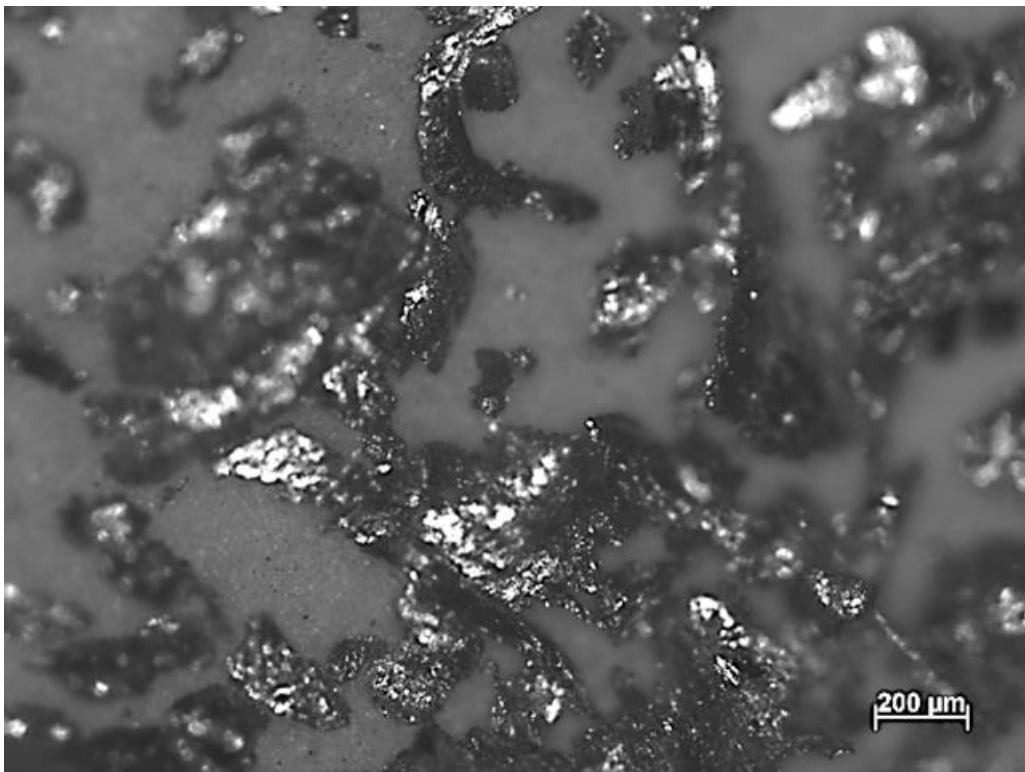
Figure 5.83: Micrograph of wear debris collected from experiments conducted at 1 kg normal load, 3 m/s sliding speed and at room temperature.
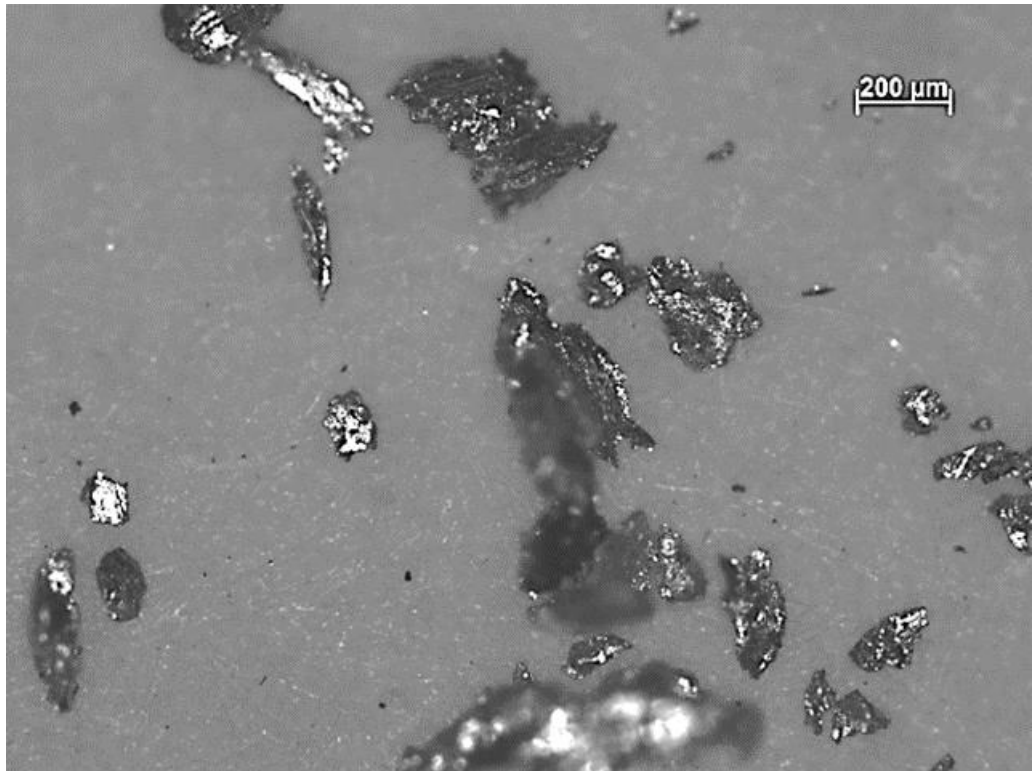
Figure 5.84: Micrograph of wear debris collected from experiments conducted at 1.5 kg normal load, 3 m/s sliding speed and at room temperature.
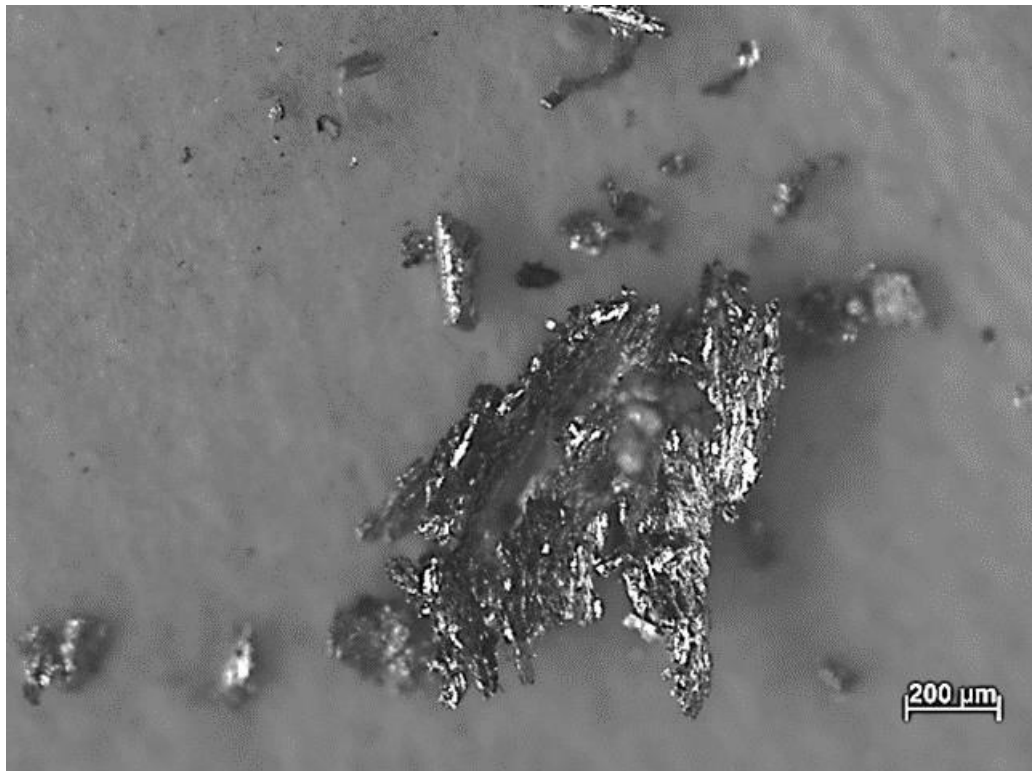
Figure 5.85: Micrograph of wear debris collected from experiments conducted at 2 kg normal load, 3 m/s sliding speed and at room temperature.

At higher temperature conditions, under 1 kg and 1.5 kg normal load conditions, the wear rate was less when compared to the wear rate at room temperature conditions. This may be due to stable oxide layer on contact surfaces at lower loading conditions (Ramesh et al., 2010). At any particular sliding speed the wear rate increased with increase in normal load and severe wear was observed at 2 kg normal load condition. At 100 °C temperature, 1 kg normal load and 3 m/s sliding speed, the negative wear indicates deposition of material to the pin specimen was more than the wear of the pin specimen. Material softening at higher temperature leads to higher flow of metal to the transverse side of the pin specimens during sliding (Figure 5.86 (d - l)). At lower normal loads (1 kg and 1.5 kg) and at higher temperatures Al 6061-T6 alloy showed better wear resistance when compared to that at room temperature. Figure 5.86 shows the cross-sections of worn pin specimens after the experiments conducted at different loading conditions. From Figure 5.83 (a-c), at room temperature, the wear of pin specimens increased with increase in normal load and sliding speed. Under room temperature, effect of normal load was more on wear when compared to the effect of sliding speed. From Figure 5.86 (d-f), at 60 °C temperature, more wear was observed at 1.25 m/s sliding speed when compared to 2 m/s and 3 m/s sliding speeds which may be due to formation of stable oxide layers at higher sliding speeds and wear increased with increase in normal load. From Figure 5.86 (g-i), at 100 °C temperature and 1 kg normal load conditions less wear was observed when compared to 60 °C temperature conditions. At 100 °C temperature, the wear was more influenced by normal load; due to softening of material severe wear was observed at 2 kg normal load condition. From Figure 5.86 (j-l), at 150 °C temperature, wear at 1 kg normal load conditions was less when compared to that at 60 °C and 100 °C temperature experimental conditions. Less wear at 1 kg normal load condition was due to formation of stable oxide layers at 150 °C temperature. As the sliding speed and normal load increased wear of pin specimen increased due to softening of materials and higher shear tractions at contact.
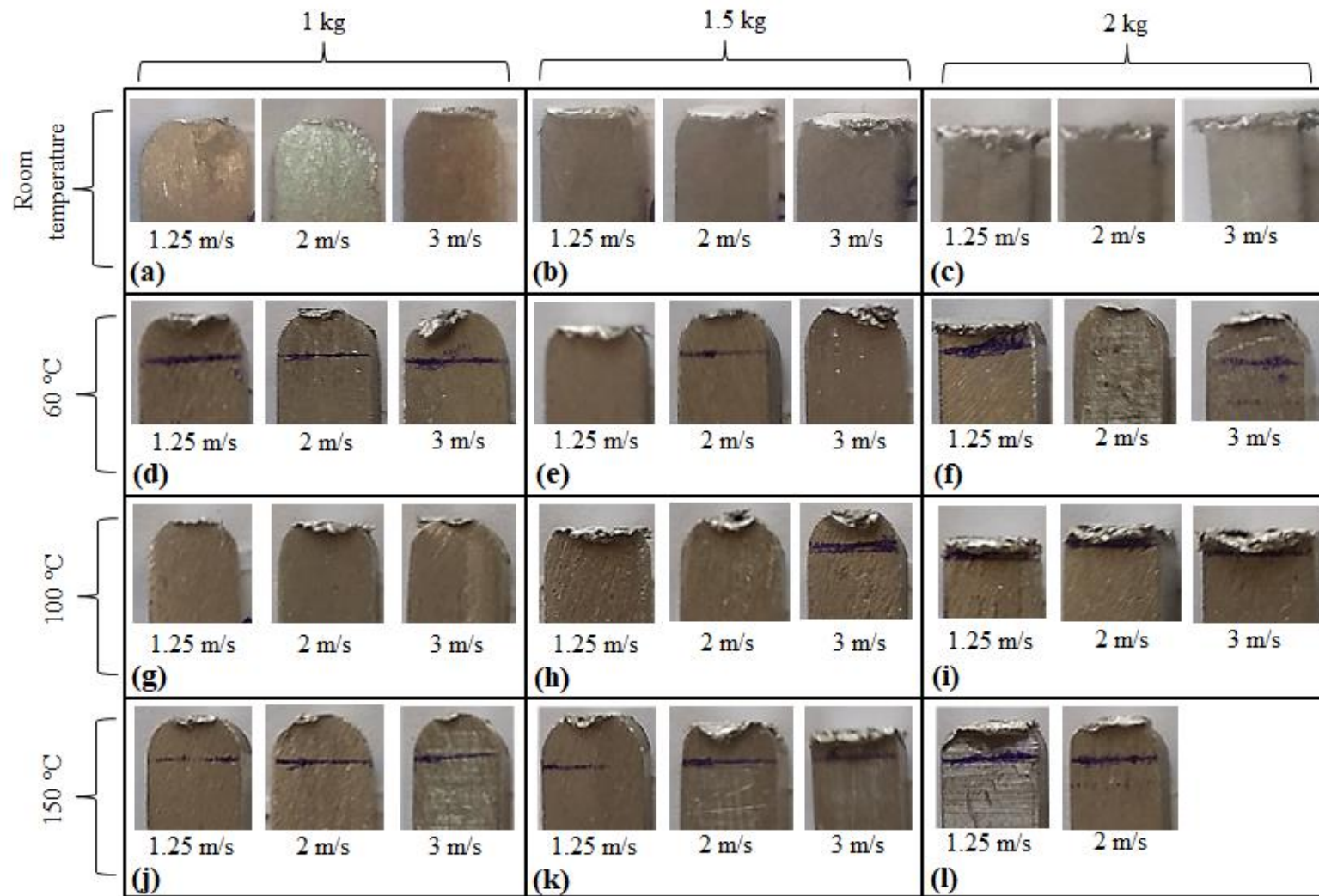
Figure 5.86: Micrographs of wear debris collected from experiments conducted at room temperature.

CHAPTER 6

CONCLUSIONS

Dry sliding coefficient of friction and wear of Al 6061-T6 alloy at different loading conditions (normal load and sliding speed) and at different temperatures were studied in detail and the following conclusions were drawn:

6.1 CONCLUSIONS FROM FRICTIONAL HEAT ESTIMATION

When two surfaces are sliding against each other, friction between the two surfaces generates heat at contact interface. The frictional heat is due to transformation of mechanical energy to heat energy. The resulted heat at contact interface changes the tribological properties of material which depends on several loading parameters. The contact interface temperature increased with increase in normal load and increase in sliding speed. Maximum contact interface temperature of 100 °C was observed at normal load of 2 kg and sliding speed of 3 m/s experimental condition. The proposed inverse heat transfer model is suitable for different type of materials where the physical problem having less convection losses. The proposed inverse heat transfer model can also be used to estimate the heat transfer coefficient during metal casting process and weld spot temperatures during welding process.

6.2 CONCLUSIONS FROM DRY SLIDING EXPERIMENTS

6.2.1 Coefficient of friction
- The initial coefficient of friction increased with the increase in normal load and sliding speed. Initial coefficient of friction decreased with the increase in temperature due to the formation of oxide layer on contact surfaces at higher temperatures when compared to the initial coefficient of friction obtained from experiments conducted at room temperature.
- The coefficient of friction stabilized at 5 m – 10 m sliding distance in all experimental conditions. Normal load showed a significant effect on stabilized coefficient of friction than on sliding speed. The stabilized coefficient of

friction increased with the increase in normal load and temperature, due to the softening of material and increase in contact area.

- At room temperature, the steady state coefficient of friction increased with the increase in normal load and temperature. At higher temperatures, a significant increase was observed in the steady state coefficient of friction at a normal load of 2 kg, due to the removal of oxide layer and the formation of metal-to-metal contact.

- The transition from unsteady state to steady state in evolution of coefficient of friction occurs at lesser sliding distance with increase in normal load, sliding speed and temperature.

- The unsteady state coefficient of friction decreased with the increase in sliding speed at 1 kg normal load, it increased with the increase in sliding speed at 2 kg normal load, and it did not change with the increase in sliding speed at 1.5 kg normal load.

- The transfer of material from pin surface to disk surface was observed from the formation of material lumps on the disk surface and this effect increased with the increase in temperature and sliding speed.

6.2.2 Wear

- From the microscopic observations of worn disk surfaces, adhesive wear and abrasive wear mechanisms were dominant in Al 6061-T6 alloy contacts. At room temperature, adhesive wear was observed at lower normal load and lower sliding speed conditions, wear mechanism changed to abrasive wear with increase in normal load and increase in sliding speed. At room temperature, wear rate decreased with increase in sliding speed from 1.25 m/s to 2 m/s and wear rate increased when sliding speed increased to 3 m/s. At higher temperatures, abrasive wear was dominant at 1 kg and 1.5 kg normal load conditions, at normal load of 2 kg wear mechanism changed to severe adhesive wear due to removal of unstable oxide layers.

- Wear rate of Al 6061-T6 alloy increased with increase in normal load. Wear resistance of Al 6061-T6 alloy improved with increase in temperature at 1 kg and 1.5 kg normal load conditions. But at 2 kg normal load, Al 6061-T6 alloy

showed more wear at higher temperatures when compared to that at room temperature.

6.3 LIMITATIONS OF THE STUDY

- The inverse heat transfer model used in this study was validated using *ANSYS* workbench. Validation of estimated contacted interface temperatures with experimentally measured contact interface temperatures can be considered for better reliability. Due to the lack of experimental facilities, the contact interface temperatures were not measured in the present study. The inverse heat transfer model used in this study is more suitable for pure conduction cases.

- The frictional heat can be estimated using tribological parameters (coefficient of friction and wear) instead of pure inverse heat transfer methods.

- The phase and chemical composition change of Al 6061-T6 alloys at higher temperatures can be conformed with SEM with EDX characterization.

- The effect of oxide layer thickness on coefficient of friction is not concentrated in this study.

6.4 SCOPE FOR FUTURE WORK

The present work can be extended to sub-zero temperature conditions, as Al 6061-T6 alloy is widely used in the aerospace industry. There is scope for improving the friction and wear characteristics of Al 6061-T6 alloy by using it as metal matrix to prepare new composite materials. The present work can be extended to choose a suitable surface coating material or a suitable solid lubricant to improve the friction and wear characteristics of Al 6061-T6 alloy. The results obtained from the present study can be used to calculate contact stresses in full sliding contacts. The present study concentrated on full sliding of aluminium-to-aluminium contacts. Tribological characteristics of Al 6061-T6 alloy at reciprocating partial slip conditions are useful for fretting studies on Al 6061-T6 alloy.

ANNEXURE I

```matlab
%one dimensional pure conduction heat transfer
problem,FEM for space and FDM for time.
clc;
clear;

%Material properties-----
%---Material – Al 6061-T6 alloy
k = 167; % Thermal conductivity in W/m.K
c = 896; % Specific heat in J/kg.K
d = 2700; % Density in kg/m^3
%---Material properties.

%Measured Temperature Data input-----
data = xlsread('FEM_FFDM_for_Time_AL6061T6.xlsx');
%-----Measured Temperature Data input.

%Mesh parameters-----
dx=0.001;% X-direction space step size in meters.
dt=0.2;% Time step size in seconds.
%-----Mesh parameters.

%geometry parameters-----
L =0.007;% distance between contact surface and
temperature measuring point (m)
tend = data(size(data,1),1);% total time duration in
seconds
A = (6*6)*10^-6; % Area of cross section
%-----geometry parameters.

%Constants required for the problem-----
M=L/dx; % M is number of elements
Pmax=(tend/dt); % Pmax is number of time steps
u=4; % u should be within the range of 2-5 as suggested
by "Z. Sun et al., 2011".
e=10^-4; % a constant for heat flux accuracy condition.
TL = 0.003; % Temperature data testing point length for
the pin surface in meters
TN = (TL/dx)+1; % Temperature data testing point node
number
%-----Constants required for the problem.

%initial and boundary conditions-----
for m=1:1:M+1
T(m,1)= data(1,3);
end
for p=1:1:Pmax
```

```matlab
T(M+1,p)=data(p,4);
end
T1 = T;
%-----initial and boundary conditions.

C = ((d*c*dx)/6)*[2 1;1 2];
K = ((k)/dx)*[1 -1;-1 1];
GC = zeros(M+1);
GK = zeros(M+1);
F = zeros(M+1,1);

for i=1:1:M

    for j=1:1:M

        if i==j
        GC (i,j)= GC (i,j)+ C (1,1);
        GK (i,j)= GK (i,j)+ K (1,1);

        GC (i,j+1)= GC (i,j+1)+ C (1,2);
        GK (i,j+1)= GK (i,j+1)+ K (1,2);

        GC (i+1,j)= GC (i+1,j)+ C (2,1);
        GK (i+1,j)= GK (i+1,j)+ K (2,1);

        GC (i+1,j+1)= GC (i+1,j+1)+ C (2,2);
        GK (i+1,j+1)= GK (i+1,j+1)+ K (2,2);
        end

    end

end
LGM = GC+ (dt*GK);
RGM = GC;
q(1)=0;
for p=2:1:Pmax
q(p)=1;
    for n=1:1:Inf
            for j=1:1:u
                con = zeros(M,1);
                for i=1:1:M
                con(i,1) = (RGM(i,M+1)*T(M+1,p-1+j-1))-
(LGM(i,M+1)*T(M+1,p+j-1));

                end

                F(1) = dt*q(p);
```

```matlab
            T(1:M,p+j-1)=
(LGM(1:M,1:M))\((RGM(1:M,1:M)*T(1:M,p-1+j-1))+F(1:M)+
con);
            end
            for j=1:1:u
                con = zeros(M,1);
                for i=1:1:M
                con(i,1) = (RGM(i,M+1)*T1(M+1,p-1+j-1))-
(LGM(i,M+1)*T1(M+1,p+j-1));

                end

                F(1) = dt*(1+e)*q(p);
                T1(1:M,p+j-1)=
(LGM(1:M,1:M))\((RGM(1:M,1:M)*T1(1:M,p-1+j-1))+F(1:M)+
con);
            end


            for j=1:1:u
            X(p+j-1)= (T1(TN,p+j-1) - T(TN,p+j-1)) /
(e*q(p));
            end
            denom=0;
            numer=0
            for j=1:1:u
            denom = denom+(X(p+j-1))^2;
            end
            for j=1:1:u
            numer = numer+(  (data(p+j-1,3)- T(TN,p+j-
1))*X(p+j-1));
            end
            dq(p)= numer/denom;
            qcor(p) = q(p)+dq(p);

            if (dq(p)/q(p))<=e

            break;
            else
            q(p)=qcor(p);
            end
    end

            q(p)
end
```

REFERENCES

- Adrian Bejan (1994). "Contact Melting Heat Transfer and Lubrication." *Advances in Heat Transfer*, 24, 1-38.

- Agbeleye, A. A., Esezobor, D. E., Balogun, S. A., Agunsoye, J. O., Solis, J. and Neville, A. (2017). "Tribological properties of aluminium-clay composites for brake disc rotor applications." *Journal of King Saud University – Science*, 32(1), 21-28.

- Alpas, A. T. and Zhang, J. (1992). "Wear rate transitions in cast Aluminum-Silicon alloys reinforced with SiC particles." *Scripta Metallurgica et Materialia*, 26, 505-509.

- Al-Qutub, A.M., Khalil, A., Saheb, N. and Hakeem, A.S. (2013). "Wear and friction behaviour of Al6061 alloy reinforced with carbon nanotubes." *Wear*, 297, 752–761.

- Ana Paula Fernandes, Marcelo Braga dos Santos and Gilmar Guimarães (2015). "An analytical transfer function method to solve inverse heat conduction problems." *Applied Mathematical Modelling*, 39(15), 6897-6914.

- Antonino Repaci (1991). "A nonlinear inverse heat transfer problem." *Computers & Mathematics with Applications*, 21(11–12), 139-143.

- Anyszka, R., Bieliński, D.M. and Strzelecki, D. (2015). "Tribological Properties of Silicone Rubber-Based Ceramizable Composites Destined for Wire Covers. Part I. Studies of Block-On-Ring Friction Contact." *Tribology in Industry*, 37(2), 154-160.

- Aweda, J.O. and Adeyemi, M.B. (2009). "Experimental determination of heat transfer coefficients during squeeze casting of aluminium." *Journal of materials processing technology*, 209, 1477–1483.

141

- Beck James, V., Ben Blackwell and Charles R. St. Clair Jr. (1985). "Inverse heat conduction. Ill-posed problems." John Wiley & Sons, Inc., A Wiley-Interscience Publication.

- Bill, R. C. (1983). "Fretting Wear and Fretting Fatigue—How Are They Related?." *ASME J. Lubr. Technol.*, 105, 230–238.

- Blau, PJ and Meyer III, HM. (2003). "Characteristics of wear particles produced during friction tests of conventional and unconventional disc brake materials." *Wear*, 255, 1261–1269.

- Borut Cerne, Joze Duhovnik and Joze Tavcar (2019). "Semi-analytical flash temperature model for thermoplastic polymer spur gears with consideration of linear thermo-mechanical material characteristics." *Journal of Computational Design and Engineering*, 6, 617–628.

- Chen, Q. and Li, D.Y. (2005). "A computational study of frictional heating and energy conversion during sliding processes." *Wear*, 259, 1382–1391.

- Choi, H.J., Lee, S.M. and Bae, D.H. (2010). "Wear characteristic of aluminum-based composites containing multi-walled carbon nanotubes." *Wear*, 270, 12–18.

- Christian Zeller, Binu Surendran and Micheal F. Zaeh (2018). "Parameterized Extended Finite Element Method for high thermal gradients." *Journal of Computational Design and Engineering*, 5, 329–336.

- Chunfeng Zhao, Zhen Luo, Yang Li, Mengnan Feng and Wenbo Xuan (2016). "Inverse heat conduction model for the resistance spot welding of aluminum alloy." *Numerical Heat Transfer, Part A: Applications*, 70(12), 1330–1344.

- Day, A. J. and Newcomb T. P. (1984). "The dissipation of frictional energy from the interface of an annular disc brake." *Proc lnstn Mech Engrs*, Vol 198D, No 11.

- Deuis, R. L., Subramanian, C. and Yellup, J. M. (1997). "Dry sliding wear of aluminium composites - a review." *Composites Science and Technology*, 57, 415-435.

- Dewan Muhammad Nuruzzaman and Mohammad Asaduzzaman Chowdhury (2012). "Effect of Normal Load and Sliding Velocity on Friction Coefficient of Aluminum Sliding Against Different Pin Materials." *American Journal of Materials Science*, 2(1), 26-31.

- Douglas Godfrey (1995). "Friction oscillations with a pin-on-disc tribometer." *Tribology International*, 28, 119-126.

- Erol Feyzullahoglu and Nehir Sakiroglu (2010). "The wear of aluminium-based journal bearing materials under lubrication." *Materials and Design*, 31, 2532–2539.

- Francis E. Kennedy, Yuan Lu and Ian Baker (2015). "Contact temperatures and their influence on wear during pin-on-disk tribotesting." *Tribology International*, 82, 534–542.

- Giovanni Straffelini and Alberto Molinari (2011). "Mild Sliding Wear of Fe–0.2%C, Ti–6%Al–4%V and Al-7072: A Comparative Study." *Tribol Lett*, 41, 227–238.

- Giovanni Straffelini (2015). "Friction and Wear: Methodologies for Design and Control" Switzerland: Springer International Publishing.

- Gupta, A. K., Kumar, P., Sahoo, R. K., Sahu, A. K. and Sarangi, S. K. (2017). "Performance measurement of plate fin heat exchanger by exploration: ANN, ANFIS, GA, and SA." *Journal of Computational Design and Engineering*, 4, 60–68.

- Habib Saeed Monir and Keyvan Zeynali (2013). "A modified friction damper for diagonal bracing of structures." *Journal of Constructional Steel Research*, 87, 17–30.

- Hegadekatte, V., Huber, N. and Kraft, O. (2006). "Modeling and Simulation of Wear in a Pin on Disc Tribometer." *Tribology Letters*, 24(1), 51-60.

- Hiroaki Nakanishi, Kenji Kakihara, Akinori Nakayama and Tomiyuki Murayama (2002). "Development of aluminum metal matrix composites (Al-MMC) brake rotor and pad." *JSAE Review*, 23, 365–370.

- Hosung Kong, Eui-Sung Yoon and Oh Kwan Kwon (1995). "Self-formation of protective oxide films at dry sliding mild steel surfaces under a medium vacuum." *Wear*, 181-183, 325-333.

- Howell, G. J. and Ball, A. (1995). "Dry sliding wear of particulate-reinforced aluminium alloys against automobile friction materials." *Wear*, 181-183, 379-390.

- Huttunen-Saarivirta, E., Kilpi, L., Hakala, T.J., Metsajoki, J. and Ronkainen, H. (2018). "Insights into the behaviour of tool steel-aluminium alloy tribopair at different temperatures." *Tribology International*, 119, 567–584.

- Ian Hutchings and Philip Shipway (2017). "Friction and Wear of Engineering Materials." Tribology (second edition).

- Imad H. Mualla and Borislav Belev (2002). "Performance of steel frames with a new friction damper device under earthquake excitation." *Engineering Structures*, 24, 365–371.

- Jerina, J. and Kalin, M. (2014). "Initiation and evolution of the aluminium-alloy transfer on hot-work tool steel at temperatures from 20 °C to 500 °C." *Wear*, 319, 234–244.

- Jiang Lan, Jiang Yan-Li, Yu Liang, Su Nan And Ding You-Dong (2012). "Thermal analysis for brake disks of SiC/6061 Al alloy co-continuous composite or CRH3 during emergency braking considering airflow cooling." *Trans. Nonferrous Met. Soc. China*, 22, 2783−2791.

- Johnson, K. L. (1985). "Contact Mechanics." Cambridge University Press.

- Joy Mathavan, J. and Amar Patnaik (2016). "Analysis of wear properties of aluminium based journal bearing alloys with and without lubrication." *IOP Conf. Series: Materials Science and Engineering*, 149, 012052.

- Kayaba, T. (1961). "A study of the wear and friction of some bearing Materials." *Wear*, 5, 173-181.

- Kim, I.-Y., Lee, J.-H., Lee, G.-S., Baik, S.-H., Kim, Y.-J. and Lee, Y.-Z. (2009). "Friction and wear characteristics of the carbon nanotube–aluminium composites with different manufacturing conditions." *Wear*, 267, 593–598.

- Komachi, Y., Tabeshpour, M. R., Golafshani, A. A. and Mualla, I. (2011). "Retrofit of Ressalat jacket platform (Persian Gulf) using friction damper device." *J Zhejiang Univ Sci A (Appl Phys & Eng)*, 12(9), 680-691.

- Korkut, M. H. (2003). "Microstructure and wear behaviour of Al2024\SiFe and Al2024\SiFe\Al2O3 composites." *Tribology International*, 36, 169–180.

- Kouami Auxence Melardot Aboua et al. (2019). "Effect of Carbon Diffusion on Friction and Wear Behaviors of Diamond-Like Carbon Coating Against Germanium in Boundary Base Oil Lubrication." *Tribology Letters*, 67, 65.

- Lee, H.-L., Lu, W.-H. and Chan, S.L.-I. (1992). "Abrasive wear of powder metallurgy Al alloy 6061-SiC composites." *Wear*, 159, 223–231.

- Like Pan, Jianmin Han, Zhiyong Yang, Jialin Wang, Xiang Li, Zhiqiang Li, and Weijing Li. (2017). "Temperature Effects on the Friction and Wear Behaviors of SiCp/A356 Composite against Semimetallic Materials." *Advances in Materials Science and Engineering*, 2017, Article ID 1824080, 12 pages, https://doi.org/10.1155/2017/1824080.

- Liliang Wang, Jingqi Cai, Jie Zhou and Jurek Duszczyk (2009). "Characteristics of the Friction Between Aluminium and Steel at Elevated Temperatures During Ball-on-Disc Tests." *Tribol Lett*, 36, 183–190.

- Lim, S. C. and Ashby, M. F. (1987). "Wear-mechanism maps." *Acta metall.*, 35(1), l-24.

- Liping Chen, Yingxin Wang, Liming Peng, Penghuai Fu and Haiyan Jiang (2014). "Study on the interfacial heat transfer coefficient between AZ91D magnesium alloy and silica sand." *Experimental Thermal and Fluid Science*, 54, 196–203.

- Maciej Dyzia (2017). "Aluminum Matrix Composite (AlSi7Mg2Sr0.03/SiCp) Pistons Obtained by Mechanical Mixing Method." *Materials*, 11, 42.

- Majcherczak, D., Dufrenoy, P. and Berthier, Y. (2007). "Tribological, thermal and mechanical coupling aspects of the dry sliding contact." *Tribology International*, 40, 834–843.

- Mark A. Sidebottom and Brandon A. Krick (2015). "Transducer Misalignment and Contact Pressure Distributions as Error Sources in Friction Measurement on Small-Diameter Pin-on-Disk Experiments." *Tribol Lett*, 58, 30.

- Matthias Scherge, Roman Böttcher, Alberto Spagni and Diego Marchetto (2018). "High-Speed Measurements of Steel–Ice Friction: Experiment vs. Calculation." *Lubricants*, 6, 26, doi:10.3390/lubricants6010026.

- Mikael Eriksson and Staffan Jacobson (2000). "Tribological surfaces of organic brake pads." *Tribology International*, 33, 817–827.

- Mondal, A, Chakraborthy, M and Murthy, BS. (2007). "Effect of TiB2 particles on sliding wear behaviour of Al–4Cu alloy." *Wear*, 262,160–166.

- Morton Antler (1981). "Sliding wear of metallic contacts." IEEE transactions on components, hybrids, and manufacturing technology, 4(1).

- Muhammad Ilman Hakimi Chua Abdullah et al. (2014). "Effect of hBN/Al$_2$O$_3$ Nanoparticle Additives on the Tribological Performance of Engine Oil." *Jurnal Teknologi (Sciences & Engineering)*, 66(3), 1–6.

- Murthy, H and Vadivuchezhian, K. (2017). "Estimation of friction distribution in partial-slip contacts from reciprocating full-sliding tests." *Tribology International*, 108, 164–173.

- Mythily Krishnan and Sharma, D.G.R. (1996). "Determination of the interfacial heat transfer coefficient h in unidirectional heat flow by Beck's non-linear estimation procedure." *Int. Comm. HeatMass Transfer*, 23(2), 203-214.

- Nakanishi, H, Kakihara, K, Nakayama, A and Murayama, T. (2002). "Development of aluminum metal matrix composite (Al-MMC) brake rotor and pad." *JSAE Rev*, 23, 365–70.

- Odabas, D. (2018). "The Influence of The Temperature on Dry Friction of AISI 3315 Steel Sliding Against AISI 3150 Steel." *IOP Conf. Series: Materials Science and Engineering*, 295.

- Pathak, J. P. and Mohan, S. (2005). "Wear of conventional and experimental aluminium bearing alloys sliding under lubrication." *Z. Metallkd.*, 96, 297-303.

- Peter J. Blau (2008). "Friction Science and Technology: From Concepts to Applications.", 2nd ed., Boca Raton: CRC Press.

- Piotr Grzes (2019). "Maximum temperature of the disc during repeated braking applications." *Advances in Mechanical Engineering*, 11(3), 1–13.

- Pujante, J., Pelcastre, L., Vilaseca, M., Casellas, D. and Prakash, B. (2013). "Investigations into wear and galling mechanism of aluminium alloy-tool steel tribopair at different temperatures." *Wear*, 308(1-2), 193-198.

- Radhika, N., Vaishnavi, A. and Chandran, G.K. (2014). "Optimisation of Dry Sliding Wear Process Parameters for Aluminium Hybrid Metal Matrix Composites." *Tribology in Industry*, 36(2), 188-194.

- Raghavendra, C. R., Basavarajappa, S. and Irappa Sogalad (2019). "Analysis of temperature field in dry sliding wear test on pin-on-disc." *Heat Mass Transfer*, 55, 1545–1552.

- Rajesh S. Godse, Shravan H. Gawande and Appasaheb A. Keste. (2016). "Tribological Behavior of High Fraction Carbon Steel Alloys." *J Bio Tribo Corros*, 2, 3.

- Ramesh, C. S., Keshavamurthy, R., Channabasappa, B. H. and Pramod, S. (2010). "Friction and wear behavior of Ni–P coated Si3N4 reinforced Al6061 composites." *Tribology International*, 43, 623–634.

- Ramesh, CS and Sheshadri, SK. (2003). "Tribological characteristics of nickel based composite coatings." *Wear*, 255, 893–902.

- Riahi, AR and Alpas, AT. (2001). "The role of tribo-layers on the sliding wear behaviour of graphite aluminium matrix composites." *Wear*. 251, 1396–407.

- Roamer Predmore, Jane Jellison, Charles L and Staugaitis (1970). "Friction and wear of steels in air and vacuum." NASA technical note, Washington, D.C., USA.

- Rubtsov, V. E. and Kolubaev, A. V. (2009). "Effect of Heat Generation Due to Plastic Deformation on Behavior of Surface-Layer Material during Sliding." *Journal of Friction and Wear*, 30(5), 324–328.

- Rusin, N. M., Skorentsev, A. L. and Kolubaev, E. A. (2016). "Dry Friction of Pure Aluminum against Steel." *Journal of Friction and Wear*, 37(1), 86–93.

- Sanjeev Das, Leonardo Pelcastre, Jens Hardell and Braham Prakash (2013). Effect of static and dynamic ageing on wear and friction behavior of aluminum 6082 alloy." *Tribology International*, 60, 1–9.

- Sarmistha Das, Varalakshmi, K., Jayaram, V. and Biswas, S. K. (2007). "Ultra Mild Wear in Lubricated Tribology of an Aluminium Alloy." *Journal of Tribology*, 129, 942-951.

- Sergey Yu. Krylov and Joost W. M. Frenken (2014). "The physics of atomic-scale friction: Basic considerations and open questions." *Phys. Status Solidi B*, 251(4), 711–736.

- Sharma, S.C. (2001). "The sliding wear behavior of Al6061–garnet particulate composites." *Wear*, 249, 1036–1045.

- Shorowordi K. M., Haseeb, A. S. M. A. and Celis, J. P. (2004). "Velocity effects on the wear, friction and tribochemistry of aluminum MMC sliding against phenolic brake pad." *Wear*, 256, 1176–1181.

- Shoubin Wang, Yuanzheng Deng and Xiaogang Sun (2018). "Solving of Two-Dimensional Unsteady Inverse Heat Conduction Problems Based on Boundary Element Method and Sequential Function Specification Method." *Complexity*.

- Shuaihang Pan, Nian Yin and Zhinan Zhang (2018). "Time- & Load-Dependence of Triboelectric Effect." *Scientific Reports*, 8, 2470, DOI:10.1038/s41598-018-20937-6.

- Singh, J. and Alpas, A.T.. (1995), "Elevated temperature wear of Al6061 and Al6061-20% Al_2O_3." *Scripta Metallurgica et Materialia*, 32(7), 1099-1105.

- Siva Sankara Raju, R., Panigrahi, M.K., Ganguly, R.I. and Srinivasa Rao, G. (2019). "Tribological behaviour of Al-1100-coconut shell ash (CSA) composite at elevated temperature." *Tribology International*, 129, 55–66.

- Srinivasa Raju, R., Jithender Reddy, G., Anand Rao, J. and Rashidi, M. M. (2016). "Thermal diffusion and diffusion thermo effects on an unsteady heat and mass transfer magnetohydrodynamic natural convection Couette flow using FEM." *Journal of Computational Design and Engineering*, 3, 349–362.

- Stachowiak, G.W. and Batchelor, A.W. (1993). "Corrosive and Oxidative Wear." *Engineering TriBology*, 24, 637-656.

- Sudarshan and Surappa, M. K. (2008). "Dry sliding wear of flyash particle reinforced A356Al composites." *Wear*, 265, 349–360.

- Suresh, S., Shenbaga Vinayaga Moorthi, N., Selvakumar, N. and Vettivel, S. C. (2014). "Tribological, tensile and hardness behavior of Tib_2 reinforced aluminium metal matrix composite." *Journal of the Balkan Tribological Association*, 20(3), 380–394.

- Suttera, G. and Ranc, N. (2010). "Flash temperature measurement during dry friction process at high sliding speed." *Wear*, 268, 1237–1242.

- Toshio Yoshimura and Kazushige Ikuta (1985). "Inverse heat-conduction problem by finite-element formulation." *International Journal of Systems Science*, 16(11), 1365-1375.

- Uthayakumar, M., Aravindan, S. and Rajkumar, K. (2013). "Wear performance of Al–SiC–B4C hybrid composites under dry sliding conditions." *Materials and Design*, 47, 456–464.

- Uyyuru, R.K., Surappa, M.K. and Brusethaug, S. (2007). "Tribological behavior of Al–Si–SiCp composites/automobile brake pad system under dry sliding conditions." *Tribology International*, 40, 365–373.

- Venkataraman, B and Sundararajan, G. (2000). "Correlation between the characteristics of the mechanically mixed layer and wear behaviour of aluminum, Al-7075 and Al MMCs." *Wear*, 245, 22–38.

- Viktoria Westlund, Jannica Heinrichs and Staffan Jacobson (2018). "On the Role of Material Transfer in Friction Between Metals: Initial Phenomena and Effects of Roughness and Boundary Lubrication in Sliding Between Aluminium and Tool Steels." *Tribology Letters*, 66, 97.

- Vilaseca, M., Molas, S. and Casellas, D. (2011). "High temperature tribological behaviour of tool steels during sliding against aluminium." *Wear*, 272, 105– 109.

- Vishweshwara, P. S., Gnanasekaran, N. and Arun, M. (2019). "Estimation of Interfacial Heat Transfer Coefficient for Horizontal Directional Solidification of Sn-5 wt%Pb Alloy Using Genetic Algorithm as Inverse Method." *Soft Computing for Problem Solving, Advances in Intelligent Systems and Computing*, 816, 447-459.

- Vishweshwara, P. S., Gnanasekaran, N. and Arun, M. (2020). "Inverse Approach Using Bio-Inspired Algorithm Within Bayesian Framework for the Estimation of Heat Transfer Coefficients During Solidification of Casting." *Journal of Heat Transfer*, 142, (012403-1)-(012403-11).

- Wang, Y., Rainforth, W. M., Jones, H., Lieblich, M. (2001). "Dry wear behaviour and its relation to micro structure of novel 6092 aluminum alloy– Ni3Al powder metallurgy composite." *Wear*, 251, 1421–1432.

- Wang, A. and Rack, H. J. al. (1991). "Transition wear behavior of SiC-particulate- and SiC-whiskerreinforced 7091 A1 metal matrix composites." *Materials Science and Engineering: A*, 147, 211-224.

- Wang, D. Z., Peng, H. X., Liu, J. and Yao, C. K. (1995). "Wear behaviour and microstructural changes of SiCw-Al composite under unlubricated sliding friction." *Wear*, 184, 187-192.

- Wang, L., He, Y., Zhou, J. and Duszczyk, J. (2010). "Effect of temperature on the frictional behaviour of an aluminium alloy sliding against steel during ball-on-disc tests." *Tribology International*, 43, 299–306.

- Wen Gao, Yong Lian, Guoliang Xie, Jinfeng Huang, Le Zhang, Minyu Ma, Chao Zhao, Zunjun Zhang, Kai Liu, Shuguang Zhang and Jin Zhang (2018). "Study of dry sliding wear characteristics of stellite 6B versus AISI M2 steel at various sliding velocities." *Wear*, 402–403, 169–178.

- Yarimitsu, S., Sasaki, S., Murakami, T. and Suzuki, A. (2016). "Evaluation of lubrication properties of hydrogel artificial cartilage materials for joint prosthesis." *Biosurface and Biotribology*, 2, 40–47.

- Yuchun Huang, Xiaoliang Shi, Kang Yang, Jialiang Zou, Qiao Shen, Yufu Wang, and Zhihai Wang (2017). "Effects of Friction Layer Thickness on the Tribological Performance of Ni3Al-Ag-MoO3." *Journal of Materials Engineering and Performance*, 26, 2313–2321.

- Zhang, A., Liang, S., Guo, Z. and Xiong, S. (2017). "Determination of the interfacial heat transfer coefficient at the metal-sand mold interface in low pressure sand casting." *Experimental Thermal and Fluid Science*, 88, 472–482.

- Zhang Xiao-Yu, Ren Ping-Di, Zhong Fa-Chun, Zhu Min-Hao And Zhou Zhong-Rong (2012). "Fretting wear and friction oxidation behavior of 0Cr20Ni32AlTi alloy at high temperature." *Trans. Nonferrous Met. Soc. China*, 22, 825-830.

- Zhizhong Sun, Henry Hu and Xiaoping Niu (2011). "Determination of heat transfer coefficients by extrapolation and numerical inverse methods in squeeze casting of magnesium alloy AM60." *Journal of Materials Processing Technology*, 211, 1432–1440.

- Zhou Sheng-ming, Xiao-bin Zhang, Zhi-peng Ding, Chun-yan Min and Guo-liang Xub Wen-ming Zhu (2007). "Fabrication and tribological properties of carbon nanotubes reinforced Al composites prepared by pressureless infiltration technique." *Composites Part A: Applied Science and Manufacturing*, 38(2), 301-306.

PUBLICATIONS BASED ON PRESENT RESEARCH WORK

International Journals

1. **I. Srinivasula Reddy**, Vadivuchezhian Kaliveeran, "Coefficient of friction of dry sliding Al 6061-T6 alloy under different loading conditions." World Journal of Engineering, https://doi.org/10.1108/WJE-06-2020-0212.

2. **I. Srinivasula Reddy**, Vadivuchezhian Kaliveeran, "Dry sliding friction and wear of Al 6061 and Al 6082 alloys under different normal loads." Materials Today: Proceedings, Vol. 27, pp 2631-2634 (2019), https://doi.org/10.1016/j.matpr.2019.11.080.

3. **Srinivasula Reddy I.**, Vadivuchezhian Kaliveeran, "Sliding of various ductile materials (Al 6061, Al 6082) using pin on disc setup." Materials Today: Proceedings, Vol. 27, pp 2688-2692 (2019), https://doi.org/10.1016/j.matpr.2019.11.248.

4. **I. Srinivasula Reddy**, Vadivuchezhian Kaliveeran, "Wear of dry sliding Al 6061-T6 alloy under different loading conditions." International Journal of Surface Engineering and Interdisciplinary Materials Science (IJSEIMS). (**Accepted**).

International Conferences

1. **Srinivasula Reddy I.**, Vadivuchezhian Kaliveeran, "Combined effect of temperature and contact pressure on coefficient of friction of dry sliding Al6061 T6 alloy contacts", Materials and Manufacturing Methods - 2019, July 5 – 7, 2019, NIT Tiruchirappalli, India.

2. **Srinivasula Reddy I.**, Vadivuchezhian Kaliveeran, "Effect of normal load on Coefficient of Friction of Al 6061 and Al 6082 Alloy contacts", 3rd International Conference on Advanced Materials and Manufacturing Processes for Strategic Sectors (ICAMPS2018), October 25-27, 2018, Thiruvananthapuram.

3. **Srinivasula Reddy I.**, Vadivuchezhian Kaliveeran, Gowtham S. and Ramesh M. R., "Wear tests on Aluminium alloys (Al 6061 and Al 6082) under dry

sliding condition using pin on disk tribometer", International Conference on Recent Advances in Material Chemistry (ICRAMC 2017), Chennai, India.

CURRICULUM VITAE

Name : SRINIVASULA REDDY I.

Permanent Address:

Tallur (Village), Tallur (Mandal), Prakasham (District), Andhra Pradesh, PIN:- 523264.

Contact No.   : +91-8985717578.

Email ID   : reddysrinu67@gmail.com

Education:

Master of Technology (2013-2015)

Discipline   : Marine Structures.

College   : Indian Institute of Technology Karnataka, Surathkal.

Bachelor of Engineering (2008-2012)

Discipline   : Civil Engineering

College   : Pondicherry Engineering College, Puducherry.